Fractional Slot Concentrated Winding Interior Permanent Magnet Machines with Reluctance Torque: Inductance-Based Methodology for Comprehensive Analysis, Design, and Control

FRACTIONAL SLOT CONCENTRATED WINDING INTERIOR PERMANENT MAGNET MACHINES WITH RELUCTANCE TORQUE: INDUCTANCE-BASED METHODOLOGY FOR COMPREHENSIVE ANALYSIS, DESIGN, AND CONTROL

By

Hao Ge, M.A.Sc., B.Sc.

A Thesis
Submitted to the School of Graduate Studies
in Partial Fulfillment of the Requirements
for the Degree
Doctor of Philosophy

McMaster University

DOCTOR OF PHILOSOPHY (2016) McMASTER UNIVERSITY
(Electrical & Computer Engineering) Hamilton, Ontario

TITLE: **Fractional Slot Concentrated Winding Interior Permanent Magnet Machines with Reluctance Torque: Inductance-Based Methodology for Comprehensive Analysis, Design, and Control**

AUTHOR: Hao Ge
M.A.Sc.
School of Electrical Engineering & Automation
(Harbin Institute of Technology, Harbin, China)

SUPERVISOR: Ali Emadi, Professor
Ph. D. (Texas A&M University)
IEEE Fellow
Canada Excellence Research Chair Hybrid Powertrain Program

NUMBER OF PAGES: XXI, 216

谨以此献给我的家人

To My Family

ABSTRACT

This thesis studies the inductance based methodology for analysis, design and control of fractional slot concentrated winding (FSCW) interior permanent magnet (IPM) machines.

The properties of FSCW are studied analytically based on the modified winding function method, which is developed based on turns function. The modified winding function method simplifies the inductance analysis of FSCW. The closed form representations of air gap inductance and mutual inductance are obtained. The inductance properties of FSCW machines with salient rotors are investigated by exploring the flux line distributions, and the equivalent air gap lengths of *d*- and *q*-axis are approximated. The inductance difference between *d*- and *q*-axis of the FSCW machine is obtained analytically and compared with the integer slot distributed winding (ISDW) machines.

An FSCW IPM machine design methodology is proposed. The relationship between the mechanical output characteristic and parameters is established, which guides the machine topology selection. The machine geometry model is developed parametrically and optimized using the response surface method (RSM), which enables the optimization to be implemented with reduced computational effort. The performances of the designed FSCW IPM machine are evaluated by comparing with the traditional designs, and it shows advantages in terms of torque capability and/or losses.

The comprehensive mathematical model of the FSCW permanent magnet synchronous machine (PMSM) is obtained, which is different from idealized PMSM model and features extra coupling terms. However, for symmetric 3-phase machines, if the windings are Y connected, the coupling terms only introduces 3rd order harmonic to *0*-axis, and the field oriented control (FOC) can still be applied. The optimal current control strategies are proposed based on nonlinear optimization algorithm. The global loss minimization and the current minimization are developed and validated by finite element analysis (FEA) and/or experiments.

The FSCW IPM machine is prototyped and tested. A simplified characterization method is developed based on the machine drive. It utilizes the voltage and current variables in the control loop to identify the flux linkage characteristics. The current minimization based optimal current control is achieved. When torque feedforward control is applied, the machine output performance, including torque capability, torque accuracy, efficiency and current transition are validated. Thermal performance of the machine is evaluated under continuous power operation and peak power operation. The FEA based thermal model is developed and calibrated using steady state experimental results. The transient thermal performance is studied by simulations and verified by experiments.

ACKNOWLEDGEMENT

First and foremost, I would like to express my gratitude to my supervisor, Dr. Ali Emadi, for his guidance, support, trust and patience on me and my research work. It has been my great honor to work with him. His motivation, enthusiasm and visionary strategies guided me through my Ph.D study, and will guide me for the rest of my life.

I would like to thank my former supervisor and colleagues. Special thanks go to Prof. Shumei Cui, who encouraged me to pursue higher level of studies. Her wisdom and broad vision has enlightened not only my research but also my life. Special thanks go to my best friend, Fan Wu, for sharing his expertise without reservation. Our endless discussion made this research program a pleasant experience.

I would also like to thank Dr. Nigel Schofield and Dr. Berker Bilgin, and my committee meeting members, Dr. Mohamed Bakr, and Dr. Shahin Sirouspour, for their insightful comments and stimulating discussions throughout my Ph.D program.

I am grateful to my colleagues in the Canada Excellence Research Chair in Hybrid Powertrain Program. I would like to thank James Jiang, Jin Ye, Haizhong Ye and Dan Manolescu for reading the thesis and for their valuable comments. Special thanks go to Fei Peng, Yu Miao, Earl Fairall and William Long for sharing their expertise and assisting with the experiments. Special thanks go to Theresa Mitchell and Dan Manolescu, who helped organize and coordinate the research needs. I want to thank

Michael Eull, Ran Gu, Yinye Yang and everyone in the lab for working and spending time together.

I further would like to thank Edward from Kries Manufacturing Inc., and Michael from Advanced Motor Solutions for their help on the prototype machining and winding. Their quality work and valuable advice made the prototype a success.

Words cannot express how grateful I am to my families for all of their encouragements, sacrifices and unwavering supports. Especially I would like to thank my wife, Ying Cui, for her sacrifice and being supportive from the beginning, thank her for being by my side and making my life colorful.

This research was undertaken, in part, thanks to funding from the Canada Excellence Research Chairs Program and the Natural Sciences and Engineering Research Council of Canada. The author also gratefully acknowledges ANSYS and JMAG for their support with Maxwell and Jmag software in this research.

CONTENTS

LIST OF FIGURES

LIST OF TABLES

LIST OF ABBREVIATIONS

2D	two dimensional
3D	three dimensional
CPSR	constant power speed range
DL	double layer
EMF	electromotive force
FEA	finite element analysis
FOC	field oriented control
FSCW	fractional slot concentrated winding
IPM	interior permanent magnet
ISDW	integer slot distributed windings
MCSRM	mutual coupled switched reluctance machine
MMF	magnetomotive force
MTPA	maximum current per ampere
MTPF	maximum torque per flux
PM	permanent magnet
PMSM	permanent magnet synchronous machine
RSM	response surface method
SL	single layer
SPM	surface mount permanent magnet
SPP	slot/pole/phase
SRM	switched reluctance machine
SynRM	synchronous reluctance machine

This page is intentionally left blank

Chapter 1
INTRODUCTION

1.1. BACKGROUND

Electric vehicles, including battery electric vehicles, hybrid electric vehicles and plug-in hybrid electric vehicles, improve fuel economy and reduce emissions. Electrical machines are the key enabler for vehicle electrification [1]. There are several desired features for electrical machines in vehicle traction application [2]:

1. High power density and high torque density,
2. Wide constant power speed range (CPSR),
3. High efficiency over wide torque-speed range,
4. High reliability and robust operation, and
5. Low cost.

Most commercial automakers, such as Toyota, GM, and Nissan, focus on interior permanent magnet (IPM) machines with conventional integer slot distributed windings (ISDW), because they feature high torque/power density and high saliency ratio, which enables wide CPSR operation. Fig. 1.1 illustrates the 3D model of 2004 Toyota Prius motor [3].

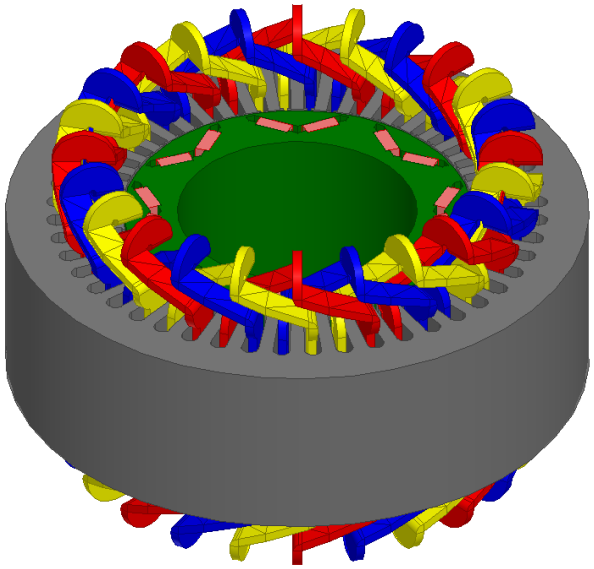

Fig. 1.1. 3D model of Toyota Prius 2004 motor [3].

In order to achieve high electromagnetic and thermal performances, high slot fill factor is desired. However, for the conventional ISDWs, the slot fill factor is typically around 35% due to the overlapped winding topology [4], and it is difficult to fabricate the stator winding.

The winding configurations with non-overlapping, concentrated, either all teeth wound or alternate teeth wound coils, are referred to as fractional slot concentrated winding (FSCW) for the rest of the thesis. The FSCW features short end winding compared to the conventional ISDW, which reduces the winding resistance and overall length of the machine [5, 6]. Therefore, high power density and torque density can be achieved [7]. Additionally, the concentrated winding topology simplifies the fabrication process and improves the winding insulation, which helps reduce the cost and improve the reliability.

1.2. OBJECTIVES

Current research of the FSCW permanent magnet (PM) machines mostly focus on the surface mount permanent magnet (SPM) machine. The knowledge of the IPM machines equipped with FSCW is still quite limited.

The primary objective of this thesis is to investigate the reluctance torque capability of FSCW machines with salient rotors. This research attempts to deliver the knowledge of achievable reluctance torque of this type of machine and contribute to the fundamental analysis method of FSCW machines.

The secondary objective of this thesis is to design a FSCW IPM machine for a light weight electric vehicle with reduced magnets. The topology selection and geometry optimization need to be investigated.

The third objective is to develop an optimal control strategy. The comprehensive mathematical model of FSCW IPM machine is derived. The optimal current control strategy is studied.

The fourth objective is to build a FSCW IPM machine prototype. The machine parameters and flux linkage characteristics should be identified. The output performance, including the torque capability and efficiency, need to be measured and validated. The thermal performance should be verified experimentally.

1.3. CONTRIBUTIONS

The author contributes to several original developments that are presented in this thesis and briefly summarized as follows:

1. The modified winding function method is derived, which simplifies the winding inductance analysis for FSCW.
2. The comprehensive inductance analysis of FSCWs is performed and the results are summarized for future reference.
3. The inductance analysis of FSCW machines with salient rotors is presented.
4. *d*- and *q*-axis inductance difference of FSCW machines with salient rotors are derived and compared to the ISDW machines.
5. The relationship between the torque-speed characteristic and the machine parameters is established based on the normalized characteristic current and saliency ratio.
6. A FSCW IPM machine is designed, and the machine shows its advantages over traditional FSCW designs with reduced magnets and improved torque capability.
7. The modified response surface method (RSM) is applied to minimize the torque ripples at different excitations, and the computational effort can be significantly reduced.
8. A thin rotor yoke design is proposed to reduce the core loss and/or increase the torque capability of FSCW IPM machines.

9. A comprehensive mathematical model of FSCW PM machine is derived. It is proven that field oriented control (FOC) can be applied if the windings are Y connected.
10. The optimal control strategies of PM machines are proposed based on nonlinear optimization algorithm.
11. The simplified parameter and flux linkage characterization method for PM machine is proposed using the inverter control variables.
12. The extended maximum torque per ampere (MTPA) control strategy is applied to the prototype machine in the feedforward control loop. The torque control accuracy, efficiency map, and transient operation are measured.

1.4. THESIS OUTLINE

This thesis is organized as follows:

Chapter 2 gives the literature review of the concentrated winding PM machines.

Different topologies of stator PM and rotor PM machines are introduced first. A brief comparison between the stator PM and rotor PM machines is performed. State of art of the FSCW PM machines is reviewed. The manufacturing technologies of the concentrated windings are summarized.

Chapter 3 presents the comprehensive inductance analysis of FSCW machines.

The modified winding function method is proposed for the inductance computation. Detailed inductance analysis of the FSCW is presented for both double layer (DL) and

single layer (SL) windings. The *d*- and *q*-axis inductances of the FSCW machine are calculated. The reluctance torque capability of the FSCW IPM machine is computed based on the *d*- and *q*-axis inductance difference, and it is compared with the ISDW machine. All the analyses are validated by FEA simulations.

Chapter 4 focuses on the FSCW IPM machine design.

A normalized mathematical model of permanent magnet synchronous machine (PMSM) is developed. The relationship between the characteristic current, saliency and machine output characteristic is established. Thin rotor yoke bridge is employed to enhance the reluctance torque and reduce core losses. The machine geometry is optimized employing the RSM. The performance of the designed machine is compared with several traditional designs, and it shows advantages in terms of torque capability and losses.

Chapter 5 proposes the control model of FSCW IPM machine and the optimal control strategies of PMSM.

The control model of FSCW IPM is derived first based on the inductance analysis. It is observed that there is cross coupling between *d*-, *q*-axis and *0*-axis. However, FOC can be applied if the 3-phase winding is Y connected. Optimal current control strategies of PMSM are proposed based on nonlinear programming. The optimal current profiles of the designed machine are obtained, and the torque-speed profile and efficiency map are predicted.

Chapter 6 presents the experimental results of the prototype.

The prototyping procedure is introduced briefly first. The characterization method of the machine is discussed systematically, and the machine and its drive are characterized experimentally. The optimal current control profiles are obtained using the characterized flux linkage. When the optimal current is applied on the torque feedforward control loop, the torque control accuracy and efficiency are measured experimentally. The FEA based thermal model is developed and calibrated using the steady state experimental measurements. The transient thermal performance of the machine is simulated and verified by experiments.

Chapter 7 concludes the thesis and presents the possible future work.

This page is intentionally left blank

Chapter 2
REVIEW OF FRACTIONAL SLOT CONCENTRATED WINDING PM MACHINES

2.1. CONCENTRATED WINDING PM MACHINE TOPOLOGIES

2.1.1. Rotor PM Topologies

The PM rotors are the most popular topologies. According to the location of the magnets, they can be categorized into surface mount PM rotor, surface inset PM rotor and interior inset PM rotors, as shown in Fig. 2.1. The interior inset rotors generally have two configuration, radial flux and tangential flux, as shown in Fig. 2.1 (c) and (d).

There are other morphed rotor topologies, as shown in Fig. 2.2. The magnet can be shaped for better air gap flux density distribution or manufacturing reasons. For example, Fig. 2.2 (a) illustrates a modified surface mount PM rotor. The bottom of the magnets is flat for easy mounting, and the top of the magnets is shaped to achieve sinusoidal or rectangular flux density distribution. More morphed topologies can be found for the interior PM rotors, as shown in Fig. 2.2 (b)-(d). The magnets can be arranged as V-shape or U-shape, and they can be arranged with multiple layers. The PM excited rotor configurations can be paired with either ISDW or FSCW stators.

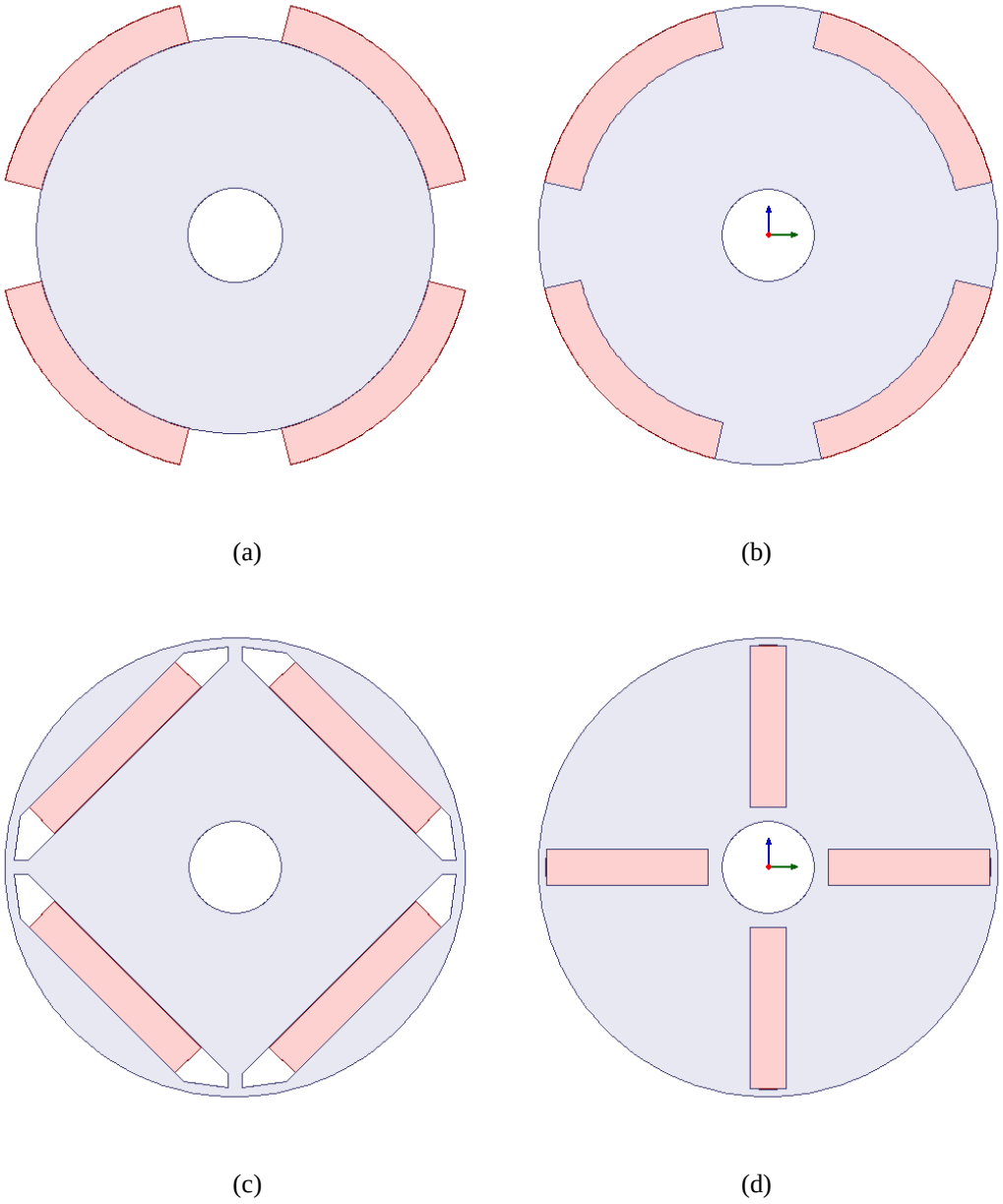

(a) (b)

(c) (d)

Fig. 2.1. Rotor PM topologies: (a) surface mount, (b) surface inset, (c) internal inset, radial flux, and (d) internal inset, tangential flux.

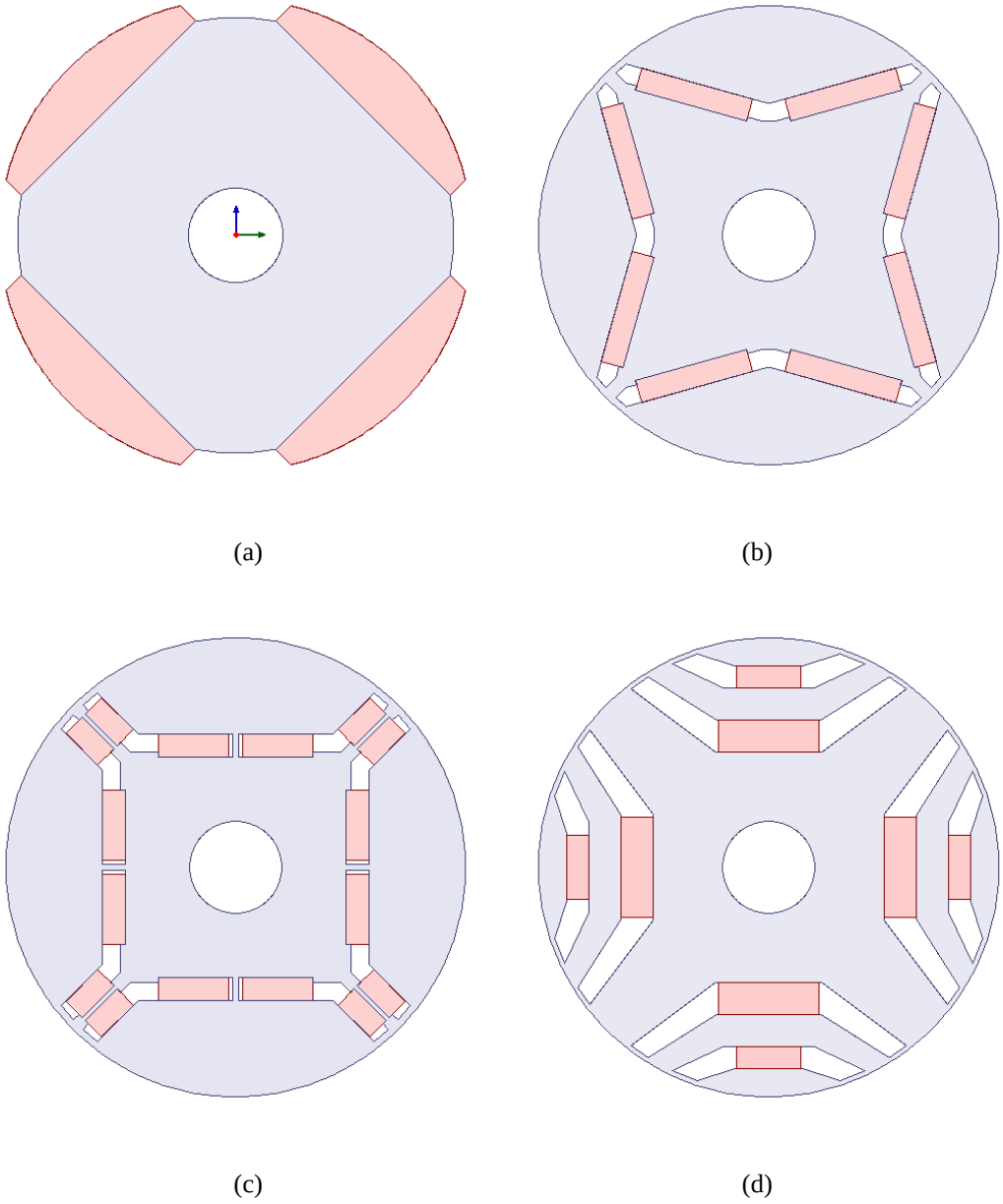

(a) (b)

(c) (d)

Fig. 2.2. Morphed rotor PM topologies: (a) surface mount PM with flat bottom and/or shaped arc, (b) internal inset, single layer V-shape PM, (c) internal inset, single layer U-shape PM, and (d) internal inset, multi-layer PM.

2.1.2. Stator PM Topologies

The mostly commonly known stator PM topologies are the double salient PM machines (also referred to as permanent magnet switched reluctance machine) and the switched flux PM machines (also referred to as flux switching machine), as shown in Fig. 2.3 (a) and (b) respectively. Both types of machines have double salient structure and concentrated windings. By locating the magnets in the stator, direct cooling of magnets becomes possible, which reduces the risk of demagnetizing and makes the stator PM brushless machines promising for vehicle applications. However, the segmented type stator reduces the rigidity and circularity.

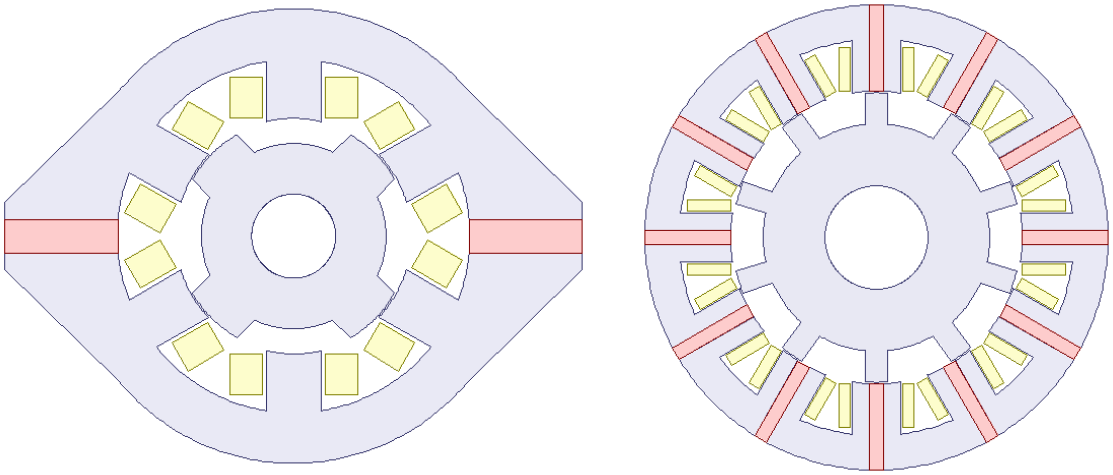

(a) (b)

Fig. 2.3. Stator PM topologies: (a) double salient PM machine, (b) flux switching PM machine.

Other topologies of stator PM machines are also found in literatures. The magnets can be located at different positions of the stator. For example, the magnets can be arranged on the top of stator teeth to construct PM flux reversal machine [8, 9], as shown

in Fig. 2.4 (a). A noval switched reluctance machine (SRM) with magnets between the stator teeth is presented in [10], as shown in Fig. 2.4 (b).

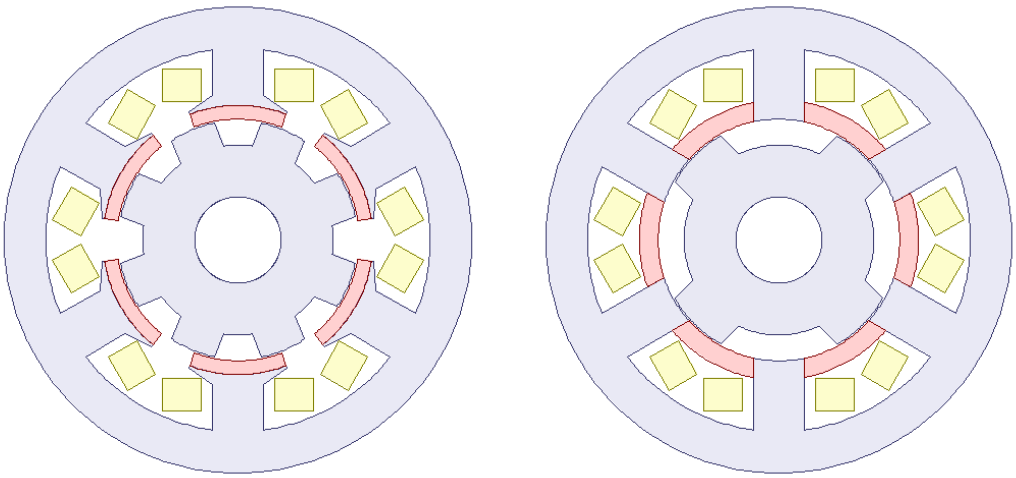

(a) (b)

Fig. 2.4. Alternative stator PM topologies: (a) PM flux reversal machine, (b) novel SRM with PM between stator teeth tip.

These types of machines share identical salient pole rotor and similar stator topologies (they all have salient pole structure). Despite of the double salient structure, the torque is predominantly produced by the interaction of PM flux and current, although the torque production mechanism does rely on the rotor saliency [11].

A comprehensive comparison between the stator PM switched flux machine and the rotor PM FSCW machine is performed in [12]. The stator PM switched flux machine is able to produce equivalent torque compared to the rotor PM machine. However, more amount of PM is required. Hence the utilization of PM material is significantly lower for PM switched flux machine. The comparison between the stator PM flux reversal machine

and the rotor PM FSCW machine is presented in [13]. The comparisons of efficiency and power factor suggest that the rotor PM machine has higher efficiency and power factor.

In general, rotor PM machine enables higher utilization of PM, and both PM and reluctance contribute to total torque production. Additionally, the stator PM machine may suffer higher cogging torque and torque ripple due to the double salient structure.

2.2. FRACTIONAL SLOT CONCENTRATED WINDING PM SYNCHRONOUS MACHINE

The FSCW PM machines have been practically applied by automotive industry. For example, Bosch has launched the integrated motor generator for single or dual clutch parallel hybrid system [14, 15], as shown in Fig. 2.5. The employment of the concentrated winding enables high performance machine design in pancake shape volume.

Fig. 2.5. Bosch integrated motor generator [15].

The winding configuration with all teeth wound, as shown in Fig. 2.6 (a), is referred to as DL winding. The winding configuration with alternative teeth wound, as shown in Fig. 2.6 (b), is referred to as SL winding.

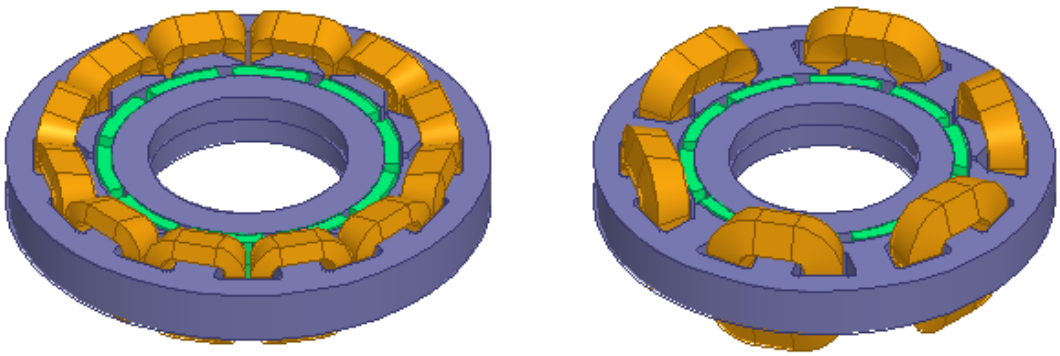

(a) (b)

Fig. 2.6. 3D model of FSCWs: (a) all teeth wound, DL, (b) alternative teeth wound, SL.

2.2.1. Advantages and Disadvantages

FSCW features several advantages and disadvantages compared to ISDW. The main advantages are summarized as follows:

1. Shorter end winding with reduced winding resistance and overall length;
2. Slot fill factor can be improved, hence the winding resistance is reduced and slot thermal conductivity is improved;
3. High power density and high efficiency due to reduced copper loss;
4. Low cogging torque;
5. Significantly reduced coil number;

6. Simplified winding insulation with improved insulation class [16]; and
7. Automatic winding technologies can be applied.

In conventional ISDW machine, the working harmonic (the harmonic which interacts with rotor flux to produce torque) of stator magnetomotive force (MMF) is the 1st order harmonic and there are odd number high order harmonics, which normally are much lower than the fundamental harmonic. However, the FSCW produces non-sinusoidal MMF along the air gap. The working harmonic is no longer the 1st order harmonic, and it contains rich contents of both low and high order harmonics. As a result, the main disadvantage of the FSCW is that high core losses are induced. In fact, researches have shown that the core losses are mainly due to the low order harmonics [17]. However, on the other hand, the excessive harmonic contents increase the leakage inductance, and enhance the field weakening capability.

2.2.2. Teeth/Pole Combination

For FSCW configuration, the teeth/pole combination is often referred to as slot/pole combination in literatures. The use of concentrated windings in high-performance PM machines is discussed in [6], where various teeth/pole combinations which enable balanced 3-phase windings are presented. The optimum winding layout is discussed systematically for regular and irregular slots distributions. The slot/pole/phase (SPP) number is identified within 1/2 to 1/4 to achieve high winding factor. The feasible teeth/pole combinations are summarized in [18]. The winding factor calculation method is presented systematically in [5] using winding phasors. The star of slots method is

proposed in [19] and [20] for the optimal winding layout design, and the winding factor can be obtained accordingly. In [20], using the star of slots method to determine the magnitudes of MMF harmonics is also introduced.

2.2.3. Inductance Analysis

The published literatures on inductance analysis of FSCW machines are mainly focused on SPM machines. The stator MMF introduces rich harmonic contents; as a result, the air gap leakage inductance of FSCW can be comparable to the magnetizing inductance [21]. Due to the increased number of turns in each slot, the slot leakage inductance is also elevated significantly. In addition, for FSCW SPM, the slot leakage inductance component may be the dominant components [22] due to large magnetic air gap (which includes the mechanical air gap and magnet thickness). The effect of teeth/pole combination on air gap leakage inductance is summarized in [23] by using classical harmonic inductance calculation method. The detailed leakage inductance analysis, including air gap harmonic leakage, slot leakage, tooth tip leakage and end winding leakage inductances are summarized in [24]. The inductance comparison between ISDW, DL FSCW and SL FSCW is reported in [25] with same SPM rotor configuration and the constraint of equal back-EMFs. Regardless of end winding leakage inductance, FSCW features much higher inductance than ISDW, and SL FSCW demonstrates higher inductance than DL FSCW due to higher air gap leakage and slot leakage components.

The *d*- and *q*-axis inductances of the FSCW machine are studied for FSCW IPM machine in [26], where the winding function method is applied. However, it requires the equivalent inverse air gap length function or air gap permeability function, which is very difficult to obtain analytically. A modified winding function method, which employs the rotor magnetic potential, is proposed in [27] to compute the inductance of FSCW IPM machine. A similar method is presented in [28] to compute the *d*- and *q*-axis inductances, which shows very good agreement with the simulation results. However, both methods need to calculate the rotor magnetic potential distribution, which increases the calculation complexity.

2.2.4. Cogging Torque

Cogging torque is caused by the interaction between PM and permeance variation in the airgap. The air gap permeance is modulated by stator slots and rotor flux barriers. The stator slots of the FSCW machines are located at different angular positions with respect to the rotor poles. Hence, the FSCW machines have inherently low cogging toque compared to ISDW machines [29].

The fractional number of SPP reduces the amplitude and increases the fundamental order of the cogging toque. Higher least common multiple of the teeth and pole number normally result in lower cogging torque. In [30], the cogging factor C_T is introduced to evaluate the cogging torque of different teeth/pole combinations. It is concluded that larger factor C_T corresponds to higher cogging torque.

$$C_T = \frac{2PQ_s}{\mathrm{LCM}(Q_s, P)} \tag{2.1}$$

2.2.5. Field Weakening Operation

Two main parameters that define field weakening capability of PMSMs are the characteristic current (I_{ch}) and saliency ratio (ρ), and both of which are the functions of winding inductance. The optimal field weakening can be achieved when the characteristic current I_{ch} is equivalent to the rated current [31, 32].

Traditionally, the inductance of SPM machine with ISDW is quite low due to the large magnetic air gap. The characteristic current is significantly higher than rated current, which makes the ISDW SPM unsuitable for field weakening operation. However, the researches on FSCW SPM machines indicate that the characteristic current can be comparable to the rated current due to the increased leakage inductance, which makes the FSCW SPM machines candidate for field weakening operation. The optimal field weakening condition analysis and experimental verification of FSCW SPM machines are presented in [33] and [34].

2.2.6. IPM Machine Equipped with FSCW

The IPM rotor introduces many merits including:

1. The rotor saliency contributes to reluctance torque production which enables higher torque density or reduction of PM material;
2. The winding inductance is increased due to smaller air gap, hence the field weakening capability is enhanced and CPSR can be extended;

3. The internal buried magnets helps reduce the risk of demagnetization;
4. Compared to the SPM rotor, the IPM rotor offers better mechanical strength, and magnets are well protected mechanically;
5. The flux barrier can be shaped to fit rectangular magnets; and
6. The assembling of magnets can be simplified.

The IPM machine equipped with FSCW is promising because of the potential of combining the benefits of FSCW and IPM rotor. However, unlike the ISDW IPM, FSCW IPMs are believed to have negligible reluctance torque in early publications [35]. Lester Chong derived the saliency ratio of the FSCW IPM based on finite element analysis (FEA) and proposed the design rules to increase the saliency ratio for radial flux I-shape PM rotor. Nevertheless, it is observed that the optimized saliency is still negligible [36, 37]. On the other hand, Massimo Barcaro [38] and Xiao Chen [39] have observed considerable reluctance torque component in FSCW IPM machines. The application of FSCW to synchronous reluctance machine (SynRM) also draws researchers' interest [40, 41], which suggest that the FSCW configuration can be used in high reluctance torque machines. The controversial results require more attention on the reluctance torque production mechanism of FSCW IPM machines.

In [42], the SPM and IPM machines equipped with FSCW are compared in terms of cogging torque, torque ripple, core losses and field weakening capability. The cogging torque of FSCW IPM can be minimized by adjusting the pole-arc to pole-pitch ratio using the same rules for SPM. The FSCW IPM introduces more core losses, especially at high speeds [43], however, the PM eddy loss is reduced [44]. The radial force, which is mainly

caused by the interaction of PM excited magnetic field and high order stator MMF harmonic is studied in [45]. The IPM configuration produces more pronounced radial forces compared to SPM configuration. The noise comparison is performed in [46], which shows that the IPM machine produces higher noises.

2.2.7. Stator Shifting and Multi-Layer Winding

In recent years, stator shifting and higher number of winding layer techniques have been proposed to reduce the core loss and improve the reluctance torque. The philosophy of both techniques is to cancel the sub-harmonics.

The general approach of stator shifting is presented in [47]. The concept of stator shifting is introduced and the harmonic cancellation mechanism is explained. The effect of stator shifting on the machine performances, including torque density, torque ripple and losses, are discussed. The doubled stator teeth method is proposed for harmonic cancellation [48, 49, 50], which can be treated as a special case of stator shifting technique. The winding arrangement and design rules are discussed in [49].

The multi-layer winding theory and the design rules are presented in [51]. It was shown that the multi-layer winding is able to reduce the first loss-producing harmonic while maintain the torque-producing harmonic [52,53].The multi-layer windings can also be considered as a special case of stator shifting technique. The power density, efficiency and torque ripple can be improved. The analytical method to calculate the slot leakage inductance of multi-layer windings are presented in [54].

2.3. MANUFACTURE OF CONCENTRATED WINDINGS

There are different technologies to manufacture concentrated windings, and they are highly dependent on how the stators are made. Generally speaking, there are two types of stators: complete core and segmented core.

2.3.1. Complete Core

The entire section of the stator lamination is punched as one piece. Fig. 2.7 (a) [55] shows a stator core of washing machine. The coil can be directly wound around the stator teeth. For volume production, the coils can be wound automatically by a needle winding machine, which allows the coils to be well organized around the teeth with very short end winding, as shown in Fig. 2.7 (b) [56]. However, large space between the adjacent coils is required for the needle to move in and out [57], which results in low slot fill factor. Additionally, the slot opening should be wider than the needle size.

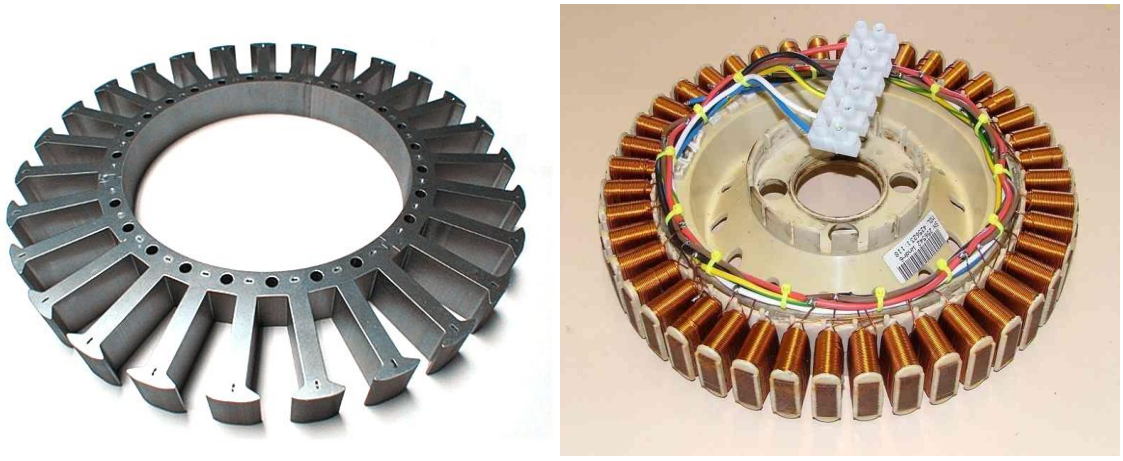

(a) (b)

Fig. 2.7. Washing machine stator: (a) stator core stack [55], (b) stator with coils [56].

One of the solutions to achieve higher slot fill factor is to use preformed coils. Fig. 2.8 shows the example of preformed coils using flat wires [58]. However, in order to apply the preformed coils in the complete core, the stator slot opening has to be configured as such that the coils can be installed, which usually requires open slot configurations. For example, the generator of Prius 2010 utilizes open slot stator [59]. The generator package and the highlighted stator cross section are shown in Fig. 2.9.

Fig. 2.8. Preformed coils of concentrated windings [58].

Fig. 2.9. Toyota Prius 2010 generator and its stator cross section [59].

2.3.2. Segmented Core

Instead of complete stator core, the stator can be segmented. There are several technologies available for segmented stator and winding manufacture. The most popular technology is to segment the stator in the yoke. The stator segment modules are identical. Each segment contains single tooth and rotor yoke, and the yoke is shaped to hold the position with adjacent modules, as shown in Fig. 2.10 [41]. The coils can be wound around each tooth individually. By employing the segmented stator, very short end winding and high slot fill factor can be achieved. The slot fill factor of the machine in Fig. 2.10 is 59%.

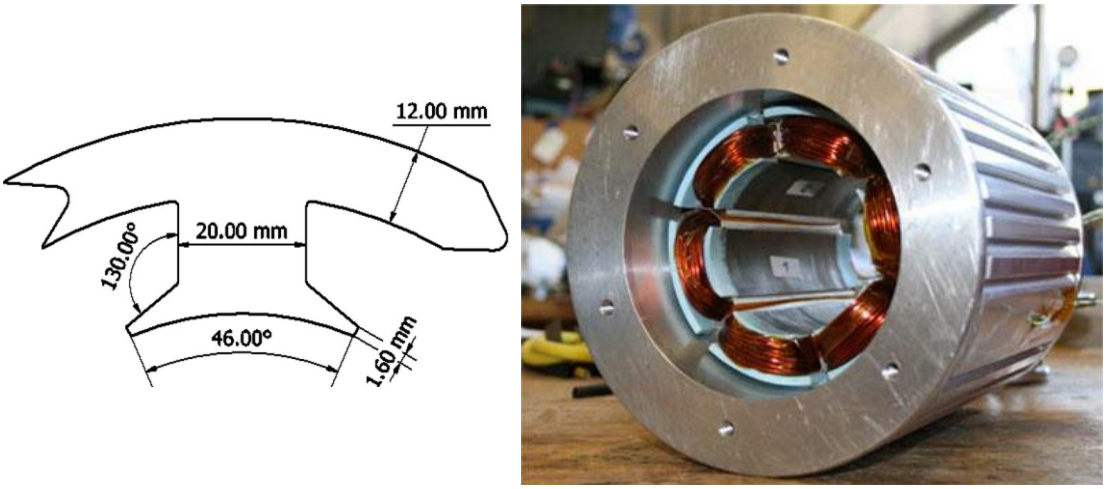

Fig. 2.10. Concentrated winding stator with segmented stator modules [41].

Another type of the segmented stator core is to separate stator teeth from yoke, as shown in Fig. 2.11 [60]. The stator teeth laminations are punched individually. The coil can be wound on each stator tooth individually. An alternative way is to use the preformed coils, and they can be installed from the bottom of the teeth.

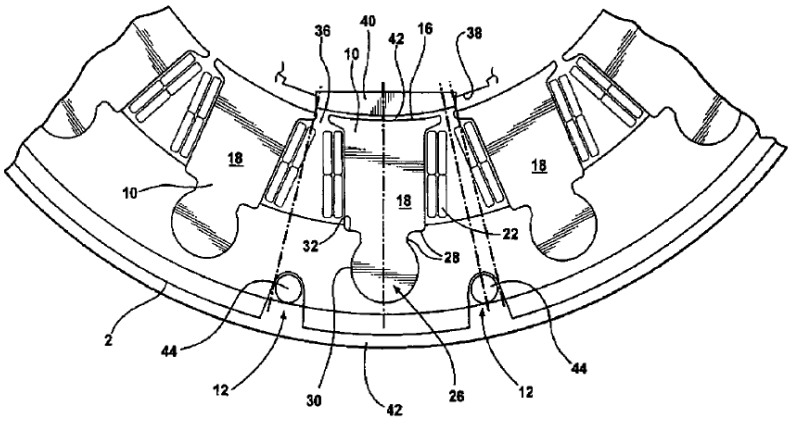

Fig. 2.11. Concentrated winding stator with inset teeth [60].

Rather than separate the stator teeth completely, a more advanced technology named joint-lapped core is proposed in [61], as shown in Fig. 2.12. The fix notch and rotational notch are formed during the punching process. The ends of the stator segment are shaped as a pair of cylindrical joints. The joints enable the stator tooth stack to rotate freely. Gaps in adjacent lamination layers are located at deviated positions.

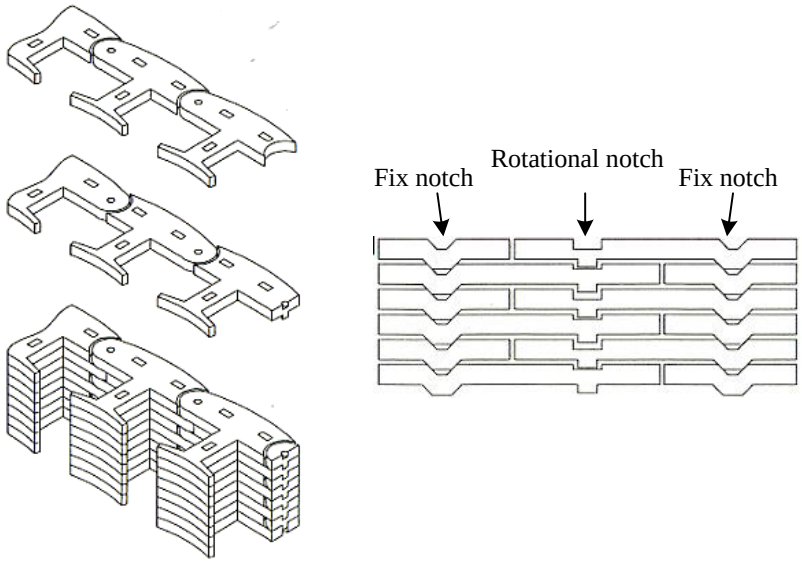

Fig. 2.12. Joint-lapped core model [61].

As shown in Fig. 2.13, the opening between the teeth stacks can be enlarged freely and coils can be wound around each tooth stack. The fabricated joint-lapped core stator in Fig. 2.13 achieved 75% slot fill factor. Another benefit of the joint-lapped core is that it is capable to achieve similar circularity and rigidity compared to the complete core.

Fig. 2.13. Joint-lapped core with winding [61].

The automotive industry has adopted the segmented stator technology. As shown in Fig. 2.14, the 2005 Honda Accord Hybrid integrated motor and generator employs the segmented stator teeth with concentrated winding [62]. The Sonata Hybrid employs very similar segmented stator for their integrated motor generator [63].

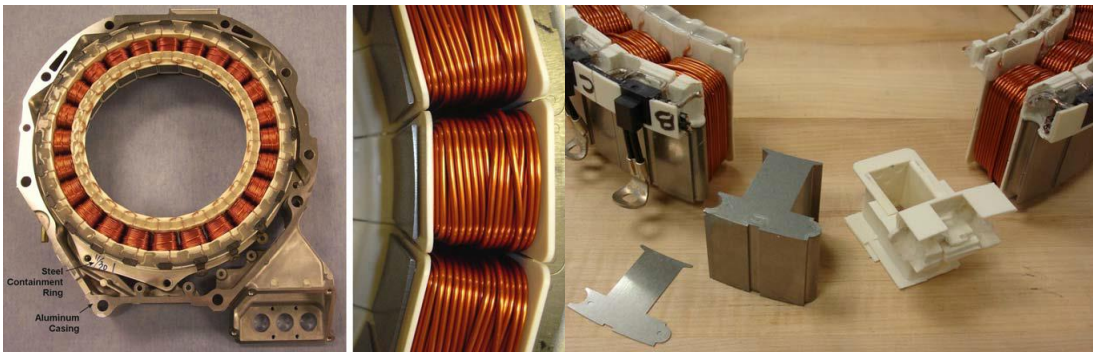

Fig. 2.14. Honda Accord Hybrid 2005 stator [62].

2.4. SUMMARY

A brief literature review of FSCW machines is presented in this chapter. The feasible topologies of concentrated winding PM machines are discussed, and A brief comparison between the stator PM and the rotor PM (FSCW PM machine) topologies is performed. Different problems related to the FSCW PM machines are reviewed in details. The available manufacture technologies of FSCW stators are discussed and their advantages and disadvantages are evaluated.

This page is intentionally left blank

Chapter 3
INDUCTANCE ANALYSIS OF FRACTIONAL SLOT CONCENTRATED WINDING MACHINES

As has been discussed in section 2.2.6, the conclusions of the reluctance torque capability of the salient rotor machines with FSCW are controversial. In this chapter, the reluctance torque capability of the FSCW machines is studied based on the inductance analysis. The air gap inductance and mutual inductance of FSCW is evaluated first, based upon which the *d*- and *q*-axis inductances are studied for FSCW machines equipped with salient rotors.

3.1. RELUCTANCE TORQUE COMPUTATION

The electromagnetic torque can be computed by the change of stored energy or co-energy [64]. The differential form of the co-energy W_f' is defined in (3.1), and the torque can be calculated by (3.2)

$$dW_f' = \psi_f di \tag{3.1}$$

$$T_e = \frac{\partial W_f'}{\partial \theta_m} \tag{3.2}$$

For pure reluctance machines, the co-energy variation during one electrical cycle is equivalent to the area covered by the flux linkage loci. For example, the torque of SRM is often computed by the co-energy locus, as shown in Fig. 3.1. For SynRM, the machine is excited by sinusoidal current, and the phase flux linkage contains the components induced by the self- and mutual inductances [65].A typical locus of SynRM is shown in Fig. 3.2.

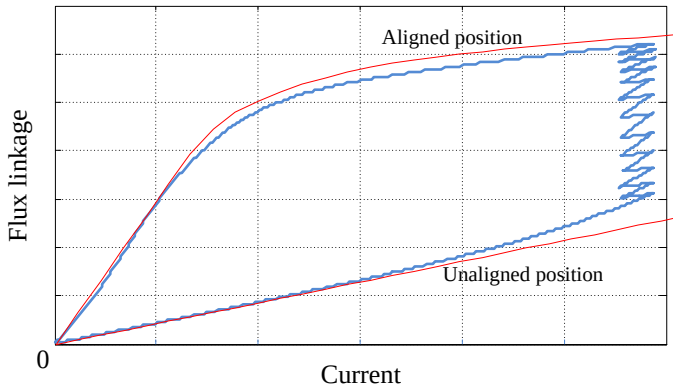

Fig. 3.1. Flux linkage loci of SRM during one electrical period.

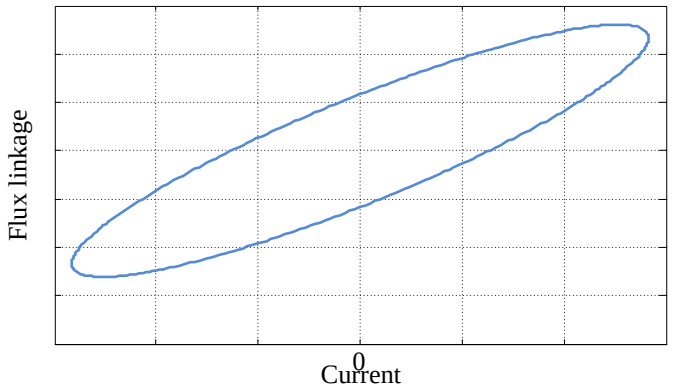

Fig. 3.2. Flux linkage loci of SynRM during one electrical period.

The IPM machines and PM assisted synchronous reluctance machines (PMA-SynRMs) are also capable of producing reluctance torque. The torque derived by flux

linkage loci is the total torque. The total torque of IPM machines can be segregated into PM torque and reluctance torque.

The *d*- and *q*-axis inductances are commonly used to analyze the reluctance torque of sinusoidal excited machines. When *d*-axis is defined on the direction of lower permeability, and *q*-axis leads 90° (for PMA-SynRMs and IPM machines, the *d*-axis is the N pole, which features lower permeability), the torque under sinusoidal excitation can be represented as [66]:

$$T_e = \frac{3}{2} P[\psi_f i_q + i_d i_q (L_q - L_d)] \tag{3.3}$$

where, ψ_f is the PM flux linkage, for pure reluctance machines, this term is zero; L_d and L_q are the *d*- and *q*-axis inductance; i_d and i_q are the *d*- and *q*-axis current. For average torque computation, machine parameters are accounted by the average value during one electric period.

The reluctance torque for salient machines can be separated from (3.3) as [38]:

$$T_{Rel} = \frac{3}{2} P(L_d - L_q) i_d i_q = \frac{3}{2} P(1-\rho) L_d i_d i_q \tag{3.4}$$

where, ρ is the saliency ratio, and $\rho = L_q / L_d$.

Saliency ratio ρ is believed to be the key metric relevant to the reluctance torque production. However, from (3.4), the reluctance torque capability is not only dependent on the saliency ratio, but proportional to the inductance difference between the *d*- and *q*-axis.

3.2. WINDING FUNCTION METHOD FOR INDUCTANCE CALCULATION

3.2.1. Conventional Winding Function Method

Winding function theory simplifies the understanding of the magnetic fields, and is very powerful to analyze the field distribution, inductance as well as torque production [67]. Fig. 3.3 demonstrates a doubly cylindrical machine with arbitrarily placed winding in the air gap.

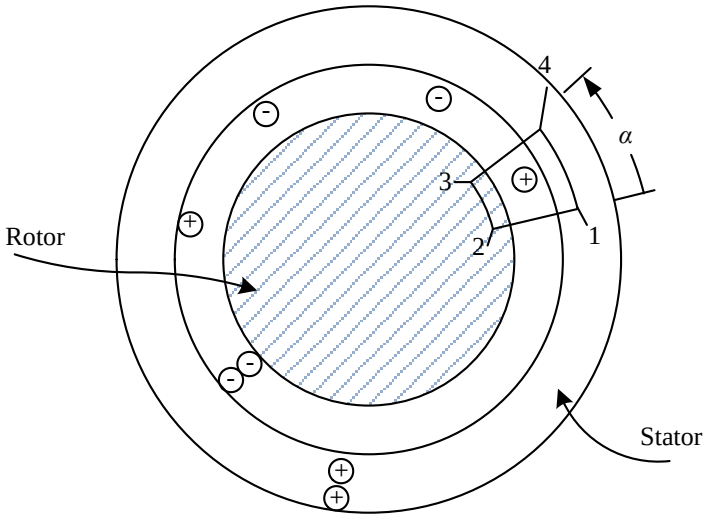

Fig. 3.3. Doubly cylindrical machine with arbitrary placed winding [67].

The turns function is employed to express the winding distribution. At angle α, winding turns carrying current in and out of the page may be defined positive and negative. The turns function for the doubly cylindrical machine in Fig. 3.3 is illustrated in Fig. 3.4.

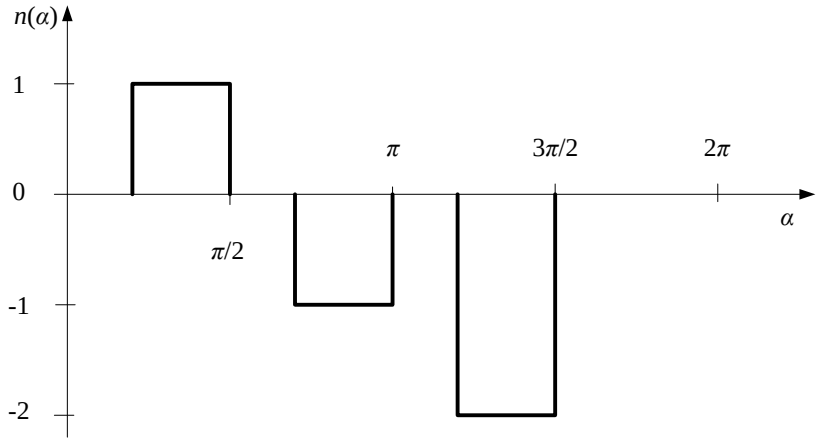

Fig. 3.4. Turns function of winding [67].

The winding function of an arbitrary winding is defined as

$$N(\alpha) = n(\alpha) - < n(\alpha) > \tag{3.5}$$

where, $< n(\alpha) >= \frac{1}{2\pi}\int_0^{2\pi} n(\alpha) d\alpha$ is the average value of the turns function.

The winding function defined in (3.5) is not unique because it depends on the initial reference of α. The reference position is purposely chosen such that the winding function is even symmetry, i.e., the winding function satisfies (3.6).

$$N(\alpha) = N(-\alpha) \tag{3.6}$$

In case of salient rotor machines, the winding function needs to be modified as (3.7) to account for the modulation effect of the uneven air gap distribution.

$$N(\alpha) = n_a(\alpha) - \frac{\int_0^{2\pi} n_a(\alpha) g^{-1}(\alpha) d\alpha}{\int_0^{2\pi} g^{-1}(\alpha) d\alpha} \tag{3.7}$$

Assuming the permeability of the core material is infinity and the MMF drop in the core is negligible, the phase MMF distribution due to the current excitation can be expressed simply by the product of the winding function and current.

$$F(\alpha) = N(\alpha) \cdot i \tag{3.8}$$

The armature reaction flux passing through the air gap can be derived from the MMF drop and permeance by

$$d\phi = F(\alpha)\mu_0 \frac{rld\alpha}{g} \tag{3.9}$$

where, μ_0 is the air gap permeability, g is the air gap length, r is the air gap radius, l is the stack length. $rld\alpha$ represents the cross section area of interest.

Therefore, the flux linkage of winding B due to the current carried by winding A can be obtained by (3.10).

$$\psi_B = \mu_0 \frac{rl}{g} \int_0^{2\pi} n_B(\alpha) F_A(\alpha) d\alpha \tag{3.10}$$

where, the subscripts differentiate the functions/variables of different windings.

Therefore, the mutual inductance between phase A and B can be obtained as (3.11). Considering that the winding function is a special case of turns function, the mutual inductance can also be calculated by (3.12).

$$M_{BA} = \frac{\psi_B}{i_A} = \mu_0 \frac{rl}{g} \int_0^{2\pi} n_B N_A(\alpha) d\alpha \tag{3.11}$$

$$M_{BA} = \frac{\psi_B}{i_A} = \mu_0 \frac{rl}{g} \int_0^{2\pi} N_B(\alpha) N_A(\alpha) d\alpha \tag{3.12}$$

For salient pole machines, the flux linkage and the mutual inductance can be obtained by modifying (3.10) and (3.11) to (3.13) and (3.14). Formula (3.14) may also be re-written as (3.15).

$$\psi_B = \mu_0 rl \int_0^{2\pi} n_B(\alpha) \frac{F_A(\alpha)}{g(\alpha)} d\alpha \tag{3.13}$$

$$M_{BA} = \frac{\psi_B}{i_A} = \mu_0 \frac{rl}{g} \int_0^{2\pi} n_B(\alpha) \frac{N_A(\alpha)}{g(\alpha)} d\alpha \tag{3.14}$$

$$M_{BA} = \frac{\psi_B}{i_A} = \mu_0 \frac{rl}{g} \int_0^{2\pi} \frac{N_A(\alpha) N_B(\alpha)}{g(\alpha)} d\alpha \tag{3.15}$$

The winding function based flux linkage computation accounts for the total flux linkage in the air gap due to armature reaction, thus the computed inductance includes the magnetizing inductance and air gap harmonic leakage inductance, and is referred to as air gap inductance.

3.2.2. Modified Winding Function method

For an arbitrary rotor position θ, the general winding function (3.7) can be modified to (3.16).

$$N(\alpha, \theta) = n(\alpha) - \frac{\int_0^{2\pi} n(\alpha) g^{-1}(\alpha, \theta) d\alpha}{\int_0^{2\pi} g^{-1}(\alpha, \theta) d\alpha} \tag{3.16}$$

Substituting (3.16) into (3.14), the inductance can be obtained as (3.17).

$$M_{BA}=\left[\begin{array}{l}\mu_0 lr\int_0^{2\pi} n_A(\alpha)n_B(\alpha)g^{-1}(\alpha,\theta)d\alpha - \\ \mu_0 lr\dfrac{\int_0^{2\pi} n_A(\alpha)g^{-1}(\alpha,\theta)d\alpha\cdot\int_0^{2\pi} n_B(\alpha)g^{-1}(\alpha,\theta)d\alpha}{\int_0^{2\pi} g^{-1}(\alpha,\theta)d\alpha}\end{array}\right] \qquad (3.17)$$

Equation (3.17) is turns function based, universal formula for inductance computation. It does not require the calculation of the winding function. There is no zero average value restriction on turns function, which makes it flexible to define the turns function properly to simplify the inductance computation. For example, in FSCW machines, the phase turns function can be defined non-zero only under the teeth with coils which belong to this phase. As a result, the integral computation of (3.17) can be restricted to the angle ranges where turns function is non-zero. When $n_B(\alpha)$ is replaced by $n_A(\alpha)$, the self-inductance formula can be obtained as (3.18).

$$L_{AA}=\mu_0 lr\int_0^{2\pi} n_A^2(\alpha)g^{-1}(\alpha,\theta)d\alpha-\mu_0 lr\frac{\left(\int_0^{2\pi} n_A(\alpha)g^{-1}(\alpha,\theta)d\alpha\right)^2}{\int_0^{2\pi} g^{-1}(\alpha,\theta)d\alpha} \qquad (3.18)$$

3.2.3. FEA Verification of Modified Winding Function Method

The modified winding function based inductance formula (3.17) is verified on a SRM and a mutual coupled switched reluctance machine (MCSRM) [68]. As shown in Fig. 3.5, the SRM and MCSRM both have 6 stator poles and 4 rotor poles, and they share the identical stator and rotor configurations. The air gap functions are the same [69].

The coil directions of SRM and MCSRM are also depicted in Fig. 3.5 (a) and (b) respectively. The corresponding turns functions of SRM and MCSRM are shown in Fig. 3.6 (a) and (b), respectively.

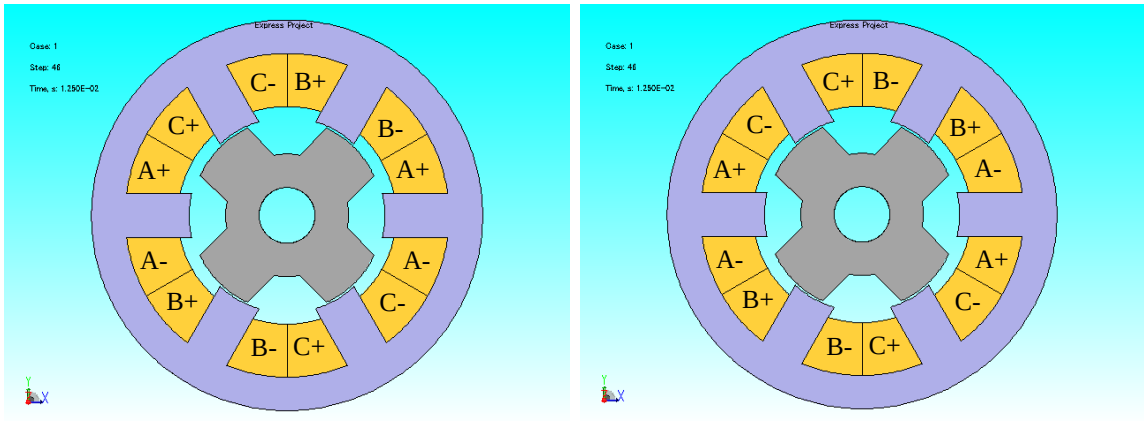

(a) (b)

Fig. 3.5. Cross section of SRM and MCSRM: (a) SRM, (b) MCSRM.

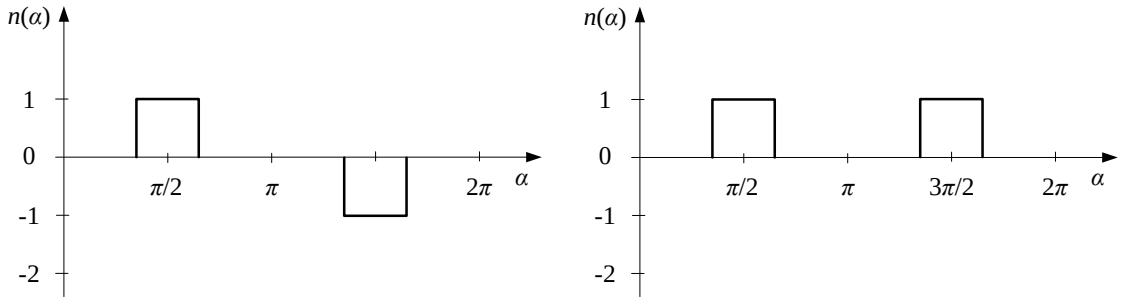

(a) (b)

Fig. 3.6. Turns function of SRM and MCSRM: (a) SRM, (b) MCSRM.

Under linear condition, the self- and mutual inductance waveforms during one electrical period are computed using the modified winding function method and FEA method. The analytical and FEA results are depicted in Fig. 3.7.

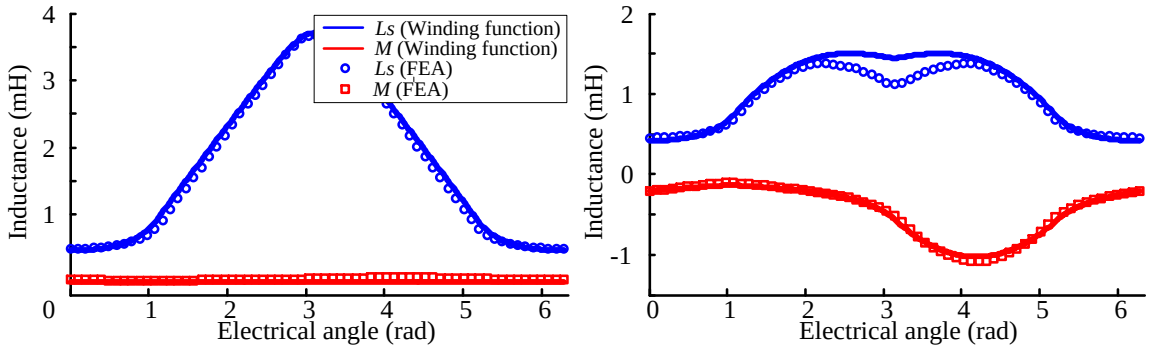

(a) (b)

Fig. 3.7. Inductance waveforms during one electrical period: (a) SRM, (b) MCSRM.

For SRM, it can be observed that the results of modified winding function method match the FEA simulation results very well. For MCSRM, despite of some error at the crest of the self-inductance waveform, the analytical results and the FEA simulation results share the same trend and they match reasonably well. The error of the self-inductance is mainly caused by the inaccurate estimation of the air gap function.

3.3. INDUCTANCE ANALYSIS OF FRACTIONAL SLOT CONCENTRATED WINDING

Winding inductance has strong impact on maximum torque capability and field weakening capability. The synchronous inductance L_s typically consists of six parts [70].

$$L_s = L_m + L_\delta + L_u + L_t + L_w + L_{sq} \tag{3.19}$$

where, L_m is the magnetizing inductance, L_δ is the air gap harmonic leakage inductance, L_u is the slot leakage inductance, L_t is the tooth tip leakage inductance, L_w is the end winding leakage inductance, and L_{sq} is the skew leakage inductance.

The air gap harmonic leakage inductance and the magnetizing inductance can be lumped together as air gap inductance, which can be directly computed using winding function method.

$$L_g = L_m + L_\delta \tag{3.20}$$

In ISDW machines, the air gap harmonic leakage inductance only takes a very small part of the air gap inductance; however, in FSCW machines, it is considerably higher. The significance of the air gap harmonic leakage inductance is evaluated by the air gap inductance factor, which is defined as the ratio of air gap inductance and the magnetizing inductance.

$$\sigma_\delta = L_g / L_m \tag{3.21}$$

The mutual inductance of FSCW behaves significantly differently from the ISDW because there is no overlap between coils. The significance of the mutual inductance is evaluated by the mutual inductance factor, which is defined as the ratio of the mutual inductance and the air gap inductance.

$$m_c = M / L_g \tag{3.22}$$

3.3.1. Magnetizing Inductance

The magnetizing inductance corresponds to the synchronous rotating (the working harmonic) magnetic field, which is directly involved in the electromechanical energy conversion. When single phase excitation is applied, the MMF amplitude corresponding to the synchronous rotating component can be computed as (3.23). When symmetric *m*-

phase excitations are applied, the amplitude of the synthetic synchronous rotating component can be computed as (3.24).

$$F_{s1} = \frac{4}{\pi}\frac{N_s k_w}{2P} I_s \tag{3.23}$$

$$F_{sm} = \frac{m}{2}\frac{4}{\pi}\frac{N_s k_w}{2P} I_s \tag{3.24}$$

where, F_{s1} and F_{sm} are the stator MMFs of single phase and m-phase current excitation, respectively, m is the phase number, N_s is the phase turn number, k_w is the winding factor of the synchronous component, I_s is the stator current, P is the pole pair number. $4/\pi$ is the coefficient of the fundamental harmonic of rectangular waveform (for full pitched winding). $m/2$ is the coefficient of the synthetic synchronous rotating MMF harmonic under m-phase symmetric excitation.

Assuming the air gap length is evenly distributed, the amplitude of the flux density B_g due to the synchronous rotating MMF harmonic can be computed as (3.25). The flux linkage can be obtained by (3.26).

$$B_g = \mu_0 F_s / g \tag{3.25}$$

$$\psi_{sp} = \frac{2}{\pi} k_w N_s l \tau_p B_g \tag{3.26}$$

where, ψ_{sp} is the flux linkage of each phase, τ_p is the rotor pole pitch, $\tau_p = \frac{\pi r}{P}$, and F_s is the amplitude of the synchronous harmonic of stator MMF. For single phase excitation, F_s is substituted by F_{s1}; for m-phase excitations, F_s is substituted by F_{sm};;

Therefore, the magnetizing inductance can be obtained as

$$L_m = \frac{\psi_{sp}}{I_s} = \frac{2}{\pi}\mu_0 \frac{l_{ef}\tau_p}{g} N_s k_w \frac{F_s}{I_s} \tag{3.27}$$

Normally the synthetic MMF is adopted to compute the magnetizing inductance. Substituting (3.24) into (3.27), the magnetizing inductance is computed as (3.28).

$$L_m = \frac{m}{2}\frac{16}{\pi}\mu_0 \frac{l_{ef} r}{g}\left(\frac{N_s k_w}{2P}\right)^2 \tag{3.28}$$

Here, in order to evaluate the significance of the air gap harmonic inductance by using the modified winding function method, single phase excitation is adopted. Substituting (3.23) into (3.27), the phase magnetizing inductance is obtained as (3.29).

$$L_m = \frac{16}{\pi}\mu_0 \frac{l_{ef} r}{g}\left(\frac{N_s k_w}{2P}\right)^2 \tag{3.29}$$

3.3.2. Air Gap Inductance

3.3.2.1. Air Gap Inductance of ISDW

The air gap inductance analysis of ISDW is calculated as a reference for the air gap inductance analysis of the FSCW. A 3-phase SL winding with unity SPP is used as an example, the winding function within one pole pair is illustrated in Fig. 3.8. Each phase occupies the entire peripheral of the air gap.

The phase airgap inductance can be obtained by using (3.30).

$$L_g = \mu_0 \frac{rl}{g} 2\pi \left(\frac{N_s}{2P}\right)^2 \tag{3.30}$$

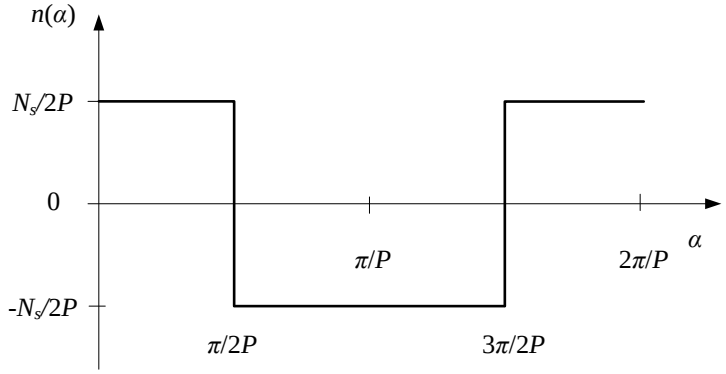

Fig. 3.8. Winding function of full pitched winding configuration with SPP = 1.

Substituting (3.30) and (3.29) into (3.21), the air gap inductance factor of ISDW can be computed as:

$$\sigma_\delta = \frac{L_g}{L_m} = \frac{\pi^2}{8} \approx 1.234 \tag{3.31}$$

In *m*-phase symmetric AC excited machine, the *km*th order (k = 1, 2, 3…) harmonics are cancelled and do not appear in synthetic MMF. Therefore, the self-inductance corresponding to *km*th order MMF should be deducted when the motor is operated under symmetric excitation [24]. In 3-phase machines, the 3rd and its multiple order harmonics are cancelled with each other. Excluding the effect of 3rd order harmonics, the air gap inductance factor can be computed as

$$\sigma_\delta = \frac{L_g}{L_m} = \frac{\pi^2}{8} - \sum_{\upsilon=3+6i}^{\infty} \frac{1}{\upsilon^2} \approx 1.1 \tag{3.32}$$

In the following analysis for FSCW, to simplify the computation, the *km*th order harmonics are not excluded.

3.3.2.2. Air Gap Inductance of DL FSCW

For DL FSCW configurations, each phase occupies 1/3 of the air gap peripheral. If the phase turns function is defined non-zero under the teeth with coils, by applying the self-inductance equation (3.18), the phase airgap inductance can be obtained by (3.33).

$$L_g = \mu_0 \frac{rl}{g}\left[\frac{2\pi}{3}\left(\frac{N_s}{2P}\right)^2 \frac{1}{SPP^2} - 2\pi < n(\alpha) >^2\right] \tag{3.33}$$

For standard 3-phase machines with 24 poles or less, different teeth/pole combinations and their winding factors are listed in Table. 3.1. The winding factor is the function of SPP value. Only those with SPP in the range of 1/4 and 1/2 are listed to avoid very low winding factor.

For each SPP value, the FSCW machine with minimum teeth number Q_{s0} and pole pair number P_0 can be considered as the unit machine, and they are defined by (3.34).

$$\begin{aligned} Q_{s0} &= Q_{s0} / \mathrm{GCD}(Q_s, P) \\ P_0 &= P / \mathrm{GCD}(Q_s, P) \end{aligned} \tag{3.34}$$

where, GCD stands for greatest common divisor, Q_s is the stator teeth number, and P is the rotor pole pair number.

For FSCW machine family with the same SPP number, the machines with higher teeth and pole pair number can be considered the multiple of the unit machine. They share similar winding configurations and inductance characteristics. Therefore, the inductance analysis is carried out based on the SPP value. For each SPP value given in Table 3.1, the winding configurations of the unit machines are illustrated in Fig. 3.9.

Table 3.1 Stator teeth/rotor pole combinations of DL FSCW machines

$2P$ / Q_s		4	6	8	10	12	14	16	18	20	22	24
6	*SPP* k_{wp} σ_δ m_c	1/2 0.866 1.46 -0.5		1/4 0.866 5.85 -0.5								
9	*SPP* k_{wp} σ_δ m_c		1/2 0.866 1.46 -0.5	3/8 0.945 3.15 -0.039	3/10 0.945 4.95 -0.039	1/4 0.866 5.85 -0.5						
12	*SPP* k_{wp} σ_δ m_c			1/2 0.866 1.46 -0.5	2/5 0.933 2.95 0		2/7 0.933 5.79 0	1/4 0.866 5.85 -0.5				
15	*SPP* k_{wp} σ_δ m_c				1/2 0.866 1.46 -0.5		5/14 0.951 3.51 -0.014	5/16 0.951 4.59 -0.014		1/4 0.866 5.85 -0.5		
18	*SPP* k_{wp} σ_δ m_c					1/2 0.866 1.46 -0.5	3/7 0.902 2.75 0	3/8 0.945 3.15 -0.039		3/10 0.945 4.92 -0.039	3/11 0.902 6.80 0	1/4 0.866 5.85 -0.5
21	*SPP* k_{wp} σ_δ m_c						1/2 0.866 1.46 -0.5	7/16 0.89 2.7 -0.007		7/20 0.953 3.67 -0.007	7/22 0.953 4.44 -0.007	
24	*SPP* k_{wp} σ_δ m_c							1/2 0.866 1.46 -0.5		2/5 0.933 2.95 0	4/11 0.949 3.45 0	
27	*SPP* k_{wp} σ_δ m_c								1/2 0.866 1.46 -0.5	9/20 0.877 2.63 -0.004	9/22 0.915 2.91 -0.004	3/8 0.945 3.15 -0.039
				$Q_s > 2P$					$Q_s < 2P$			

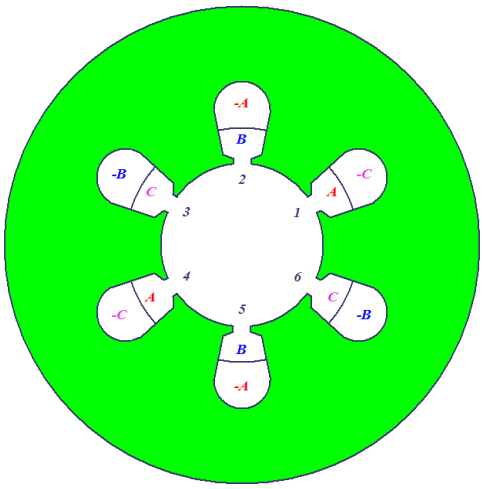

(a) SPP = 1/4, 1/2

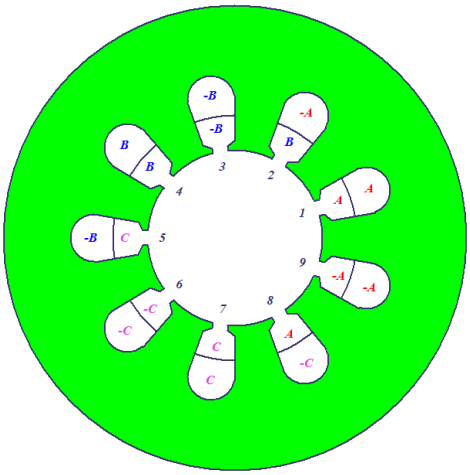

(b) SPP = 3/8, 3/10

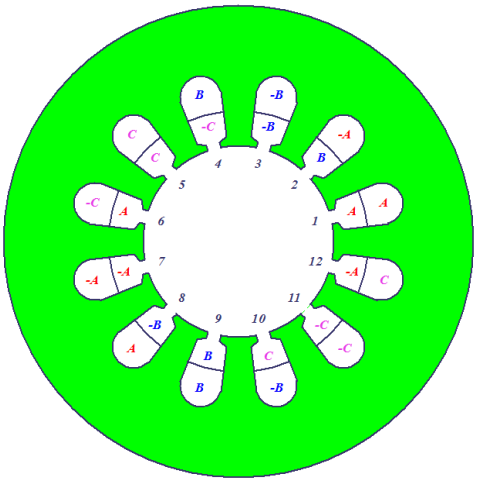

(c) SPP = 2/5, 2/7

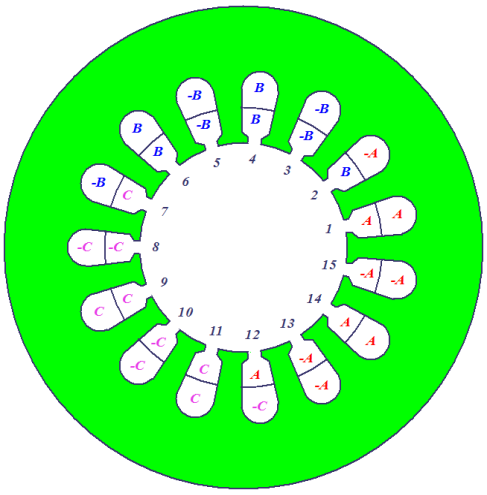

(d) SPP = 5/14, 5/16

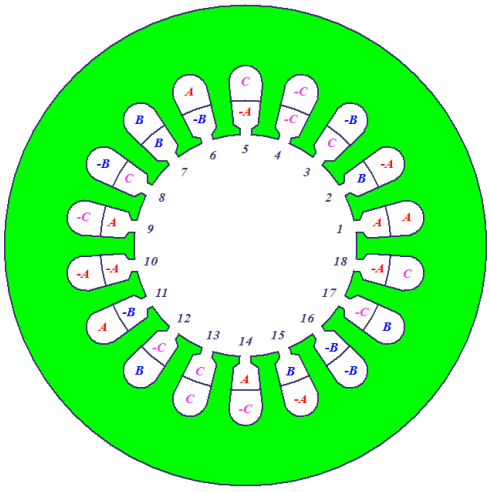

(e) SPP = 3/7, 3/11

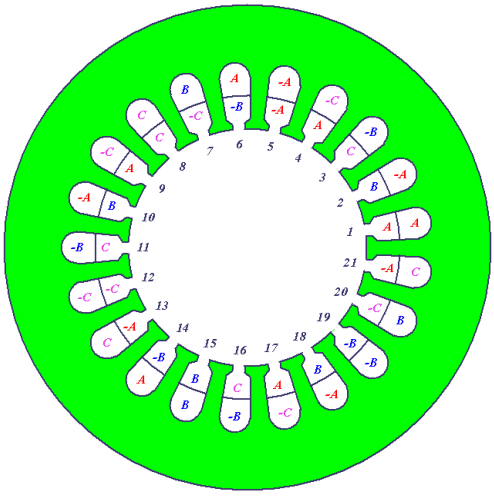

(f) SPP = 7/16

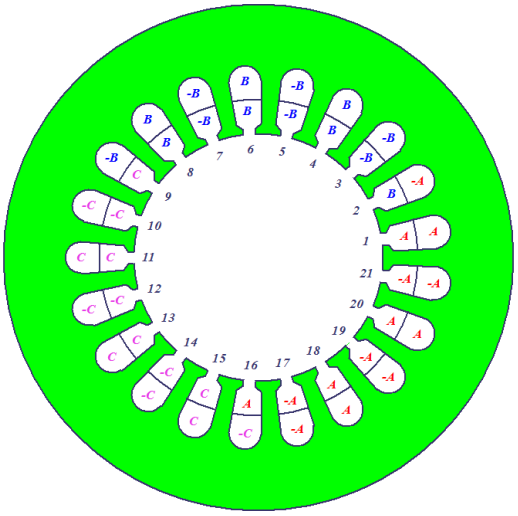

(g) SPP = 7/20, 7/22

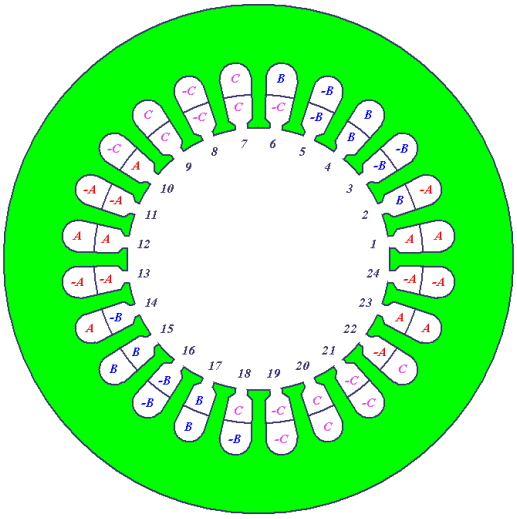

(h) SPP = 4/11

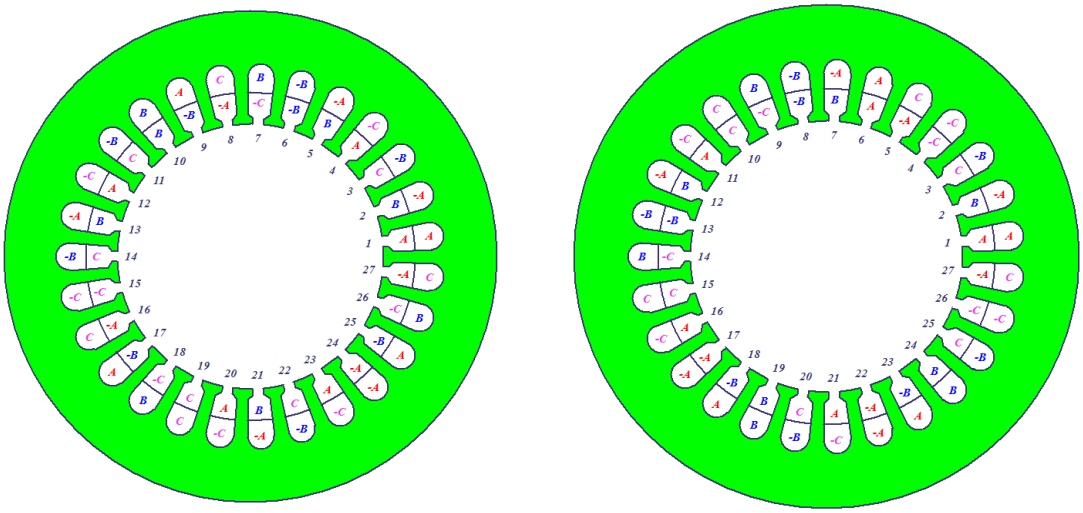

(i) SPP = 9/20 (j) SPP = 9/22

Fig. 3.9. Winding configurations of DL FSCWs with different SPP numbers.

Case 1, SPP = 1/2 or 1/4

For the teeth/pole combinations with SPP = 1/2 or 1/4, the winding configuration is illustrated in Fig. 3.9 (a). The second term in the bracket of (3.33) is not zero. The average value of turns function can be calculated as

$$< n(\alpha) >= \frac{1}{3}\frac{N_s}{2P \cdot SPP} \tag{3.35}$$

Substituting (3.35) into (3.33), the air gap inductance can be calculated as (3.36), and the air gap inductance factor, which is the ratio of the air gap inductance and magnetizing inductance, is computed as (3.37).

$$L_g = \frac{4\pi}{9}\mu_0 \frac{rl}{g}\frac{1}{SPP^2}\left(\frac{N_s}{2P}\right)^2 \tag{3.36}$$

$$\sigma_\delta = \frac{L_g}{L_m} = \frac{\pi^2}{36K_w^2}\frac{1}{SPP^2} \tag{3.37}$$

Case 2, SPP = 3/8 or 3/10

For teeth/pole combinations with SPP = 3/8 or 3/10, the winding configuration is illustrated in Fig. 3.9 (b), the average values of the turns functions are non-zero either, and it can be calculated as

$$< n(\alpha) >= \frac{1}{9}\frac{N_s}{2P \cdot SPP} \tag{3.38}$$

Substituting (3.38) into (3.33), the air gap inductance can be computed as (3.39). The air gap inductance factor can be computed accordingly as (3.40).

$$L_g = \frac{52\pi}{81}\mu_0 \frac{rl}{g}\frac{1}{SPP^2}(\frac{N_s}{2p})^2 \tag{3.39}$$

$$\sigma_\delta = \frac{L_g}{L_m} = \frac{52\pi^2}{1296K_w^2}\frac{1}{SPP^2} \tag{3.40}$$

Case 3, SPP = 2/5 or 2/7, 3/7 or 3/11, 4/11

For teeth/pole combinations with SPP = 2/5 or 2/7, 3/7 or 3/11, and 4/11, the winding configurations are illustrated in Fig. 3.9 (c), (e) and (h), respectively. In this case, the average values of turns functions are zero.

$$< n(\alpha) >= 0 \tag{3.41}$$

Substituting (3.41) into (3.33), the air gap inductance can be computed as (3.42). The air gap inductance factor can be computed accordingly as (3.43).

$$L_g = \frac{2\pi}{3}\mu_0 \frac{rl}{g}\frac{1}{SPP^2}(\frac{N_s}{2p})^2 \tag{3.42}$$

$$\sigma_\delta = \frac{L_g}{L_m} = \frac{\pi^2}{24K_w^2}\frac{1}{SPP^2} \tag{3.43}$$

Case 4, SPP = 5/14 or 5/16

For teeth/pole combinations with SPP = 5/14 or 5/16, the winding configuration is illustrated in Fig. 3.9 (d), the average value of turns function is computed as

$$< n(\alpha) >= \frac{1}{15}\frac{N_s}{2P \cdot SPP} \tag{3.44}$$

The air gap inductance and air gap inductance factor can be computed as (3.45) and (3.46), respectively.

$$L_g = \frac{148\pi}{225}\mu_0 \frac{rl}{g}\frac{1}{SPP^2}(\frac{N_s}{2P})^2 \tag{3.45}$$

$$\sigma_\delta = \frac{L_g}{L_m} = \frac{37\pi^2}{900K_w^2}\frac{1}{SPP^2} \tag{3.46}$$

Case 5, SPP = 7/16, 7/20 or 7/22

For teeth/pole combinations with SPP = 7/16, 7/20 or 7/22, the winding configurations are illustrated in Fig. 3.9 (f) and (g), the average values of the turns functions are computed as

$$< n(\alpha) >= \frac{1}{21} \frac{N_s}{2P \cdot SPP} \tag{3.47}$$

The air gap inductance and air gap inductance factor can be computed as (3.48) and (3.49), respectively.

$$L_g = \frac{292\pi}{441} \mu_0 \frac{rl}{g} \frac{1}{SPP^2} (\frac{N_s}{2P})^2 \tag{3.48}$$

$$\sigma_\delta = \frac{L_g}{L_m} = \frac{73\pi^2}{441K_w^2} \frac{1}{SPP^2} \tag{3.49}$$

Case 6, SPP = 9/20, 9/22

For teeth/pole combinations with SPP = 9/20 and 9/22, the winding configurations are illustrated in Fig. 3.9 (i) and (j). The average values of turns function are computed as

$$< n(\alpha) >= \frac{1}{27} \frac{N_s}{2P \cdot SPP} \tag{3.50}$$

The air gap inductance and air gap inductance factor can be computed as (3.51) and (3.52), respectively.

$$L_g = \frac{382\pi}{576} \mu_0 \frac{rl}{g} \frac{1}{SPP^2} (\frac{N_s}{2P})^2 \tag{3.51}$$

$$\sigma_\delta = \frac{L_g}{L_m} = \frac{121\pi^2}{2916K_w^2} \frac{1}{SPP^2} \tag{3.52}$$

By substituting the winding factors and SPP values into the air gap inductance factor formulas, the air gap inductance factors of different teeth/pole combinations are computed,

and they are summarized in Table. 3.1. The analyzed results match the conclusions in [23]. It can be observed that the inductance factor increases as the SPP number decreases. Comparing the FSCW with the ISDW with the same pole number, the air gap inductance factors are normally much higher than 1, which means the air gap inductance of FSCW are much higher than ISDW machines.

3.3.2.3. Air Gap Inductance of SL FSCW

For SL FSCW configurations, each phase occupies 1/6 of the peripheral of the air gap. If the phase turns function is defined non-zero under the teeth with coils, by applying the self-inductance equation (3.18), the phase airgap inductance can be obtained as (3.53).

$$L_g = \mu_0 \frac{rl}{g}\left[\frac{\pi}{3}\left(\frac{N_s}{P}\right)^2 \frac{1}{SPP^2} - 2\pi < n(\alpha) >^2\right] \tag{3.53}$$

For standard 3-phase machines with 24 poles or less, different teeth/pole combinations as well as their winding factors are listed in Table. 3.2. Because the stator teeth number must be the multiple of 6, there are much fewer options of the teeth/pole combinations compared to the DL winding configuration.

Similar to the analysis above, only those combinations with SPP between 1/4 and 1/2 are analyzed to avoid very low winding factor. The analysis is also carried out based on the SPP number. For each SPP value given in Table 3.2, the winding configurations are illustrated in Fig. 3.10.

Table 3.2 Stator teeth/rotor pole combinations of SL FSCW machines

2P / *Qs*		**4**	**6**	**8**	**10**	**12**	**14**	**16**	**18**	**20**	**22**	**24**
6	*SPP* k_{wp} σ_δ m_c	1/2 0.866 3.66 -0.2		1/4 0.866 14.62 -0.2								
12	*SPP* k_{wp} σ_δ m_c			1/2 0.866 3.66 -0.2	2/5 0.966 5.51 0		2/7 0.966 10.8 0	1/4 0.866 14.62 -0.2				
18	*SPP* k_{wp} σ_δ m_c					1/2 0.866 3.66 -0.2	3/7 0.902 5.4 -0.019	3/8 0.945 6.43 -0.019		3/10 0.945 7.93 -0.019	3/11 0.902 13.34 -0.019	1/4 0.866 14.62 -0.2
24	*SPP* k_{wp} σ_δ m_c							1/2 0.866 3.66 -0.2		2/5 0.966 5.51 0	4/11 0.958 6.78 0	
				$Q_s > 2P$					$Q_s < 2P$			

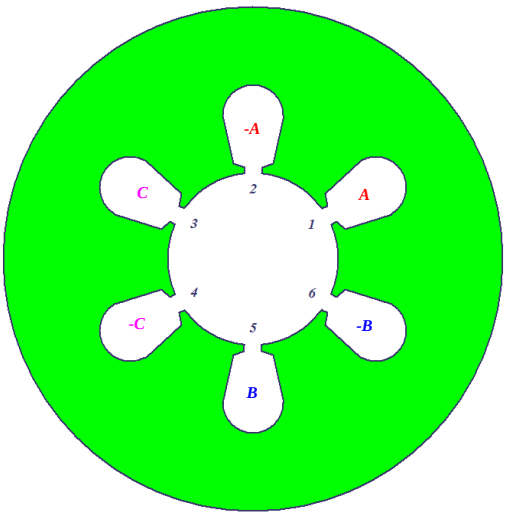

(a) SPP = 1/2, 1/4

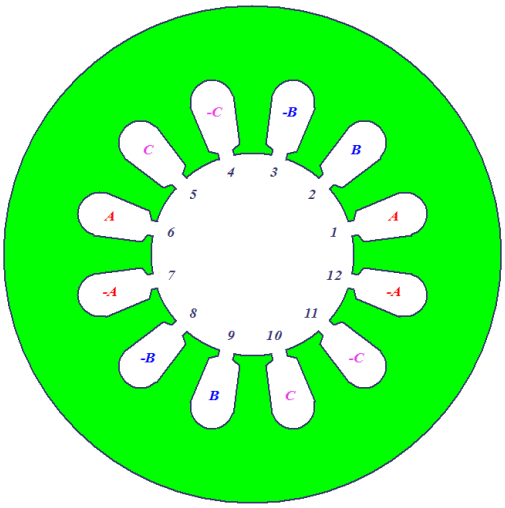

(b) SPP = 2/5, 2/7

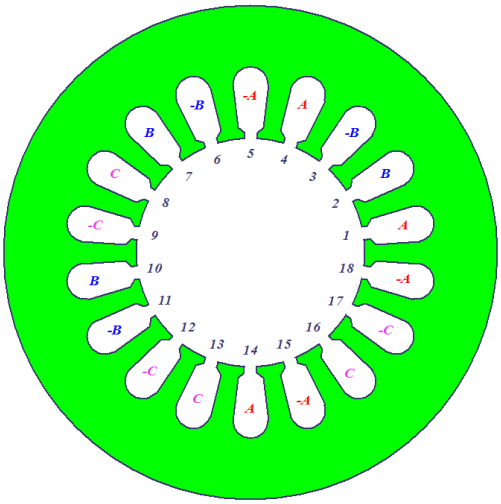

(c) SPP = 3/7, 3/11

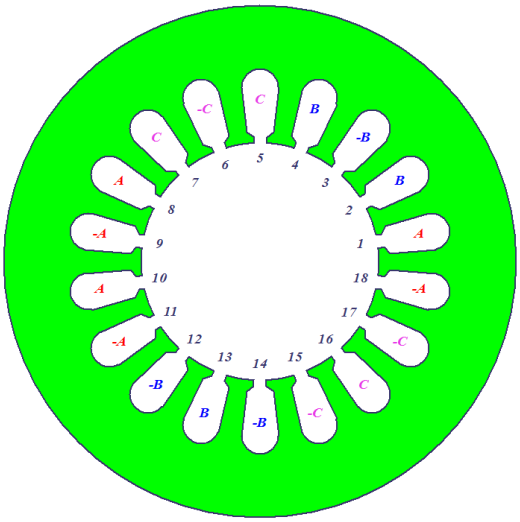

(d) SPP = 3/8, 3/10

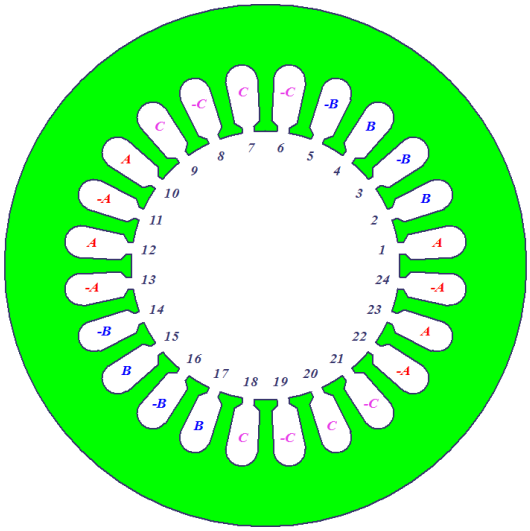

(e) SPP = 4/11

Fig. 3.10. Winding configurations of SL FSCWs with different SPP numbers.

Case 1, SPP = 1/2 or 1/4.

For teeth/pole combinations with SPP = 1/2 or 1/4, the winding configuration is illustrated in Fig. 3.10 (a). The average value of the turns function can be calculated as

$$< n(\alpha) >= \frac{1}{6}\frac{N_s}{P \cdot SPP} \tag{3.54}$$

The air gap inductance and the air gap inductance factor can be computed as (3.55) and (3.56), respectively.

$$L_g = \frac{5\pi}{18}\mu_0 \frac{rl}{g}\frac{1}{SPP^2}(\frac{N_s}{P})^2 \tag{3.55}$$

$$\sigma_\delta = \frac{L_g}{L_m} = \frac{5\pi^2}{4 \cdot 18K_w^2}\frac{1}{SPP^2} \tag{3.56}$$

Case 2, SPP = 2/5 or 2/7, 4/11

For teeth/pole combinations with SPP = 2/5 or 2/7, 4/11, the winding configurations are illustrated in Fig. 3.10 (b) and (e), respectively. The average values of the turns function are zero.

$$< n(\alpha) >= 0 \tag{3.57}$$

The air gap inductance and air gap inductance factor can be computed as (3.58) and (3.59), respectively.

$$L_g = \frac{\pi}{3}\mu_0 \frac{rl}{g}\frac{1}{SPP^2}(\frac{N_s}{P})^2 \tag{3.58}$$

$$\sigma_\delta = \frac{L_g}{L_m} = \frac{\pi^2}{4 \cdot 3K_w^2}\frac{1}{SPP^2} \tag{3.59}$$

Case 3, SPP = 3/7 or 3/11, 3/8 or 3/10

For teeth/pole combinations with SPP = 3/7 or 3/11, 3/8 or 3/10, the winding configurations are illustrated in Fig. 3.10 (c) and Fig. 3.10 (d), respectively. The average value of the turns function are computed as

$$< n(\alpha) >= \frac{1}{18} \frac{N_s}{P \cdot SPP} \tag{3.60}$$

The air gap inductance and air gap inductance factor can be computed as (3.61) and (3.62), respectively.

$$L_g = \frac{53\pi}{162} \mu_0 \frac{rl}{g} \frac{1}{SPP^2} (\frac{N_s}{P})^2 \tag{3.61}$$

$$\sigma_\delta = \frac{L_g}{L_m} = \frac{53\pi^2}{4 \cdot 162 K_w^2} \frac{1}{SPP^2} \tag{3.62}$$

The air gap inductance factor of each teeth/pole combination is computed, and summarized in Table. 3.2. It can be observed that the inductance factor increases as the SPP value decreases too. Comparing the air gap inductance factor of the SL winding with the DL winding configurations, the SL configurations exhibit much higher inductance.

3.3.3. Mutual Inductance

3.3.3.1. Mutual Inductance of ISDW

The mutual inductance of ISDW is analyzed here as a reference for FSCW. Again, 3-phase SL winding machine with unity SPP is used as an example. The winding functions of phase A and B are illustrated in Fig. 3.11.

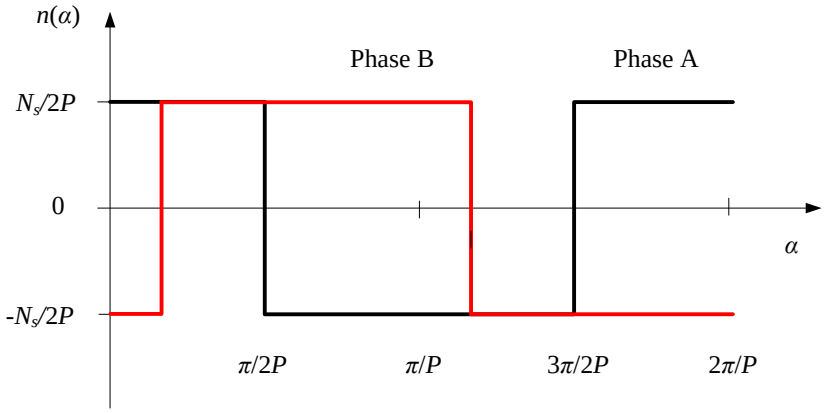

Fig. 3.11. Winding functions of full pitched winding configuration with SPP = 1.

For ISDW configurations, the winding function is non-zero everywhere, and each phase occupies the entire peripheral of the air gap. The angular difference between phases is $2\pi/3$. If the air-gap is assumed even everywhere, the second term of mutual inductance (3.17) is zero because the average value of winding function is zero. The mutual inductance formula can be computed as (3.63). Substituting (3.63) and (3.30) into (3.22), the mutual inductance factor is calculated as (3.64).

$$M = -\frac{2\pi}{3}\mu_0 \frac{lr}{g}\left(\frac{N_s}{2P}\right)^2 \tag{3.63}$$

$$m_c = \frac{M}{L_g} = -\frac{1}{3} \tag{3.64}$$

The mutual inductance is verified by FEA simulations on two different machine models. The models of 8-pole machines with SPP = 1 and SPP = 2 are shown in Fig. 3.12 (a) and (b). They share the same rotor configuration with evenly distributed air gap. To minimize the effect of tooth tip leakage and slot leakage components, the air gap is

configured to be very small; hence the air gap inductance component is the dominant component.

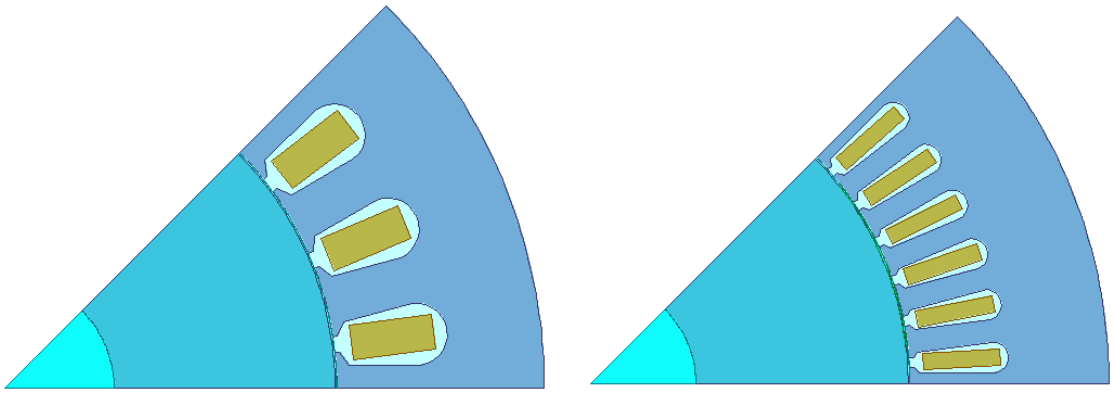

(a) (b)

Fig. 3.12. Cross sections of 8-pole ISDW machines: (a) SPP = 1, (b) SPP = 2.

The simulated inductances are listed in Table 3.3. The mutual inductance is about 1/3 of the self-inductance, and this matches the analysis of (3.64). When SPP = 1, the mutual inductance is slightly lower than 1/3 of the self-inductance. When SPP = 2, the mutual inductance is slightly higher than 1/3 of the self-inductance. The mutual inductance factor of the sinusoidally distributed winding is -1/2, which can be verified by using the winding function method.

Table 3.3 Simulated self- and mutual inductances of the ISDW machines

SPP = 1		**SPP = 2**	
Self-inductance (mH)	0.47327	Self-inductance (mH)	0.43326
Mutual inductance (mH)	-0.14993	Mutual inductance (mH)	-0.16219

3.3.3.2. Mutual Inductance of DL FSCW

For FSCW, the mutual inductance can be calculated by applying (3.17). The turns function of each phase is non-zero under the teeth with coils. Because there is no overlap between phases, the first term of (3.17) is always zero. When the air gap is evenly distributed, the mutual inductance can be simplified as

$$M = -2\pi \frac{\mu_0 lr}{g} < n(\alpha) >^2 \tag{3.65}$$

For all the teeth/pole combinations listed in Table 3.1, the analysis is carried out based on SPP values.

Case 1, SPP = 1/2 or 1/4.

For teeth/pole combinations with SPP = 1/2 or 1/4, the winding configuration is illustrated in Fig. 3.9 (a). Substituting the average value of turns function (3.35) into (3.65), the mutual inductance can be calculated as (3.66). Substituting (3.66) and (3.36) into (3.22), the mutual inductance factor can be calculated as (3.67).

$$M = -2\pi \frac{1}{9} \frac{\mu_0 lr}{g} \left(\frac{N_s}{2P \cdot SPP} \right)^2 \tag{3.66}$$

$$m_c = \frac{M}{L_g} = -\frac{1}{2} \tag{3.67}$$

Case 2, SPP = 3/8 or 3/10

For teeth/pole combinations with SPP = 3/8 or 3/10, the winding configuration is illustrated in Fig. 3.9 (b). Substituting (3.38) into (3.65), the mutual inductance and the mutual inductance factor can be calculated as (3.68) and (3.69), respectively.

$$M = -2\pi \frac{1}{81} \frac{\mu_0 lr}{g} \left(\frac{N_s}{2P \cdot SPP} \right)^2 \tag{3.68}$$

$$m_c = \frac{M}{L_g} = -\frac{1}{26} \tag{3.69}$$

Case 3, SPP = 2/5 or 2/7, 3/7 or 3/11, 4/11

For teeth/pole combinations with SPP = 2/5 or 2/7, 3/7 or 3/11, and 4/11, the winding configurations are illustrated in Fig. 3.9 (c), (e) and (h), respectively. The average values of the turns functions are zero, Hence the mutual inductance and the mutual inductance factor are zero.

$$M = 0 \tag{3.70}$$

$$m_c = \frac{M}{L_g} = 0 \tag{3.71}$$

Case 4, SPP = 5/14 or 5/16

For teeth/pole combinations with SPP = 5/14 or 5/16, the winding configuration is illustrated in Fig. 3.9 (d). Substituting (3.44) into (3.65), the mutual inductance and the mutual inductance factor can be calculated as (3.72) and (3.73), respectively.

$$M = -2\pi \frac{1}{225} \frac{\mu_0 lr}{g} \left(\frac{N_s}{2P \cdot SPP} \right)^2 \tag{3.72}$$

$$m_c = \frac{M}{L_g} = -\frac{1}{74} \tag{3.73}$$

Case 5, SPP = 7/16, 7/20 or 7/22

For teeth/pole combinations with SPP = 7/16, 7/20 or 7/22, the winding configurations are illustrated in Fig. 3.9 (f) and (g), respectively. Substituting (3.47) into (3.65), the mutual inductance and the mutual inductance factor can be calculated as (3.74) and (3.75), respectively.

$$M = -2\pi \frac{1}{441} \frac{\mu_0 lr}{g} \left(\frac{N_s}{2P \cdot SPP} \right)^2 \tag{3.74}$$

$$m_c = \frac{M}{L_g} = -\frac{1}{146} \tag{3.75}$$

Case 6, SPP = 9/20, 9/22

For teeth/pole combinations with SPP = 9/20 and 9/22, the winding configurations are illustrated in Fig. 3.9 (i) and (j), respectively. Substituting (3.50) into (3.65), the mutual inductance and the mutual inductance factor can be calculated as (3.76) and (3.77), respectively.

$$M = -2\pi \frac{1}{729} \frac{\mu_0 lr}{g} \left(\frac{N_s}{2P \cdot SPP} \right)^2 \tag{3.76}$$

$$m_c = \frac{M}{L_g} = -\frac{1}{242} \tag{3.77}$$

The mutual inductance factors of DL FSCW winding are summarized in Table 3.1. For most of the teeth/pole combinations, the mutual inductance factor is negligible. Hence the mutual inductance is considerably smaller than the self-inductance and may be neglected. However, in case of SPP = 1/2 or 1/4, the mutual inductance factor is -1/2. It is interesting to notice that the mutual inductance factor of the sinusoidally distributed winding is also -1/2. This phenomenon will be discussed later in section 3.4.1.

3.3.3.3. Mutual Inductance of SL FSCW

For all the teeth/pole combinations listed in Table 3.2. The analysis is also carried out based on the SPP values.

Case 1, SPP = 1/2 or 1/4.

For the teeth/pole combinations with SPP = 1/2 or 1/4, the winding configuration is illustrated in Fig. 3.10 (a). Substituting (3.54) into (3.65), the mutual inductance can be calculated as (3.78). Substituting (3.78) and (3.55) into (3.22), the mutual inductance factor can be calculated by (3.79).

$$M = -2\pi \frac{1}{36} \frac{\mu_0 lr}{g} \left(\frac{N_s}{P \cdot SPP} \right)^2 \tag{3.78}$$

$$m_c = \frac{M}{L_g} = -\frac{1}{5} \tag{3.79}$$

Case 2, SPP = 2/5 or 2/7, 4/11

For teeth/pole combinations with SPP = 2/5 or 2/7, 4/11, the winding configurations are illustrated in Fig. 3.10 (b) and (e), respectively. The average values of the turns function are zero. Hence the mutual inductance factors are also zero.

$$M = 0 \tag{3.80}$$

$$m_c = \frac{M}{L_g} = 0 \tag{3.81}$$

Case 3, SPP = 3/7 or 3/11, 3/8 or 3/10

For teeth/pole combinations with SPP = 3/7 or 3/11, 3/8 or 3/10, the winding configurations are illustrated in Fig. 3.10 (c) and (d), respectively. Substituting (3.60) into (3.65), the mutual inductance can be calculated as (3.82). Substituting (3.82) and (3.61) into (3.22), the mutual inductance factor can be calculated as (3.83).

$$M = -2\pi \frac{1}{324} \frac{\mu_0 lr}{g} \left(\frac{N_s}{P \cdot SPP} \right)^2 \tag{3.82}$$

$$m_c = \frac{M}{L_g} = -\frac{1}{53} \tag{3.83}$$

The mutual inductance factors for SL FSCW winding are summarized in Table 3.2. For most of the teeth/pole combinations, the mutual inductance factor is negligible. Hence the mutual inductance is considerably smaller than the self-inductance and may be neglected. Only when SPP = 1/2 or 1/4, the mutual inductance factor is -0.2. For same SPP number, comparing the mutual inductance factors of SL winding in Table 3.2 with

those of DL winding in Table 3.1, the SL winding exhibits much lower mutual inductance factor.

The SL winding configurations exhibits zero slot leakage coupling between coils. Hence the total mutual inductance of the SL FSCW is negligible. The negligible mutual inductance enables SL FSCW machines a candidate for fault tolerant operation. The failure of one phase does not affect other phases, which is termed as magnetic isolation in fault tolerant machines [71].

3.4. INDUCTANCE ANALYSIS OF FRACTIONAL SLOT CONCENTRATED WINDING MACHINES WITH SALIENT ROTORS

3.4.1. DL FSCW with More Stator Teeth Than Rotor Poles

Section 3.3 presents the comprehensive inductance analysis of FSCW, where evenly distributed air gap is assumed in all the analysis. When the FSCW machines are equipped with salient rotors, the inductance variation behaves differently.

As has been discussed in the conventional winding function based inductance method, the inverse air gap function $g^{-1}(\alpha,\theta)$ is very difficult to obtain analytically. However, it is not necessary to obtain the inverse air gap function in the entire air gap peripheral. The minimum and maximum inductances during one electrical period are desired to approximate the inductance variation.

The minimum inductance is obtained when the air gap length is maximized and vice versa. To investigate the maximum and minimum air gap length, the flux line distribution

of FSCW machines with salient rotors are studied here. As shown in Fig. 3.13 and 3.14, three phase windings are marked by different colors: phase A (yellow), phase B (blue), phase C (red). The FSCW machines are excited by single phase current (phase A is excited). In Fig. 3.13 and 3.14, when *d*-axis is aligned with A-axis, the flux line distribution is referred to as the *d*-axis flux distribution. It corresponds to the maximum equivalent air gap length and minimum inductance. When *q*-axis is aligned with A-axis, the flux line distribution is referred to as the *q*-axis flux distribution. It corresponds to the minimum equivalent air gap length and maximum inductance.

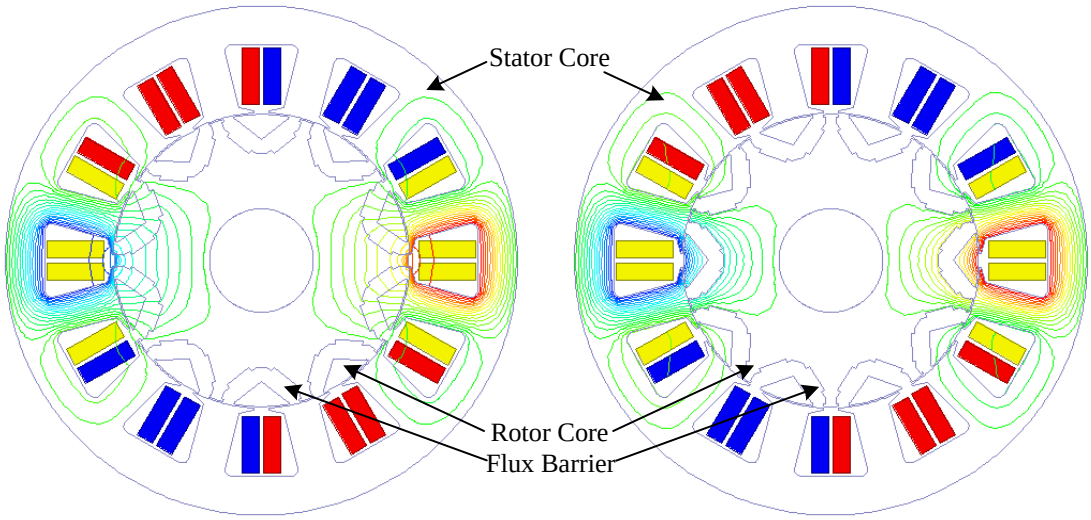

Fig. 3.13. Flux line distributions of DL FSCW 12/10 machine with salient rotor:

(a) *d*-axis flux distribution, (b) *q*-axis flux distribution.

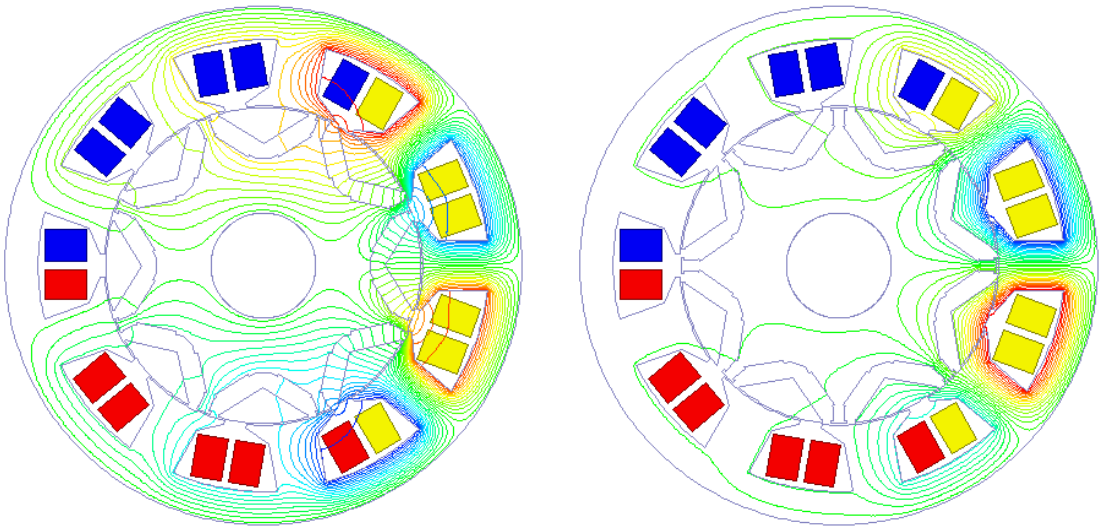

(a) (b)

Fig. 3.14. Flux line distributions of DL FSCW 9/8 machine with salient rotor:

(a) *d*-axis flux distribution, (b) *q*-axis flux distribution.

When the modified winding function based inductance calculation method is applied, the air gap length is only required where the turns function is non-zero. In the figures of *d*-axis flux distributions, the flux lines coming out of the excited teeth have to travel through the mechanical air gap and the flux barrier, hence the equivalent *d*-axis air gap length can be approximated by (3.84). In the figures of *q*-axis flux distributions, the flux lines coming out of the excited teeth only need to travel through the mechanical air gap, hence the equivalent *q*-axis air gap length can be approximated by (3.85).

$$g_d = g + T_b \tag{3.84}$$

$$g_q = g \tag{3.85}$$

where, T_b is the thickness of the flux barriers.

This conclusions of the equivalent *d*- and *q*-axis air gap length can be applied to FSCW machines when average values of the turns functions are very small, in which case, the flux coming out of rotor tends to travel back to excited stator teeth. When SPP ≠ 1/2, for FSCW machines with more stator teeth than rotor poles, very big difference between the *d*- and *q*-axis equivalent air gap lengths can be achieved according to (3.84) and (3.85). When the effect of flux barrier opening is accounted, the *q*-axis inductance will be reduced.

For the 12/10 machine in Fig. 3.13, the self- and mutual inductance waveforms and their Fourier series are shown in Fig. 3.15 (a) and (b) respectively. For the 9/8 machine in Fig. 3.14, the self- and mutual inductance waveforms and their Fourier series are shown in Fig. 3.16 (a) and (b) respectively. The 0^{th} order harmonic corresponds to the average value of the inductance.

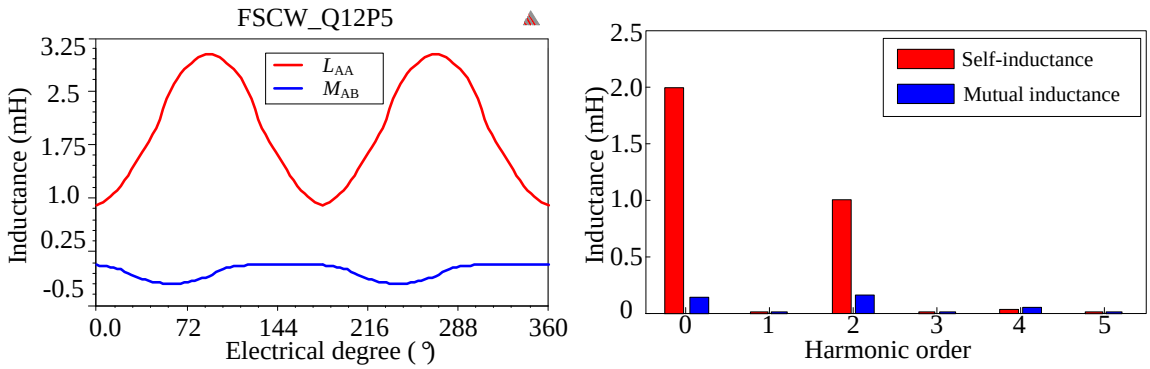

(a) (b)

Fig. 3.15. Self- and mutual inductances of the DL 12/10 machine:

(a) inductance waveforms, (b) inductance Fourier series.

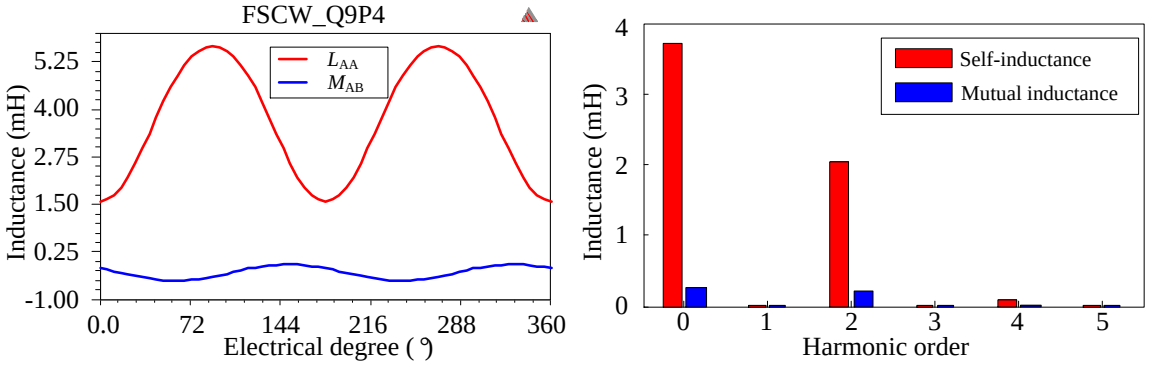

(a) (b)

Fig. 3.16. Self- and mutual inductances of the DL 9/8 machine:

(a) inductance waveforms, (b) inductance Fourier series.

When SPP = 1/2, the average value of the turns function is not zero any more. The flux coming out of the excited teeth does not travel back to other excited stator teeth. Fig. 3.17 (a) and (b) show the *d*- and *q*-axis flux distributions of a 12/8 machine.

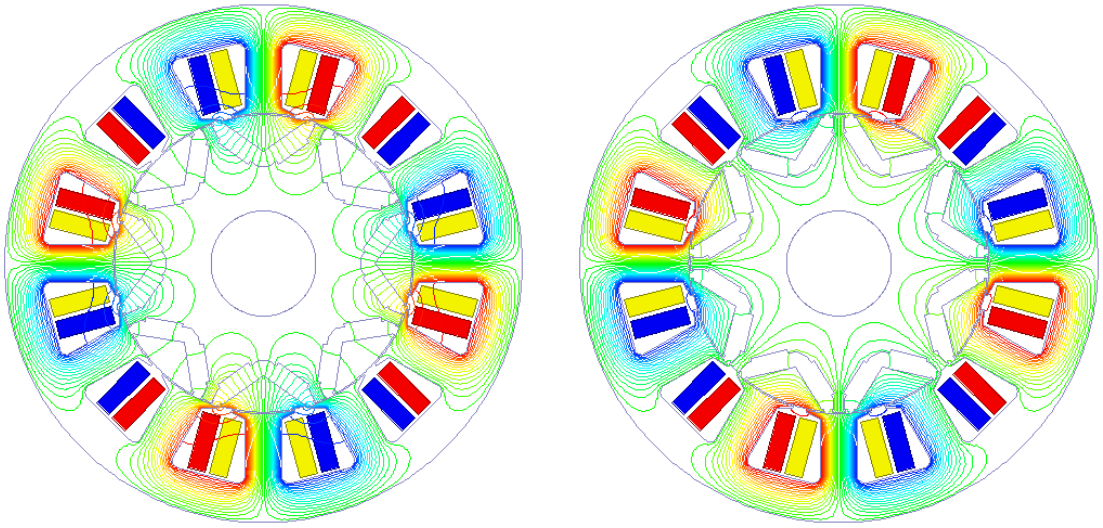

(a) (b)

Fig. 3.17. Flux line distributions of DL FSCW 12/8 machine with salient rotor:

(a) *d*-axis flux distribution, (b) *q*-axis flux distribution.

When the flux barrier opening is ignored and the ribs between the flux barriers are small enough, the *d*- and *q*-axis equivalent air gap length may be approximated by (3.86) and (3.87). This also explains why the air gap inductance factor corresponds to this SPP number is lower than other SPP numbers.

$$g_d = 2(g + T_b) \tag{3.86}$$

$$g_q = 2g \tag{3.87}$$

However, in *d*-axis flux distribution, there will be significant amount of leakage flux traveling back to the adjacent teeth via the ribs, hence the equivalent *d*-axis inductance will be increased. The *q*-axis inductance will be reduced due to the flux barrier opening. For the 12/8 machine, the self- and mutual inductance waveforms and Fourier series are shown in Fig. 3.18 (a) and (b). The mutual inductance is no longer negligible compared to the self-inductance.

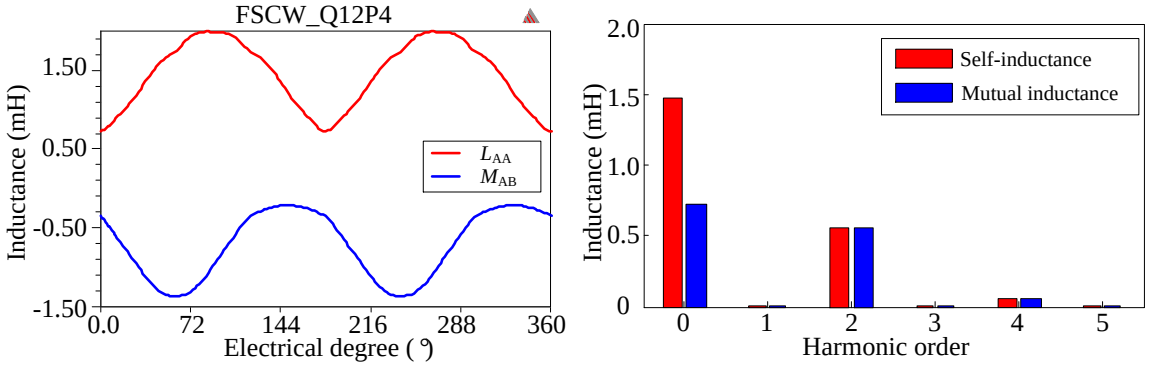

(a) (b)

Fig. 3.18. Self- and mutual inductances of the DL 12/8 machine:

(a) inductance waveforms, (b) inductance Fourier series.

For all 3 teeth/pole combinations in Fig. 3.13, 3.14 and 3.17 above, comparing the average values of mutual inductance and the self-inductance, it is observed that the simulation results well match the mutual inductance factors in Table 3.1. It may be concluded that the mutual inductance factor in Table 3.1 is feasible for salient rotors machines if the inductance average value is considered.

Due to zero or very low mutual inductance factor of the 12/10 and 9/8 machines, the 2^{nd} order mutual inductance harmonic is also considerably lower than the 2^{nd} order self-inductance harmonic. However, it is interesting to notice that the 12/8 machine exhibits comparable 2^{nd} order harmonics of mutual inductance and self-inductance. As can be observed in Fig. 3.17, the flux coming out of the excited teeth travels back to the adjacent teeth, and each adjacent tooth carries half of the flux lines, hence the mutual inductance factor is -1/2. The flux linkage variation of the excited phase and the unexcited phase are approximately the same. Hence the 2^{nd} order of the self- and mutual inductance harmonics are equivalent.

As has been mentioned earlier, the mutual inductance factor of pure sinusoidally distributed winding is also -1/2. Fig. 3.19 shows the cross section of an ISDW machine, which shares same rotor configuration as the 12/8 machine in Fig. 3.17. The *d*- and *q*-axis flux distributions are also illustrated in Fig. 3.19. The inductance waveforms during one electrical period and their Fourier series are shown in Fig. 3.20. The average value of the self- and mutual inductances is roughly -1/3, which satisfies the analytical mutual inductance factor. Again, the 2^{nd} order harmonics of the self- and mutual inductances are comparable. The flux line surrounding the exited coils links the coils belonging to

adjacent phases. Hence the 2nd order of the self- and mutual inductance harmonics are also equivalent.

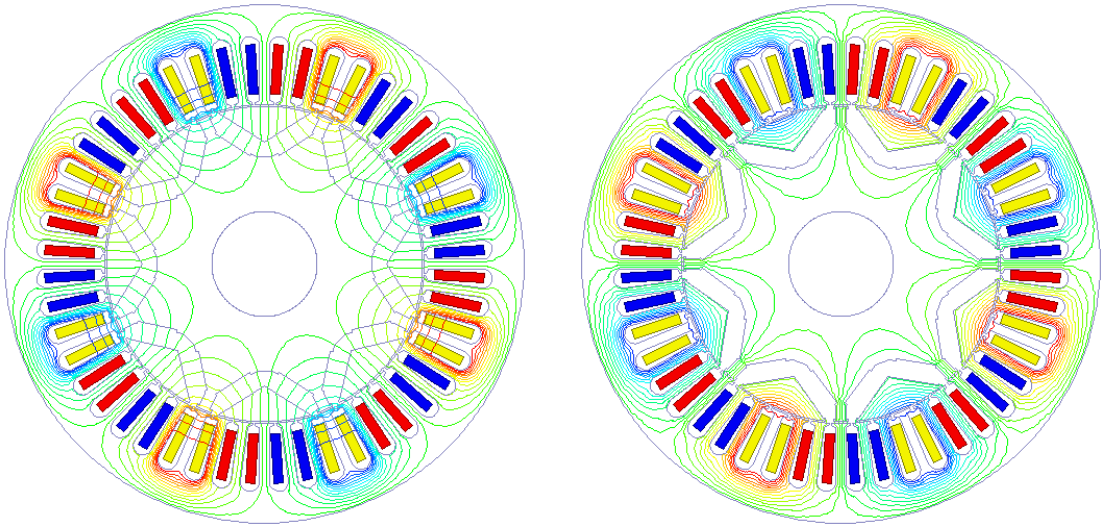

(a) (b)

Fig. 3.19. Flux line distributions of ISDW 48/8 machine with salient rotor:

(a) *d*-axis flux distribution (b) *q*-axis flux distribution.

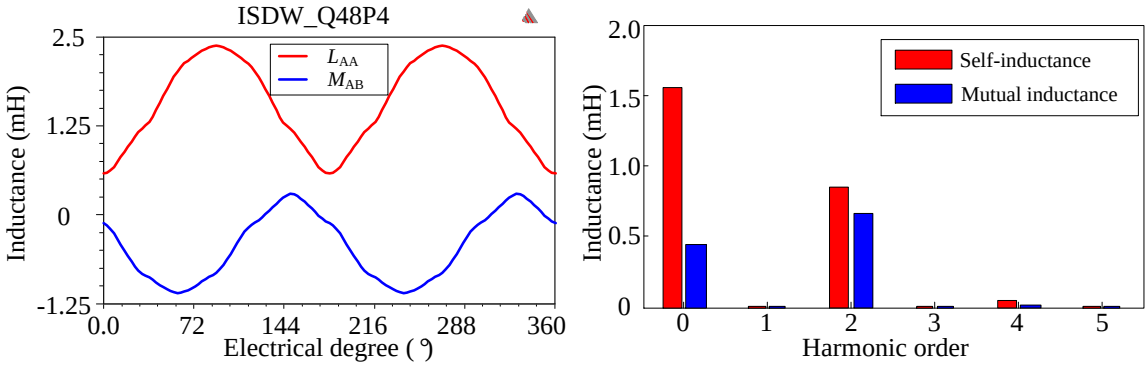

(a) (b)

Fig. 3.20. Self- and mutual inductances of the 48/8 machine:

(a) inductance waveforms, (b) inductance Fourier series.

As a summary, for the DL FSCW machines with more stator teeth than rotor poles, the equivalent *d*- and *q*-axis air gap lengths can be approximated by the air gap length and flux barrier length. The difference may be adjusted effectively by changing the thickness of the flux barriers and air gap. Hence high saliency can be achieved.

3.4.2. SL FSCW with More Stator Teeth Than Rotor Poles

Fig. 3.21 illustrates the *d*- and *q*-axis flux distributions of a 12/10 SL FSCW machine. When SL FSCW configurations are adopted, the equivalent air gap lengths change significantly. In the *d*-axis flux distribution, the flux line travels through one mechanical air gap and one flux barrier. However, in the *q*-axis flux distribution, a significant amount of flux travels into the adjacent teeth through the rotor iron above the flux barriers, which are referred to as the rotor islands in this thesis. The equivalent air gap length is almost twice the mechanical air gap length. As a result, the *q*-axis inductance will be reduced significantly.

One solution for this is to reduce the rotor yoke thickness of the rotor, as shown in Fig. 3.22. At high excitation level, the bridges at the rotor bottom tend to saturate. The flux tends to travel back to the adjacent teeth. As a result, the equivalent *d*-axis air gap length is almost doubled. Hence the saliency can be improved. More details of the effects of the thin rotor yoke bridges on reluctance torque and core losses will be discussed in details in section 4.6.

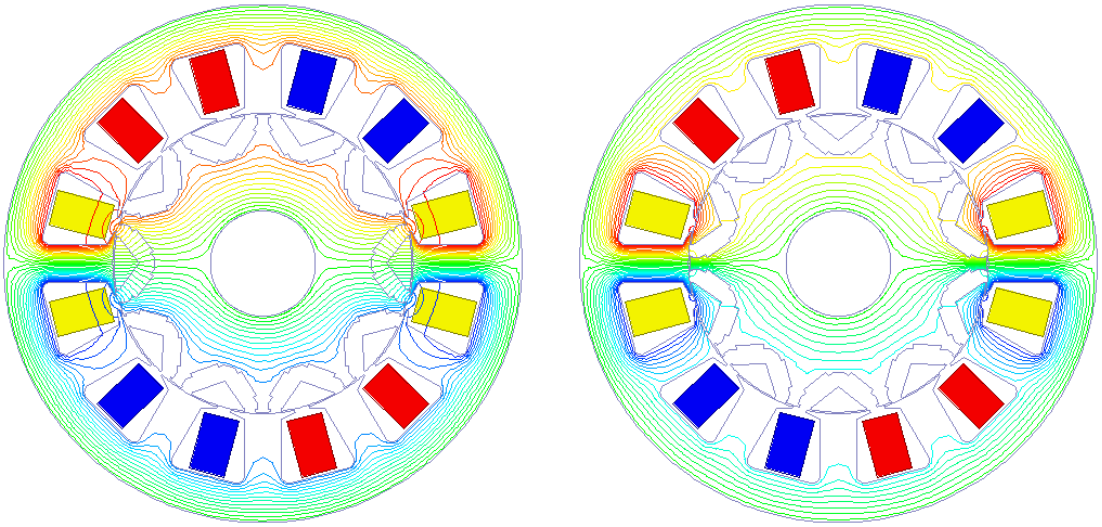

(a) (b)

Fig. 3.21. Flux line distributions of SL FSCW 12/10 machine with salient rotor: (a) *d*-axis flux distribution, (b) *q*-axis flux distribution.

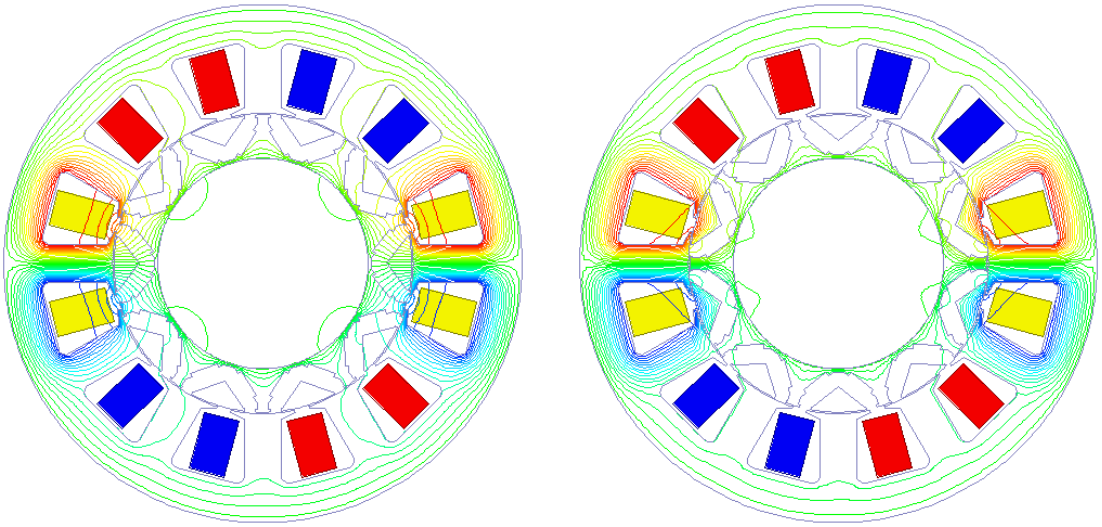

(a) (b)

Fig. 3.22. Flux line distributions of SL FSCW 12/10 machine with salient rotor (thin rotor yoke bridges): (a) *d*-axis flux distribution, (b) *q*-axis flux distribution.

The inductance waveforms and Fourier series of the SL machine in Fig. 3.22 are reported in Fig. 3.23. Comparing the winding inductance profile of the SL 12/10 machine with the DL 12/10 machine, the SL machine exhibits much lower mutual inductance. The 2nd order harmonics are comparable, which indicates they have comparable reluctance torque capability.

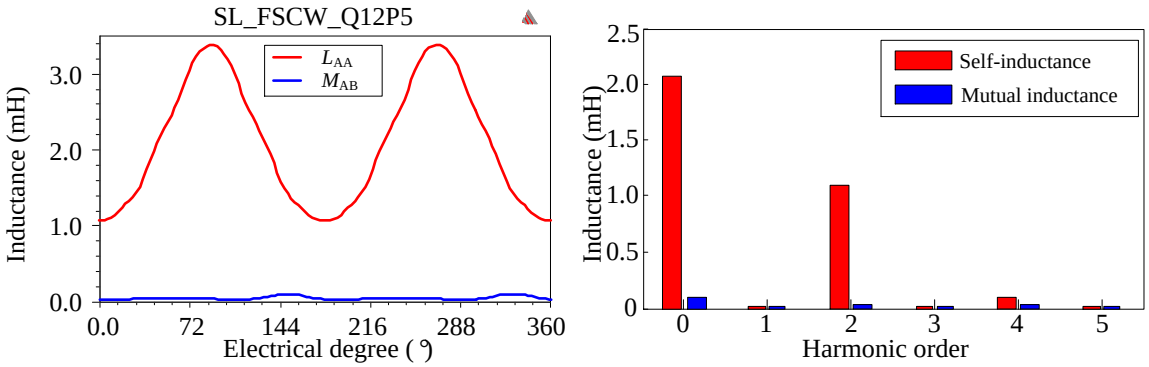

(a) (b)

Fig. 3.23. Self- and mutual inductances of the SL 12/10 machine (thin rotor yoke bridges): (a) inductance waveforms, (b) inductance Fourier series.

When SPP = 1/2, the average value of the turns function is not zero any more. The flux coming out of the excited teeth travels back to the adjacent stator teeth, as shown in Fig. 3.24. In the *d*-axis flux distribution, the flux has to travel through two mechanical air gaps and two flux barriers, and in the *q*-axis flux distribution, the flux travels through two mechanical air gap only. Big difference between the *d*- and *q*-axis equivalent air gap lengths can be achieved. The self- and mutual inductance waveforms and Fourier series are shown in Fig. 3.24. It is observed that the mutual inductance of the SL 12/8 machine is quite low, which doesn't quite match the mutual inductance factor in Table 3.2.

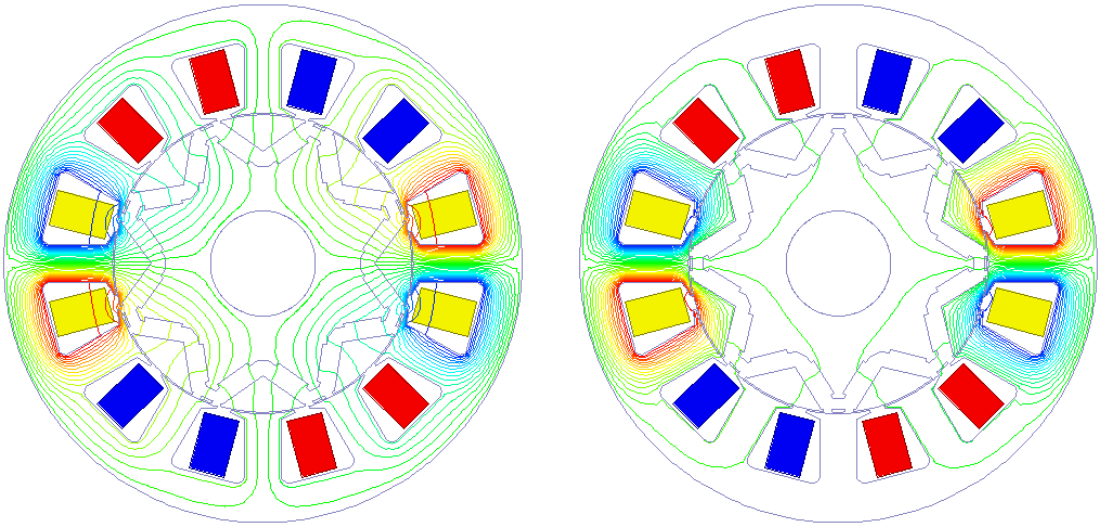

(a) (b)

Fig. 3.24. Flux line distributions of SL FSCW 12/8 machine with salient rotor:

(a) *d*-axis flux distribution, (b) *q*-axis flux distribution.

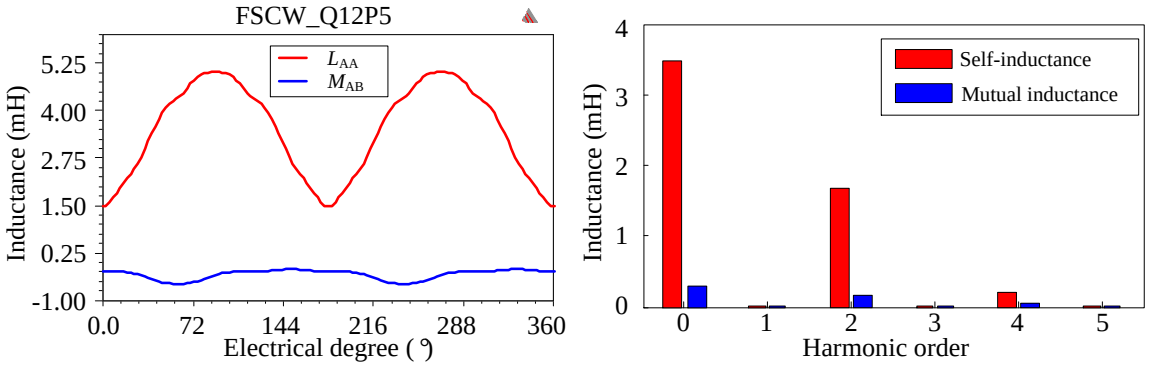

(a) (b)

Fig. 3.25. Self- and mutual inductances of the SL 12/8 machine:

(a) inductance waveforms, (b) inductance Fourier series.

3.4.3. DL FSCW with Fewer Stator Teeth Than Rotor Poles

The FSCW machines with fewer stator teeth than rotor poles are investigated on a 12/14 machine. The flux line distributions are illustrated in Fig. 3.26. Comparing Fig. 3.26 to Fig. 3.13, the flux line distributions are very similar to those of the 12/10 machine, because they share same winding layout. However, because there are fewer stator teeth than the rotor poles, each tooth spans more than one rotor pole. Therefore, in the *d*-axis flux line distribution, flux tends to travel through the rotor ribs, which increases the inductance; on the *q*-axis flux distribution, the rotor magnetic steel island is too small, which decreases the inductance. Overall, the inductance difference between the maximum and minimum is significantly reduced.

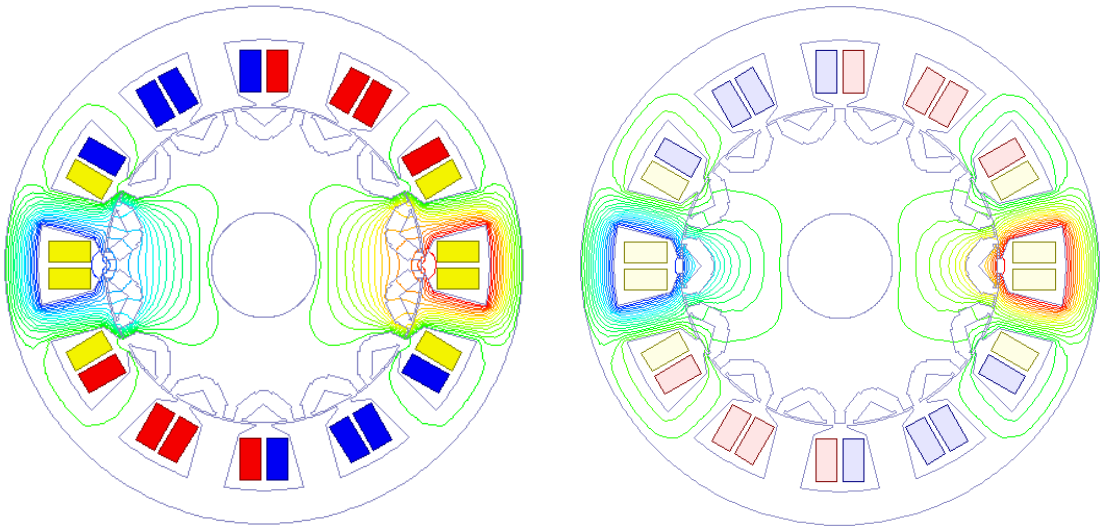

(a) (b)

Fig. 3.26. Flux line distributions of DL FSCW 12/14 machine with salient rotor: (a) *d*-axis flux distribution, (b) *q*-axis flux distribution.

In some publications, this is explained as that rotor permeance variation is filtered out by the oversized stator tooth span [72]. When the 12/14 machine in Fig. 3.26 is configured with same turn number as the 12/10 machine in Fig. 3.13, the winding inductance waveforms and their Fourier series are shown in Fig. 3.27. It can be observed that the 2nd order inductance harmonic of the 12/14 machine is about 40% of that of the 12/10 machine; hence the saliency will be significantly reduced.

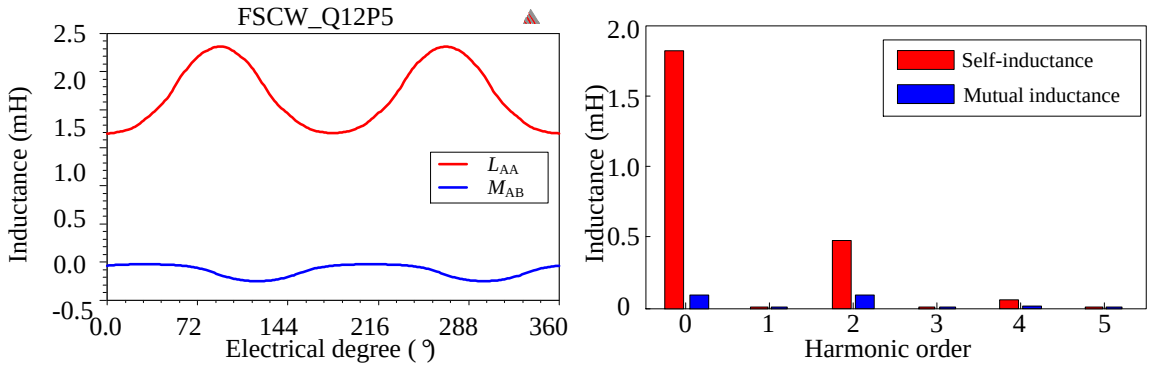

(a) (b)

Fig. 3.27. Self- and mutual inductances of the DL 12/14 machine:

(a) inductance waveforms, (b) inductance Fourier series.

Similar phenomena can be found on SL FSCW machines, which will not be discussed in details here. Generally, it can be concluded that the topologies with fewer stator teeth than rotor poles are not suitable for high saliency design. Though this conclusion is derived based on the DL machine, it can be applied to SL, or multiple layer winding machines.

3.5. *d*- AND *q*-AXIS INDUCTANCE ANALYSIS OF FRACTIONAL SLOT CONCENTRATED WINDING MACHINES WITH SALIENT ROTORS

3.5.1. General Formula of *d*- and *q*-axis Inductance

The *d*- and *q*-axis inductances can be obtained from the self-inductance L_g and mutual inductance *M*. As has been seen in section 3.4, the self- and mutual inductance only contain even order harmonics due to the rotor symmetry. They can be represented by the Fourier series (3.88) and (3.89), respectively.

$$L_g = L_0 + L_2 \cos 2\theta + \cdots \tag{3.88}$$

$$M = M_0 + M_2 \cos 2(\theta + \frac{2}{3}\pi) + \cdots \tag{3.89}$$

where, L_0 is the average value of self-inductance, L_2 is the 2nd order harmonic of the self-inductance; M_0 is the average value of mutual inductance, M_2 is the 2nd order harmonic of mutual inductance. The harmonics of higher order are ignored because they are considerably lower than the 2nd order harmonic and do not contribute to the average torque production.

By transforming the self- and mutual inductance from static frame to synchronous rotating frame, the closed form of the *d*- and *q*-axis inductances can be obtained as (3.90) and (3.91).

$$L_d = (L_0 - M_0) + (\frac{L_2}{2} + M_2) \tag{3.90}$$

$$L_q = (L_0 - M_0) - (\frac{L_2}{2} + M_2) \tag{3.91}$$

For distributed winding, the 2nd order harmonic of the self- and mutual inductance are equivalent, and the *d*- and *q*-axis inductance formulas can be simplified as

$$L_d = (L_0 - M_0) + \frac{3}{2} L_2 \tag{3.92}$$

$$L_q = (L_0 - M_0) - \frac{3}{2} L_2 \tag{3.93}$$

However, for FSCW machine, it is more complicated. The mutual inductance is dependent on the teeth/pole combination. For FSCW machines with SPP ≠ 1/2 or 1/4, the mutual inductance is negligible. Therefore, it is reasonable to assume that M_2, the 2nd order harmonic of the mutual inductance, is negligible, and the *d*- and *q*-axis inductance formulas can be simplified as

$$L_d = (L_0 - M_0) + \frac{1}{2} L_2 \tag{3.94}$$

$$L_q = (L_0 - M_0) - \frac{1}{2} L_2 \tag{3.95}$$

For DL FSCW with SPP = 1/2 or 1/4, the mutual inductance factor is -1/2, and the 2nd order harmonic of the mutual inductance is roughly equivalent to the 2nd order harmonic of the self-inductance. As a result, the *d*- and *q*-axis inductances can be represented by (3.92) and (3.93).

3.5.2. Analysis of *d*- and *q*-axis Inductance Difference of FSCW Machine with Salient Rotor

From equation (3.4), the reluctance torque capability can be estimated by the inductance difference of the *d*- and *q*-axis inductances, which can be obtained from (3.90) and (3.91) as

$$L_{dif} = L_2 + 2M_2 \tag{3.96}$$

For ISDW or DL FSCW machines with SPP = 1/2 or 1/4, the inductance difference (3.96) can be simplified to (3.97). For FSCW machines with SPP ≠ 1/2 or 1/4, the mutual inductance is often considered negligible, and the inductance difference can be simplified to (3.98).

$$L_{dif} = 3L_2 \tag{3.97}$$

$$L_{dif} = L_2 \tag{3.98}$$

The 2nd order harmonic of self-inductance can be approximated by the maximum and minimum values of the self-inductance, which can be calculated by using the modified winding function method and the equivalent *d*- and *q*-axis air gap lengths.

$$L_2 = \frac{L_{g\max} - L_{g\min}}{2} \tag{3.99}$$

Assuming the FSCW and ISDW machines are equipped with same rotors, the *d*- and *q*-axis inductance difference may be compared by applying the constraint of same phase turn number. Hence they have same current load. If PM is employed in the rotor, a more

fair constraint is that the PM flux linkages in both machines are equivalent, i.e., the winding turn numbers meet (3.100).

$$k_{CW} N_{CW} = k_{DW} N_{DW} \tag{3.100}$$

where, N_{CW} and N_{DW} are the phase turn numbers of the FSCW and ISDW, k_{CW} and k_{DW} are the winding factor of the FSCW and ISDW.

When SPP ≠ 1/2 or 1/4, the air gap winding inductance can be calculated using modified winding function method, and the inductances of ISDW and FSCW machines can be calculated by (3.101) and (3.102) respectively.

$$L_{CW} = \frac{\upsilon\pi}{3} \mu_0 \frac{rl}{g_{eq}} \left(\frac{N_{CW}}{P \cdot \upsilon} \right)^2 \frac{1}{SPP^2} \tag{3.101}$$

$$L_{DW} = \mu_0 \frac{rl}{g_{eq}} \left(\frac{N_{DW}}{2P} \right)^2 2\pi \cdot (1-\varepsilon), 0 \le \varepsilon < 1 \tag{3.102}$$

where, g_{eq} is the equivalent air gap length of *d*- or *q*-axis, υ is number of winding layers, and $\upsilon = 1, 2$, ε is used to account for the short pitch and the distribution effect of the winding, and for full pitched winding with SPP = 1, ε = 0.

The maximum and minimum self-inductance can be approximated by substituting the minimum and maximum airgap lengths into (3.101) and (3.102). Thus the 2nd order self-inductance harmonic of the FSCW and ISDW can be computed as (3.103) and (3.104) respectively.

$$L_{2CW} = \frac{\upsilon\pi}{2\cdot 3}\mu_0 rl\left(\frac{N_{CW}}{P\cdot\upsilon}\right)^2 \frac{1}{SPP^2}\left(\frac{1}{g_q}-\frac{1}{g_d}\right) \tag{3.103}$$

$$L_{2DW} = \frac{(1-\varepsilon)}{2}\mu_0 rl\left(\frac{N_{DW}}{2P}\right)^2 2\pi\left(\frac{1}{g_q}-\frac{1}{g_d}\right), 0\le\varepsilon<1 \tag{3.104}$$

In case of DL FSCW with SPP ≠ 1/2 or 1/4, for the same rotor configuration, the 2nd order self-inductance ratio of the FSCW and ISDW machines can be derived as

$$\frac{L_{2CW}}{L_{2DW}} = \frac{1}{3}\frac{1}{(1-\varepsilon)}\frac{1}{SPP^2}\left(\frac{k_{DW}}{k_{CW}}\right)^2 \tag{3.105}$$

In case of SL FSCW with SPP ≠ 1/2 or 1/4, the equivalent air gap length is `doubled, and equation (3.105) can still be used for SL FSCW machines. From (3.97), (3.98) and (3.105), the *d*- and *q*-axis inductance difference ratio of the FSCW and ISDW can be calculated by (3.106). If the winding factor of the FSCW and ISDW are close enough, the ratio of inductance differences can be approximated as (3.107).

$$\frac{L_{difCW}}{L_{difDW}} = \frac{L_{2CW}}{3L_{2DW}} = \frac{1}{9}\frac{1}{(1-\varepsilon)}\frac{1}{SPP^2}\left(\frac{k_{DW}}{k_{CW}}\right)^2 \tag{3.106}$$

$$\frac{L_{difCW}}{L_{difDW}} \overset{\varepsilon\to 0}{\approx} \frac{1}{9}\frac{1}{SPP^2} \tag{3.107}$$

When (3.107) is unity, SPP = 1/3, which corresponds to same teeth number and pole number. Equation (3.107) indicates that, for FSCW machines with more teeth than poles, the machine with lower SPP number features higher inductance difference between *d*- and *q*-axis.

3.5.3. Simulation of *d*- and *q*-axis Inductance Difference of FSCW Machine with Salient Rotor

Comparative studies are performed to investigate the inductance difference. Two comparisons are studied here, and each comparison group has the same rotor pole configuration but different stator teeth number. The ISDW machines and the FSCW machines with SPP = 1/2 are included in each comparison.

The first comparison is performed on the 10-pole machines. The geometry and inductance profiles of the 60/10 ISDW machines are illustrated in Fig. 3.28 (a) and Fig. 3.29, respectively. The geometry and inductance profiles of the 15/10 machine are reported in Fig. 3.28 (b) and Fig. 3.30. The geometry and inductance profiles of the 12/10 machine are reported in Fig. 3.13 and Fig. 3.15. The constraint applied to this comparison is that all machines have same phase turn number.

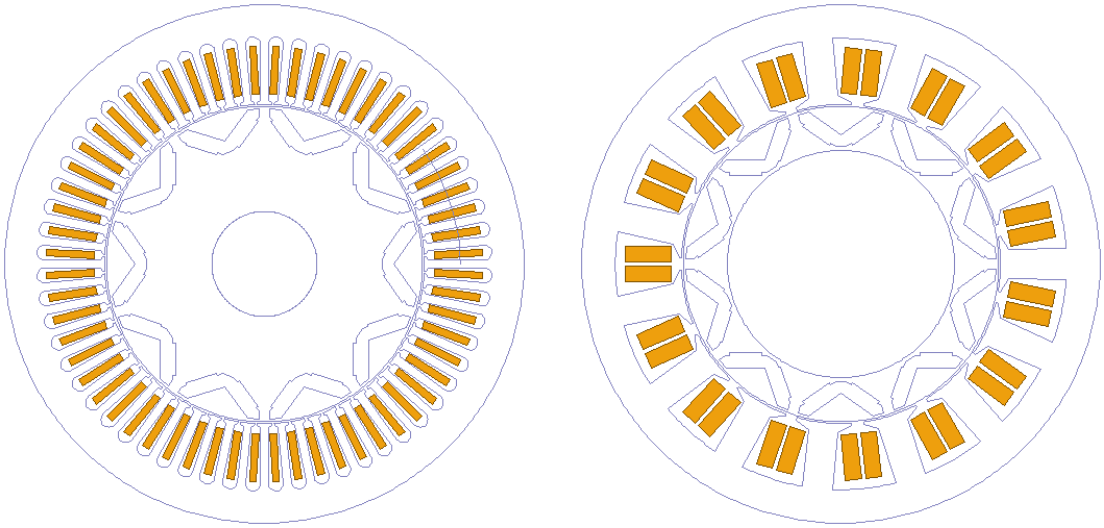

(a) (b)

Fig. 3.28. Cross sections of 10-pole machines: (a) Q_s = 60, P = 5, (b) Q_s = 15, P = 5.

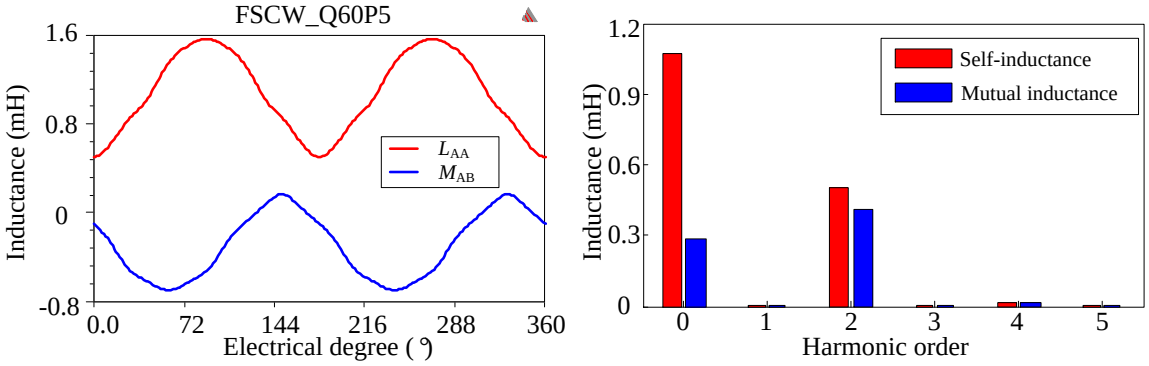

(a) (b)

Fig. 3.29. Self- and mutual inductances of the 60/10 machine:

(a) inductance waveforms, (b) inductance Fourier series.

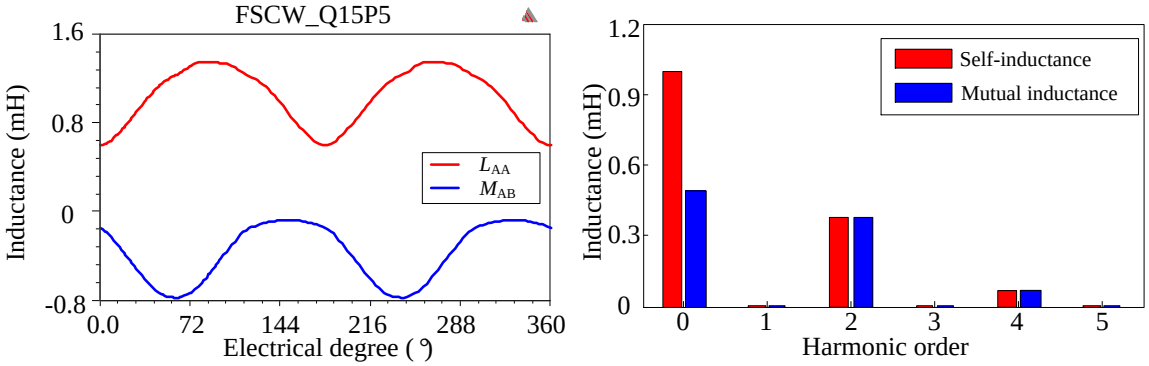

(a) (b)

Fig. 3.30. Self- and mutual inductances of the DL 15/10 machine:

(a) inductance waveforms, (b) inductance Fourier series.

The second comparison is performed on the 8-pole machines. The geometry and inductance profiles of the 48/8 ISDW machine are illustrated in Fig. 3.19 and Fig. 3.10. The geometry and inductance profiles of the 12/8 machine are reported in Fig. 3.17 and Fig. 3.18. The geometry and inductance profiles of the 9/8 machine are reported in Fig.

3.14 and Fig. 3.16. Again, the constraint applied to this comparison is that all machines have same phase turn number.

The 2nd order self-inductance harmonics of the 10-pole machines are reported in Table 3.4. The 2nd order self-inductance harmonics of the 8-pole machines are reported in Table 3.5.

Table 3.4 Effect of teeth number on machine inductance for 10-pole machines

Teeth/Pole	L_2 (mH)	L_{diff} (mH)
60/10	0.505	1.515
12/10	1.024	1.024
15/10	0.378	1.135

Table 3.5 Effect of teeth number on machine inductance for 8-pole machines

Teeth/Pole	L_2 (mH)	L_{diff} (mH)
48/8	0.853	2.559
9/8	2.046	2.046
12/8	0.590	1.771

For both 10-pole and 8-pole machines, the ISDW machines feature highest inductance difference. The FSCW machines exhibit lower inductance difference. The inductance difference ratio between the 12/10 and 60/10 machines, and the inductance difference ratio between the 9/8 and 48/8 machines confirm the analysis of (3.107). It is also observed that, the FSCW machines with SPP = 1/2 features lower inductance difference than the ISDW machines.

3.5.4. Saturation Effect

The saturation effect is investigated by simulating the reluctance torque production of the FSCW machines at different excitation levels. The 10-pole and 8-pole configurations are studied here, and their geometries are shown in Fig. 3.13 and 3.14. The ISDW machines are used as references to evaluate the FSCW machine reluctance torque performances. The reluctance torque production is studied under nonlinear condition. The machines are excited by sinusoidal currents. Again, the phase turn numbers of the FSCW and ISDW are the same in these simulations.

The reluctance torque waveforms of the 60/10 and 12/10 machines are illustrated in Fig. 3.31 (a) and (b), respectively. The average torque of both machines at each current is illustrated in Fig. 3.31 (c). Because the flux lines of the FSCW machines are focused on a few teeth and poles, the FSCW machine is more likely to be saturated. When the current is lower than 20 A, the bridges between rotor islands of the FSCW machines are more saturated than the ISDW machine, which reduces the leakage flux. Hence the FSCW machine produces higher reluctance torque. However, as current goes higher, the teeth and rotor islands of the FSCW machines will be more saturated, hence the reluctance torque is reduced. The torque ratio at each current is calculated and reported in Fig. 3.31 (d). The torque ratio approaches the theoretical value as excitation current increases, but it becomes lower at high current level because the FSCW is more saturated. As indicated in Fig. 3.31 (c), the linear torque/current ratio of the ISDW machine is 0.4637 Nm/A, and the linear torque/current ratio of the FSCW is 0.3101 Nm/A, and the ratio is very close to the theoretical inductance difference ratio calculated from (3.107).

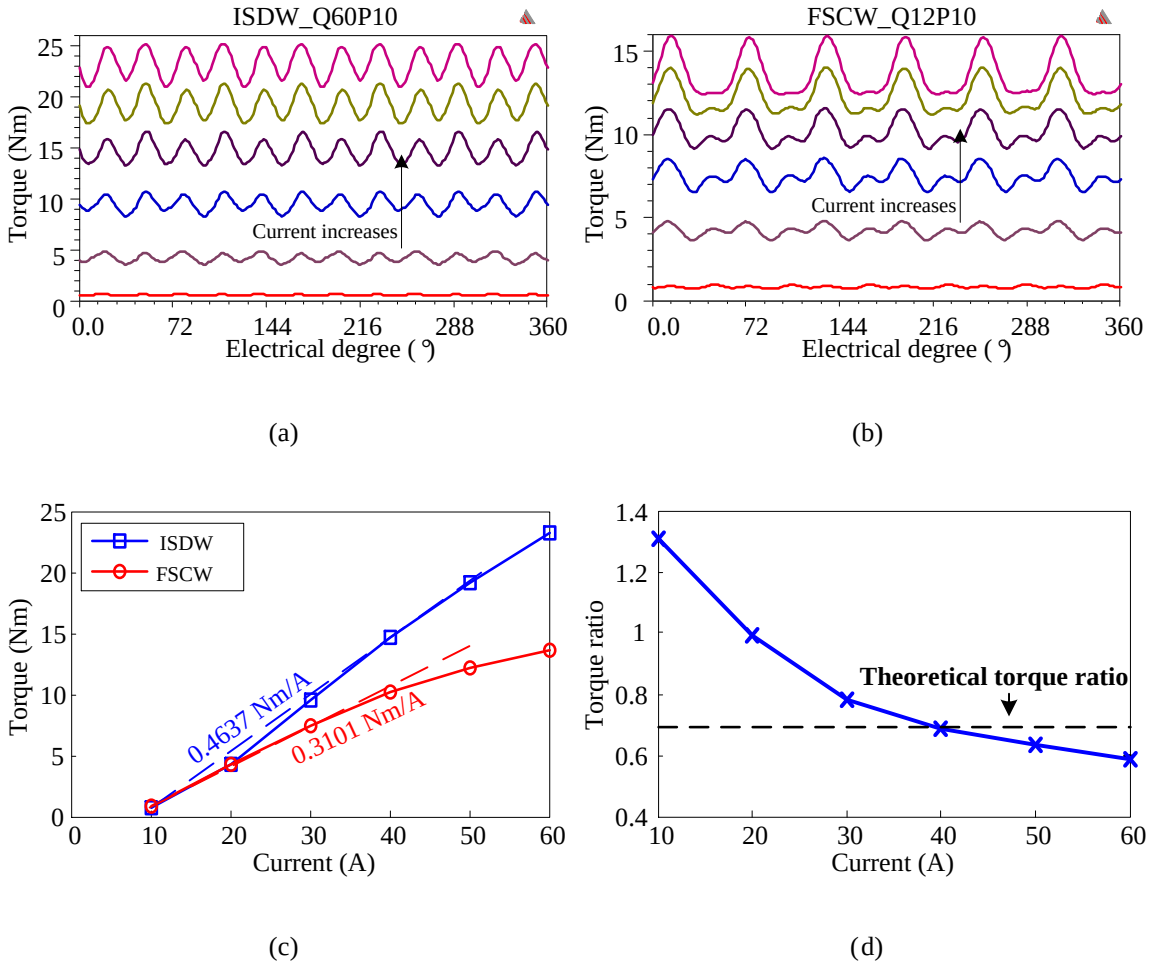

Fig. 3.31. Reluctance torque of 10-pole machines: (a) reluctance torque waveforms of the ISDW machine, (b) reluctance torque waveforms of the DL FSCW machine, (c) average reluctance torque versus current, and (d) torque ratio between FSCW and ISDW machines.

The reluctance torque waveforms of the 48/8 and 9/8 machines are illustrated in Fig. 3.32 (a) and (b), respectively. The average torque of both machines at each current is illustrated in Fig. 3.32 (c). The torque ratio at each current is calculated and reported in Fig. 3.32 (d). The torque ratio approaches the theoretical value as excitation current increases, but it becomes lower at high current level because the FSCW is more saturated. As indicated in Fig. 3.32 (c), the linear torque/current ratio of the ISDW machine is

0.4035 Nm/A, and the linear torque/current ratio of the FSCW is 0.2979 Nm/A, which is also very close to the theoretical inductance difference ratio of (3.107).

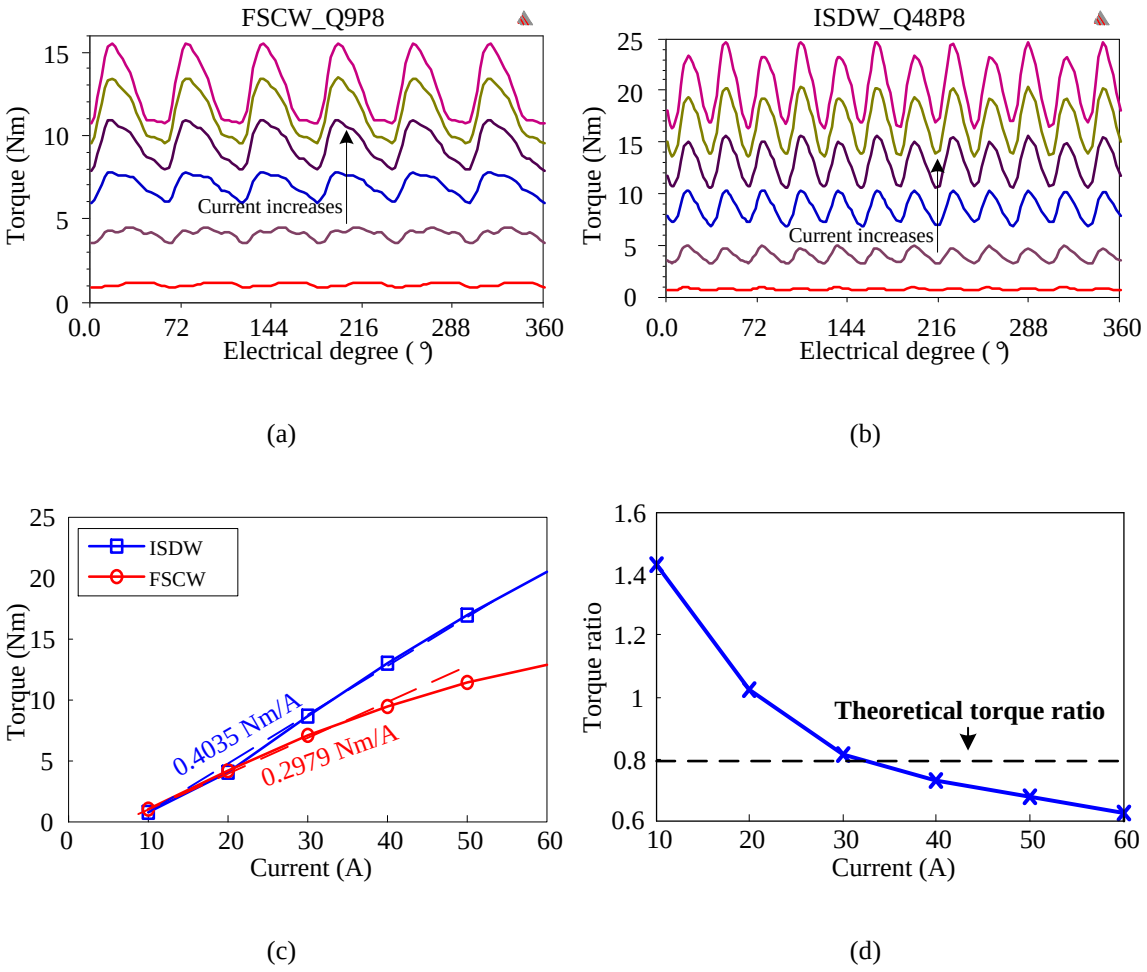

Fig. 3.32. Reluctance torque of 8-pole machines: (a) reluctance torque waveforms of the ISDW machine, (b) reluctance torque waveforms of the DL FSCW machine, (c) average reluctance torque versus current, and (d) torque ratio between FSCW and ISDW machines.

The reluctance torque production is also studied on machines with SPP = 1/2. Fig. 3.33 (a) and (b) shows the reluctance torque waveforms of the 15/10 and 12/8 machines. The average torque at each current is obtained and reported in Fig. 3.33 (c) and (d).

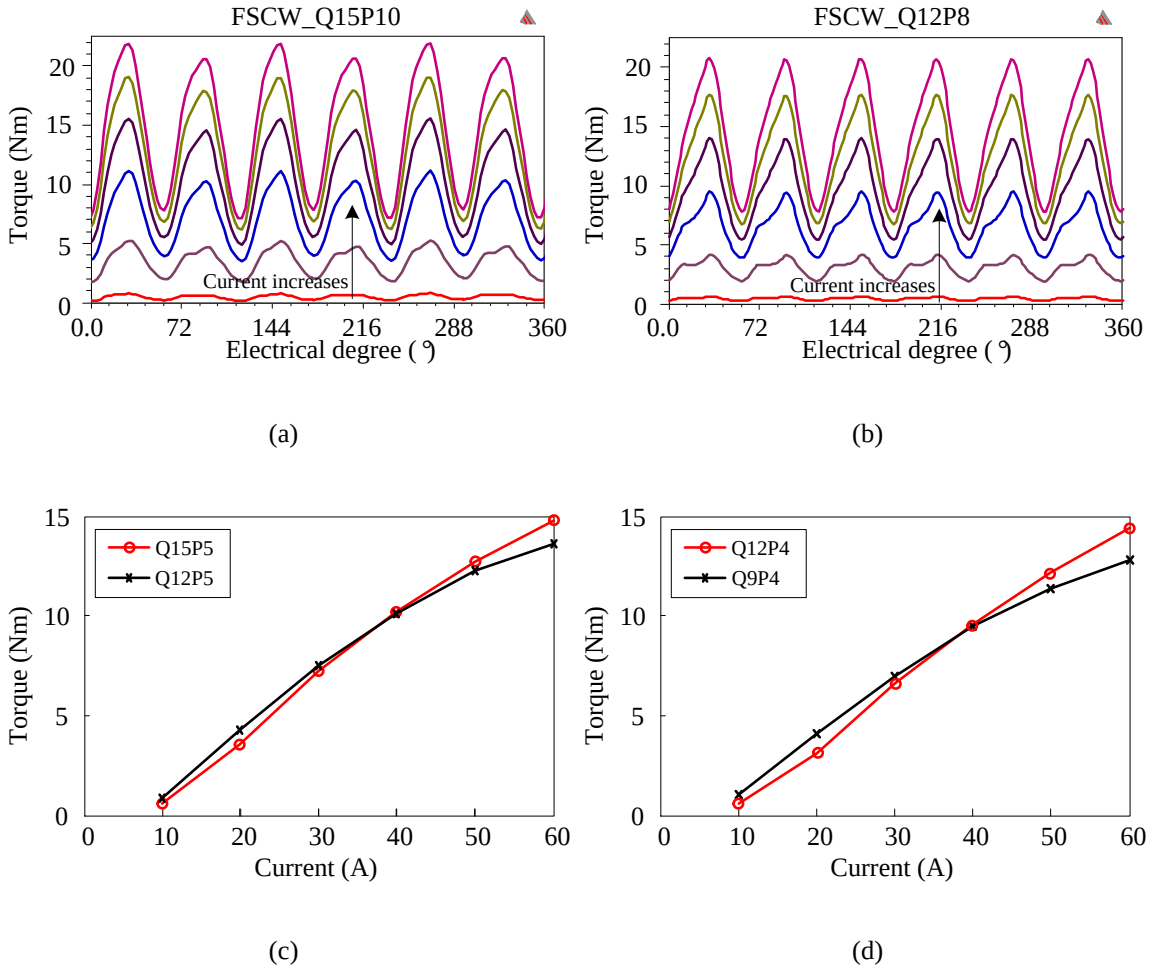

Fig. 3.33. Reluctance torque of FSCW machines: (a) reluctance torque waveforms of the 15/10 machine, (b) reluctance torque waveforms of the 12/8 machine, (c) average reluctance torque of 10-pole FSCW machines, and (d) average reluctance torque of 8-pole FSCW machines.

Compared to the torque waveforms in Fig. 3.31 and 3.32, the FSCW machines with SPP = 1/2 feature much higher torque ripple. The machines with SPP = 1/2 produce slightly higher torque at high current level, mainly because the more evenly distributed flux line makes the machine less saturated.

3.6. CONCLUSIONS

In this chapter, the inductance of the FSCW machines is analyzed comprehensively. The modified winding function based inductance calculation method is proposed, based on which the air gap inductance and mutual inductance of the FSCW are analyzed. The air gap inductance factor and mutual inductance factor are summarized for research reference.

The inductance of FSCW machines equipped with salient rotors is analyzed based on FEA simulations. The equivalent air gap lengths can be obtained from the flux line distributions, and they can be used in the modified winding function method to approximate the inductance variation. The self- and mutual inductances of different FSCW machines are simulated and the results reveal the average values of the self- and mutual inductances match the analysis of mutual inductance factor very well. The FSCW machines with more rotor poles than stator teeth are not suitable for high saliency machines.

The general forms of *d*- and *q*-axis inductances are obtained and the *d*- and *q*-axis inductance difference of the FSCW machines are approximated using the modified winding function method. The inductance difference is compared with the ISDW machines analytically, and verified by FEA simulations. The saturation effect on reluctance torque production is also studied by FEA simulations. Generally speaking, the employment of the FSCW decreases the *d*- and *q*-axis inductance difference as well as the reluctance torque. Additionally, the FSCWs generate excessive MMF harmonics which is

more likely to saturate the stator and rotor core. Hence the reluctance torque capability deteriorates at high excitation level.

Chapter 4
DESIGN METHODOLOGY OF FRACTIONAL SLOT CONCENTRATED WINDING INTERIOR PERMANENT MAGNET MACHINES

This chapter presents the design methodology of FSCW IPM machine. The relationship between the machine parameters and the output characteristics is investigated to establish the insight of choosing machine parameters according to the specifications. In the initial design, the topology is selected, and the motor geometry model is developed parametrically. The Response surface method (RSM) is applied to optimize the machine design. To evaluate the performance of the machine, the optimized design is compared with a few alternative designs.

4.1. RELATIONSHIP BETWEEN MACHINE PARAMETERS AND TORQUE-SPEED CHARACTERISTIC

4.1.1. Idealized Mathematical Model of PMSM

Ideally, the inductances and PM flux linkage of PMSMs are constant under synchronous rotating *dq* frame. The *0*-axis is isolated and can be neglected. The voltage and flux linkage equations of IPMs under *dq* frame are shown in (4.1) and (4.2) respectively, and the torque equation is represented by (4.3). The equivalent circuits under *d*- and *q*-axis are represented in Fig. 4.1.

$$\begin{aligned} u_d &= R_s i_d + p\psi_d - \psi_q \omega \\ u_q &= R_s i_q + p\psi_q + \psi_d \omega \end{aligned} \tag{4.1}$$

$$\begin{aligned} \psi_d &= L_d i_d + \psi_f \\ \psi_q &= L_q i_q \end{aligned} \tag{4.2}$$

$$T_e = \psi_d i_q - \psi_q i_d \tag{4.3}$$

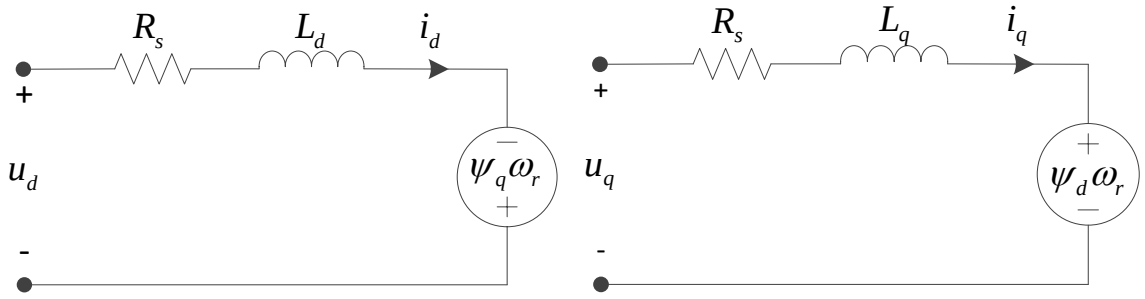

(a) (b)

Fig. 4.1. Equivalent circuits of PM machine: (a) *d*-axis circuit (b) *q*-axis circuit.

The phase current is constrained by a certain value. In most applications, the machine is driven by voltage source inverter; hence the terminal voltage of PMSM is limited.

$$\begin{aligned} i_s &= \sqrt{i_d^2 + i_q^2} \le i_{\lim} \\ u_s &= \sqrt{u_d^2 + u_q^2} \le u_{\lim} \end{aligned} \tag{4.4}$$

where, $i_{\lim}$ is stator current limitation; $u_{\lim}$ is phase voltage limitation.

Under steady state, substituting (4.1) to (4.4), the voltage limit is reformulated as (4.5). At high speed operation, the resistance voltage drop is negligible; thus equation (4.5) is simplified to be (4.6).

$$(-L_q i_q \omega_r + R_s i_d)^2 + (\psi_f \omega_r + L_d i_d \omega_r + R_s i_q)^2 \le u_{\lim}^2 \tag{4.5}$$

$$(L_q i_q)^2 + (\psi_f + L_d i_d)^2 \le \frac{u_{\lim}^2}{\omega^2} \tag{4.6}$$

Equation (4.6) reveals that the voltage limit is a set of concentric ellipses, which locate at the center $(-\psi_f / L_d, 0)$. The current corresponds to the center is defined as the characteristic current I_{ch}.

$$I_{ch} = \psi_f / L_d \tag{4.7}$$

The optimum current trajectory under the *d*- and *q*-axis current plane is shown in Fig. 4.2 [73]. The optimal current operation area is bounded by the MTPA trajectory, the maximum torque per flux (MTPF) trajectory, and the current limit circle. The MTPA trajectory starts from the origin and intersects with the current limit circle at point A, and the voltage ellipse which intersects with point A denotes the rated speed ω_1. The MTPF trajectory starts from the characteristic current C and intersects with the current limit circle at point B, and the voltage ellipse which intersects with point B determines speed ω_2. For speed below ω_1, the current is solely constrained by the current limit, and for speed above ω_2 the current is solely constrained by the voltage limit. When the speed is between ω_1 and ω_2, the current is bounded by both voltage and current limits. For some PMSMs, the characteristic current may locate outside the current limit circle, and there is no MTPF trajectory.

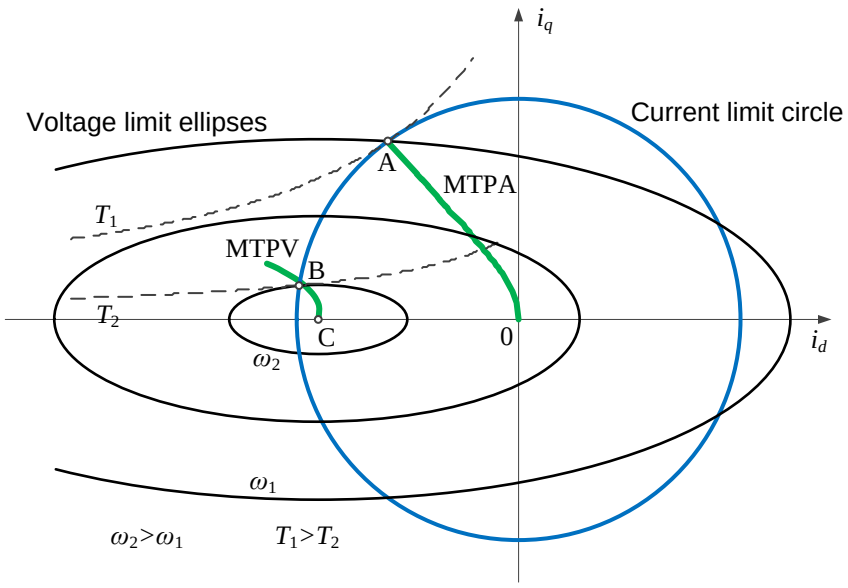

Fig. 4.2. Operation area on *d*- and *q*-axis current plane.

4.1.2. Normalized Model of PMSM

The output characteristic of PMSM is dependent on five parameters: i_{lim}, u_{lim}, L_d, L_q, and ψ_f. The normalized model can be employed to describe the torque-speed characteristic of PMSMs [74, 75]. However, the existing model is developed based on normalized back-EMF or PM flux linkage [76]. It can be confusing and hardly brings the insight of the relationship between machine parameters and output characteristics.

A new normalized model is developed here, and the base values of PMSM parameters and variables are listed in Table 4.1. The current and flux linkage base values are defined by the rated operating point, which is indicated by point A in Fig 4.2.

Table 4.1 Base value definitions of PMSM

Base current	$I_{base} = I_r = i_{\lim}$
	$I_{dr} = \dfrac{-\psi_f + \sqrt{\psi_f^2 + 8(L_d - L_q)^2 I_r^2}}{4(L_d - L_q)}$
	$I_{qr} = \sqrt{I_r^2 - I_{dr}^2}$
Base voltage	$U_{base} = U_r = u_{\lim}$
Base flux linkage	$\psi_{base} = \sqrt{(\psi_f + L_d I_{dr})^2 + (L_q I_{qr})^2}$
Base frequency	$\omega_b = \dfrac{U_{base}}{\psi_{base}}$
Base speed	$\Omega_{base} = \dfrac{\omega_{base}}{P}$
Base time	$t_b = \dfrac{1}{\omega_b}$
Base Inductance	$L_{base} = \dfrac{\psi_{base}}{I_{base}}$
Base power	$P_{base} = \dfrac{3}{2} U_{base} I_{base}$
Base torque	$T_{base} = \dfrac{P_{base}}{\Omega_{base}} = \dfrac{3}{2} P \psi_{base} I_{base}$

When (4.1) is divided by U_{base}, the normalized voltage equation is derived as (4.8). When (4.2) is divided by ψ_{base}, the normalized flux linkage equation can be obtained as (4.9). The superscript '*' is used to indicate the normalized values.

$$\begin{aligned} u_d^* &= d\frac{\psi_d^*}{t^*} - \psi_q^* \omega_r^* + R_s^* i_d^* \\ u_q &= d\frac{\psi_q^*}{t^*} + \psi_d^* \omega_r^* + R_s^* i_d^* \end{aligned} \tag{4.8}$$

$$\begin{aligned}\psi_d^* &= L_d^* i_d^* + \psi_f^* \\ \psi_q^* &= L_q^* i_q^*\end{aligned} \tag{4.9}$$

The electromagnetic torque can be formulated in per-unit form.

$$T_e^* = \psi_d^* i_q^* - \psi_q^* i_d^* = \psi_f^* i_q^* + (L_d^* - L_q^*) i_d^* i_q^* \tag{4.10}$$

In this normalized analysis, saliency ratio ρ and characteristic current I_{ch}^* are employed to determine the output characteristic.

$$\begin{aligned}\rho &= \frac{L_q}{L_d} = \frac{L_q^*}{L_d^*} \\ I_{ch}^* &= \frac{\psi_f^*}{L_d^*}\end{aligned} \tag{4.11}$$

4.1.3. Normalized Output Characteristics of PMSM

According to the base values defined above, the voltage and current limitation is always unity, i.e., $u_{\lim}^* = 1, i_{\lim}^* = 1$. Neglecting the stator resistor voltage drop, (4.3) and (4.6) are normalized as:

$$\sqrt{i_d^{*2} + i_q^{*2}} \le 1 \tag{4.12}$$

$$(\rho L_d^* i_q^*)^2 + (L_d^* I_{ch}^* + L_d^* i_d^*)^2 \le \left(\frac{1}{\omega_r^*}\right)^2 \tag{4.13}$$

In per-unit system, the rated *d*- and *q*-axis currents are obtained as

$$I_{dr}^{*}=\frac{-I_{ch}^{*}+\sqrt{I_{ch}^{*\,2}+8(1-\rho)^{2}}}{4(1-\rho)}$$
$$I_{qr}^{*}=\sqrt{1-I_{dr}^{*\,2}} \tag{4.14}$$

At point A, the flux linkage and speed are unity as well, which can be expressed as:

$$(\rho L_{d}^{*} i_{qr}^{*})^{2}+(L_{d}^{*} I_{ch}^{*}+L_{d}^{*} i_{dr}^{*})^{2}=1^{2} \tag{4.15}$$

Substituting equation (4.14) into (4.15), it is obvious that L_d^* , I_{ch}^* and ρ are dependent, and only two of them are required to describe the machine characteristics. Here, I_{ch}^* and ρ are chosen as the independent parameters, the per-unit *d*-axis inductance is derived as

$$L_{d}^{*}=\frac{1}{\sqrt{(I_{ch}^{*}+i_{dr}^{*})^{2}+\rho^{2}(1-i_{dr}^{*\,2})}} \tag{4.16}$$

Therefore, with the information of normalized characteristic current and saliency ratio, the output characteristic is uniquely determined. For normal saliency machines (saliency greater than one), the torque-speed and power-speed characteristics with respect to the parameters are demonstrated graphical in Fig. 4.3, where the *x*-axis is the characteristic current and *y*-axis is the saliency ratio. The blue curves are torque-speed profiles and the magenta curves are power-speed profiles.

The theoretical maximum speed is determined by the characteristic current only. When characteristic current is lower than 1, the maximum speed is infinite. When characteristic current is greater than 1, the maximum speed is finite. Regardless of the characteristic current value, in constant torque range ($\omega^{*} \le 1$), the increase of the

characteristic current or the saliency ratio improve the torque capability. When the characteristic current is lower than unity, the increase of characteristic current improves the torque capability in the entire speed range. When the characteristic is greater than unity, the increase of characteristic current reduces the speed range. The increase of saliency ratio improves the torque/power capability.

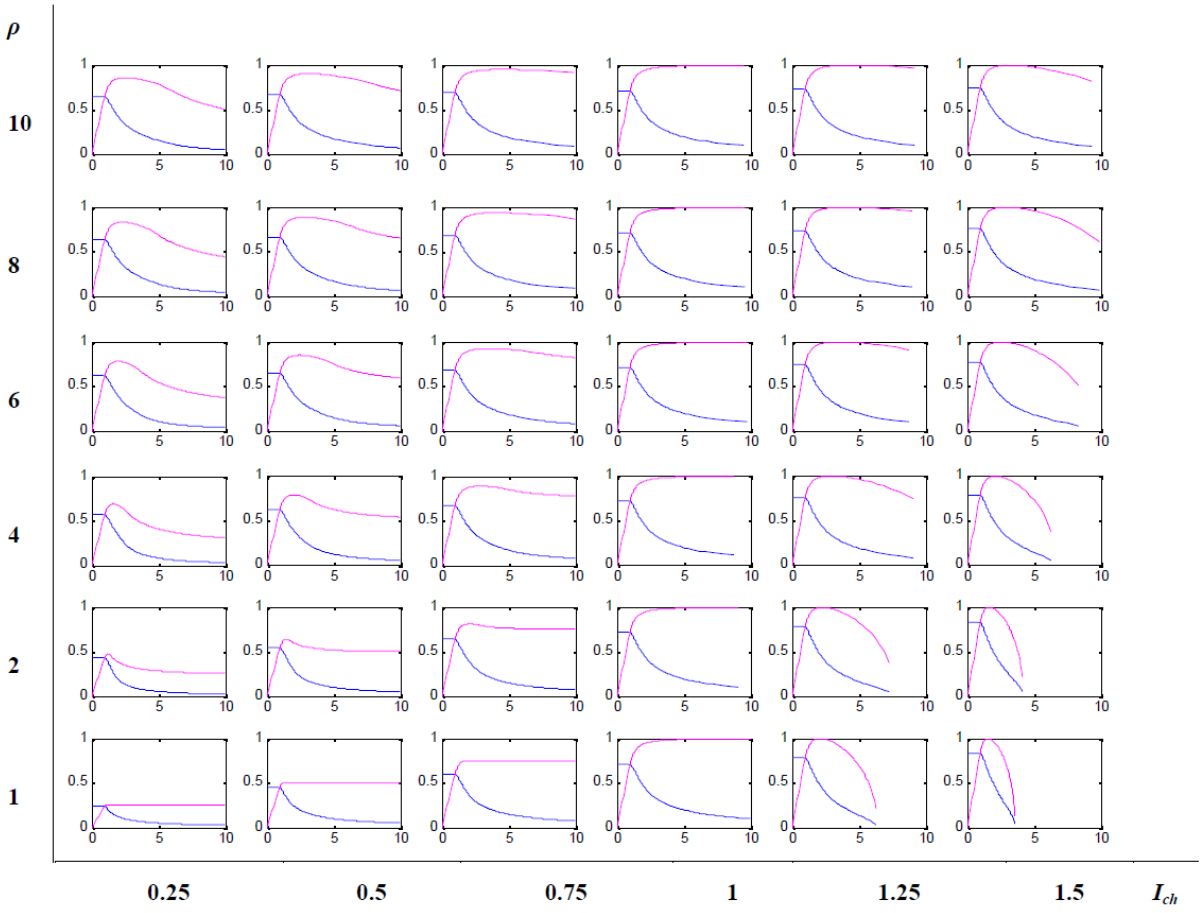

Fig. 4.3. Normalized torque and power versus speed characteristics.

In the field weakening range, the voltage approaches its limit, when the current approaches the limit, the per-unit power also indicate the power factor, which has strong impact on the machine efficiency. For a given machine with fixed parameters, by

choosing the characteristic current as the base current, the power factor can be analyzed in the field weakening range. In other words, the power factor of the machine may be evaluated by the ratio of the current and the characteristic current. For example, the current range which enables power factor to be above 0.8 at per-unit speed 3 are computed and illustrated in Fig. 4.4.

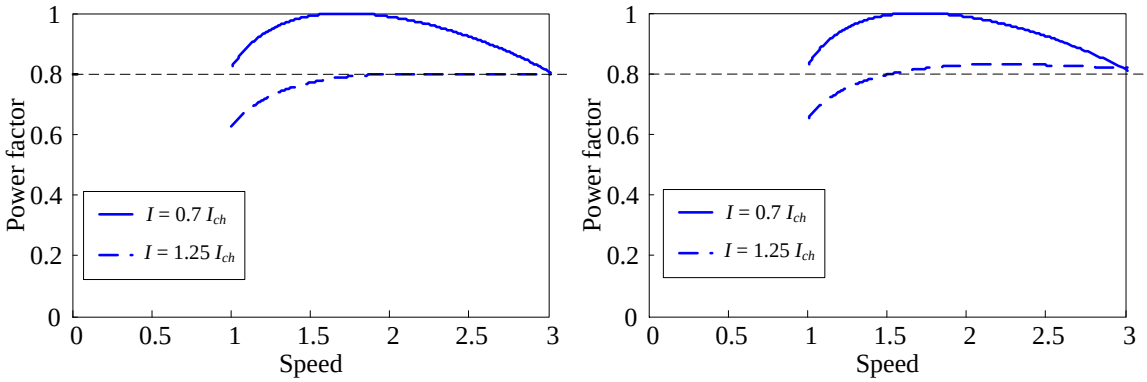

Fig. 4.4. Power factor prediction under different current excitations: (a) ρ = 1.0, (b) ρ = 1.6.

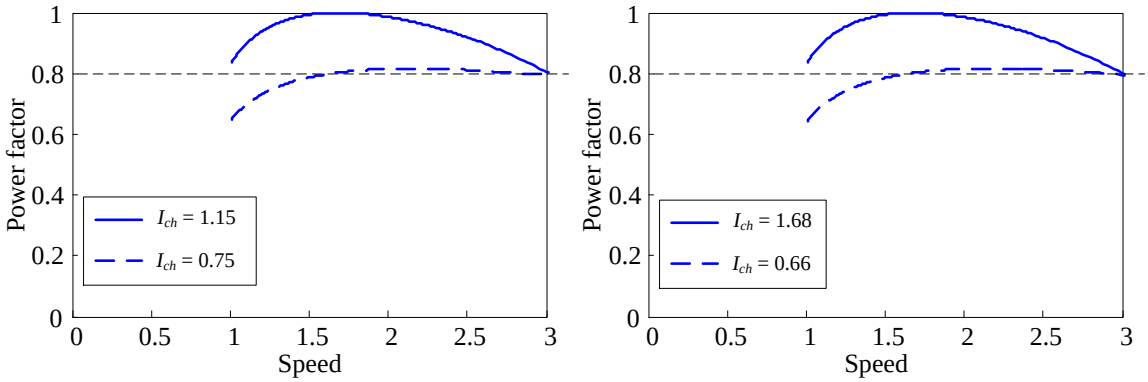

Fig. 4.5. Power factor properties of different characteristic currents: (a) ρ = 2.0, (b) ρ = 3.0.

On the other hand, the power factor prediction method can be used to guide the machine parameter selection. Assuming the saliency ratio is already known, for given power factor requirement, the range of per-unit characteristic current can be evaluated. For example, the normalized characteristic current in the range displayed in Fig. 4.5 exhibits power factor higher than 0.8 at per-unit speed 3. For same power factor requirement, higher saliency ratio enables the machine to operate in wider range.

4.2. INITIAL DESIGN

4.2.1. Machine Specifications

The machine is targeted on a light weight electric vehicle application. The New European Drive Cycle (NEDC) is used to evaluate the output characteristic, as illustrated in Fig. 4.6 (a). The operation point distribution is displayed in Fig. 4.6 (b). The specification of the machine is summarized in Table 4.2.

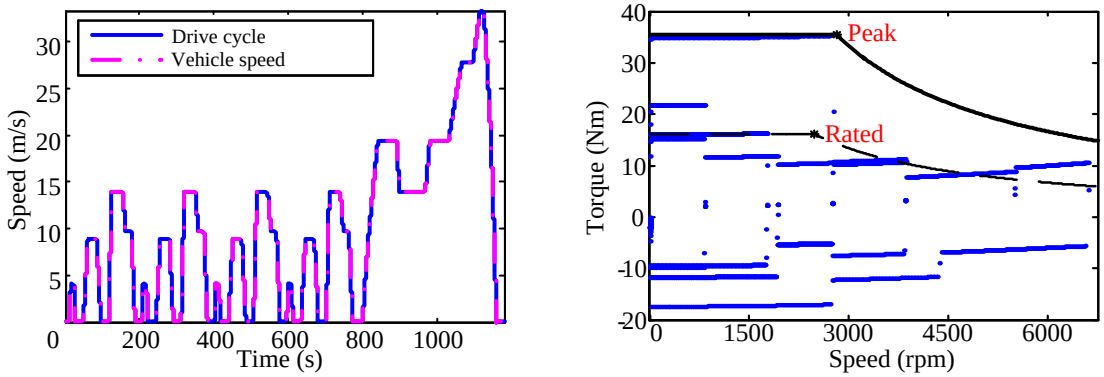

(a) (b)

Fig. 4.6. Motor drive cycle simulation: (a) vehicle speed of NEDC drive cycle, (b) operation point distribution and the torque-speed requirement.

Table 4.2 Target machine specifications

Maximum output power (kW)	12
Maximum Torque (Nm)	35
Maximum Speed (rpm)	6500
Base Speed (rpm)	2750
Rated Power (kW)	5.4
Rated torque (Nm)	16

4.2.2. Topology Selection

4.2.2.1. Teeth/Pole Combination

Maximum Speed

The relationship between the mechanical speed and excitation frequency can be established as

$$\Omega = \frac{60f}{P} \tag{4.17}$$

It is desirable to maintain the excitation frequency below 400 Hz mainly for two reasons: (1) the increase of the excitation frequency increases the core loss significantly; (2) the increased frequency requires higher PWM switching frequency, which may increase the inverter loss considerably. Here, the maximum pole pair number is extended to 5 (542 Hz), and the available teeth/pole combinations are 6/4, 9/6, 12/8, 15/10, 9/8, and 12/10.

Cogging Torque

For teeth/pole combination with SPP = 1/2, it can be proven that the least common multiple can be computed as (4.18).

$$LCM(Q_s, P) = 2mP = \frac{2m}{Q} \cdot QP, \text{SPP} = \frac{1}{2}, \frac{1}{4} \tag{4.18}$$

Normally, $2m/Q \leq 1$. As a result, the teeth/pole combinations with SPP = 1/2 generally produce high cogging torque. Machines with $2P = Q_s \pm 1$ and $2P = Q_s \pm 2$ exhibit low cogging torque and the least common multiples are proven as (4.19) and (4.20) respectively.

$$LCM(Q_s, P) = 2QP,\ 2P = Q_s \pm 1 \tag{4.19}$$

$$LCM(Q_s, P) = QP,\ 2P = Q_s \pm 2 \tag{4.20}$$

Unbalanced Magnetic Pull

The asymmetric arrangement of the coils causes unbalanced MMF and magnetic pull even without mechanical eccentricity. Machines with $2P = Q_s \pm 1$ exhibit high winding factors and low cogging torque. However, they suffer from unbalanced magnetic pull, as shown in Fig. 4.7. unbalanced magnetic pull may cause serious noise and vibration in high power machines.

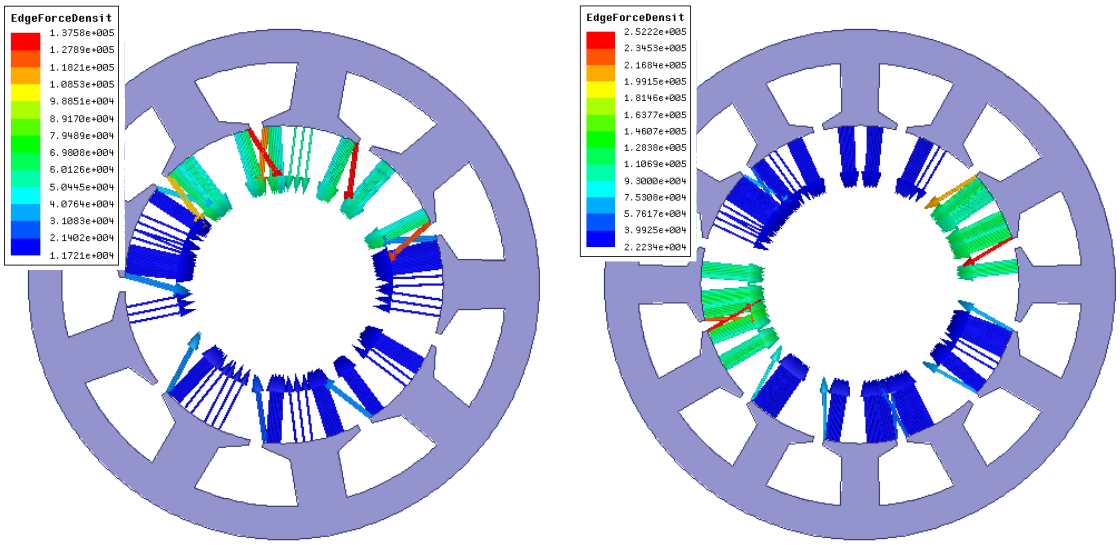

(a) (b)

Fig. 4.7. Magnetic pull force: (a) Q_s = 9, P = 4, (b) Q_s = 12, P = 5.

In practice, the teeth/pole numbers with $2P = Q_s \pm 2$ are preferred. From the discussion above, the feasible teeth/pole combination is 12/10, which enables the design to achieve high winding factor, low cogging torque and balanced magnetic pull.

4.2.2.2. Winding Layer Configuration

The SL winding and DL winding configurations are illustrated in Fig. 4.8 (a) and (b) respectively. Compared to DL winding, the SL winding requires fewer coils, and each slot only fits one coil. Significant higher insulation class can be achieved, and the manufacture process is simpler.

However, SL winding often has longer end winding. The SL winding also suffers from high spatial MMF harmonics. For 12/10 machine, the stator MMF distributions of SL and DL windings and their Fourier series are illustrated in Fig. 4.9 (a), and (b),

respectively. The SL winding has much higher 1st order harmonic content. Hence flux tends to travel long path, as shown in Fig. 4.10 (a) and (b). In DL machines, the 1st order harmonic content is lower and the flux tends to travel short path from one tooth to the adjacent tooth, as shown in Fig. 4.10 (c) and (d).

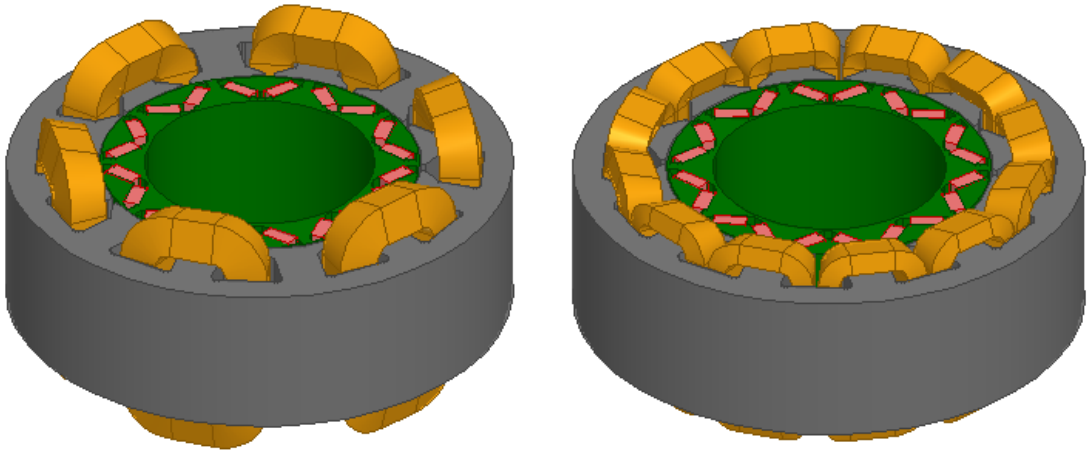

(a) (b)

Fig. 4.8. 3D models of FSCW machines: (a) SL winding configuration, (b) DL winding configuration.

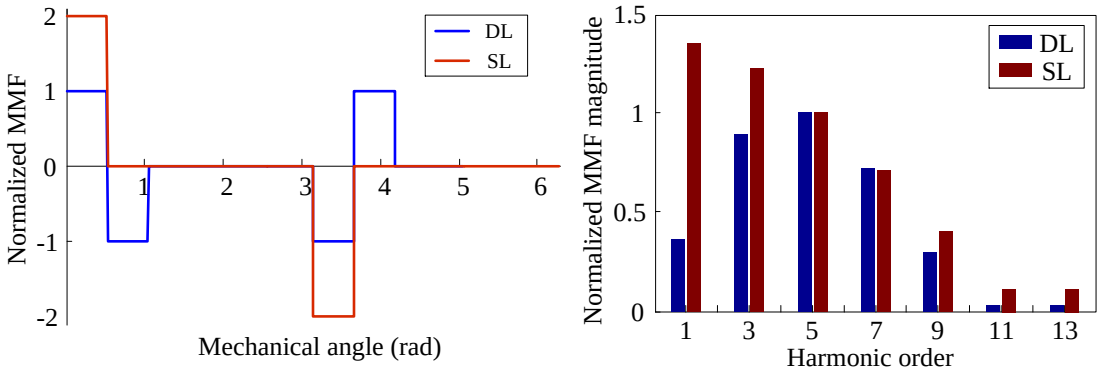

(a) (b)

Fig. 4.9. MMF of 12/10 machine: (a) MMF waveforms, (b) MMF Fourier series.

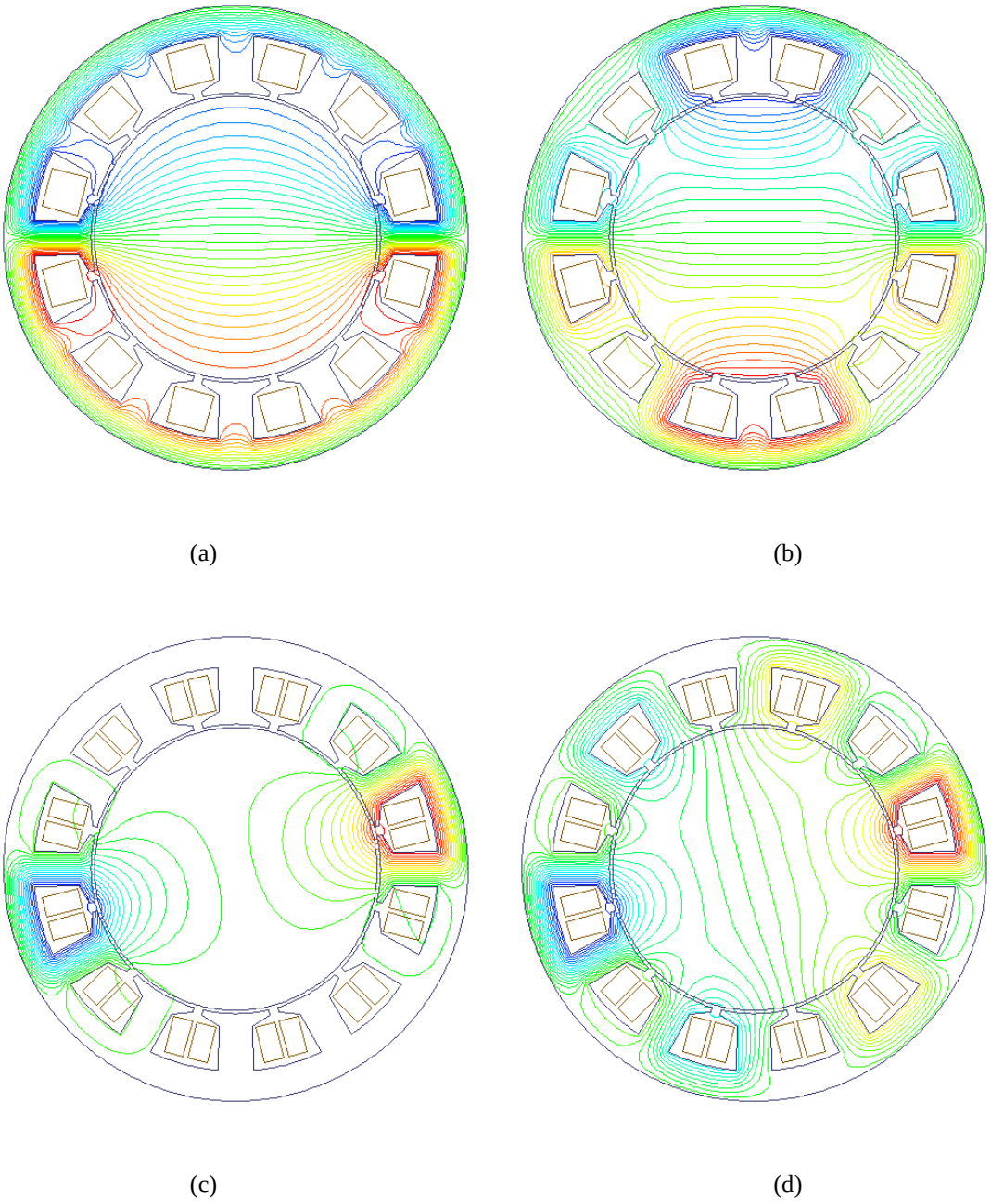

(a) (b)

(c) (d)

Fig. 4.10. Flux line distributions of FSCW machines: (a) SL, single phase excitation, (b) SL, 3-phase excitation, (c) DL, single phase excitation, and (d) DL, 3-phase excitation.

The significant higher 1st order harmonic increases the core loss and PM eddy current loss. The stator and rotor are more likely to saturate. The merits and demerits of SL and DL FSCW and ISDW are summarized in Table 3.3.

Table 4.3 Comparison of different winding configurations

	Single layer winding	**Double layer winding**	**Distributed winding**
Coil number	Fewer	Few	Many
Manufacturability	Easier	Easy	Difficult
Fill factor	Higher	High	Low
Insulation class	Higher	High	Medium
Fault tolerant	Better	Good	N/A
End winding	Short	Shorter	Long
Spatial harmonics	Richer	Rich	Low

Though SL configuration features drawbacks of higher losses, considering the significantly simplified manufacture, SL winding configuration is still preferred. Higher insulation class is another reason because it is very important to improve the reliability of the machine. The rotor losses due to the richer spatial harmonics can be reduced by employing the thin rotor yoke bridge, which will be explained in section 4.6.

It is beneficial to use the SL winding in this application, because the higher inductance reduces the characteristic current, which will locate inside the current limit circle. Hence the power factor can be improved when the machine is partially loaded in deep field weakening range.

4.2.2.3. Stator and Rotor Model

When SL winding is required, the flux travels long path. A feasible solution is proposed in Chapter 3 by reducing the thickness of the rotor yoke. This idea can be analogized from the segmented rotor SRM, which was first proposed by Mecrow in 2003 [77].The cross sections with the flux line distributions of the segmented SRM are shown in Fig. 4.11. The rotor segments modulate the flux distribution and force the flux line to travel short path, which attenuates the low order harmonic of stator MMF.

The segmented rotor SRM has uneven stator teeth. The thick teeth are twice the width of the thin teeth because the thin teeth carry half the flux of the thick teeth, and the teeth tip widths are chosen as such to maximize the inductance difference between the unaligned and aligned positions.

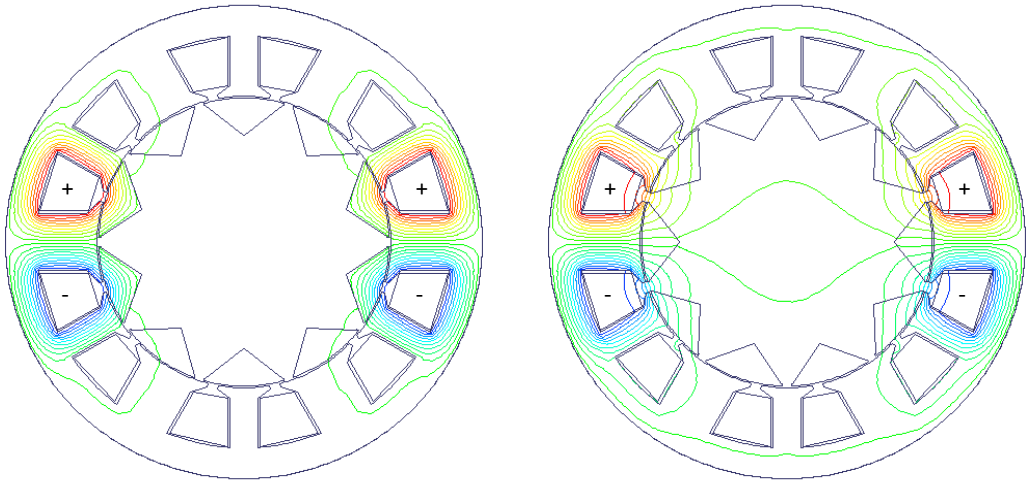

(a) (b)

Fig. 4.11. Flux line distributions of segmented rotor SRM: (a) aligned position, (b) unaligned position.

The magnets can be arranged between the rotor segments, such that PM torque can be introduced while maintaining the reluctance torque capability. In order to the reduce the manufacturing complexity, the V-shape rotor is employed, which provide mechanical protection for magnets and enable the deployment of rectangular shaped magnets, as shown in Fig. 4.12. In the proposed IPM machines, the stator also has uneven thickness. The saturation level of the thick and thin teeth can be equivalent to enhance the torque and reduce the core loss. The rotor segments are connected by bridges on the outer and inner peripherals.

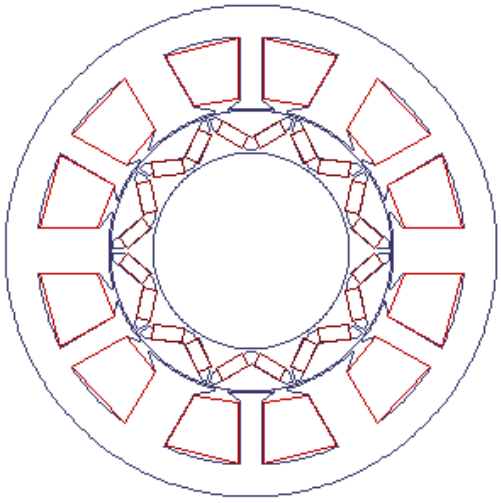

Fig. 4.12. Cross section of the proposed SL FSCW IPM machine.

4.2.3. Geometry Modeling

4.2.3.1. Stator Geometry Modeling

The parameterized stator lamination is illustrated in Fig. 4.13. Other than the stator teeth number and rotor pole pair number, the uneven teeth stator core can be uniquely

defined by 8 parameters, and they are summarized in Table 3.4 with the initial values provided.

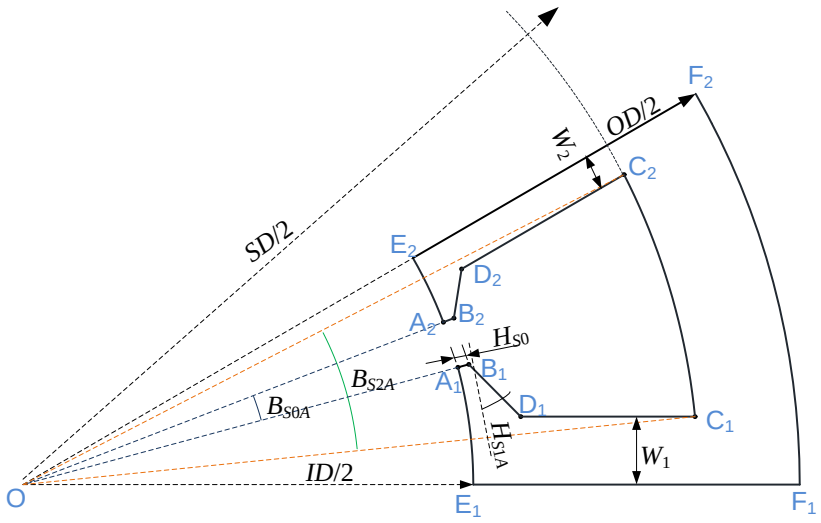

Fig. 4.13. Parameterized stator geometry.

Table 4.4 Stator parameters and initial values

Stator outer diameter (*OD*)	138 mm
Stator inner diameter (*ID*)	80 mm
Slot bottom diameter (*SD*)	120 mm
Slot bottom angle (B_{S2A})	20 °
Tooth width ratio (*k*)	0.75
Slot open angle (B_{S0A})	6 °
Slot tip height (Hs_1)	0.5 mm
Slot wedge angle (H_{S1A})	25 °

By applying the geometrical and magnetic constraints, the Cartesian coordinates of each vertex in Fig. 4.13 can be computed using the parameters provided in Table 4.4. Geometrically, the thick tooth tip, thin tooth tip and the slot open angle meet (4.21).

$$\angle \mathrm{A}_1\mathrm{OE}_1 + \angle \mathrm{A}_2\mathrm{OE}_2 + B_{S0A} = \frac{2\pi}{Q_s} \tag{4.21}$$

As described in [77], to minimize the unaligned permeance and maximize the aligned permeance, the thick tooth arc is equivalent to the rotor segment pole arc, and the gap between the rotor segments equals to the stator tooth opening.

$$\begin{aligned} \angle \mathrm{A}_1\mathrm{OE}_1 &= \frac{\pi}{2P} \cdot \beta \\ \angle \mathrm{A}_1\mathrm{OE}_1 + B_{S0A} &= \frac{\pi}{2P}(1 - \cdot\beta) + \frac{\pi}{2P} \end{aligned} \tag{4.22}$$

where, β is the rotor magnetic island arc pitch.

Combining (4.21) and (4.22), the relationship between the thick tooth and thin tooth tip can be derived as

$$\angle \mathrm{A}_1\mathrm{OE}_1 - \angle \mathrm{A}_2\mathrm{OE}_2 = \frac{\pi}{P} - \frac{2\pi}{Q_s} \tag{4.23}$$

Substituting (4.23) into (4.22), $\angle \mathrm{A}_1\mathrm{OE}_1$ and $\angle \mathrm{A}_2\mathrm{OE}_2$ can be computed as (4.24), and $\angle \mathrm{A}_2\mathrm{OE}_1$ can be calculated accordingly.

$$\begin{aligned} \angle \mathrm{A}_1\mathrm{OE}_1 &= \frac{\pi}{2P} - \frac{B_{S0A}}{2} \\ \angle \mathrm{A}_2\mathrm{OE}_2 &= \frac{2\pi}{Q_s} - \frac{\pi}{2P} - \frac{B_{S0A}}{2} \end{aligned} \tag{4.24}$$

$$\angle \mathrm{A}_2\mathrm{OE}_1 = \frac{\pi}{2P} + \frac{B_{S0A}}{2} \tag{4.25}$$

In segmented rotor SRM, the widths of the thin teeth are always half of the thick teeth. However, when the PM is employed, the saturation level of the thin teeth and thick teeth is different. The ratio *k* is defined to adjust the teeth widths, i.e., $W_2 = kW_1$. This can be approximated by (4.26). Geometrical constraint (4.27) also applies.

$$k \cdot \angle \mathrm{C_1OE_1} = \angle \mathrm{C_2OE_2} \tag{4.26}$$

$$\angle \mathrm{C_1OE_1} + \angle \mathrm{C_2OE_2} + B_{S2A} = \frac{2\pi}{Q_s} \tag{4.27}$$

Combining (4.26) and (4.27), $\angle \mathrm{C_1OE_1}$ and $\angle \mathrm{C_2OE_2}$ can be solved as

$$\begin{aligned} \angle \mathrm{C_1OE_1} &= \frac{1}{1+k}\left(\frac{2\pi}{Q_s} - B_{S2A}\right) \\ \angle \mathrm{C_2OE_2} &== \frac{k}{1+k}\left(\frac{2\pi}{Q_s} - B_{S2A}\right) \end{aligned} \tag{4.28}$$

Vertex D_1 is the intersection of B_1D_1 and C_1D_1, which needs to be computed under Cartesian coordinate. The functions of B_1D_1 and C_1D_1 are represented by (4.29). The coordinates of D_1 is derived as (4.30).

$$\begin{aligned} y - B_{1y} &= k_1(x - B_{1x}) \\ y &= C_{1y} \end{aligned} \tag{4.29}$$

$$\begin{aligned} D_{1x} &= \frac{\left(\frac{ID}{2} + H_{S0}\right)\cdot \sin\left(\frac{\pi}{2P} - \frac{B_{S0A}}{2}\right) - \frac{SD}{2}\cdot \sin\frac{1}{1+k}\left(\frac{2\pi}{Q_s} - \mathrm{B_{S2A}}\right)}{\tan\left(\frac{\pi}{2} - \frac{\pi}{2P} + \frac{B_{S0A}}{2} - \mathrm{H_{S1A}}\right)} + \left(\frac{ID}{2} + H_{S0}\right)\cdot \cos\left(\frac{\pi}{2P} - \frac{B_{S0A}}{2}\right) \\ D_{1y} &= \frac{SD}{2}\cdot \sin\frac{1}{1+k}\left(\frac{2\pi}{Q_s} - \mathrm{B_{S2A}}\right) \end{aligned} \tag{4.30}$$

where, k_1 is the slope of segment B_1D_1, and k_1=-tan$\left(\frac{\pi}{2}-\frac{\pi}{2P}+\frac{B_{S0_A}}{2}-H_{S1_A}\right)$.

Similarly, D_2 is the intersection of B_2D_2 and C_2D_2.

$$\begin{aligned} y-B_{2y}&=k_2(x-B_{2x})\\ y-C_{2y}&=k_3(x-C_{2x}) \end{aligned} \tag{4.31}$$

where, $k_2=\tan\left(\frac{\pi}{2}+\frac{\pi}{2P}+\frac{B_{S0A}}{2}-H_{S1A}\right)$, $k_3=\tan\frac{2\pi}{Q_s}$. The coordinate of D_2 can be solved as

$$D_{2x}=\frac{\begin{array}{l}\frac{SD}{2}\cdot\sin\left(\frac{1}{1+k}\frac{2\pi}{Q_s}+\frac{k}{1+k}B_{S2A}\right)-\left(\frac{ID}{2}+H_{S0}\right)\cdot\sin\left(\frac{\pi}{2P}+\frac{B_{S0A}}{2}\right)\\ +\tan\left(\frac{\pi}{2}+\frac{\pi}{2P}+\frac{B_{S0A}}{2}-H_{S1A}\right)\cdot\left(\frac{ID}{2}+H_{S0}\right)\cdot\cos\left(\frac{\pi}{2P}+\frac{B_{S0A}}{2}\right)\\ -\tan\frac{2\pi}{Q_s}\cdot\frac{SD}{2}\cdot\cos\left(\frac{1}{1+k}\frac{2\pi}{Q_s}+\frac{k}{1+k}B_{S2A}\right)\end{array}}{\tan\left(\frac{\pi}{2}+\frac{\pi}{2P}+\frac{B_{S0\_A}}{2}-H_{S1\_A}\right)-\tan\frac{2\pi}{Q_s}}$$

$$D_{2y}=\frac{\begin{array}{l}\tan\frac{2\pi}{Q_s}\cdot\tan\left(\frac{\pi}{2}+\frac{\pi}{2P}+\frac{B_{S0A}}{2}-H_{S1A}\right)\\ \cdot\left[\left(\frac{ID}{2}+H_{S0}\right)\cdot\cos\left(\frac{\pi}{2P}+\frac{B_{S0A}}{2}\right)-\frac{SD}{2}\cdot\cos\left(\frac{1}{1+k}\frac{2\pi}{Q_s}+\frac{k}{1+k}B_{S2A}\right)\right]\\ +\tan\left(\frac{\pi}{2}+\frac{\pi}{2P}+\frac{B_{S0A}}{2}-H_{S1A}\right)\cdot\frac{SD}{2}\cdot\sin\left(\frac{1}{1+k}\frac{2\pi}{Q_s}+\frac{k}{1+k}B_{S2A}\right)\\ -\tan\frac{2\pi}{Q_s}\cdot\left(\frac{ID}{2}+H_{S0}\right)\cdot\sin\left(\frac{\pi}{2P}+\frac{B_{S0A}}{2}\right)\end{array}}{\tan\left(\frac{\pi}{2}+\frac{\pi}{2P}+\frac{B_{S0\_A}}{2}-H_{S1\_A}\right)-\tan\frac{2\pi}{Q_s}} \tag{4.32}$$

The Cartesian coordinate of each vertex in Fig 4.13 is summarized in Table 4.5.

Table 4.5 Cartesian coordinate of each vertex of stator geometry model

A_1	$A_{1x} = \frac{ID}{2}\cdot\cos\left(\frac{\pi}{P}-\frac{B_{S0A}}{2}\right)$ $A_{1y} = \frac{ID}{2}\cdot\sin\left(\frac{\pi}{P}-\frac{B_{S0A}}{2}\right)$
A_2	$A_{2x} = \frac{ID}{2}\cdot\cos\left(\frac{\pi}{P}+\frac{B_{S0A}}{2}\right)$ $A_{2y} = \frac{ID}{2}\cdot\sin\left(\frac{\pi}{P}+\frac{B_{S0A}}{2}\right)$
B_1	$B_{1x} = \left(\frac{ID}{2}+H_{S0}\right)\cdot\cos\left(\frac{\pi}{P}-\frac{B_{S0A}}{2}\right)$ $B_{1y} = \left(\frac{ID}{2}+H_{S0}\right)\cdot\sin\left(\frac{\pi}{P}-\frac{B_{S0A}}{2}\right)$
B_2	$B_{2x} = \left(\frac{ID}{2}+H_{S0}\right)\cdot\cos\left(\frac{\pi}{P}+\frac{B_{S0A}}{2}\right)$ $B_{2y} = \left(\frac{ID}{2}+H_{S0}\right)\cdot\sin\left(\frac{\pi}{P}+\frac{B_{S0A}}{2}\right)$
C_1	$C_{1x} = \frac{SD}{2}\cdot\cos\frac{1}{1+k}\left(\frac{2\pi}{Q_s}-\mathrm{B_{S2A}}\right)$ $C_{1y} = \frac{SD}{2}\cdot\sin\frac{1}{1+k}\left(\frac{2\pi}{Q_s}-\mathrm{B_{S2A}}\right)$
C_2	$C_{2x} = \frac{SD}{2}\cdot\cos\left(\frac{1}{1+k}\frac{2\pi}{Q_s}+\frac{k}{1+k}\mathrm{B_{S2A}}\right)$ $C_{2y} = \frac{SD}{2}\cdot\sin\left(\frac{1}{1+k}\frac{2\pi}{Q_s}+\frac{k}{1+k}\mathrm{B_{S2A}}\right)$
D_1	$D_{1x} = \frac{\left(\frac{ID}{2}+H_{S0}\right)\cdot\sin\left(\frac{\pi}{2P}-\frac{B_{S0A}}{2}\right)-\frac{SD}{2}\cdot\sin\frac{1}{1+k}\left(\frac{2\pi}{Q_s}-\mathrm{B_{S2A}}\right)}{\tan\left(\frac{\pi}{2}-\frac{\pi}{2P}+\frac{B_{S0A}}{2}-\mathrm{H_{S1A}}\right)}+\left(\frac{ID}{2}+H_{S0}\right)\cdot\cos\left(\frac{\pi}{2P}-\frac{B_{S0A}}{2}\right)$ $D_{1y} = \frac{SD}{2}\cdot\sin\frac{1}{1+k}\left(\frac{2\pi}{Q_s}-\mathrm{B_{S2A}}\right)$

D_2	$$\frac{SD}{2}\cdot\sin\left(\frac{1}{1+k}\frac{2\pi}{Q_s}+\frac{k}{1+k}\mathrm{B_{S2A}}\right)-\left(\frac{ID}{2}+\mathrm{H_{S0}}\right)\cdot\sin\left(\frac{\pi}{2P}+\frac{\mathrm{B_{S0A}}}{2}\right)$$ $$+\tan\left(\frac{\pi}{2}+\frac{\pi}{2P}+\frac{\mathrm{B_{S0A}}}{2}-\mathrm{H_{S1A}}\right)\cdot\left(\frac{ID}{2}+\mathrm{H_{S0}}\right)\cdot\cos\left(\frac{\pi}{2P}+\frac{\mathrm{B_{S0A}}}{2}\right)$$ $$D_{2x}=\frac{-\tan\frac{2\pi}{Q_s}\cdot\frac{SD}{2}\cdot\cos\left(\frac{1}{1+k}\frac{2\pi}{Q_s}+\frac{k}{1+k}\mathrm{B_{S2A}}\right)}{\tan\left(\frac{\pi}{2}+\frac{\pi}{2P}+\frac{\mathrm{B_{S0\_A}}}{2}-\mathrm{H_{S1\_A}}\right)-\tan\frac{2\pi}{Q_s}}$$ $$\tan\frac{2\pi}{Q_s}\cdot\tan\left(\frac{\pi}{2}+\frac{\pi}{2P}+\frac{\mathrm{B_{S0A}}}{2}-\mathrm{H_{S1A}}\right)$$ $$\cdot\left[\left(\frac{ID}{2}+\mathrm{H_{S0}}\right)\cdot\cos\left(\frac{\pi}{2P}+\frac{\mathrm{B_{S0A}}}{2}\right)-\frac{SD}{2}\cdot\cos\left(\frac{1}{1+k}\frac{2\pi}{Q_s}+\frac{k}{1+k}\mathrm{B_{S2A}}\right)\right]$$ $$+\tan\left(\frac{\pi}{2}+\frac{\pi}{2P}+\frac{\mathrm{B_{S0A}}}{2}-\mathrm{H_{S1A}}\right)\cdot\frac{SD}{2}\cdot\sin\left(\frac{1}{1+k}\frac{2\pi}{Q_s}+\frac{k}{1+k}\mathrm{B_{S2A}}\right)$$ $$D_{2y}=\frac{-\tan\frac{2\pi}{Q_s}\cdot\left(\frac{ID}{2}+\mathrm{H_{S0}}\right)\cdot\sin\left(\frac{\pi}{2P}+\frac{\mathrm{B_{S0A}}}{2}\right)}{\tan\left(\frac{\pi}{2}+\frac{\pi}{2P}+\frac{\mathrm{B_{S0A}}}{2}-\mathrm{H_{S1\_A}}\right)-\tan\frac{2\pi}{Q_s}}$$
E_1	$$E_{1x}=ID$$ $$E_{1y}=0$$
E_2	$$E_{2x}=ID\cdot\cos\left(\frac{2\pi}{Q_s}\right)$$ $$E_{2y}=ID\cdot\sin\left(\frac{2\pi}{Q_s}\right)$$
F_1	$$F_{1x}=OD$$ $$F_{1y}=0$$
F_2	$$F_{2x}=OD\cdot\cos\left(\frac{2\pi}{Q_s}\right)$$ $$F_{2y}=OD\cdot\sin\left(\frac{2\pi}{Q_s}\right)$$

4.2.3.2. Rotor Geometry Modeling

The parameterized rotor lamination is illustrated in Fig. 4. 14. The V-shape rotor core can be uniquely defined by 8 parameters, and they are summarized in Table 4.6 with the initial values provided.

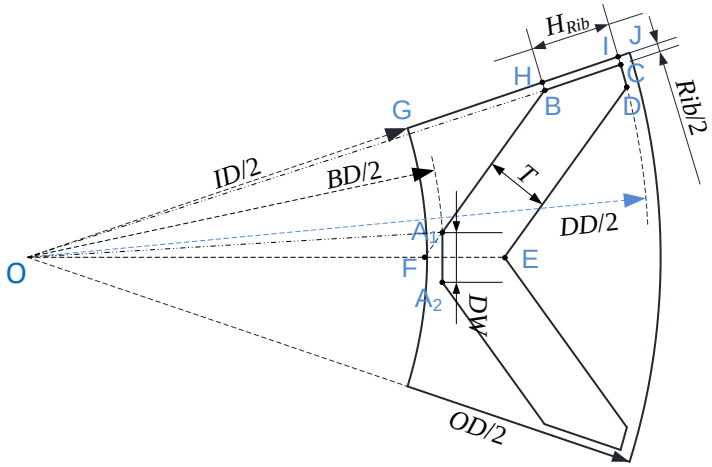

Fig. 4.14. Parameterized rotor geometry.

Table 4.6 Rotor parameters and initial values

Rotor outer diameter (*OD*)	79 mm
Rotor inner diameter (*ID*)	55 mm
Flux barrier outer diameter (*DD*)	77.5 mm
Flux barrier bottom diameter (*BD*)	57 mm
Rib thickness (*Rib*)	1 mm
Rib height (H_{Rib})	3 mm
Flux barrier bottom width (*DW*)	2 mm
Flux barrier thickness (*T*)	4 mm

The width of the rib can be approximated by the lengths of the arcs IC and HB.

$$\begin{aligned} 2\frac{DD}{2}\angle \mathrm{COH} &= Rib \\ 2(\frac{DD}{2} - H_{Rib})\angle \mathrm{BOH} &= Rib \end{aligned} \tag{4.33}$$

The flux barrier bottom width *DW* can be approximated by the length of the arc $\mathrm{A_1A_2}$.

$$BD \cdot 2\angle \mathrm{A_1OE} = DW \tag{4.34}$$

Vertex F is the intersection of the extension of segment $\mathrm{A_1B}$ and *x*-axis, and it is derived as

$$\begin{aligned} F_x &= B_x - \frac{1}{k_1} B_y \\ F_y &= 0 \end{aligned} \tag{4.35}$$

where, k_1 is the slope of $\mathrm{A_1B}$, $k_1 = \dfrac{A_{1y} - B_y}{A_{1x} - B_x}$.

The distance between $\mathrm{A_1B}$ and DE is *T*. The coordinate of E can be calculated.

$$\begin{aligned} E_x &= B_x - \frac{1}{k_1} B_y + \frac{\sqrt{1+k_1^2}}{k_1} T \\ E_y &= 0 \end{aligned} \tag{4.36}$$

Vertex D is the intersection of DE and arc IC. IC can be approximated by line IC which is perpendicular to OJ. DE and IC are represented by (4.37) and (4.38), respectively.

$$y - B_y = k_1 \left(x - B_x \right) - \sqrt{1+k_1^2} \cdot T \tag{4.37}$$

$$y - I_y = k_2(x - I_x) \tag{4.38}$$

where, k_2 is the slope of segment D_1E_2, and $k_2 = -\tan(\frac{\pi}{2} - \frac{\pi}{2P})$.

The coordinate of each vertex in Fig. 4.14 is summarized in Table 4.7.

Table 4.7 Cartesian coordinate of each vertex of rotor geometry model

A_1	$A_{1x} = \frac{BD}{2} \cdot \cos\left(\frac{DW}{BD}\right)$ $A_{1y} = \frac{BD}{2} \cdot \sin\left(\frac{DW}{BD}\right)$
B	$B_x = \left(\frac{TD}{2} - H_{Rib}\right) \cdot \cos\left(\frac{\pi}{2P} - \frac{Rib}{DD - 2H_{Rib}}\right)$ $B_y = \left(\frac{TD}{2} - H_{Rib}\right) \cdot \sin\left(\frac{\pi}{2P} - \frac{Rib}{DD - 2H_{Rib}}\right)$
C	$C_{1x} = \frac{DD}{2} \cdot \cos\left(\frac{\pi}{2P} - \frac{Rib}{DD}\right)$ $C_{1y} = \frac{DD}{2} \cdot \sin\left(\frac{\pi}{2P} - \frac{Rib}{DD}\right)$
D	$D_{1x} = \frac{I_y - B_y + k_1 B_x - k_2 I_x + \sqrt{1+k_1^2} \cdot T}{k_1 - k_2}$ $D_{1y} = \frac{k_1 k_2 (B_x - I_x) + k_1 I_y - k_2 B_y - k_2 \sqrt{1+k_1^2} \cdot T}{k_1 - k_2}$
E	$E_x = B_x - \frac{1}{k_1} B_y + \frac{\sqrt{1+k_1^2}}{k_1} T$ $E_y = 0$
F	$F_x = B_x - \frac{1}{k_1} B_y$ $F_y = 0$
G	$G_{1x} = \frac{ID}{2} \cdot \cos\left(\frac{\pi}{2P}\right)$ $G_{1y} = \frac{ID}{2} \cdot \sin\left(\frac{\pi}{2P}\right)$

I	$I_x = \frac{DD}{2}\cos\frac{\pi}{2P}$ $I_y = \frac{DD}{2}\sin\frac{\pi}{2P}$
J	$J_x = \frac{OD}{2}\cos\frac{\pi}{2P}$ $J_y = \frac{OD}{2}\sin\frac{\pi}{2P}$

So far the stator and rotor geometry models are parameterized. The coil span is equivalent to the rotor pole, which results in unity winding factor. Hence the PM utilization is maximized.

The teeth width and teeth width ratio between the thin teeth and thick teeth are tuned first such that the torque can be maximized and the stator teeth saturation levels in the thick and thin teeth are equivalent, and the output torque is maximized. The flux saturation of the teeth is evaluated by the flux density distribution along the red semi-circle, as shown in Fig. 4.15. At different current magnitude, the current angle is chosen as such that maximum torque is achieved.

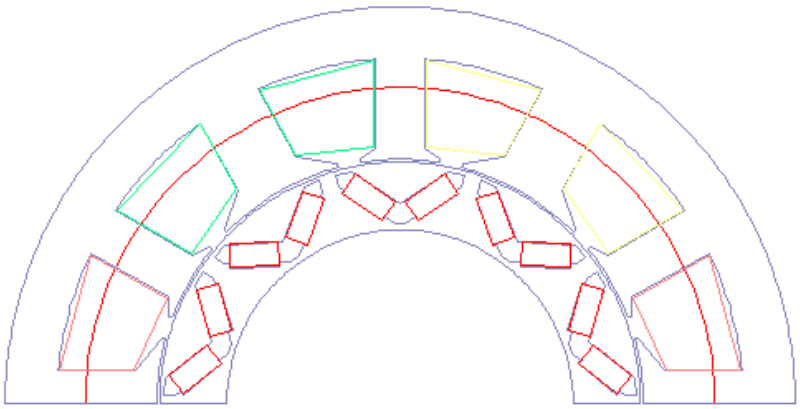

Fig. 4.15. Stator teeth flux-density measurement reference position.

The flux density is measured when the rotor rotates every 22.5° at 20 A, 40 A, 50 A, and 70 A. When the teeth width ratio is 0.74, the stator teeth flux density distributions are illustrated in Fig. 4.16. When the machine is loaded at nominals conditions, 40 A and 50 A, the flux density in the thick teeth and thin teeth are comparable. When the machine is loaded at 20 A, the thin teeth has higher flux density. When the machine is loaded at peak current, the thick teeth is slightly saturated.

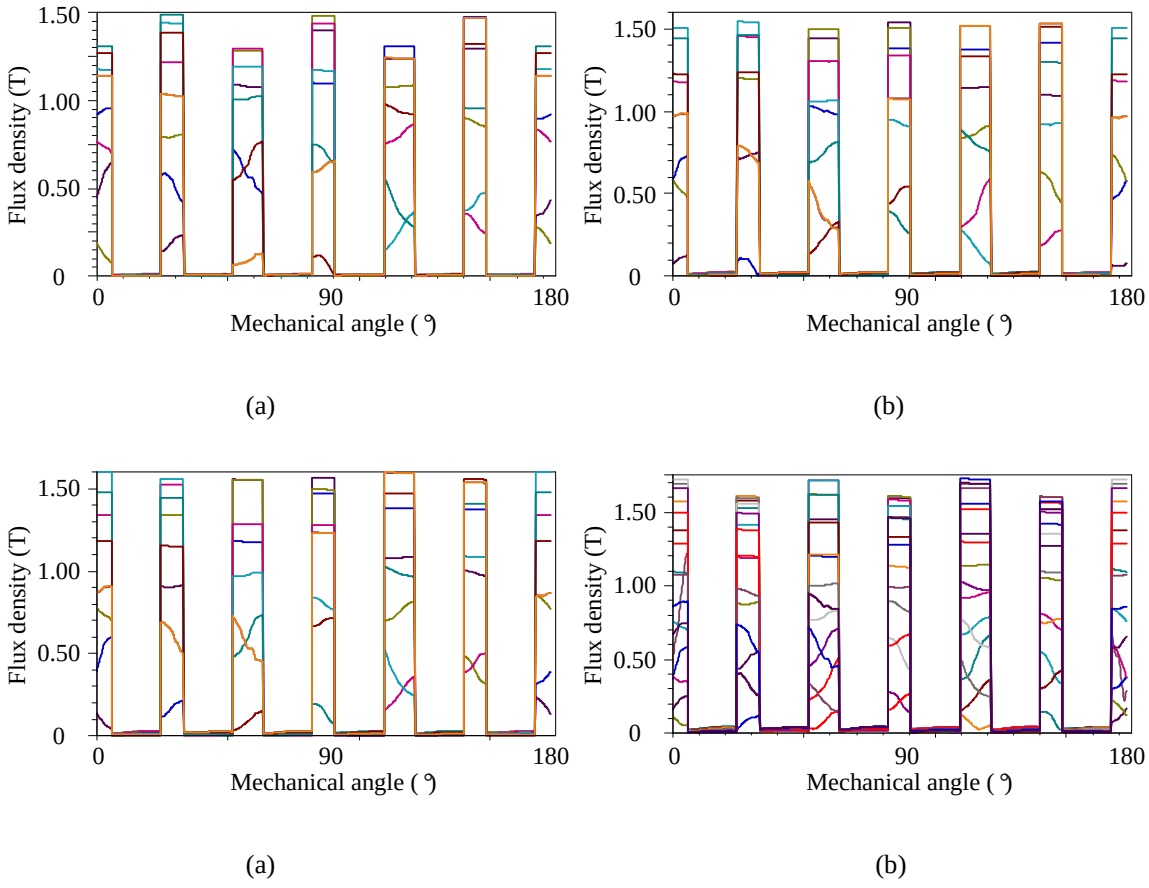

Fig. 4.16. Stator teeth flux density: (a) 20 A, (b) 40 A, (c) 50 A, and (d) 70 A.

4.3. RESPONSE SURFACE METHOD BASED GEOMETRY OPTIMIZATION

4.3.1. Concept of Response Surface Method

RSM has been recognized as an effective approach to model the electrical machine performance [78]. The relationship between the objective function and the design parameters can be modeled statistically by fitting method. The objective function is referred to as the response, and the relationship between the design variables and objective function is referred to as the response surface. In the electrical machine design, the response is generally obtained from FEA simulations. In many cases, the response surface can be fitted by polynomial model. The second order response surface model can be written as

$$y = \beta_0 + \sum_{i=1}^{k} \beta_i x_i + \sum_{i=1}^{k} \beta_{ii} x_i^2 + + \sum_{i \neq j}^{k} \beta_{ij} x_i x_i + \varepsilon \qquad (4.39)$$

where, x_i is the design parameter, β is termed as regression coefficient, and ε is residual, which is treated as statistical error.

When multiple parameter sets are experimented (simulated in FEA), the responses and the design variables can be formulated into matrix form as (4.40).

$$Y = X\hat{\beta} \qquad (4.40)$$

where, Y is vector of responses, X is matrix of variables, $\hat{\beta}$ is the coefficient estimate.

The least square method is employed to estimate the regression coefficients, which can be obtained from the design parameters and responses using (4.41). Therefore, in the

feasible range of design parameters, the response can be estimated by (4.42) neglecting the residual ε.

$$\hat{\beta} = (X^T Y)^{-1} X^T Y \tag{4.41}$$

$$\hat{y} = \hat{\beta}_0 + \sum_{i=1}^{k} \hat{\beta}_i x_i + \sum_{i=1}^{k} \hat{\beta}_{ii} x_i^2 + + \sum_{i \neq j}^{k} \hat{\beta}_{ij} x_i x_i \tag{4.42}$$

The optimal design variable set can be predicted using the response surface and the problem can be described as

$$\begin{aligned} &\text{minimize} \quad \hat{y} \\ &\text{subject to} \quad \hat{y} = \hat{\beta}_0 + \sum_{i=1}^{k} \hat{\beta}_i x_i + \sum_{i=1}^{k} \hat{\beta}_{ii} x_i^2 + + \sum_{i \neq j}^{k} \hat{\beta}_{ij} x_i x_i \\ &\qquad\qquad x_{i\min} \leq x_i \leq x_{i\max} \end{aligned} \tag{4.43}$$

where, $x_{i\min}$ and $x_{i\max}$ define the boundary of the design variables.

The response surface (4.39) may be extended to multiple responses. *Y* becomes matrix of responses combined by multiple vectors of response. Equation (4.41) can still be employed to estimate the regression coefficient. The optimization objective should be modified accordingly.

4.3.2. Application of Response Surface Method

The rotor flux barriers have strong impact on the machine torque performances. 3 parameters, *ID*, *Hrib*, *Rib*, are selected to shape the flux barrier. The stator slot opening B_{s0} also influences the torque ripple. Here, 4 parameters are involved in the optimization.

The individual and interaction effects of parameters are evaluated at 3 different excitations, 40 A, 60 A, and 70 A. The central composite design (CCD) is employed to estimate the property of response surface. The average torque and torque ripple responses with respect to CCD are simulated by FEA and listed in Table 4.8, where the first design parameters set locates in the middle of the design area. For each design parameter, the low variation is referred to as low level and the high variation is referred to as high level.

Table 4.8 Design variables and responses

B_{s0} (mm)	*ID* (mm)	H_{rib} (mm)	*Rib* (mm)	40 A		60 A		70 A	
				$T_{average}$ (Nm)	T_{ripple}	$T_{average}$ (Nm)	T_{ripple}	$T_{average}$ (Nm)	T_{ripple}
5	62	2.20	3.25	23.42	0.08	28.17	0.07	25.36	0.12
4	58	2.6	3	23.15	0.12	28.11	0.10	25.08	0.17
6	58	2.6	3	23.26	0.11	28.17	0.09	25.25	0.11
4	58	2.6	3.5	23.19	0.10	28.09	0.13	25.16	0.25
6	58	2.6	3.5	23.29	0.07	28.15	0.05	25.32	0.06
4	58	1.8	3	23.24	0.09	28.25	0.12	25.32	0.21
6	58	1.8	3	23.35	0.07	28.25	0.09	25.46	0.12
4	58	1.8	3.5	23.31	0.12	28.21	0.15	25.38	0.26
6	58	1.8	3.5	23.41	0.12	28.24	0.11	25.52	0.13
4	64	2.6	3	23.21	0.10	27.95	0.13	25.04	0.22
6	64	2.6	3	23.31	0.10	27.98	0.08	25.20	0.09
4	64	2.6	3.5	23.3	0.09	27.90	0.18	25.05	0.31
6	64	2.6	3.5	23.42	0.08	27.94	0.05	25.24	0.04
4	64	1.8	3	23.48	0.13	28.08	0.17	25.22	0.28
6	64	1.8	3	23.55	0.13	28.10	0.11	25.39	0.11
4	64	1.8	3.5	23.59	0.17	27.98	0.20	25.20	0.33
6	64	1.8	3.5	23.67	0.17	28.04	0.12	25.38	0.11

It is observed that the parameters' variations do not have much influence on the average torque. But the torque ripple varies significantly. Hence it is chosen as the optimization objective. The effect of each term is calculated by the difference between the responses of low level and high level [79], and they are shown in Fig. 4.17.

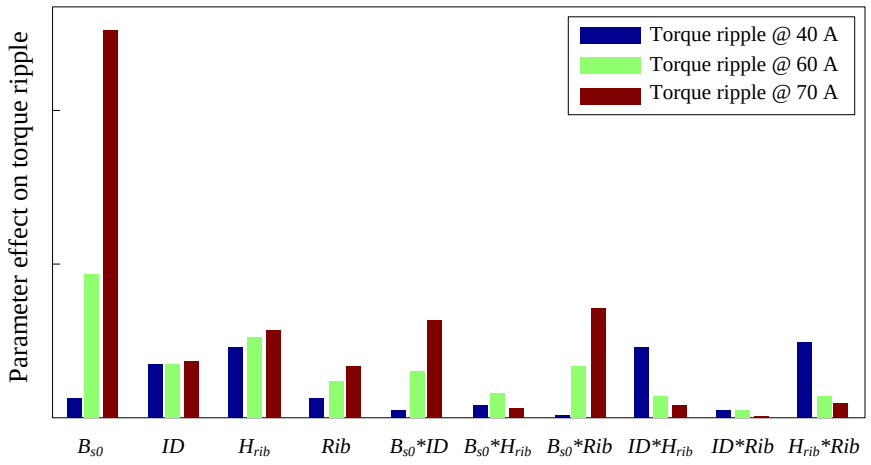

Fig. 4.17. Individual and interactional effects on torque ripple.

When the machine is loaded at different current, the significance of the each parameter's effect on torque ripple can be highly different. All parameters have to be considered in the optimization to achieve low torque ripple at all three current levels.

The initial estimated response surface can be used to predict the optimal design variables set x which minimizes the response $\hat{y}$. The response of x is evaluated again through FEA simulations and is referred to as y. The new parameter set x and response y can be used to update the response surface, which helps increase the fidelity of the response surface, and a new optimal parameter set can be obtained again. The optimization procedure can be summarized by the flowchart in Fig. 4.18.

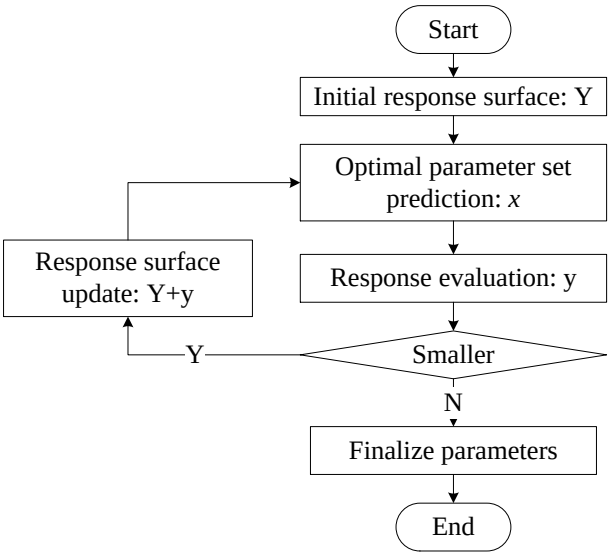

Fig. 4.18. Torque ripple optimization flowchart.

The RSM based optimization method enables the optimization to be implemented within a few steps, which greatly reduced the computational effort. Three design variables sets are obtained from the optimization, the torque waveforms are shown in Fig. 4.19. Tthe average torque and torque ripple are listed in Table 4.9.

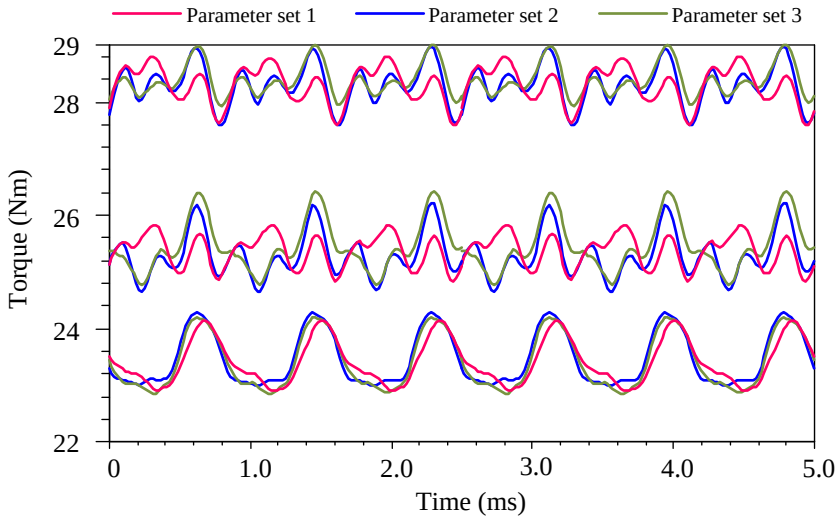

Fig. 4.19. Torque waveforms of three optimized parameter sets.

Table 4.9 Average torque and torque ripple of optimized designs

	40 A		60 A		70 A	
	$T_{average}$ (Nm)	T_{ripple}	$T_{average}$ (Nm)	T_{ripple}	$T_{average}$ (Nm)	T_{ripple}
Parameter set 1	23.47	0.055	28.28	0.049	25.29	0.062
Parameter set 2	23.42	0.057	28.37	0.038	25.45	0.065
Parameter set 3	23.42	0.053	28.29	0.043	25.37	0.039

Design parameter set 3 exhibits the lowest torque ripple and is chosen as the final design. The finalized parameters of the stator and rotor are shown in Table 4.10, where the parameters are adjusted slightly for manufacture reasons.

Table 4.10 Finalized stator and rotor geometry parameters

Stator outer diameter (*OD*)	138 mm	Rotor outer diameter (*OD*)	84 mm
Stator inner diameter (*ID*)	85 mm	Rotor inner diameter (*ID*)	60.5 mm
Slot bottom diameter (*SD*)	120 mm	Flux barrier outer diameter (*DD*)	82.5 mm
Slot bottom angle (B_{S2A})	20.35 °	Flux barrier bottom diameter (*BD*)	62.5 mm
Tooth width ratio (*k*)	0.74	Rib thickness (*Rib*)	3 mm
Slot open angle (B_{S0A})	5.4 °	Rib height (H_{Rib})	2 mm
Slot tip height (Hs_1)ab	0.6 mm	Flux barrier bottom width (*DW*)	2 mm
Slot wedge angle (H_{S1A})	25 °	Flux barrier thickness (*T*)	4 mm

4.4. ROTOR MECHANICAL STRENGTH VALIDATION

The reduced rotor yoke size may bring mechanical failure. The rotor centrifugal stress analysis is performed based on FEA simulation. The rotor material is M15 29G silicon steel, and the mechanical strength is reported at 358 MPa yield strength, and 490 MPa tensile strength.

The stress distributions at 7000 rpm and 10000 rpm are simulated and reported in Fig. 4.20 (a) and (b) respectively. At 7000 rpm, the stress is lower than 40 MPa in most area, and the peak stress is 52 MPa which appears at the bottom bridge. At 10000 rpm, the stress is below 80 MPa in most area, and the peak stress is 105.88 MPa. The peak stress at 7000 rpm is about 1/7 of the material yield strength, and the peak stress at 10000 rpm is about 1/3 of the material yield strength.

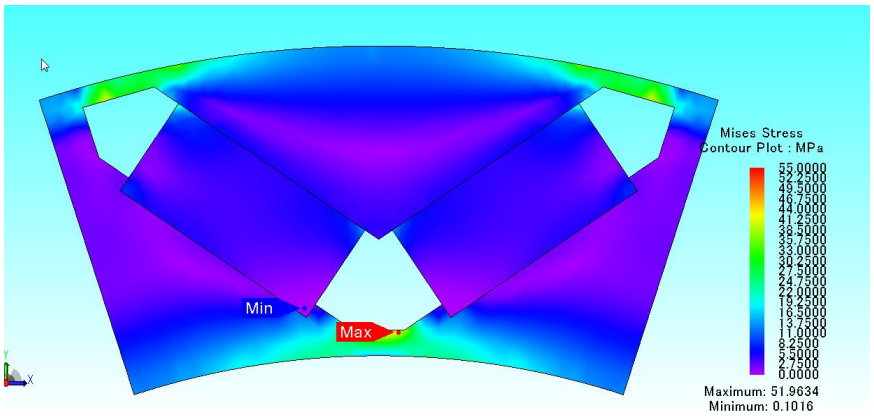

(a)

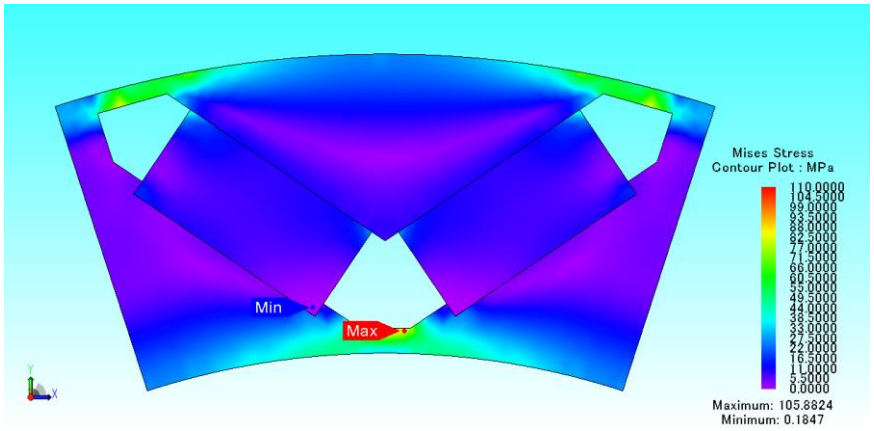

(b)

Fig. 4.20. Rotor centrifugal stress analysis: (a) 7000 rpm, (b) 10000 rpm.

4.5. PERFORMANCE EVALUATION

4.5.1. Comparison with SPM Design

A DL winding 12/10 SPM machine is used as the benchmark. For manufacture reasons, the arc shape magnets are mounted in the surface slots and fastened by anchors, as shown in Fig. 4.21.

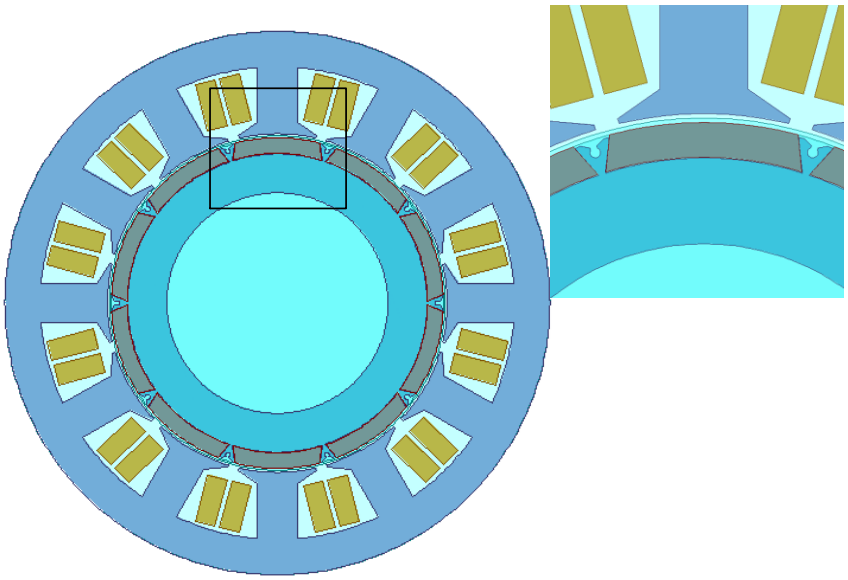

Fig. 4.21. Geometry of benchmark SPM machine.

The SL IPM machine and the benchmark machine share the same stack length, stator outer diameter and inner diameter. Same turn number, strands number and wire gauge are used. The slot areas of both machines are the same. The SL IPM uses 24% less PM material than the benchmark machine. The parameters of the SPM machine are summarized in Table 4.11.

The benchmark machine is designed for low speed application. Hence the comparison will be carried out in constant torque range. The average output torque, cogging torque, core loss, rotor loss, and PM eddy current loss are evaluated under the MTPA control strategy.

Table 4.11 SPM geometry parameters

Stator outer diameter	138 mm	Rotor outer diameter	84 mm
Stack length	120 mm	Rotor inner diameter	56 mm
Slot bottom diameter	120 mm	Magnet thickness	4 mm
Stator inner diameter	86 mm	Rotor pole embrace	0.833
Tooth width	10 mm	PM material	N38H
Slot opening	2.8 mm	Coil turn number	11

Average Torque and Torque Ripple

The output torque of the SPM and SL IPM machines are compared based on FEA simulations. Both machines operate at 2400 rpm under MTPA control strategy. For the SPM machine, pure *q*-axis current is injected due to the minimal saliency ratio. The torque waveforms of the SPM and SL IPM machines are shown in Fig. 4.22 (a) and (b), respectively.

The average torque is illustrated in Fig. 4.23 (a). It is observed that the torque difference between the two machines is minimal. The torque ripples are shown in Fig. 4.23 (b). The torque ripples of both machine are comparable at low current level and at high current level, the SL IPM machine exhibits much lower torque ripple.

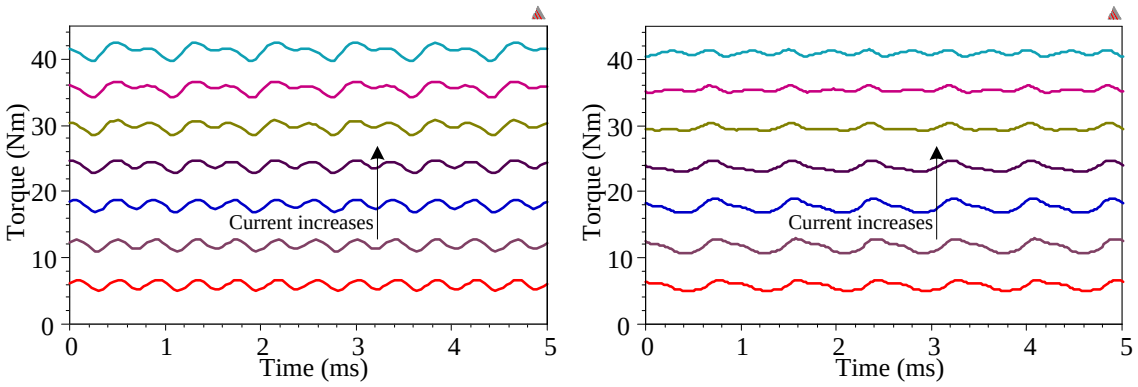

(a) (b)

Fig. 4.22. Torque waveforms under MTPA control: (a) SPM, DL, (b) IPM, SL.

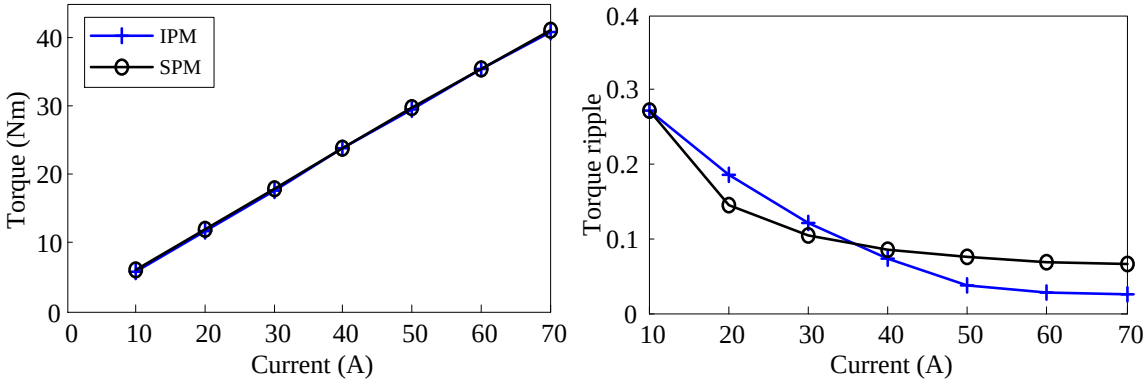

(a) (b)

Fig. 4.23. Torque performance under MTPA control: (a) average torque, (b) torque ripple.

Cogging Torque

The cogging torque of the SPM and the SL IPM are also compared based on FEA simulations. Both machines spin at 2400 rpm, the cogging torque waveforms are illustrated in Fig. 4.24.

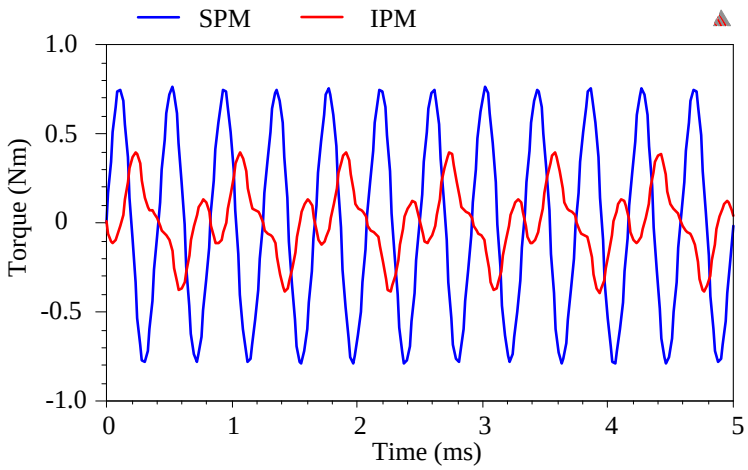

Fig. 4.24. Cogging torque at 2400 rpm.

The cogging torque of the SL IPM machine is about half of the benchmark machine. However, this does not draw the general conclusion that the uneven teeth stator IPM machines produce lower cogging torque than traditional SPM design. The cogging torque of the benchmark machine is not minimized due to the mechanical fixture iron between the magnets.

Core Loss and PM loss

The core loss and PM losses are simulated using FEA. Bulky magnets (not segmented) are mounted or buried in the rotors. Different loss components of the SPM and SL IPM are summarized in Fig. 4.25.

The magnets in the SPM are directly exposed to the air gap, such that significant higher PM eddy current loss is induced by the excessive stator MMF harmonic contents. However, in the SL IPM, the magnets are buried in the rotor and the stator MMF harmonics are filtered by the rotor iron. Additionally, the magnets are segmented by two

pieces for each pole. Therefore, the PM eddy current loss is much lower in the IPM design. On the other hand, the IPM rotor iron is directly exposed to the stator MMF; hence the rotor core loss is much higher than the SPM machines. The total losses of the SL IPM machine, including the core losses of stator and rotor and the PM eddy current loss, are lower than the SPM machine. The rotor losses of the SL IPM, including PM loss and rotor core loss, are still much lower.

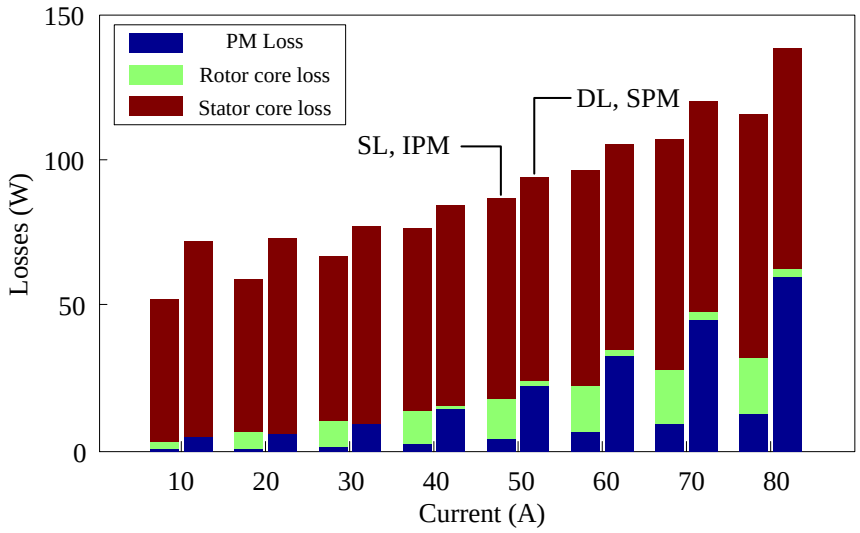

Fig. 4.25. Losses under MTPA control.

4.5.2. Comparison with Traditional IPM Design

The performance of the uneven teeth SL IPM machine is also compared with the DL V-shape IPM and I-shape IPM. The SL IPM machine and the DL machines share the same stack length, stator outer diameter and inner diameter. The double layer V-shape rotor machine has the same rotor configurations as the SL machine. The amount of PM of the I-shape rotor is same as that of the V-shape rotor. The air gap length, slot area, slot

opening and the phase winding turns in all three machines are the same. The cross sections of the DL configurations are shown in Fig. 4.26 (a) and (b), respectively.

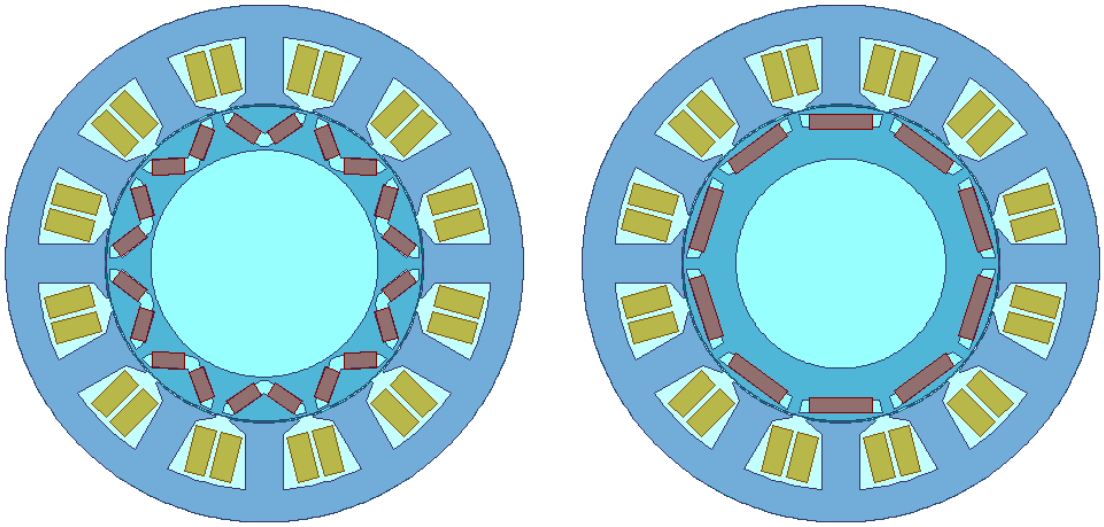

(a) (b)

Fig. 4.26. Cross section of DL IPM machines: (a) V-shape rotor, (b) I-shape rotor.

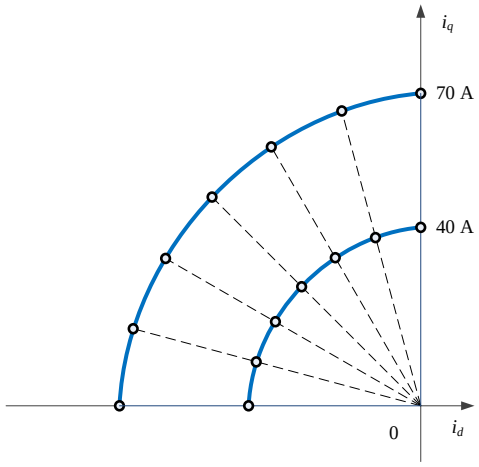

Fig. 4.27. Excitation currents locations on *d*- and *q*-axis current plane.

It is quite complicated to make comprehensive comparisons between the SL IPM and DL IPM designs in the entire torque and speed range. In this thesis, the comparisons are

performed based on same excitations. As shown in Fig. 4.27, the excitation currents locate on the constant current circle in the second quadrature of the current plane. For each current level, 7 different current vectors are applied on these machines.

Torque versus Excitation Angle

The output torque of each machine at each excitation is simulated, and the torque waveforms are shown in Fig. 4.28. The average torque versus current angle at 40 A is illustrated in 4.29 (a), and the average torque at 70 A is illustrated in Fig. 4.29 (b).

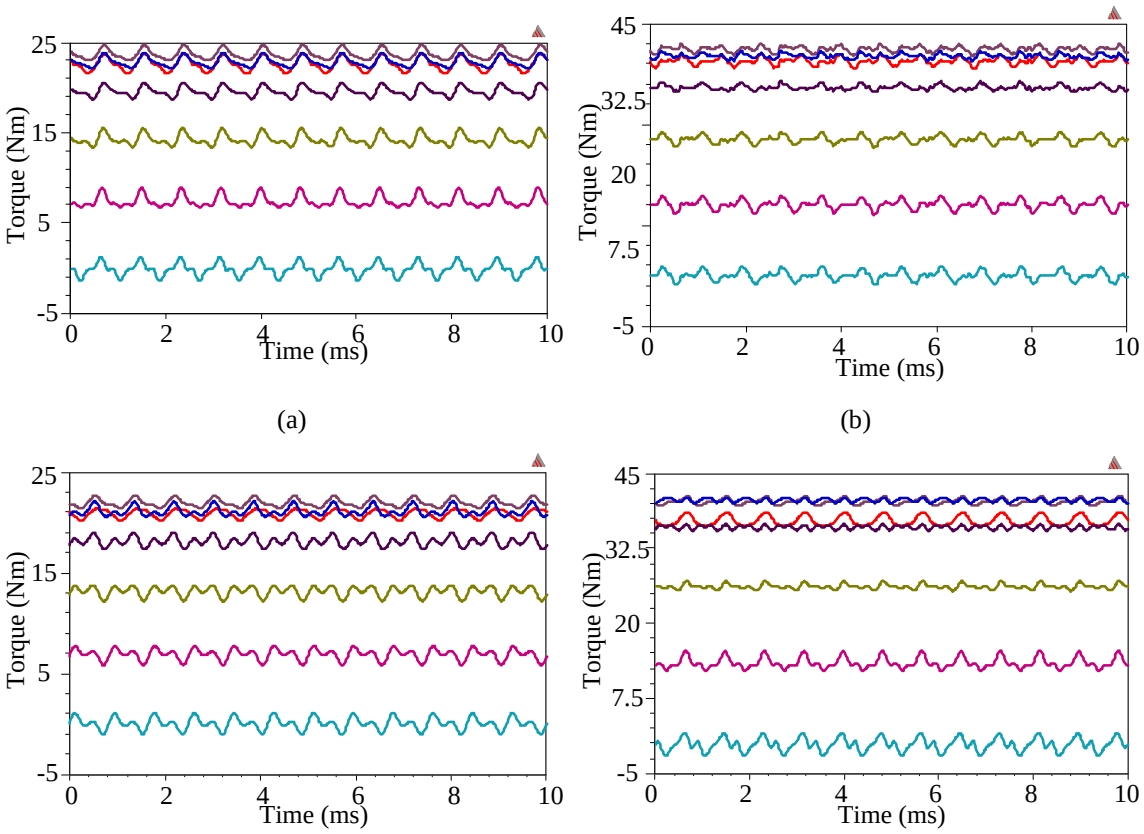

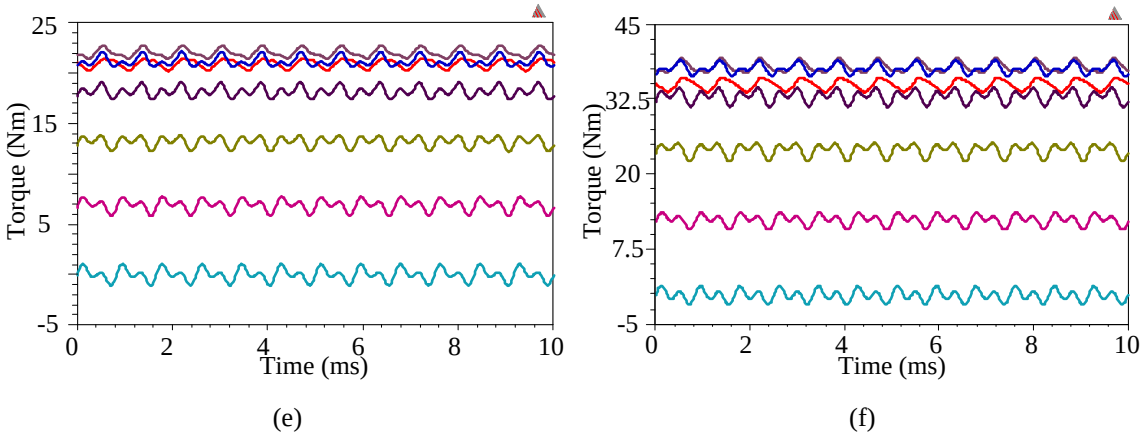

Fig. 4.28. Torque waveforms under different current excitation: (a) SL, V-shape rotor, 40 A, (b) SL, V-shape rotor, 70 A, (c) DL, V-shape rotor, 40 A, (d) DL, V-shape rotor 70 A, (e) DL, I-shape rotor, 40 A, and (f) DL, I-shape rotor, 70 A.

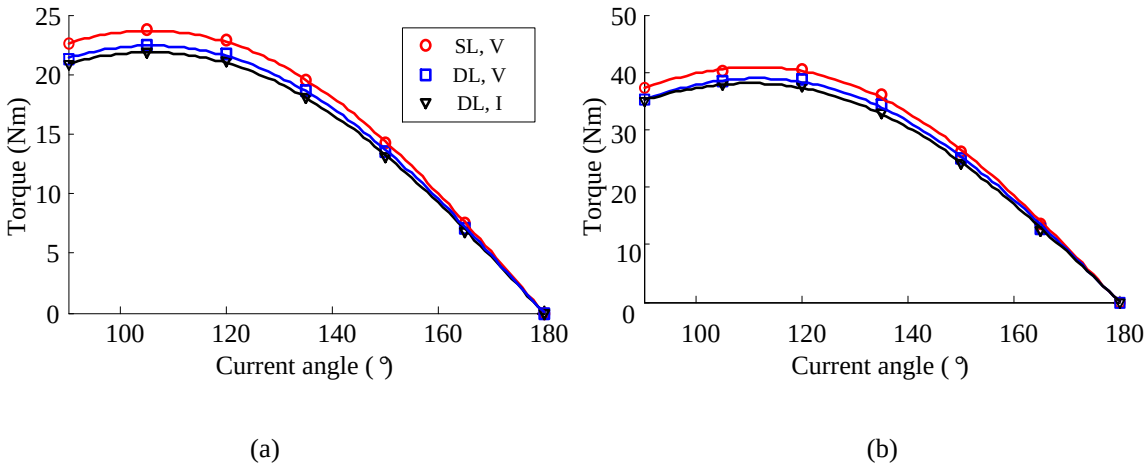

Fig. 4.29. Average torque versus current excitation angle: (a) 40 A, (b) 70 A.

As shown in Fig. 4.30, the output torque of IPM machines comprises of PM torque and reluctance torque, which may be expressed using sum of sine functions by curve fitting method.

$$T_e = T_{\mathrm{PM}} \sin(\alpha) + T_{\mathrm{Rel}} \sin(2\alpha) \tag{4.44}$$

where, T_{PM} is the amplitude of PM torque, T_{Rel} is the amplitude of reluctance toque.

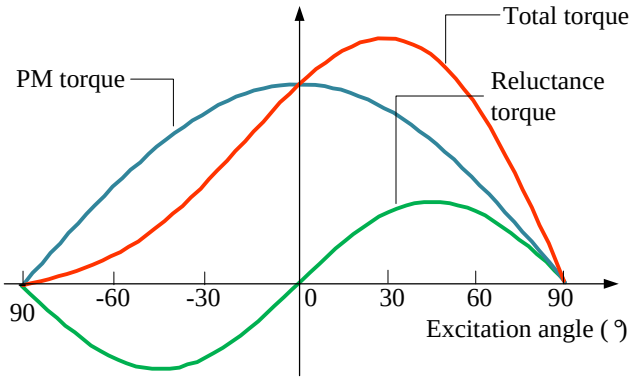

Fig. 4.30. Torque components of IPM machine.

The PM torque and reluctance torque components are separated by curve fitting method, and they are summarized in Table 4.12.

Table 4.12 Torque components of IPM machines

	40 A			70 A		
	T_{PM} (Nm)	T_{Rel} (Nm)	T_{Rel}/T_{PM} (%)	T_{PM} (Nm)	T_{Rel} (Nm)	T_{Rel}/T_{PM} (%)
SL, V	22.66	3.56	15.69	37.21	9.22	24.76
DL, V	21.40	3.46	16.18	35.31	8.91	25.22
DL, I	20.94	3.25	15.51	35.11	7.91	22.52

At 40 A and 70 A, the SL, V-shape rotor machine produces highest PM torque and reluctance torque. The DL, V-shape rotor machines produce higher torque than I-shape rotor machine. At high current level, both V-shape rotor machines produce higher reluctance torque than I-shape rotor machine by over 10%. The uneven stator teeth, SL winding, V-shape rotor machine has highest torque capability.

Core Loss and PM loss

The PM eddy current loss and core losses are evaluated by FEA simulations. Again, bulky magnets are assumed. At 40 A, the losses of each machine are summarized in Fig. 4.31 (a). At 70 A, the losses of each machine are summarized in Fig. 4.31 (b).

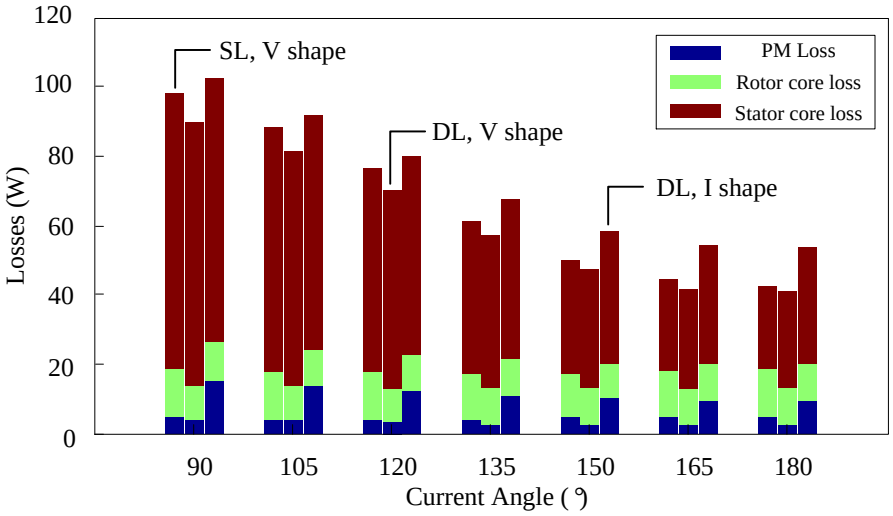

(a)

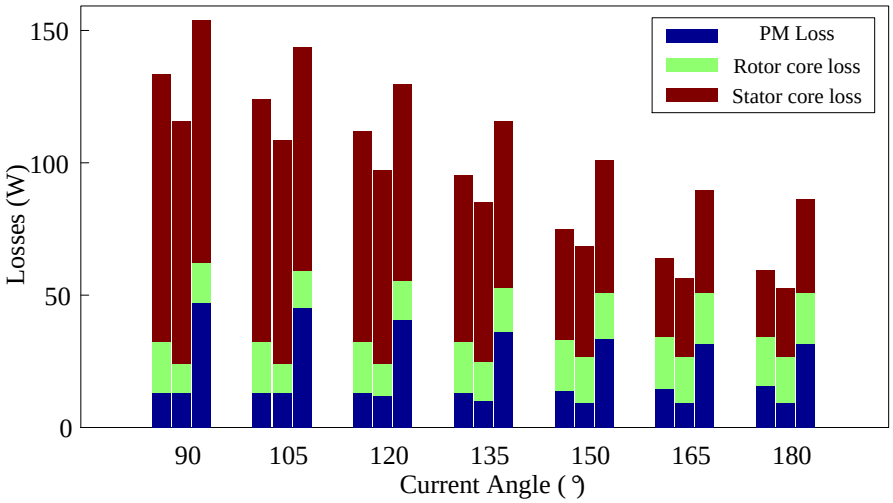

(b)

Fig. 4.31. Losses of the IPM machines under different excitation angles: (a) 40 A, (b) 70 A.

Because the magnets in the V-shape rotor are segmented, the PM losses of the V-shape rotor are much lower. The DL, V-shape rotor generates lowest PM losses and I-shape rotor generates he highest PM losses. When the current angle increases, the stator core loss of the SL V-shape rotor machine reduces significantly, and the total losses difference between the SL and DL V-shape machine is mainly due to the PM eddy current loss.

Overall, the SL, V-shape rotor machine shows its advantage over the conventional DL design in terms of torque capability, at the cost of slightly higher core loss and PM eddy losses. The PM eddy losses can be further mitigated by employing segmented magnets.

4.6. DISCUSSION OF ROTOR YOKE DESIGN

Rotor geometry design has strong impact on core losses and PM eddy current loss. The impact of the PM location have been studied in [80, 81]. The rotor yoke design also influences the losses of the machine. The rotor yoke cut method is introduced to increase the magnetic resistance for low order harmonics, and reduce the rotor losses effectively [17]. In this SL V-shape rotor design, the very thin bridges on the inner peripheral of the rotor have similar effect of increasing the magnetic resistance for the low order MMF harmonics.

In many designs, especially when the ISDW is employed, the rotor yoke is usually designed to be thicker to achieve low yoke flux density. For FSCW machines, the influence of rotor yoke thickness on the machine performances are investigated on the DL

and uneven stator teeth SL FSCW machines. Two V-shape rotors are shown in Fig. 4.32, and they have identical flux barrier and rotor outer diameter.

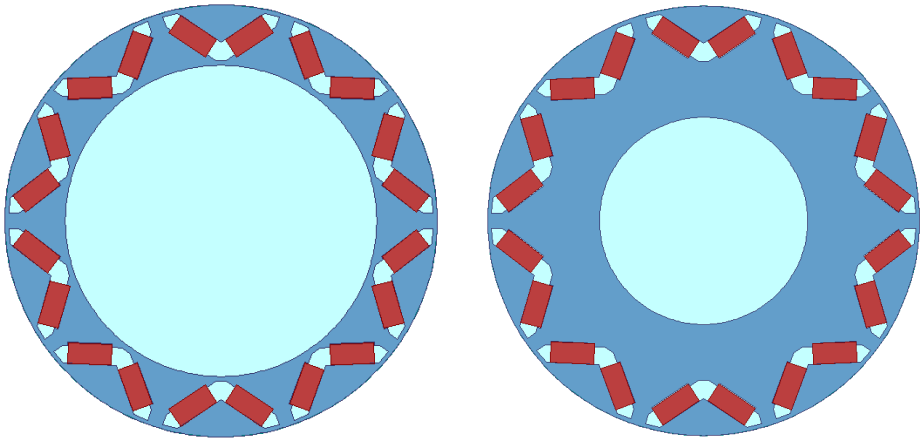

(a) (b)

Fig. 4.32. V-shape rotor configurations: (a) thin rotor yoke bridges, (b) thick rotor yoke bridges.

4.6.1. DL FSCW Machine

The output toque versus the excitation current angle is investigated at 40 A and 70 A, and the comparative results are shown in Fig. 4.33 (a). The total loss, including stator core loss, rotor core loss and PM loss are illustrated in Fig. 4.33 (b).

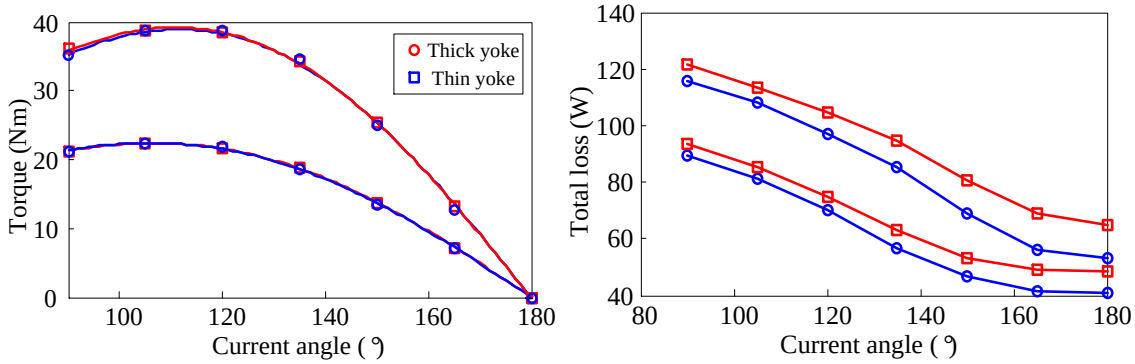

(a) (b)

Fig. 4.33. Performances versus excitation angle (DL): (a) average torque, (b) core loss and PM loss.

The average torque of both rotors is equivalent and the difference is minimal. However, the rotor with thin yoke features lower losses. The loss components are illustrated in Fig. 4.34 (a), (b) and (c), respectively.

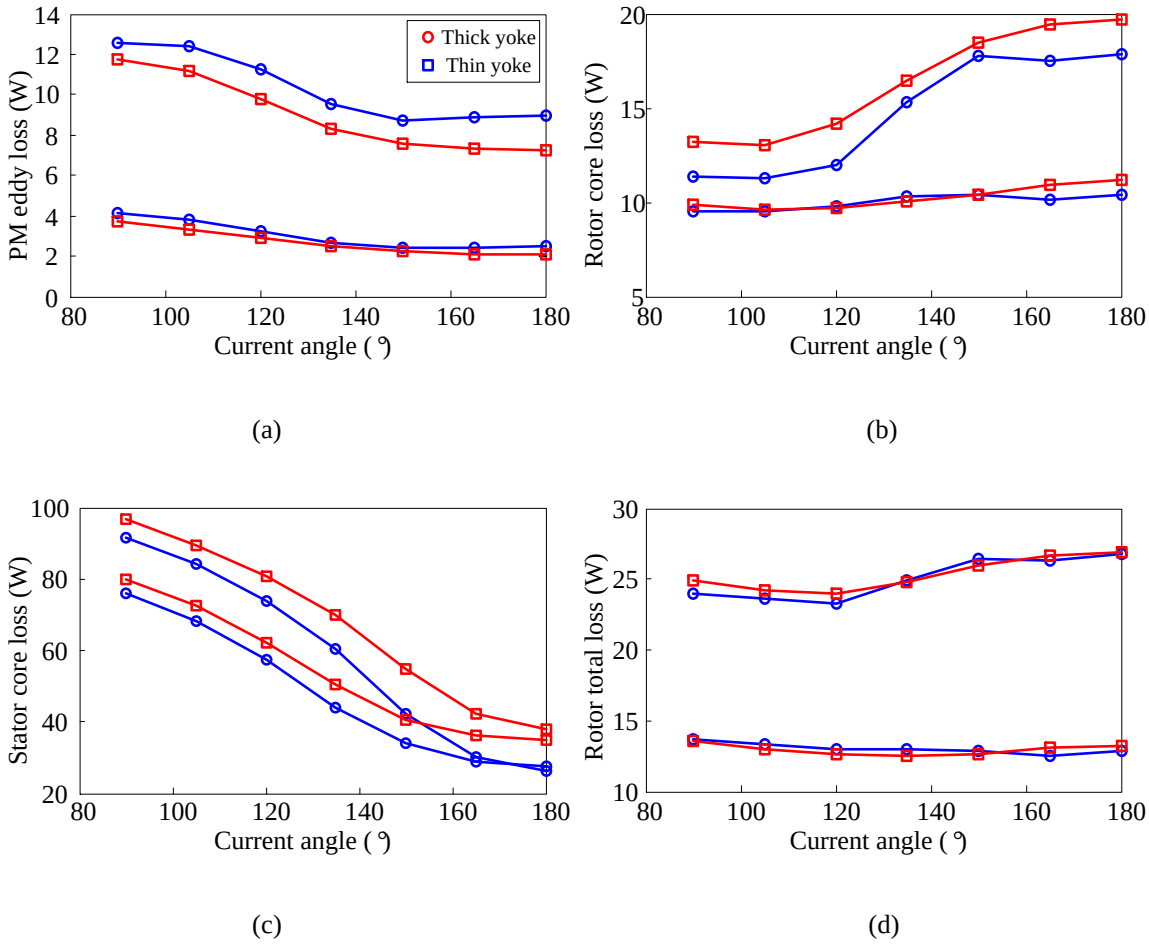

Fig. 4.34. Loss components versus excitation angle (DL): (a) PM loss, (b) rotor core loss, (c) stator core loss, and (d) rotor total losses.

As shown in Fig. 4.9 and Fig. 4.10 (b), the DL winding still generates 1st order harmonic, which is attenuated by the high reluctance of the rotor yoke. As a result, the thin yoke design reduces the stator core loss and rotor core loss effectively at the cost of

slightly increased PM loss. The total rotor losses of the thin yoke and thick yoke design are comparable, as shown in Fig. 4.34 (d).

4.6.2. SL FSCW Machine

The output toque versus the excitation current angle is investigated at 40 A and 70 A, and the comparative torque results for both rotor configurations are shown in Fig. 4.35 (a). The total losses are illustrated in Fig. 4.35 (b).

When the thin rotor yoke is employed, considerable higher torque capability can be achieved, especially at high current level. The PM torque component of the thin yoke design and thick yoke design are comparable, because when the current excitation angle is 90°, the average torque of these two machines are equivalent. Hence the increased torque mainly comes from the reluctance torque component. The thin yoke design features much lower losses at all different excitation, as shown in Fig. 4.35 (b).

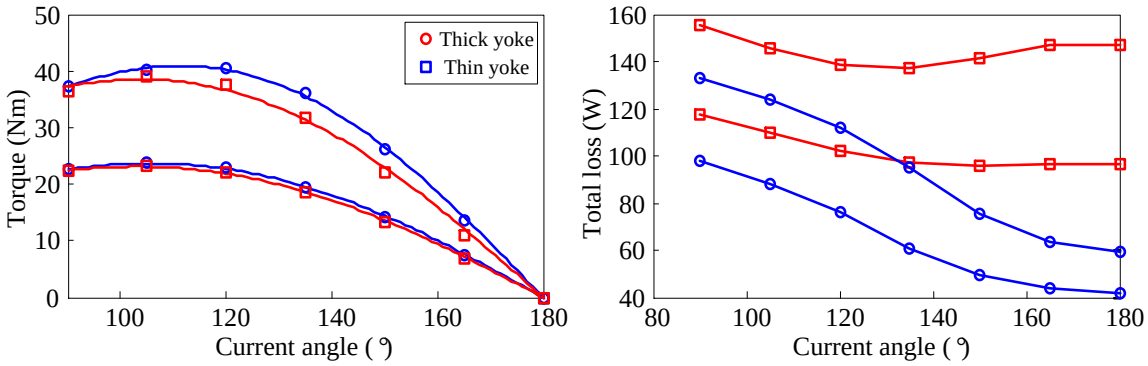

(a) (b)

Fig. 4.35. Performance versus excitation angle (SL): (a) average torque, (b) core loss and PM loss.

The loss components at different current excitations are illustrated in Fig. 4.36 (a), (b), and (c), respectively. The PM eddy current loss, stator core loss and rotor core loss are all reduced significantly in the thin rotor yoke design. The total rotor loss, as shown in Fig. 4.36 (d), can be reduced by up to 50%.

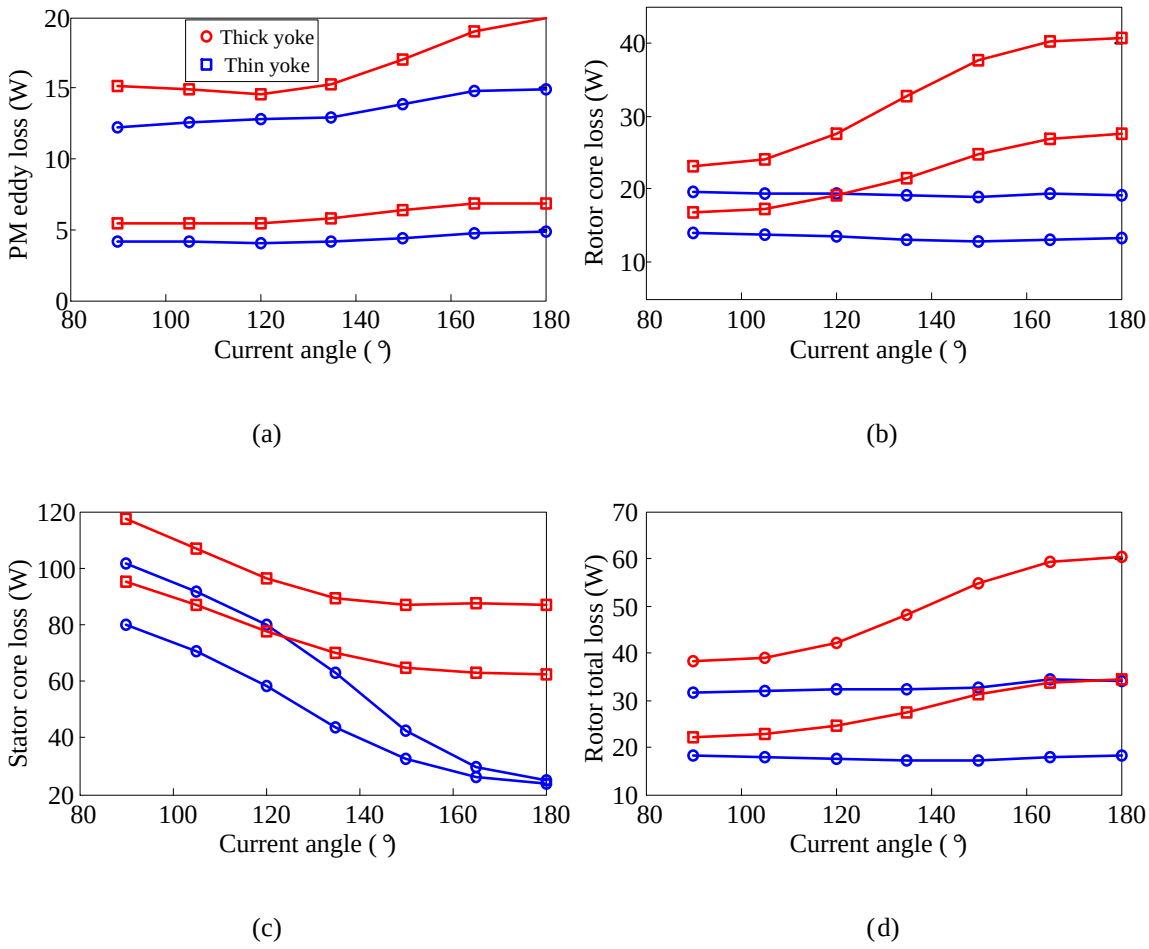

Fig. 4.36. Loss components versus excitation angle (SL): (a) PM loss, (b) rotor core loss, (c) stator core loss, and (d) rotor total losses.

Fig. 4.37 shows the flux density distribution when the machines are excited at 70 A, 135°, the saturation level of the thin rotor yoke design is much lower on the stator yoke and rotor ribs. Hence the reluctance torque is enhanced. In the thin rotor yoke design, the

saturated rotor bridges at the bottom of the flux barrier significantly attenuate the 1st order harmonic, which helps reduce the core losses and PM loss.

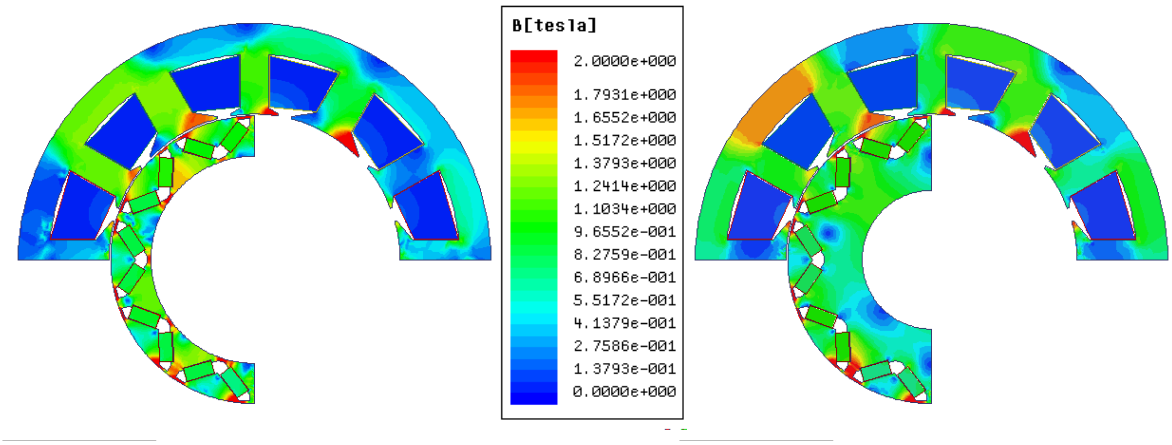

Fig. 4.37. Flux density distribution: (a) thin rotor yoke bridges, (b) thick rotor yoke bridges.

Regardless of the winding configuration (SL or DL), the thin rotor yoke helps reduce the core losses, especially at high current level. Because the SL winding features higher 1st order harmonic, the thin rotor yoke design enables more reduction of the core losses.

4.7. CONCLUSIONS

In this chapter, the design methodology of FSCW IPM machines is presented. A SL winding FSCW machine is designed and the performance is verified by FEA simulations.

The relationship between the machine parameters and the output characteristic is investigated first. The topology of the machine is selected according to its specification. The machine geometry is modeled parametrically and RSM is employed to optimize the torque ripples. The response surface can be updated by adding the optimized design

parameters and corresponding response evaluations. The optimized design can be obtained with reduced computational effort.

The performance of the design is validated by comparing the torque and losses with several conventional designs. It is proven that this design is able to deliver higher torque with reduced amount of PM usage.

The influence of the rotor yoke thickness on torque production and losses for FSCW machines is discussed. Thin rotor yoke increases the reluctance for the low order harmonics, which reduces the core loss of FSCW machines. The torque capability can be enhanced significantly when SL winding configuration is employed.

This page is intentionally left blank

Chapter 5
CONTROL STRATEGY

The modeling and analysis methods of PMSM have been researched since 1980s [82]. In many publications, The FSCW PMSM is considered ideal, and the mathematical model described in (4.1) - (4.4) are directly used [83]. In this chapter, the comprehensive mathematical model of the FSCW PMSM under *d*- and *q*-axis is investigated. Based on the machine model it is proven that the FOC can be applied to the FSCW machines. The optimal current control strategies are studied based on nonlinear optimization algorithm.

5.1. COMPREHENSIVE MATHEMATICAL MODEL OF FRACTIONAL SLOT CONCENTRATED WINDING PM MACHINE UNDER *dq* FRAME

5.1.1. Inductance Model Under *dq* Frame

Under the stationary frame, the stator winding inductances can be represented by the self- and mutual inductance in the matrix form as (5.1). Each term in (5.1) can be represented by the Fourier series as (5.2) and (5.3) according to the inductance analysis of salient rotor FSCW machines in Chapter 3.

$$L_s = \begin{pmatrix} L_{AA} & M_{AB} & M_{AC} \\ M_{BA} & L_{BB} & M_{BC} \\ M_{CA} & M_{CB} & L_{CC} \end{pmatrix} \tag{5.1}$$

$$\begin{aligned} L_{AA} &= L_0 + L_2\cos 2\theta + \cdots \\ L_{BB} &= L_0 + L_2\cos 2(\theta - \frac{2}{3}\pi) + \cdots \\ L_{BB} &= L_0 + L_2\cos 2(\theta + \frac{2}{3}\pi) + \cdots \end{aligned} \tag{5.2}$$

$$\begin{aligned} M_{AB} = M_{BA} &= M_0 + M_2\cos 2(\theta + \frac{2}{3}\pi) + \cdots \\ M_{AC} = M_{CA} &= M_0 + M_2\cos 2(\theta - \frac{2}{3}\pi) + \cdots \\ M_{BC} = M_{CB} &= M_0 + M_2\cos 2\theta + \cdots \end{aligned} \tag{5.3}$$

The most significant harmonic contents are the first two terms, and the higher order inductance harmonics may be neglected. The stationary 3-phase system can be transformed to the 2-phase synchronous rotating frame. The *d*- and *q*-axis inductances are derived by (5.4).

$$L_{dq0} = C_{dq0}^{-1} L_s C_{dq0} \tag{5.4}$$

where,

$$C_{dq0}^{-1} = \frac{2}{3}\begin{pmatrix} \cos\theta & \cos(\theta - \frac{2}{3}\pi) & \cos(\theta + \frac{2}{3}\pi) \\ -\sin\theta & -\sin(\theta - \frac{2}{3}\pi) & -\sin(\theta + \frac{2}{3}\pi) \\ \frac{1}{2} & \frac{1}{2} & \frac{1}{2} \end{pmatrix},\ C_{dq0} = \begin{pmatrix} \cos\theta & -\sin\theta & 1 \\ \cos(\theta - \frac{2}{3}\pi) & -\sin(\theta - \frac{2}{3}\pi) & 1 \\ \cos(\theta + \frac{2}{3}\pi) & -\sin(\theta + \frac{2}{3}\pi) & 1 \end{pmatrix}.$$

Substituting the inductance (5.1), (5.2) and (5.3) into (5.4), the inductance matrix under the synchronous rotating frame is derived as (5.5).

$$L_{dq0}=\begin{pmatrix} L_0-M_0+\dfrac{L_2+2M_2}{2} & 0 & \left(L_2-M_2\right)\cos 3\theta \\ 0 & L_0-M_0-\dfrac{L_2+2M_2}{2} & -\left(L_2-M_2\right)\sin 3\theta \\ \dfrac{L_2-M_2}{2}\cos 3\theta & -\dfrac{L_2-M_2}{2}\sin 3\theta & L_0+2M_0 \end{pmatrix} \quad (5.5)$$

5.1.2. PM Flux Linkage Model Under *dq* Frame

The PM flux linkage of the FSCW machines is studied by FEA simulations. For SL and DL FSCW machines with V-shape rotor discussed in Chapter 4, the induced flux linkages are reported in Fig. 5.1 (a) and (b), respectively. The most significant harmonic content is the fundamental term, and high order harmonics are negligible. In some designs, the 3rd order harmonic may not be negligible. The 3-phase flux linkage can be represented as

$$\psi_f=\psi_{f1}\begin{pmatrix}\cos\theta\\ \cos(\theta-\frac{2}{3}\pi)\\ \cos(\theta+\frac{2}{3}\pi)\end{pmatrix}+\psi_{f3}\begin{pmatrix}\cos 3\theta\\ \cos 3(\theta-\frac{2}{3}\pi)\\ \cos 3(\theta+\frac{2}{3}\pi)\end{pmatrix} \quad (5.6)$$

where, ψ_{f1} and ψ_{f3} are 1st and 3rd order harmonics of the flux linkage.

Equation (5.6) can be pre-multiplied by C_{dq0}^{-1}, and the flux linkage under the synchronous rotating frame can be obtained as

$$\psi_{fdq0}=\begin{pmatrix}\psi_{f1}\\ 0\\ \psi_{f3}\cos(3\theta)\end{pmatrix} \quad (5.7)$$

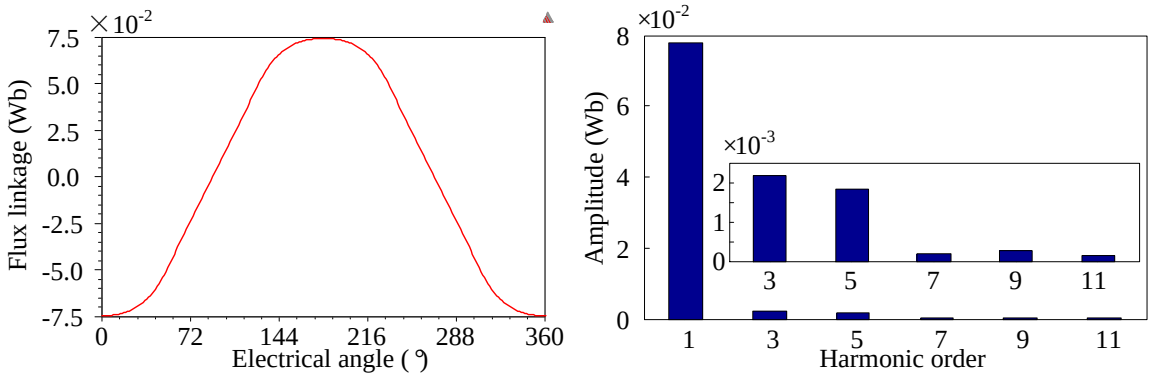

(a)

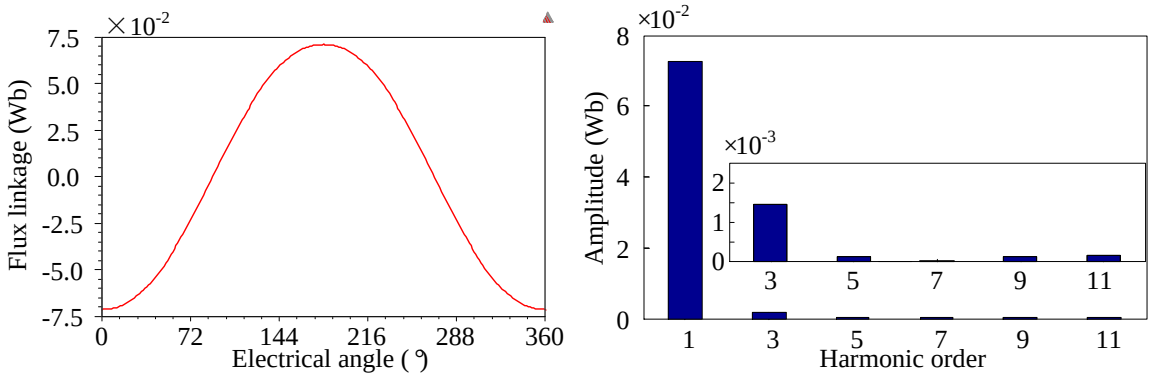

(b)

Fig. 5.1. PM flux linkage waveforms and Fourier series: (a) SL machine, (b) DL machine.

5.1.3. Voltage and Flux Linkage Equations Under *dq* Frame

The voltage equation under synchronous rotating frame can be expressed as

$$\begin{pmatrix} u_d \\ u_q \\ u_0 \end{pmatrix} = \begin{pmatrix} R_s & & \\ & R_s & \\ & & R_s \end{pmatrix} \begin{pmatrix} i_d \\ i_q \\ i_0 \end{pmatrix} + \frac{d}{dt} \begin{pmatrix} \psi_d \\ \psi_q \\ \psi_0 \end{pmatrix} + \omega_r \begin{pmatrix} 0 & -1 & 0 \\ 1 & 0 & 0 \\ 0 & 0 & 0 \end{pmatrix} \begin{pmatrix} \psi_d \\ \psi_q \\ \psi_0 \end{pmatrix} \tag{5.8}$$

Combining (5.5) and (5.7), the flux linkage model of FSCW machines under synchronous rotating frame can be obtained as (5.9).

$$\begin{pmatrix}\psi_d\\ \psi_q\\ \psi_0\end{pmatrix}=\begin{pmatrix} L_0-M_0+\frac{L_2+2M_2}{2} & 0 & (L_2-M_2)\cos 3\theta\\ 0 & L_0-M_0-\frac{L_2+2M_2}{2} & -(L_2-M_2)\sin 3\theta\\ \frac{L_2-M_2}{2}\cos 3\theta & -\frac{L_2-M_2}{2}\sin 3\theta & L_0+2M_0\end{pmatrix}\begin{pmatrix}i_d\\ i_q\\ i_0\end{pmatrix}+\begin{pmatrix}\psi_{f1}\\ 0\\ \psi_{f3}\cos(3\theta)\end{pmatrix} \quad (5.9)$$

In (5.9), *0*-axis is coupled with *d*- and *q*-axis. The coupling from *d*- and *q*-axis introduces flux linkage to *0*-axis, and *0*-axis flux linkage is no longer zero. The coupling from *0*-axis to *d*- and *q*-axis introduces extra flux linkages to *d*- and *q*-axis. As a result, the derivatives of flux linkage in (5.8) introduce extra voltage terms on *d*- and *q*-axis and *0*-axis.

If the 3-phase windings are Y connected, the *0*-axis current is zero, as shown in (5.10). Substituting (5.10) into the flux linkage equation (5.9), the coupling from *0*-axis current to *d*- and *q*-axis flux linkages is zero.

$$i_0=(i_a+i_b+i_c)/3=0 \quad (5.10)$$

The flux linkage equation can be simplified to (5.11). Therefore, the voltage equation (5.8) can be divided by two parts as (5.12) and (5.13).

$$\begin{pmatrix}\psi_d\\ \psi_q\\ \psi_0\end{pmatrix}=\begin{pmatrix} L_0-M_0+\frac{L_2+2M_2}{2} & 0\\ 0 & L_0-M_0-\frac{L_2+2M_2}{2}\\ \frac{L_2-M_2}{2}\cos 3\theta & -\frac{L_2-M_2}{2}\sin 3\theta\end{pmatrix}\begin{pmatrix}i_d\\ i_q\end{pmatrix}+\begin{pmatrix}\psi_{f1}\\ 0\\ \psi_{f3}\cos(3\theta)\end{pmatrix} \quad (5.11)$$

$$\begin{pmatrix}u_d\\ u_q\end{pmatrix}=\begin{pmatrix}R_s & \\ & R_s\end{pmatrix}\begin{pmatrix}i_d\\ i_q\end{pmatrix}+\frac{d}{dt}\begin{pmatrix}\psi_d\\ \psi_q\end{pmatrix}+\omega_r\begin{pmatrix}0 & -1\\ 1 & 0\end{pmatrix}\begin{pmatrix}\psi_d\\ \psi_q\end{pmatrix} \quad (5.12)$$

$$u_0 = \frac{d}{dt}\psi_0 \tag{5.13}$$

where, $\psi_0 = i_d \frac{L_2 - M_2}{2}\cos 3\theta - i_q \frac{L_2 - M_2}{2}\sin 3\theta + \psi_{f3}\cos(3\theta)$.

Equation (5.12) is exactly the same as ideal PMSM voltage equation. However, as shown in (5.13), the *0*-axis voltage is not zero.

$$\begin{aligned} u_0 = p\psi_0 &= \frac{L_2 - M_2}{2}\left(i_d p\cos 3\theta - i_q p\sin 3\theta\right) - 3\psi_{f3}\sin(3\theta) \\ &= -\frac{3\left(L_2 - M_2\right)}{2}\omega_r\left(i_d \sin 3\omega t + i_q \cos 3\omega t\right) - 3\psi_{f3}\sin(3\omega t) \end{aligned} \tag{5.14}$$

The *0*-axis voltage can be considered the common component of the 3-phase voltage. Because u_0 is 3rd order harmonic, it will be cancelled in the 3-phase line to line voltages. Therefore, the induced line to line voltage is still sinusoidal. In voltage source PWM drive, space vector modulation technique or 3rd order harmonic injection is usually employed to improve the DC link voltage utilization. Here, it may be considered that the machine itself injects 3rd order voltage harmonic. Hence the FOC technique can also be applied to the FSCW machines.

5.2. PERMANENT MAGNET SYNCHRONOUS MACHINE OPTIMAL CONTROL STRATEGY

The loss minimization/efficiency enhancement control methods have gained a lot of research interests. Most of the loss minimization methods are developed analytically based on loss models, and they generally utilize the derivative method or Lagrangian

method [84]. The parameter independent searching method is proposed in [85], which iterates the control variables to minimize the input power. The more complex experimental data based loss minimization technique is developed in [86], which requires multiple experiments to obtain the optimum current at each operation point. Other approaches such as the power factor tuning [87] and dynamic losses minimization [88, 89] are also developed to enhance the machine efficiency.

To compute the optimum current at a given torque and speed point, a typical approach is to calculate the intersection of the constant torque trajectory and the MTPA trajectory as the optimum current reference unless it violates the voltage limit. Otherwise, the intersection of the constant torque trajectory and the voltage limit ellipse will be adopted as the optimum current reference.

The idea of employing nonlinear optimization to achieve the global loss minimization is presented in this chapter. In order to be consistent with the published paper [90], the Toyota Prius 2004 motor is used as the example here. The alternative current minimization control strategy, which is also referred to as the speed range extended MTPA control will be applied to the SL FSCW machine designed in Chapter 4, and the experimental details are presented in Chapter 6.

5.2.1. Nonlinear Flux Linkage Model

In practice, the PMSM model is highly nonlinear due to the saturation and cross-coupling effect [91]. However, in many loss minimization publications, the linear *d*- and *q*-axis inductances [92, 93] or the current-dependent self-inductance functions [94] are

often employed, and sometimes the cross magnetization is neglected [95]. The current-dependent self- and mutual inductance are able to fully address the nonlinearities of the PMSM [96]. The flux linkage equations are modified to (5.15).

$$\begin{aligned} \psi_d &= L_d i_d + M_{dq} i_q + \psi_f \\ \psi_q &= L_q i_q + M_{qd} i_d \end{aligned} \tag{5.15}$$

where, M_{dq} and M_{qd} are current dependent mutual inductances between *d*- and *q*-axis. Equation (5.15) is used in the following optimization problem analysis.

5.2.2. PMSM Loss Model

The controllable PMSM power losses comprise 3 parts, copper loss P_{Cu}, core loss P_{Fe} and stray loss P_{stray}. The stray loss, which consists of the losses arising from non-uniform current and magnetic flux distortion, is ignored here.

The copper loss P_{Cu} is generated by the stator winding resistance. Here, the eddy current loss in the coils is not included, and this is the case for most of the electrical machines with stranded coils.

$$P_{Cu} = \frac{3}{2} R_s \cdot (i_d^2 + i_q^2) \tag{5.16}$$

The core loss P_{Fe} consists of hysteresis loss P_h, eddy current loss P_c and excessive loss P_e. When the magnetic steel is excited by sinusoidal magnetic field, the core loss can be expressed by the classical formula (5.17).

$$P_{Fe} = P_h + P_c + P_e \tag{5.17}$$

where, $P_h = k_h f B_m^2$ is the hysteresis loss, $P_c = k_c (f B_m)^2$ is the eddy current loss and $P_e = k_e (f B_m)^{1.5}$ is the excessive loss; k_h, k_c and k_e are the coefficients of loss components, B_m is the flux density magnitude, and f is the excitation frequency.

In electric machines, the loss formula may be expressed by the flux linkage and electrical speed, which can be easily derived either from simulations or experiments [97]. Therefore, the core loss can be modeled as [98, 99].

$$P_{Fe} = k_e' \omega_r^{1.5} \psi_m^{1.5} + (k_h' \omega_r + k_c' \omega_r^{\,2}) \psi_m^2 \tag{5.18}$$

where, ψ_m is the flux linkage magnitude, and ψ_m is calculated from the d- and q-axis flux linkage, $\psi_m = (\psi_d^2 + \psi_q^2)$; ω_r is the electrical rotating speed, k_h' , k_c' and k_e' are the coefficient of each loss component.

The core loss model of (5.18) is based on the assumption of sinusoidal excitation. However, the d-axis armature reaction may cause significant amount of harmonics, especially when the q-axis current is low.

Fig. 5.2 shows the 1/8 model of the Toyota Prius 2004 motor. The waveforms and spectrums of the air gap flux density distribution under different excitations are illustrated in Fig. 5.3. The air gap flux density waveforms indicate that the flux density in the stator and rotor are distorted.

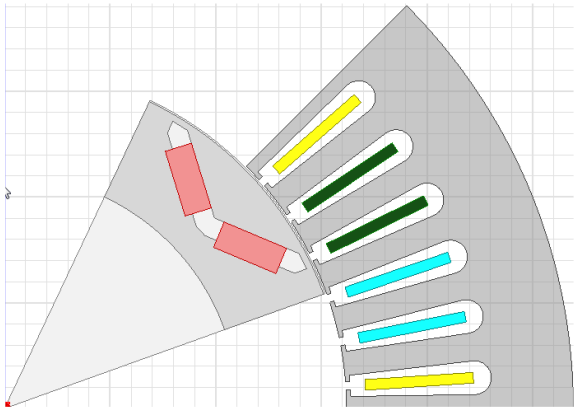

Fig. 5.2. 2D model of Toyota Prius 2004 motor.

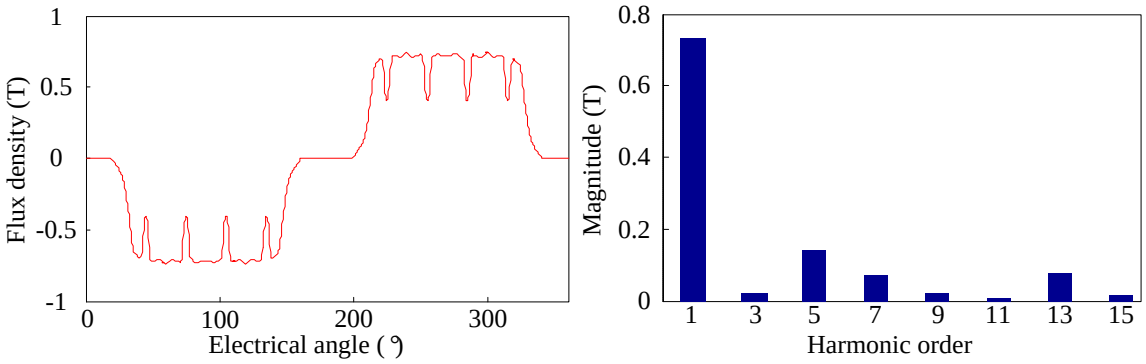

(a)

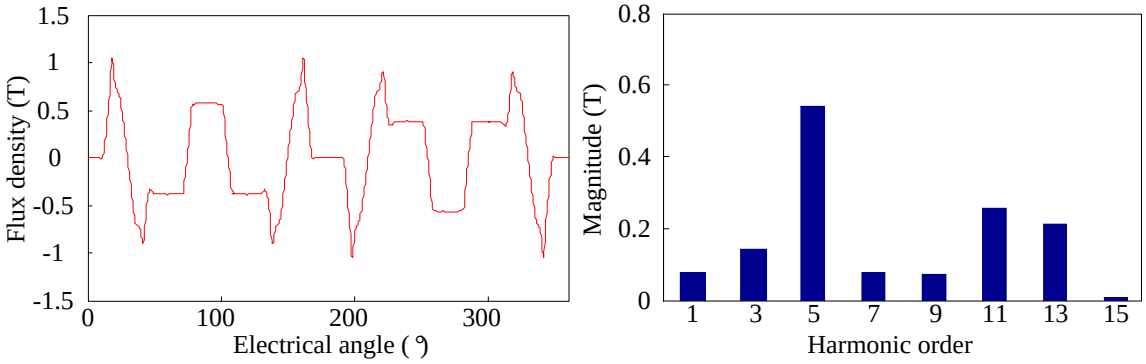

(b)

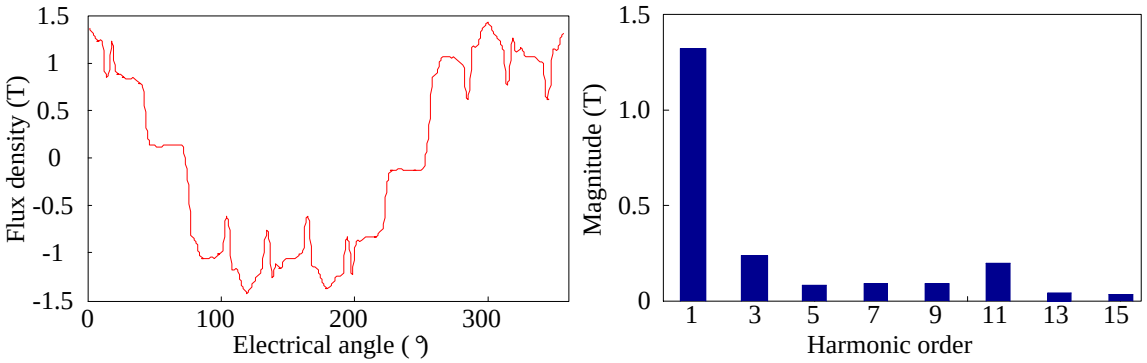

(c)

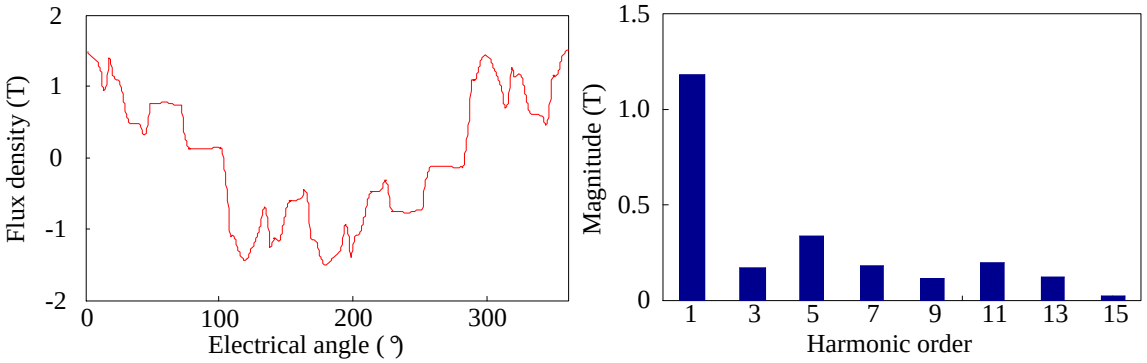

(d)

Fig. 5.3. Air gap flux density distributions and spectrums: (a) i_d = 0, i_q = 0, (b) i_d = 150 A, i_q = 0, (c) i_d = 0, i_q = 150 A, and (d) i_d = 150 A, i_q = 150 A.

The core loss under multiple frequency excitations can be modified as

$$\begin{aligned} P_{Fe} &= \sum_{i=1,3,5,\cdots}^{\infty} (k_e' \omega_{ri}^{1.5} \psi_{mi}^{1.5} + (k_h' \omega_{ri} + k_c' \omega_{ri}^2) \psi_{mi}^2) \\ &\overset{\omega_{ri}=i\cdot\omega_r}{=} \sum_{i=1,3,5,\cdots}^{\infty} (k_h' i \psi_{mi}^2 \omega_r + k_e' i^{1.5} \psi_{mi}^{1.5} \omega_r^{1.5} + k_c' i^2 \psi_{mi}^2 \omega_r^2) \\ &= \omega_r \sum k_h' i \psi_{mi}^2 + \omega_r^{1.5} \sum k_e' i^{1.5} \psi_{mi}^{1.5} + \omega_r^2 \sum k_c' i^2 \psi_{mi}^2 \end{aligned} \tag{5.19}$$

If the core loss at a certain speed ω_r* is derived, the core loss may be written as

$$P_{Fe} = g(\omega_r) P_{Fe\_\omega_r^*}(\psi_{mi}) \tag{5.20}$$

where, $g(\omega_r) = \dfrac{P_{Fe}(\omega_r)}{P_{Fe}(\omega_r^*)} = \dfrac{a \cdot \omega_r + b \cdot \omega_r^{1.5} + c \cdot \omega_r^{2}}{a \cdot \omega_r^* + b \cdot \omega_r^{*1.5} + c \cdot \omega_r^{*2}}$ is the speed dependent loss coefficient function; $P_{Fe\_\omega_r^*}(\psi_{mi})$ is the core loss at the speed ω_r*, which can be derived from either simulation or the experimental method; $a = k_h^{'} \sum i \psi_{mi}^2$, $b = k_e^{'} \sum i^{1.5} \psi_{mi}^{1.5}$, $c = k_c^{'} \sum i^2 \psi_{mi}^2$.

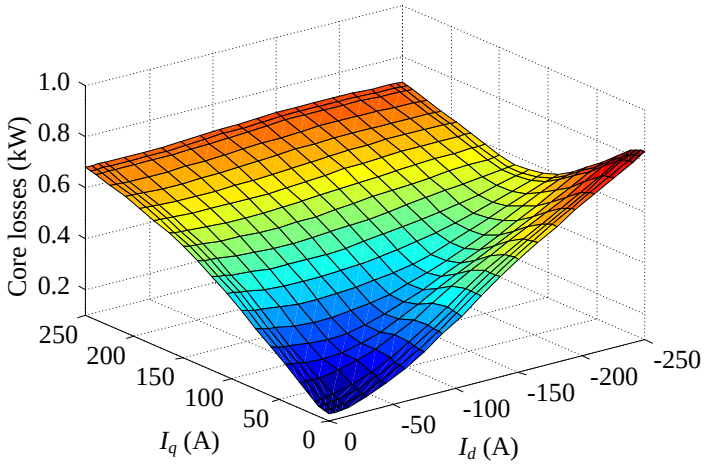

Fig. 5.4. Core loss map at 3000 rpm.

Each current vector (i_d, i_q) corresponds to unique ψ_{mi}, the core loss at speed ω_r* can be written as $P_{Fe\_\omega_r^*}(\psi_{mi}) = P_{Fe\_\omega_r^*}(i_d, i_q)$. For the PMSM shown in Fig. 5.2, the core loss versus *d*- and *q*-axis current at 3000 rpm is illustrated in Fig. 5.4. The speed dependent loss coefficient function $g(\omega_r)$ can be approximated using curve fitting of the no-load core loss, as shown in Fig. 5.5.

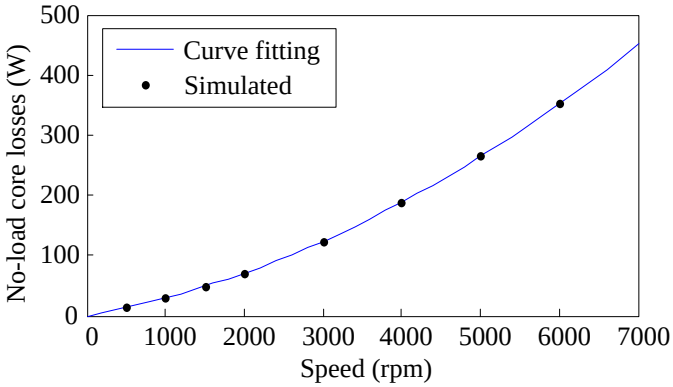

Fig. 5.5. No-load core loss versus speed.

5.2.3. Loss Minimization Control

The objective is to minimize the total losses while maintaining the desired speed ω_r and torque T_r. It can be modeled as a nonlinear optimization problem as (5.21).

$$\begin{aligned}
\text{minimize} \quad & \frac{3}{2}R_s \cdot (i_d^2 + i_q^2) + g(\omega_r) \cdot P_{Fe_\omega_r^*}(i_d, i_q) \\
\text{subject to} \quad & \frac{3}{2}P(\psi_d i_q - \psi_q i_d) - T_r = 0 \\
& i_d^2 + i_q^2 \le i_{\lim}^2 \\
& (-\omega_r \psi_q + R_s i_d)^2 + (\omega_r \psi_d + R_s i_q)^2 \le u_{\lim}^2 \\
& \psi_d = L_d i_d + M_{dq} i_q + \psi_f \\
& \psi_q = L_q i_q + M_{qd} i_d
\end{aligned} \tag{5.21}$$

The optimization problem (5.21) is relatively complicated. To simplify the problem, the steady-state voltage equation, flux linkage equation and torque equation are reformulated in matrix form.

$$u_s = \omega_r J \psi_s + R_s i_s \tag{5.22}$$

$$\psi_s = L_s i_s + B\psi_f \tag{5.23}$$

$$T_e = \frac{3}{2} P i_s^{'} J \psi_s \tag{5.24}$$

where, $u_s = \begin{pmatrix} u_d \\ u_q \end{pmatrix}$, $i_s = \begin{pmatrix} i_d \\ i_q \end{pmatrix}$, $\psi_s = \begin{pmatrix} \psi_d \\ \psi_q \end{pmatrix}$, $R_s = \begin{pmatrix} R_s & 0 \\ 0 & R_s \end{pmatrix}$, $L_s = \begin{pmatrix} L_d & M_{dq} \\ M_{qd} & L_q \end{pmatrix}$, $B = \begin{pmatrix} 1 \\ 0 \end{pmatrix}$, and $J = \begin{pmatrix} 0 & -1 \\ 1 & 0 \end{pmatrix}$.

Substitute (5.22)-(5.24) into (5.21), the optimization problem can be simplified to (5.25).

$$\begin{aligned} \text{minimize } & \frac{3}{2} i_s^{'} R_s i_s + g(\omega_r) \cdot P_{Fe\_\omega_r^*}(i_s) \\ \text{subject to } & \frac{3}{2} P i_s^T J \psi_s - T_r = 0 \\ & \psi_s - (L_s i_s + B \psi_f) = 0 \\ & \left\| i_s \right\| - i_{\lim} \le 0 \\ & \left\| (\omega_r J L_s + R_s) i_s + \omega_r J B \psi_f \right\| - u_{\lim} \le 0 \end{aligned} \tag{5.25}$$

The current-dependent inductance matrix L_s is very complicated because it contains multiple nonlinear functions of self- and mutual inductances. The LUT based *d*- and *q*-axis flux linkage profiles can be directly used in the constraints. The optimization problem (5.25) is modified to (5.26).

$$\begin{aligned} \text{minimize } & \frac{3}{2} i_s^{'} R_s i_s + g(\omega_r) \cdot P_{Fe\_\omega_r^*}(i_s) \\ \text{subject to } & \frac{3}{2} P i_s^T J \psi_s(i_s) - T_r = 0 \\ & \left\| i_s \right\| - i_{\lim} \le 0 \\ & \left\| \omega_r J \psi_s(i_s) + R_s i_s \right\| - u_{\lim} \le 0 \end{aligned} \tag{5.26}$$

At each required speed ω_r, $g(\omega_r)$ is a constant value, and the core loss function $P_{Fe\_\omega_r^*}(i_s)$ is also LUT based as shown in Fig. 5.4. The optimization problem (5.25) and (5.26) can be solved using nonlinear programming [100]. The *d*- and *q*-axis flux linkage profiles of the Toyota 2004 motor in Fig. 5.2 are shown in Fig. 5.6.

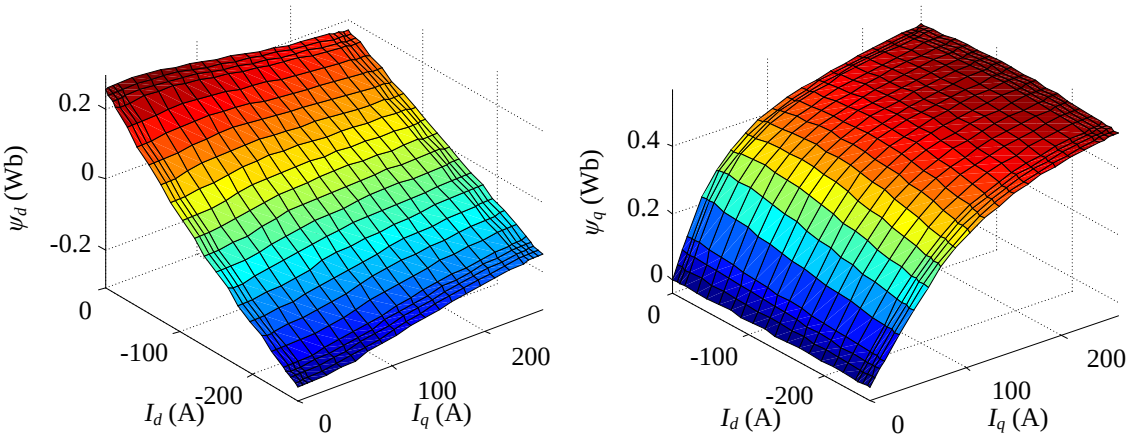

(a) (b)

Fig. 5.6. Flux linkage profiles of Prius 2004 motor: (a) *d*-axis flux linkage, (b) *q*-axis flux linkage.

To acquire optimal current profiles in the full torque-speed range, the torque limit at each speed is derived first, which can also be implemented using the nonlinear optimization algorithm. At each speed, (5.26) is implemented and solved at different torque levels until the torque approaches its limit. The flowchart of the optimization procedure is depicted in Fig. 5.7. The optimized *d*- and *q*-axis current references are shown in Fig. 5.8 (a) and (b), respectively.

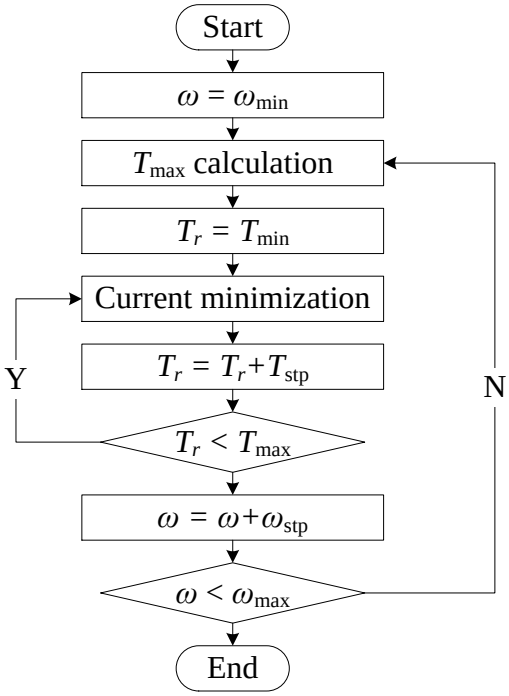

Fig. 5.7. Global loss minimization flowchart.

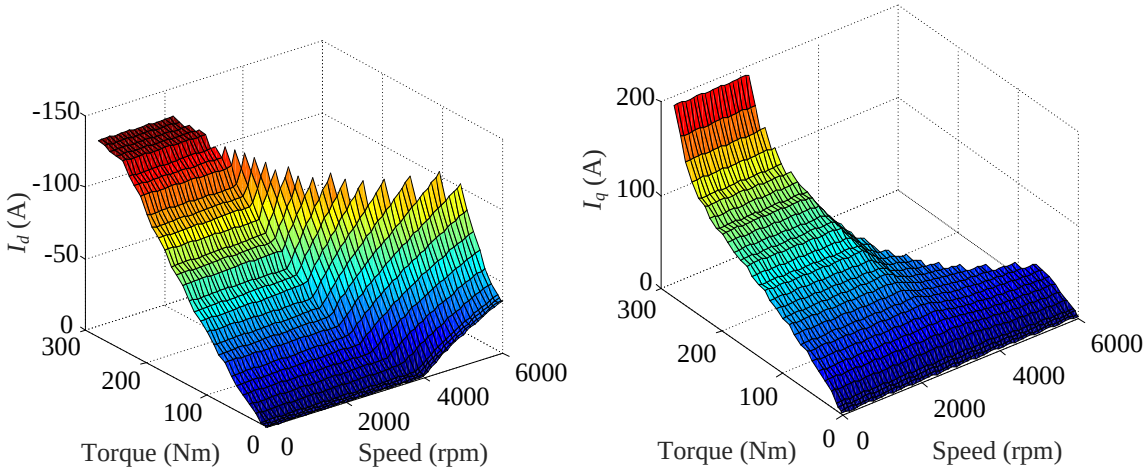

(a) (b)

Fig. 5.8. Optimized current profiles of Prius 2004 motor: (a) *d*-axis current, (b) *q*-axis current.

The optimized results are verified by the FEA simulations. The torque obtained from FEA simulations are compared with the torque references, and the torque accuracy ζ_T is shown in Fig. 5.9 (a). The FEA simulated core losses are compared with the nonlinear optimization results, and the relatively core loss difference is mapped in Fig. 5.9 (b).

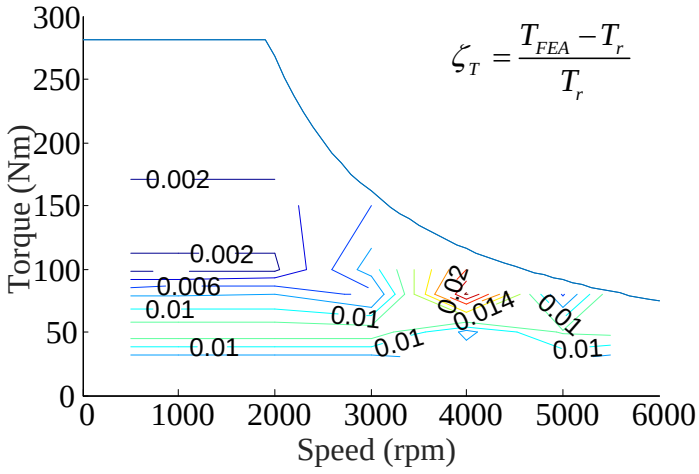

(a)

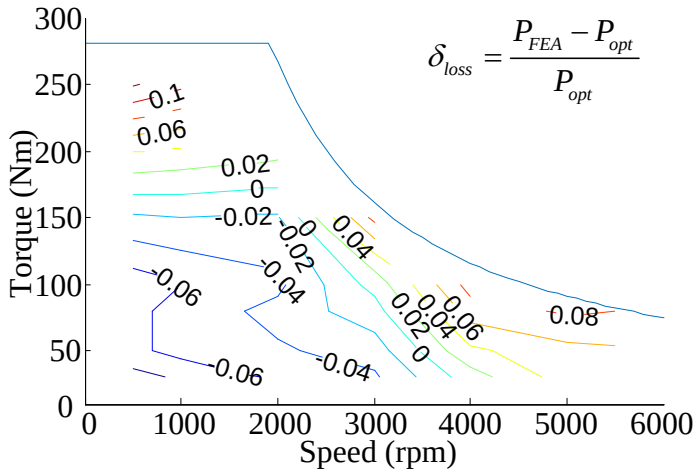

(b)

Fig. 5.9. FEA verification of optimization result: (a) torque error, (b) core loss error.

The relative output torque error is within 1% in most of the operation area. The core loss error δ_{loss} on the full operation map is within 8%. The core loss demonstrates relatively higher error, because the core loss function is assumed to be separable, which is not exactly true. Considering the copper loss is comparable with the core losses, this method is accurate enough to account for the total losses in the entire speed and current range. The simulation results confirm the feasibility of the nonlinear optimization algorithm, the speed and torque at each operation points can be satisfied by the constraints. When mechanical loss is considered, which can be obtained from [101], the efficiency map corresponding to the optimized *d*- and *q*-axis current is estimated using the output power and total losses, and it is illustrated in Fig. 5.10.

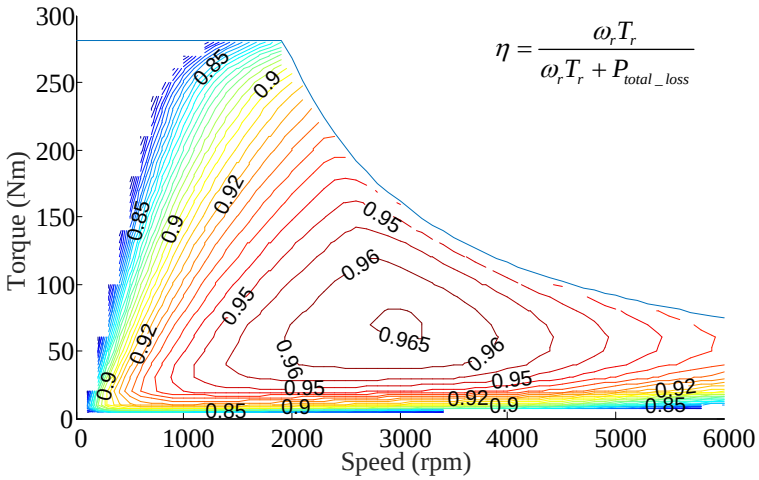

Fig. 5.10. Predicted efficiency map of Prius 2004 motor.

5.2.4. Current Minimization Control

The core loss of PMSM is very difficult to obtain. This makes the total loss minimization difficult to practice. A more practical alternative is to minimize the current. The current minimization technique is referred to as speed range extended MTPA control

strategy. The objective function in (5.26) can be modified to (5.27). The flux linkage profiles of the FSCW machine are reported in Fig. 5.11. The extend MTPA current profile is derived and illustrated in Fig. 5.12.

$$\text{minimize} \left\| i_s \right\| \tag{5.27}$$

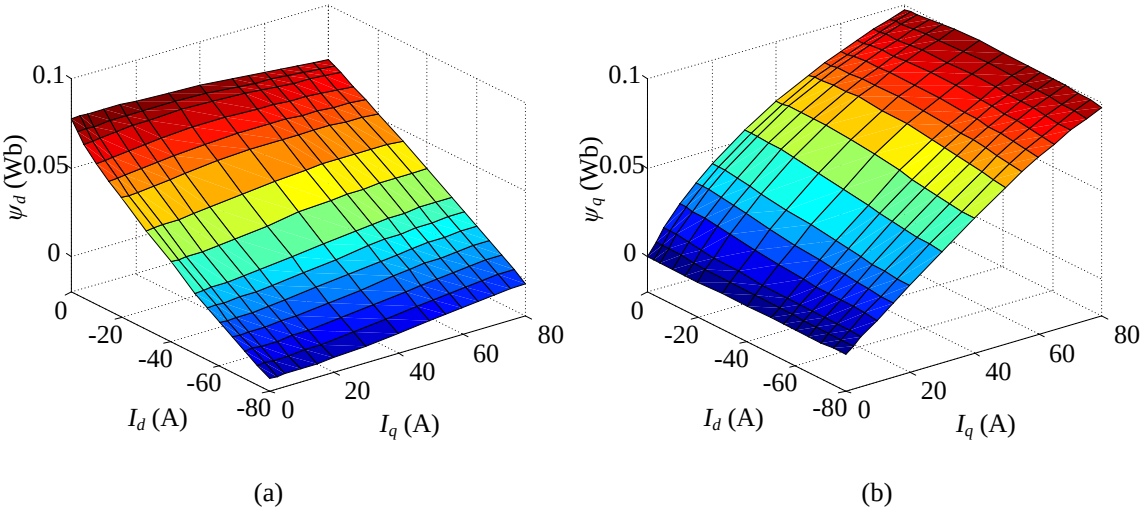

Fig. 5.11. Flux linkage profiles of the FSCW machine: (a) *d*-axis flux linkage, (b) *q*-axis flux linkage.

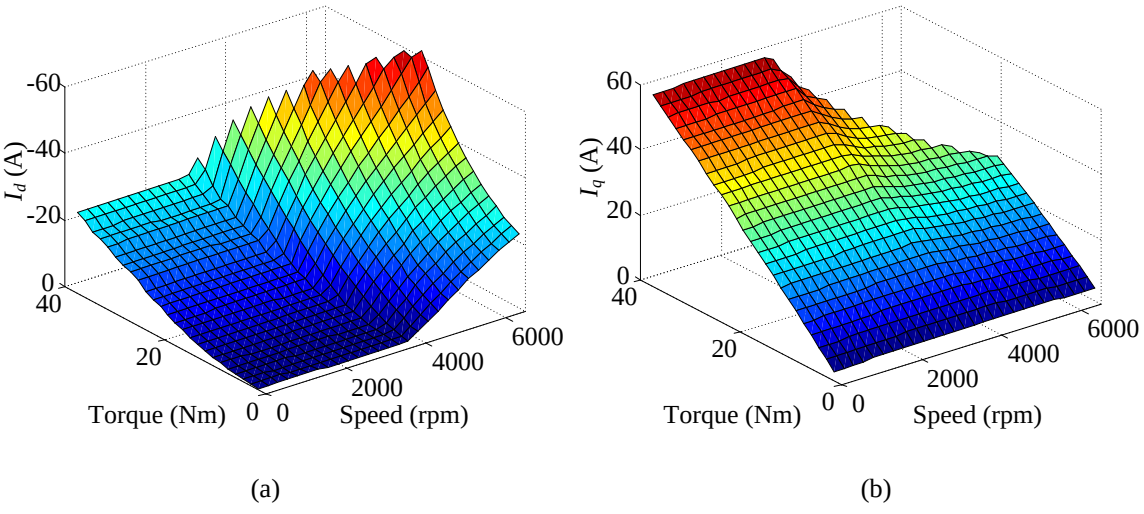

Fig. 5.12. Extended MTPA current profiles of the FSCW machine:

(a) *d*-axis current, (b) *q*-axis current.

In order to obtain the efficiency map, the core loss and mechanical loss need to be included. As has been discussed in section 5.2.2, the core loss is modeled by the speed dependent loss function and excitation dependent coefficient function. The speed dependent loss coefficient is derived from the no-load core loss results of FEA simulations, which is illustrated in Fig. 5.13 (a). The core loss with respect to different excitation current at 2400 rpm is reported in Fig. 5.13 (b). In practice, because of the PWM drive, the core loss will be elevated. A correction factor of 2 is employed here to account for the core loss, which is calibrated by the measured efficiency map reported in Chapter 6.

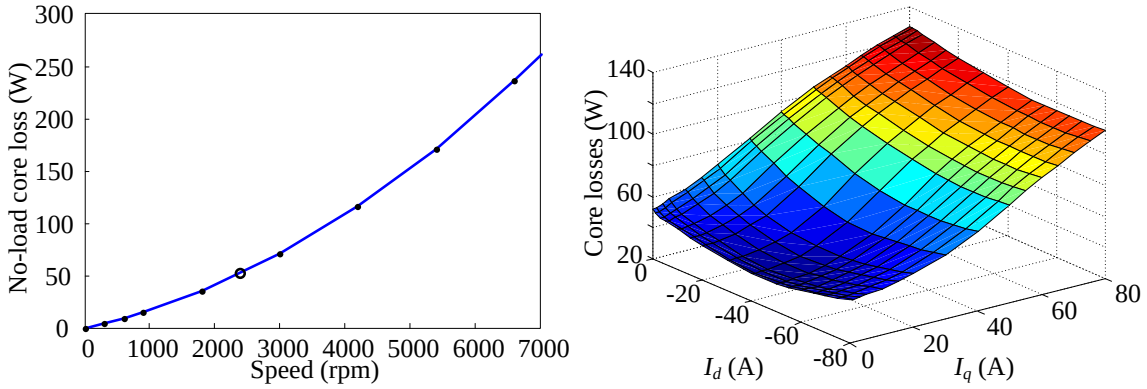

(a) (b)

Fig. 5.13. Core loss model: (a) no-load core loss, (b) core loss map at 2400 rpm.

The mechanical loss is estimated from the experimental no-load losses by deducting the simulated no-load core loss. The estimated mechanical loss is illustrated in Fig. 5.14. With the information of core loss, mechanical loss and copper loss, the efficiency map of the machine is predicted and illustrated in Fig. 5.15. The efficiency map of the machine is verified experimentally in Chapter 6.

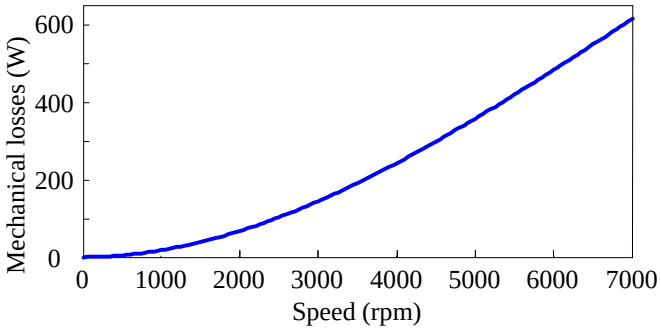

Fig. 5.14. Estimated mechanical loss versus speed.

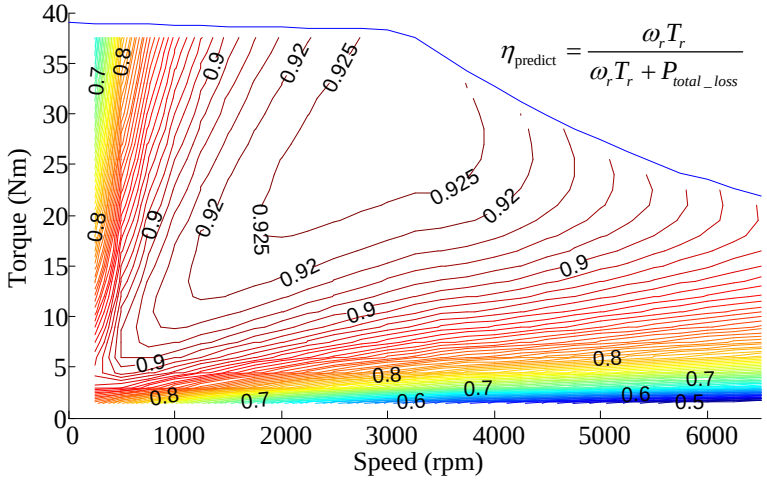

Fig. 5.15. Predicted efficiency map of the FSCW machine.

5.3. CONCLUSIONS

The comprehensive mathematical model of FSCW PM machine is derived. Compared to the idealized PMSM mathematical model, there are coupling terms between the *0*-axis and *d*-, *q*-axis. When the windings are Y connected, the coupling from *0*-axis to *d*- and *q*-axis can be eliminated. Though the coupling from *d*- and *q*-axis to *0*-axis

introduces extra 3rd order *0*-axis voltage, which does not affect the application of FOC control technology.

The optimal control strategies for PMSMs are studied. The loss minimization control and current minimization control (speed range extended MTPA control) are proposed based on the nonlinear optimization algorithm. The loss minimization is applied on the Toyota Prius 2004 motor, and the torque and loss accuracies are verified by FEA simulations. The current minimization is applied on the FSCW IPM machine designed in Chapter 4, and the torque-speed profile and efficiency performances are predicted.

Chapter 6
EXPERIMENTAL VERIFICATION AND THERMAL ANALYSIS

6.1. EXPERIMENTAL SETUP

6.1.1. Machine Prototype

The stator and rotor of the machine are laser cut using M15 29G silicon steel with C5 coating. The stator and rotor laminations are shown in Fig. 6.1 (a) and (b), respectively.

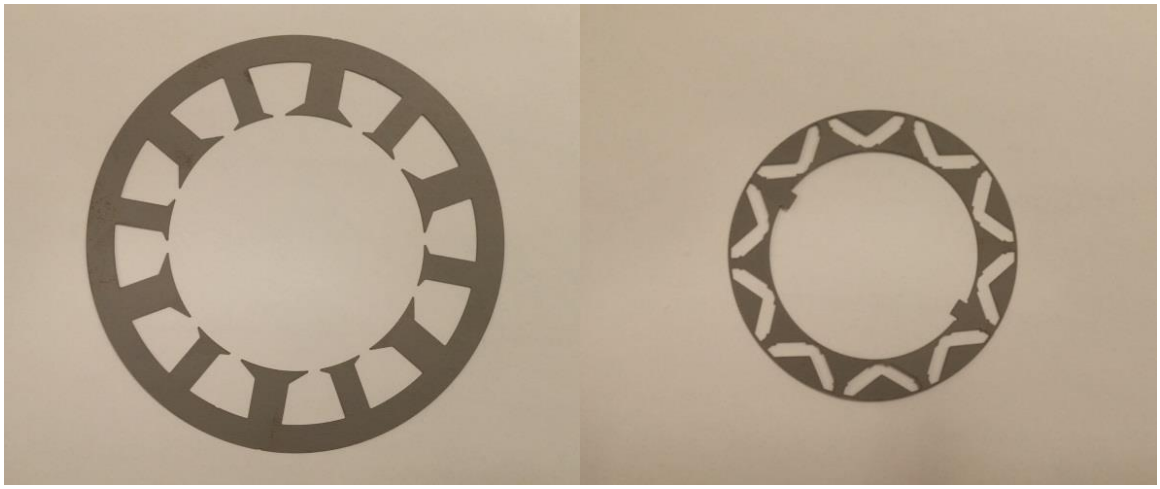

(a) (b)

Fig. 6.1. Laminations of the prototype machine: (a) stator, (b) rotor.

The coils are wound around the thick teeth. The stator stack with coils is shown in Fig. 6.2 (a). The cooling fan is shaft mounted at the end of the machine, as shown in Fig.

6.2 (b). The insulation is H class and the allowable maximum temperature is 180 ℃. The thermal couplers are buried in windings, which measures the winding temperature.

(a) (b)

Fig. 6.2. Machine prototype: (a) stator stack with coils, (b) motor with cooling fan.

6.1.2. Test Bench Setup

The system characterization diagram is demonstrated in Fig 6.3. The machine under testing (PMSM) is coupled with the dynamometer (dyno), and a rotary torque meter (TM) is connected between them. The torque meter is rated at 50 Nm with 0.2% accuracy. A TI 28335 DSC based micro controller is used as the main control unit (MCU). The machine is under current control. The shaft speed is regulated by the dyno.

The major components of the experiment setup are shown in Fig. 6.4. The control & data log computer has access to all the control variables in MCU, including rotor position, *d*- and *q*-axis current and voltage information.

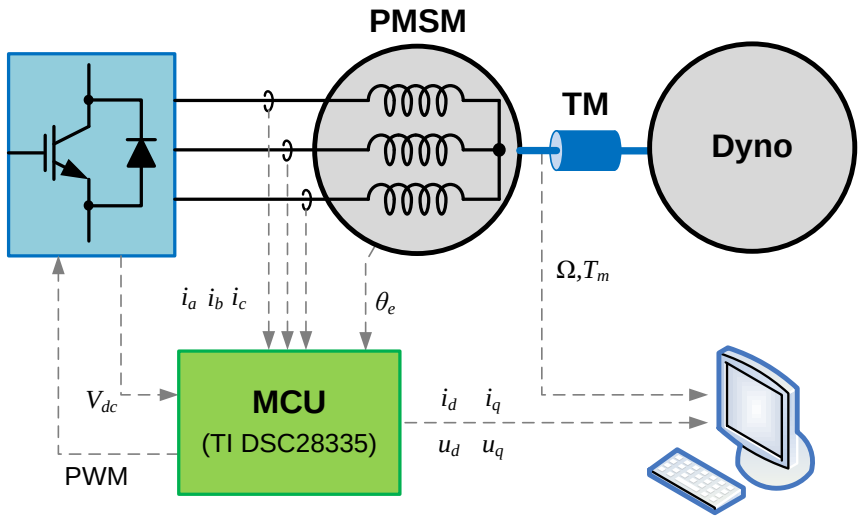

Fig. 6.3. Diagram of the experiment setup.

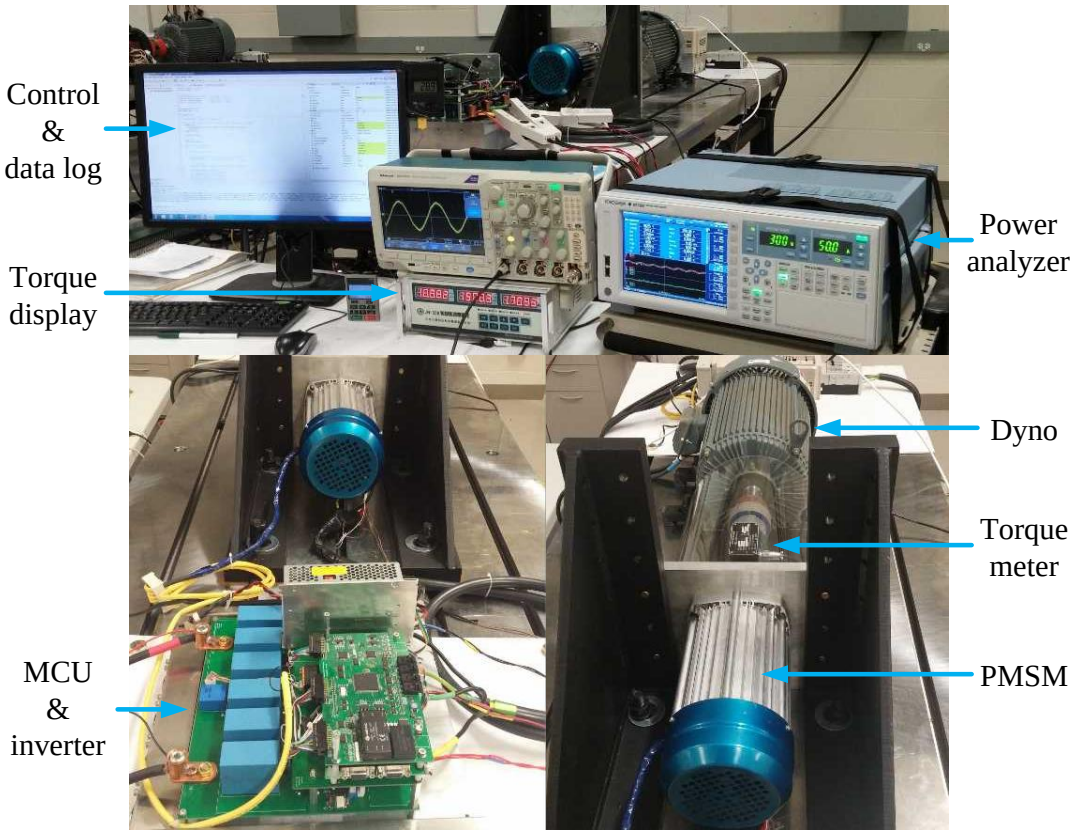

Fig. 6.4. Major components of the experiment setup.

6.2. INVERTER CHARACTERIZATION

6.2.1. DC Current Characterization

Prior to the motor characterization, the inverter nonlinearity has to be characterized and compensated. The DC current injection method is employed as the self-commissioning technique for the inverter nonlinearity characterization [102]. Meanwhile, the overall resistance of the inverter and machine can be identified, which will be used for flux linkage characterization. The nonlinear effects of the inverter can be different at different voltage levels and switching frequencies. Therefore, the self-commissioning needs to be performed at the operating DC link voltage and switching frequency. In this case, the PMSM and the dyno drives share the same DC link, which is rectified from 3-phase 120 VAC input. The measured DC link voltage varies between 290 V and 295 V. The PWM switching frequency is 10 kHz with 800 ns dead time.

As shown in Fig. 6.5, the staircase DC current is imposed into the winding. To avoid uneven current in 3 phases, only β-axis current is applied, such that the current only flows through phase B and C with the same amplitude. The voltage applied to the motor can be calculated using DC link voltage and the PWM information from the control loop.

$$\begin{aligned} u_\alpha &= u_\alpha^r \cdot V_{dc} / \sqrt{3} \\ u_\beta &= u_\beta^r \cdot V_{dc} / \sqrt{3} \end{aligned} \tag{6.1}$$

where, u_α and u_β are the calculated α- and β-axis voltage, u_α^r and u_β^r are per-unit values of α- and β-axis voltage in the control loop. It needs to be noted that, there is no compensation in (6.1), hence u_α and u_β include error voltage.

In order to avoid resistance variation caused by temperature rise, the experiments need to be implemented within a short period of time, such that the motor winding temperature can be maintained within a small range. In this case, the test is carried out when room temperature is 23 ℃ and winding initial temperature is 75 ℃.

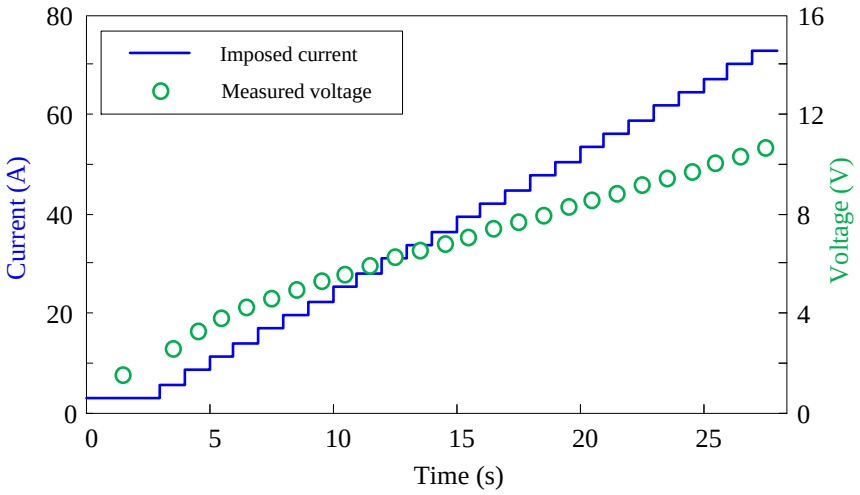

Fig. 6.5. Imposed stair case DC current on *β*-axis and measured *β*-axis voltage.

The estimated *β*-axis voltage versus current is shown in Fig. 6.6. When the current is above 30 A, the voltage and current establish linear relationship, and the overall resistance of inverter and motor can be evaluated by linear curve fitting. The identified resistance is 0.1039 Ω. The residual of the linear curve fitting corresponds to the dead time and the switching device voltage drop. The nonlinear voltage error can be calculated by deducting the resistance voltage drop from the estimated *β*-axis voltage by (6.2).

$$u_{\beta\_error} = u_{\beta} - R_s i_{\beta} \tag{6.2}$$

The characterized error voltage is also illustrated in Fig. 6.6 by solid red curve. It can be found that the voltage error is almost constant above 30 A.

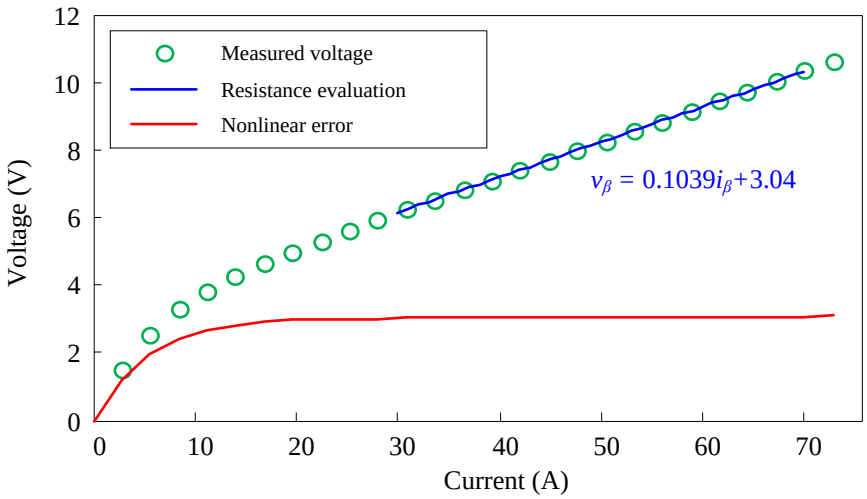

Fig. 6.6. Measured β-axis voltage versus current and the characterized β-axis error voltage.

6.2.2. Inverter Nonlinearity Compensation

So far the inverter nonlinear voltage errors have been characterized. Hence the phase voltage error can be obtained by converting the β-axis error voltage to the stationary frame. Because the α-axis current is zero, α-axis voltage is constantly zero. Therefore, phase error voltage can be calculated by (6.3). The error voltage lookup table is established as shown in Fig. 6.7.

$$u_{ph\_error} = \frac{\sqrt{3}}{2} u_{\beta\_error} \tag{6.3}$$

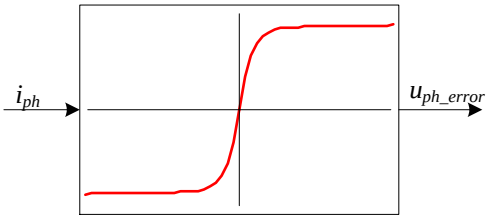

Fig. 6.7. Nonlinear error voltage compensation block.

Fig. 6.8 (a) shows the current waveform when 50% of maximum current is applied. At different excitation levels, the normalized Fourier series of phase current are shown in Fig. 6.8 (b), and the high order harmonic contents are highlighted in zoomed window.

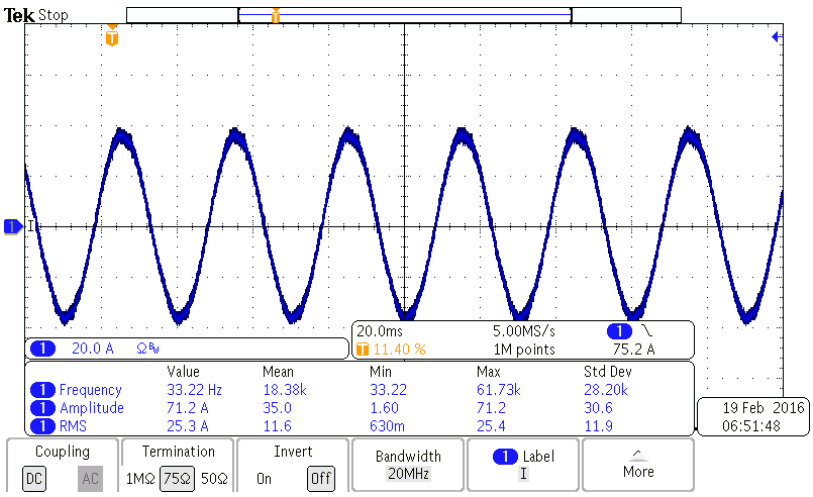

(a)

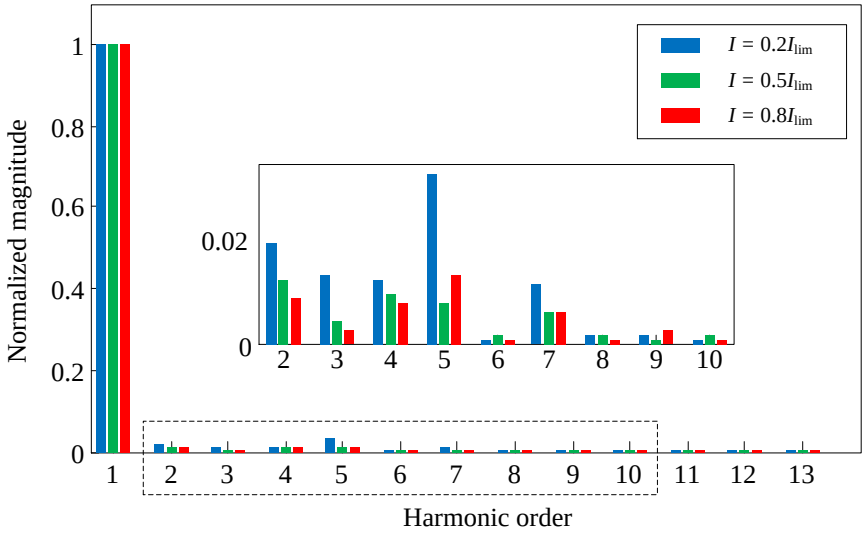

(b)

Fig. 6.8. Phase current with nonlinearity compensation: (a) current waveform of 50% maximum current, (b) Fourier series at different current levels.

Generally, the harmonic contents are below 2% of the fundamental content. The highest harmonic can be 3.3% of the fundamental content when 20% of maximum current is applied. The current waveform and Fourier series both indicate that the current distortion is very low. The motor can be assumed to be driven by pure sinusoidal current. Under steady state, the *d*- and *q*-axis current can be assumed constant.

6.3. MACHINE CHARACTERIZATION

The PMSM characterization process comprises of three steps: back-EMF measurement, no-load torque measurement and flux linkage characterization. Back-EMF measurement can be used to validate the difference between the prototype machine and the simulation model. No-load torque characterization is used to calibrate the mechanical loss, and it will be compensated in the torque control afterwards.

6.3.1. Back-EMF Measurement

The back-EMF waveforms at different speeds are measured and shown in Fig. 6.9. At different speeds, the back-EMF waveforms show very similar trends.

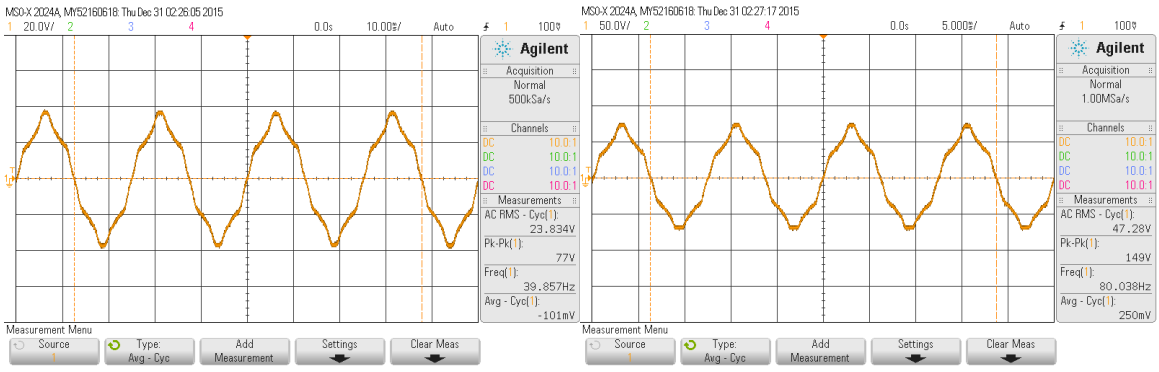

(a) (b)

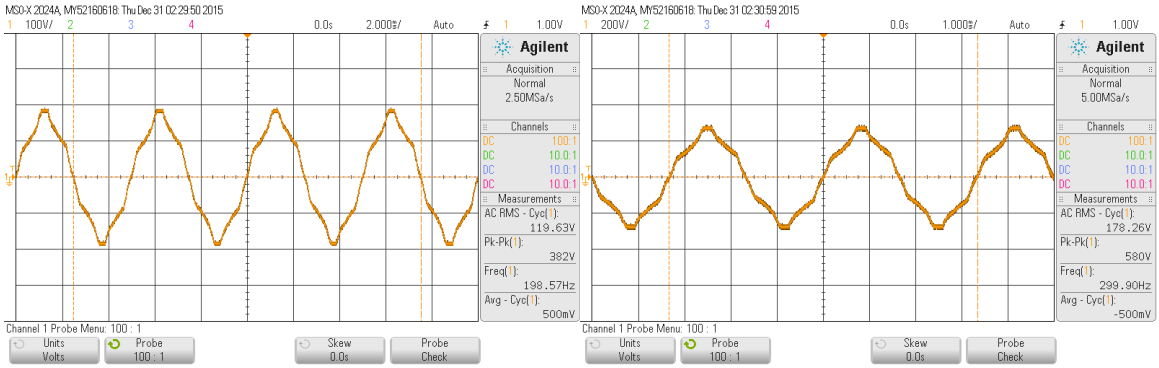

(c) (d)

Fig. 6.9. Measured line to line back-EMF waveforms: (a) 480 rpm, (b) 960 rpm, (c) 2400 rpm, and (d) 3600 rpm.

As shown in Fig. 6.10, it is observed that the back-EMF of the prototype machine almost overlaps with the simulation result. The measured back-EMF is about 2% lower than the simulated result in terms of the RMS value.

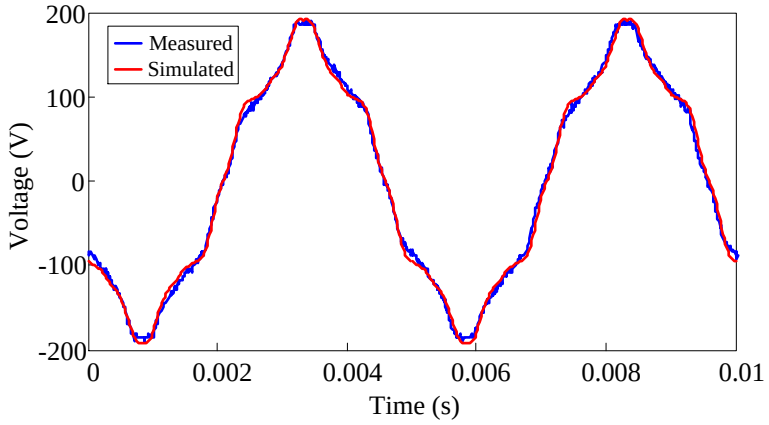

Fig. 6.10. Measured and simulated line to line back-EMF waveforms at 2400 rpm.

However, it is also discovered that 3-phase back-EMFs are not exactly symmetric. As shown in Fig. 6.11. The back-EMF of terminal AB and AC are almost the same;

however, the back-EMF of terminal BC is slightly lower (about 3%), which suggest that phase A induces higher back-EMF than phase B and phase C.

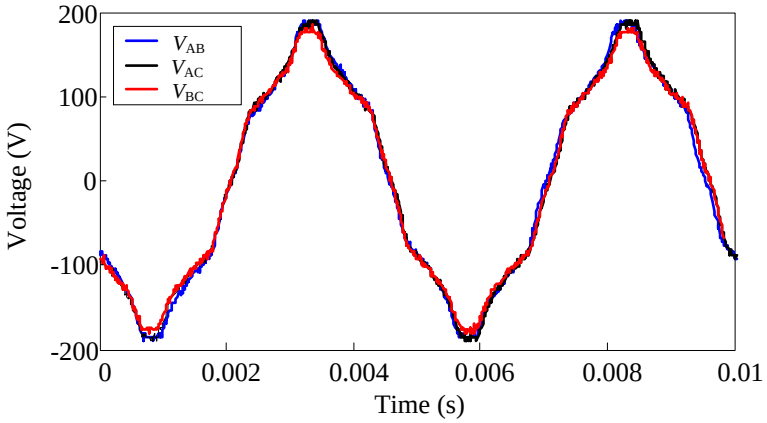

Fig. 6.11. Measured 3-phase back-EMF waveforms at 2400 rpm.

6.3.2. No-Load Loss Measurement

The no-load torque is measured when rotor is able to run freely. The speed is regulated by the dyno from 250 rpm to 6750 rpm upwards and downwards. When speed is stable, the no-load torque is measured at each speed. The measured no-load torque at different speeds is displayed in Fig. 6.12.

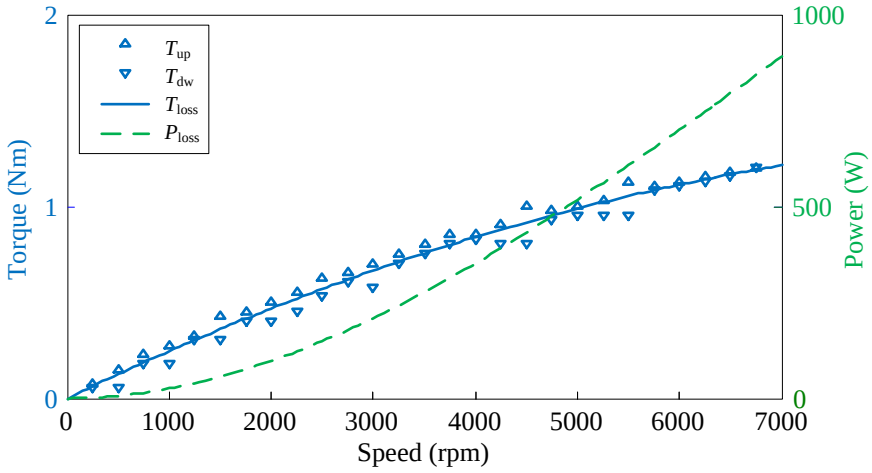

Fig. 6.12. No-load torque and no-load loss.

The no-load torque-speed profile is derived by curve fitting the recorded speed and no-load torque, and the no-load loss can be estimated accordingly. As has been introduced in Chapter 5, the mechanical loss of the machine is estimated by deducting the no-load core loss from the measured no-load loss.

6.3.3. Flux Linkage Characterization

The flux linkage characterization can be done following the steps in [103]. However, the current references are under the rotor frame, and *d*- and *q*-axis currents are commanded instead of current amplitude and angle. The dyno spins the PMSM to the desired speed, which should be high enough to produce measurable back-EMF but below the rated value. In this case, the speed is 2400 rpm, which is 4/5 of the rated speed and the back-EMF is sufficiently higher than resistance voltage drop. *d*- and *q*-axis currents can be applied without approaching the voltage limit in the entire current limit area.

6.3.3.1. Rotor Initial Position Calibration

Prior than the flux linkage characterization, the rotor position has to be calibrated. Normally the initial position of *d*-axis can be determined by injecting DC current into α-axis, and the readout of the rotor position is the initial position. However, if the 3-phase resistances are not symmetric, then current in phase B and C may not be equivalent; hence the synthetic field may not align with α-axis. As a result, a small offset may be introduced in the initial position. On the other hand, if the amplitude of the DC current is not high enough, the cogging torque may pull the rotor and a small offset may be introduced as well.

Another commonly adopted procedure is to compare the back-EMF waveform with the position sensor readout. Ideally, the PM flux linkage, phase back-EMF and line to line back-EMF follow the relationship illustrated in Fig. 6.13. The line-to-line back-EMF leads 30° of phase back-EMF (V_{AB} to V_A), the intersection of V_{AB} and V_{CA} can be used as the 0° reference. The back-EMF method requires the synchronization of rotor position and back-EMF signals, which can be difficult to achieve. The prototype machine features unsymmetrical back-EMF, and is difficult to distinguish the initial position using this method.

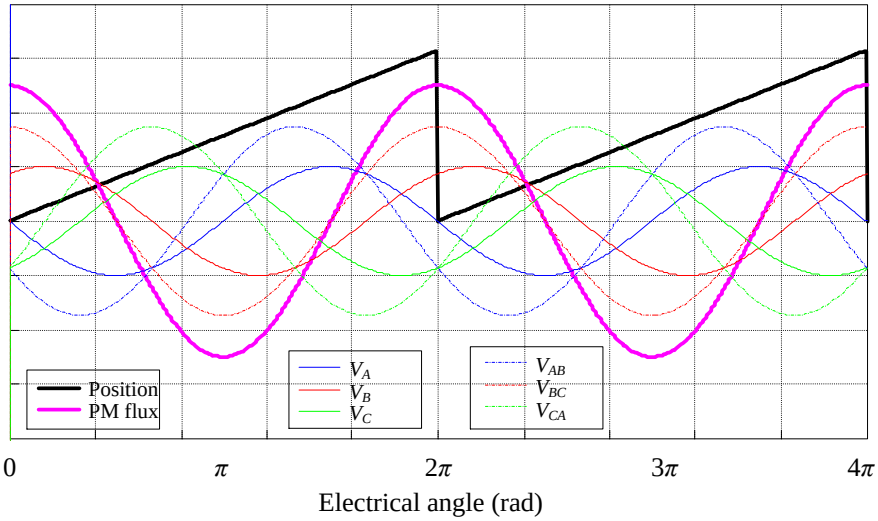

Fig. 6.13. Rotor position with respect to back-EMF waveforms.

A different procedure is introduced here to calibrate the rotor position by injecting DC current into β-axis. In this case, the current only flows through phase B and C, the unsymmetrical resistance does not affect current distribution. When positive current is injected, d-axis is aligned with β-axis. When negative current is injected, d-axis is aligned with the negative direction of β-axis. The initial position can be calculated by the average

value. The rotor initial position is measured at 5 different positions corresponding to 5 pole pairs. Table 6.1 shows the calibrated initial position.

Table 6.1 Measurement of normalized rotor initial position

	Measure 1	Measure 2	Measure 3	Measure 4	Measure 5	Initial position
Positive	0.484982	0.484249	0.483028	0.483761	0.483028	0.73545789
Negative	0.988278	0.986813	0.984615	0.989744	0.986081	

6.3.3.2. *d*- and *q*-axis Voltage Estimation

The characterized inverter with nonlinearity compensation is used to characterize the PM machine. Similar to the inverter nonlinearity characterization, *d*- and *q*-axis voltages are acquired from DC link voltage and PWM information as shown in (6.4).

$$\begin{aligned} u_d' &= u_d^r \cdot V_{dc} / \sqrt{3} \\ u_q' &= u_d^r \cdot V_{dc} / \sqrt{3} \end{aligned} \tag{6.4}$$

where, u_d' and u_q' are the calculated *d*- and *q*-axis voltage, u_d^r and u_q^r are the per-unit value of *d*- and *q*-axis voltage references in the control loop.

However, there exist time delays between the voltage reference in the control loop and the voltage applied to the motor, including computational delay T_c and PWM delay T_{PWM}. The sampling and updating scheme of PWM is shown in Fig. 6.14. At the pinnacle of the triangular waveform $T(k\text{-}0.5)$, the feedback signals are sampled to calculate the PWM reference $u(k)$. It will not be loaded until the beginning of next switching period $T(k)$, thus $T_c = T_s / 2$. The PWM reference updating scheme acts as a zero-order hold, thus $T_{\text{PWM}} \approx T_s / 2$ [104]. As a result, the total time delay T_{delay} is equivalent to the PWM

period. The voltage derived from (6.4) needs to be calibrated by rotating a certain angle using (6.5).

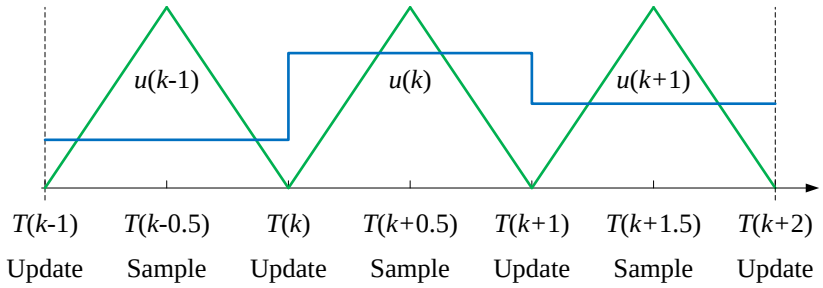

Fig. 6.14. PWM sampling and updating scheme.

$$\begin{pmatrix} u_d \\ u_q \end{pmatrix} = \begin{pmatrix} \cos\theta_{delay} & \sin\theta_{delay} \\ -\sin\theta_{delay} & \cos\theta_{delay} \end{pmatrix} \begin{pmatrix} u'_d \\ u'_q \end{pmatrix} \tag{6.5}$$

where, θ_{delay} is the angle delay corresponding to the time delay between the voltage applied to the motor and voltage reference in the control loop, $\theta_{delay} = 2\pi f T_{delay}$, and f is the synchronous frequency.

6.3.3.3. Flux Linkage Profiles

When machine operates at steady state, the flux linkages can be computed by (6.6), where the *d*- and *q*-axis current references and the overall resistance of the inverter and motor are utilized. The characterized *d*- and *q*-axis flux linkage profiles are shown in Fig. 6.15 (a) and (b), respectively.

$$\begin{aligned} \psi_q &= \frac{R_s i_d - u_d}{\omega_r} \\ \psi_d &= \frac{u_q - R_s i_q}{\omega_r} \end{aligned} \tag{6.6}$$

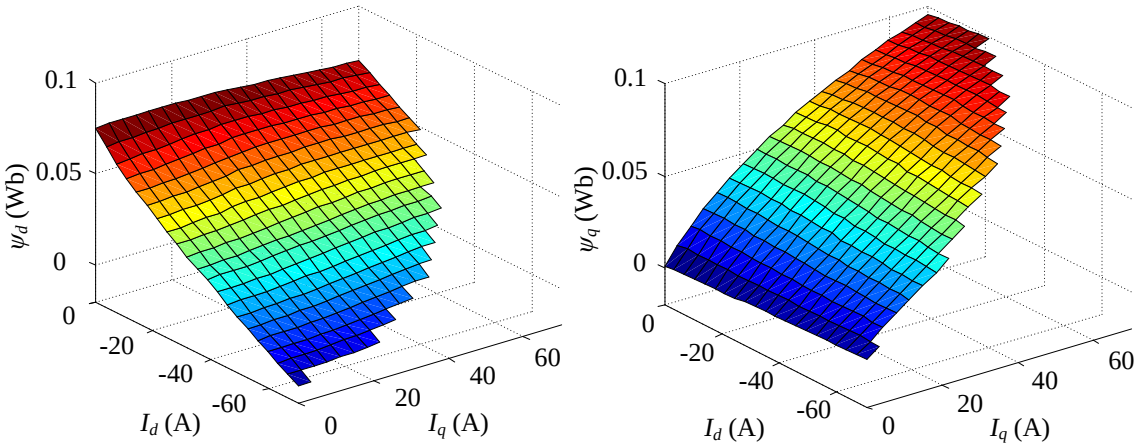

(a) (b)

Fig. 6.15. Characterized flux linkage profiles: (a) *d*-axis flux linkage, (b) *q*-axis flux linkage.

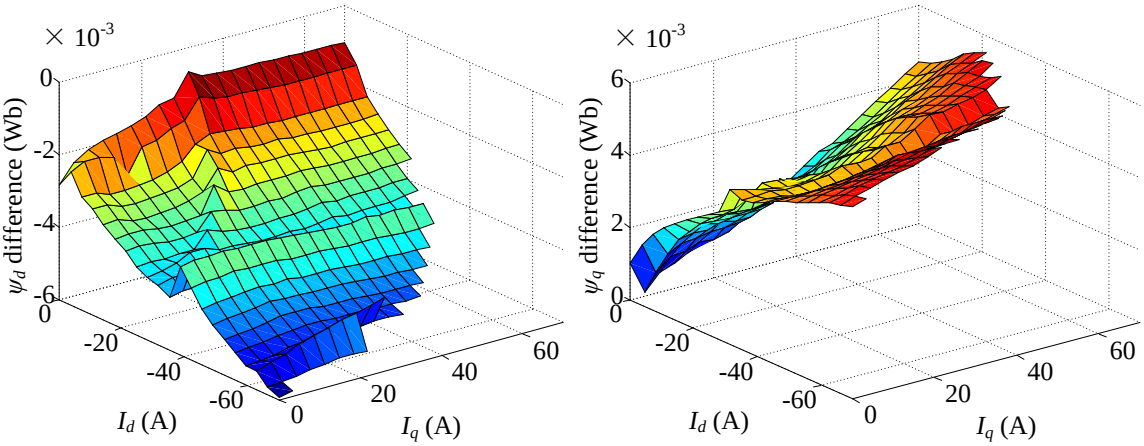

(a) (b)

Fig. 6.16. Flux linkage differences between measured and simulated results:

(a) *d*-axis flux linkage difference, (b) *q*-axis flux linkage difference.

The measured flux linkages are compared with the simulated flux linkage in Fig. 5.11, and the differences are illustrated in Fig. 6.16. The differences between the measured and simulated results can be caused by a few reasons. For example, laser cut changes the magnetic property of the material at the cutting edge [105], and manufacturing tolerance

introduces geometry mismatch between the simulation model and prototype. The rotor initial position error introduces projection errors. However, this does not affect the output torque if torque equation (4.3) is adopted.

The flux linkage profiles are further verified by comparing the torque computed from the flux linkage profiles T_{cal} and the experimental output torque T_{exp}, which is the sum of the mechanical torque output and no-load torque. The relative errors are mapped in Fig. 6.17. The maximum error is about 3%, corresponding to 300 W power losses or 2.5% of the maximum power. It occurs when current approaches the limit. The torque error is mainly caused by ignoring the core loss in PMSM model, and it tends to increase as current increases. The torque error is quite acceptable considering that core loss can be a few percent of the output power.

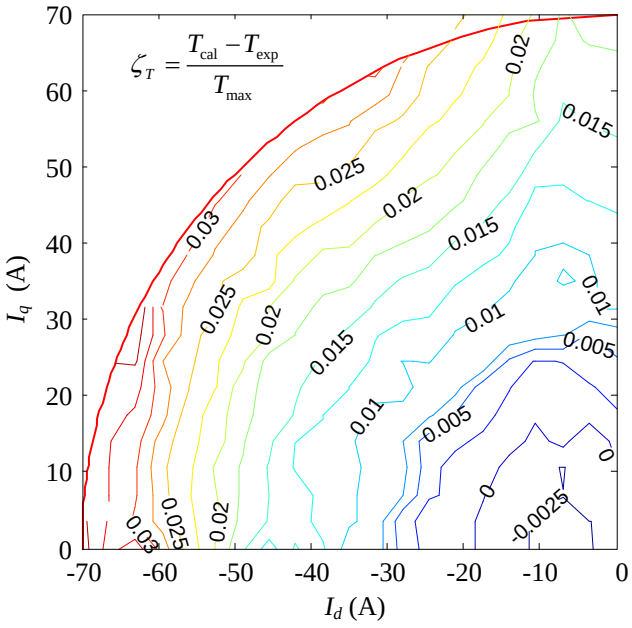

Fig. 6.17. Flux linkage verification by measured torque.

6.4. EXTENDED MAXIMUM TORQUE PER AMPERE CONTROL

6.4.1. Extended MTPA Current Profiles

The extended MTPA current profiles are computed according to the measured flux linkage profiles, as shown in Fig. 6.18 (a) and (b), respectively. The no-load torque has been considered and compensated in the MTPA current profiles. The contour of the *d*- and *q*-axis current is reported in Fig. 6.19.

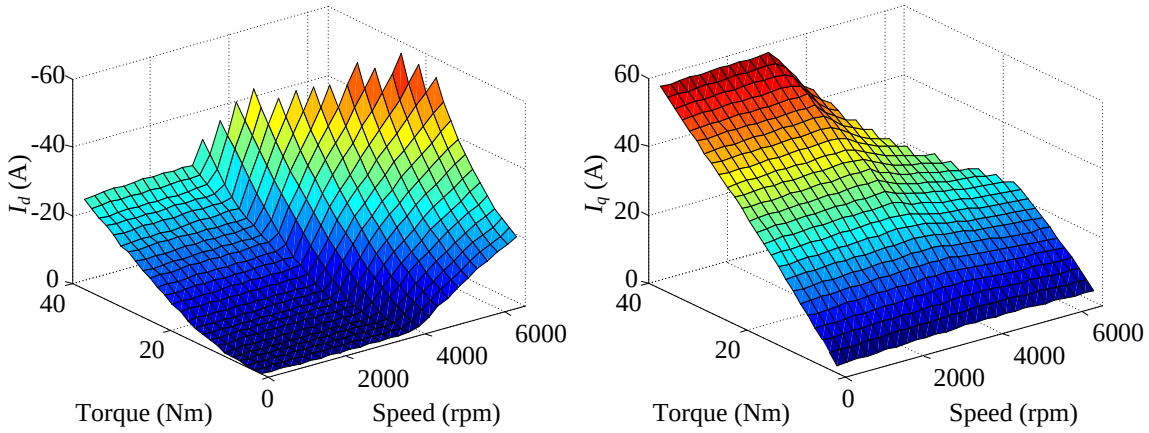

(a) (b)

Fig. 6.18. Extended MTPA current profiles: (a) *d*-axis current (b) *q*-axis current.

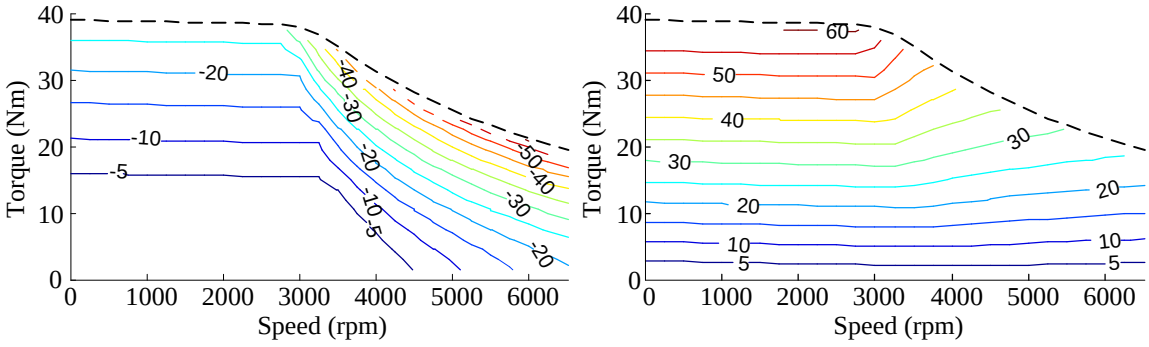

(a) (b)

Fig. 6.19. Extended MTPA current profile contours (unit: A): (a) *d*-axis current, (b) *q*-axis current.

In the constant torque range, it is observed that, for the same torque requirement, the *d*- and *q*-axis currents remain unchanged under different speed, which is the same as traditional MTPA strategy. As the speed goes up, the *d*-axis current increases to maintain the voltage limit, while the *q*-axis current decreases to achieve the desired torque.

The extended MTPA current profiles are verified analytically on the *d*- and *q*-axis current plane in Fig. 6.20. The flux linkage contour, MTPA trajectory (light blue curve), constant speed trajectories of 3250 rpm, 4250 rpm and 5750 rpm (dark blue curves) and constant torque trajectories of 6 Nm, 19.5 Nm and 31.5 Nm (grey curves) are illustrated.

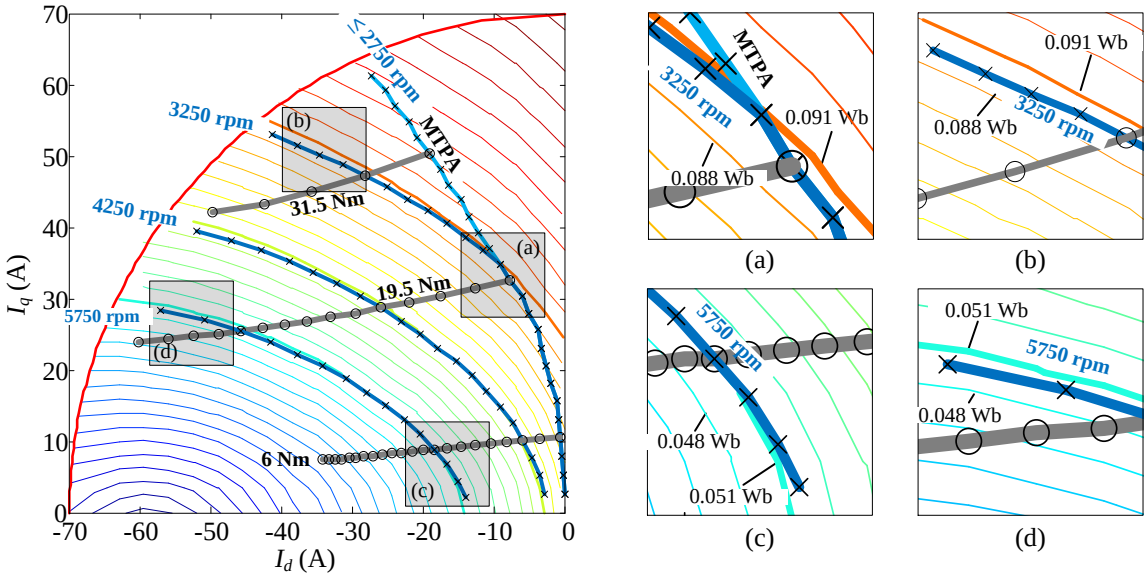

Fig. 6.20. Optimized current points distribution on d- and q-axis current plane: (a) current trajectory deviates from MTPA trajectory, (b) current trajectory goes away from flux linkage curve of 0.091 Wb, (c) current trajectory goes towards flux linkage curve of 0.051 Wb, and (d) current trajectory goes away from flux linkage curve of 0.051 Wb.

At each speed, the optimized *d*- and *q*-axis current references are marked as (×) for different torque requirements. At each torque, the optimized current are marked as (○) for

different speed requirements. When the speed is below 2750 rpm, the optimized current overlaps the MTPA trajectory. As speed increases to 3250 rpm, the current trajectory starts to deviate from the MTPA trajectory at about 21 Nm, where the voltage limit is approached. The details are highlighted in Fig 6.20 (a). After that, the current trajectory tends to overlap with the highlighted orange constant flux linkage curve of 0.091 Wb. As speed goes up to 4250 rpm and/or 5750 rpm, the back-EMF is higher than the voltage limit, and the current trajectories are completely off the MTPA trajectory. They also tend to overlap with the highlighted constant flux curves. Due to the resistance voltage drop, the current trajectories along the constant flux curves move towards the direction which reduces the flux linkage. This property can be observed in Fig. 6.20 (b), (c) and (d).

6.4.2. Torque Feedforward Control

The extended MTPA current profiles are applied to the PM machine in the torque feedforward control loop. The steady state and transition control performance are investigated. The experiments are carried out between 250 rpm and 6500 rpm with speed step of 250 rpm and torque step of 1.5 Nm. The torque control accuracy is verified by comparing the difference between the desired torque and output torque. The relative torque errors are shown in Fig. 6.21. The output torque error is less than 3% in the entire operation range. In constant torque range and the majority of the field weakening range, 2% torque control accuracy can be achieved. In the deep field weakening range, the error can be up to 2.75% at maximum output power. The torque error tends to increase as the speed and torque increase, which is mainly caused by increased core loss.

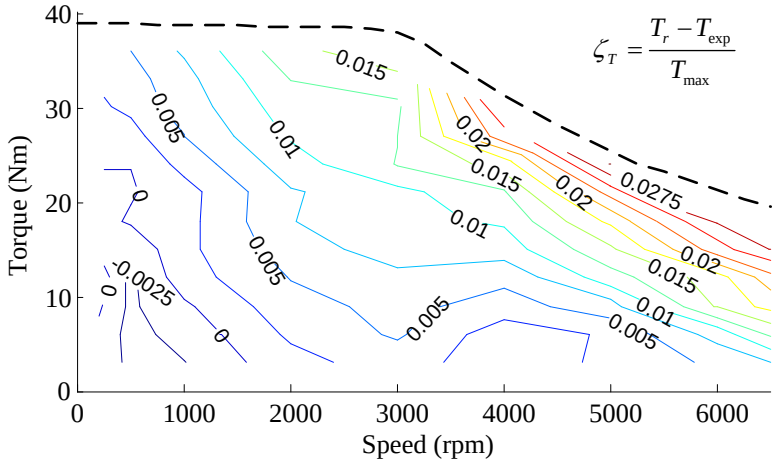

Fig. 6.21. Torque control accuracy.

The motor efficiency in the entire torque-speed range is measured and Fig. 6.22 shows the area with efficiency above 50%. The peak efficiency of the motor can be as high as 92.5% when the speed and torque are close to the knee point. The 90% efficiency contour covers very wide area. Recalling the predicted motor efficiency map of Fig. 5.15, the difference between the measured efficiency and the calculated efficiency is calculated and reported in Fig. 6.23. It is observed that when torque is above 6 Nm, the efficiency difference in the entire torque-speed range is within 0.5%.

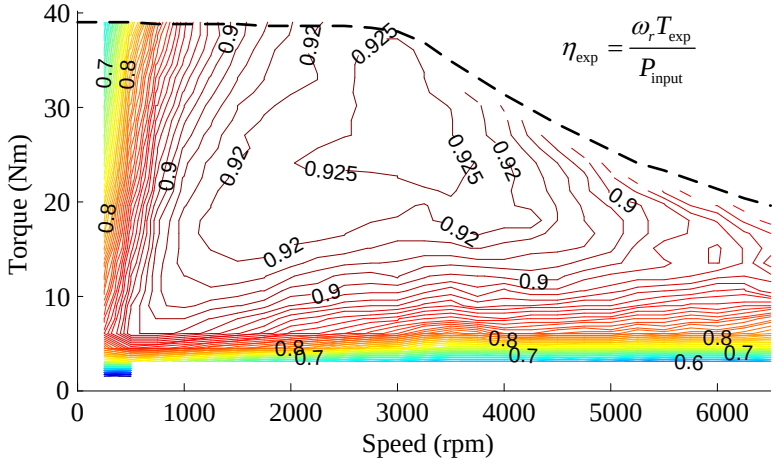

Fig. 6.22. Measured efficiency map under extended MTPA control.

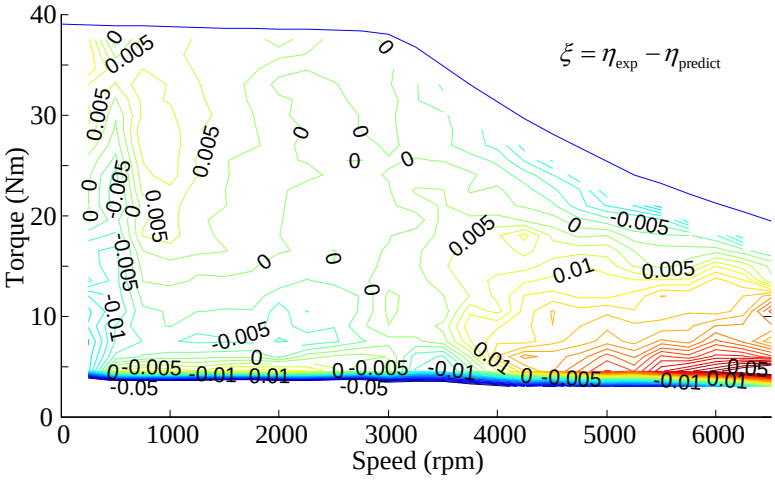

Fig. 6.23. Efficiency difference between measured and predicted results.

The transient performance is measured at 2400 rpm, 3250 rpm, 4250 rpm, and 5750 rpm. Torque commands are given at 1.5 Nm, 13.5 Nm, 25.5 Nm and 37.5 Nm at each speed. During the transition from one torque reference to the next, the torque reference ramps up and down between steady states and the transition takes about 100 ms. The current waveforms are measured and displayed in Fig. 6.24.

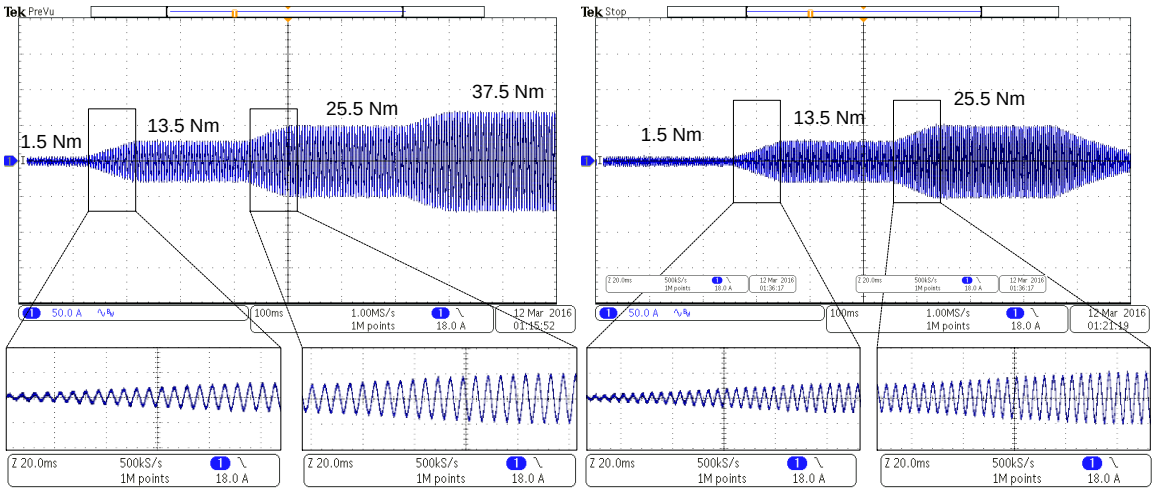

(a) (b)

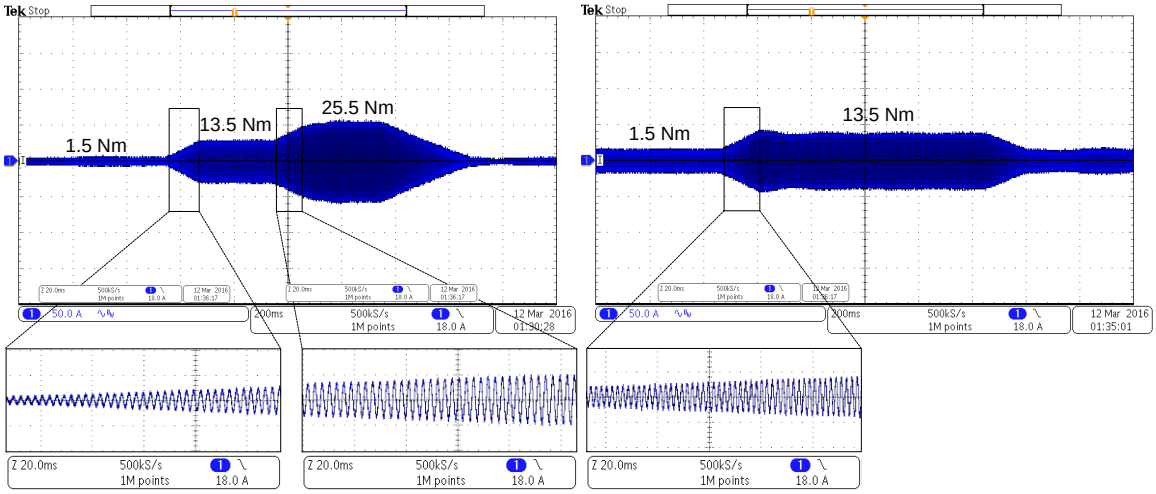

(c) (d)

Fig. 6.24. Current waveforms with torque feedforward control:

(a) 2400 rpm (MTPA), (b) 3250 rpm (partly MTPA trajectory and partly field weakening),

(c) 4250 rpm (field weakening), and (d) 5750 rpm (deep field weakening).

The current waveforms during transition are highlighted in zoomed windows. The current transition is very smooth without overshoot. For same desired torque at different speed, the current may be different, because field weakening current can be different. For example, the current amplitude at 1.5 Nm, 5750 rpm is significantly higher than those at other speeds.

6.5. THERMAL PERFORMANCE

6.5.1. Thermal Model

An FEA based thermal model is developed for this machine and the quarter 3D model is shown in Fig. 6.25. The stator, rotor, coil, and shaft are included in this model.

The thermal properties of the materials normally can be found from the datasheet, and the mechanical and thermal properties of the materials are summarized in Table 6.2.

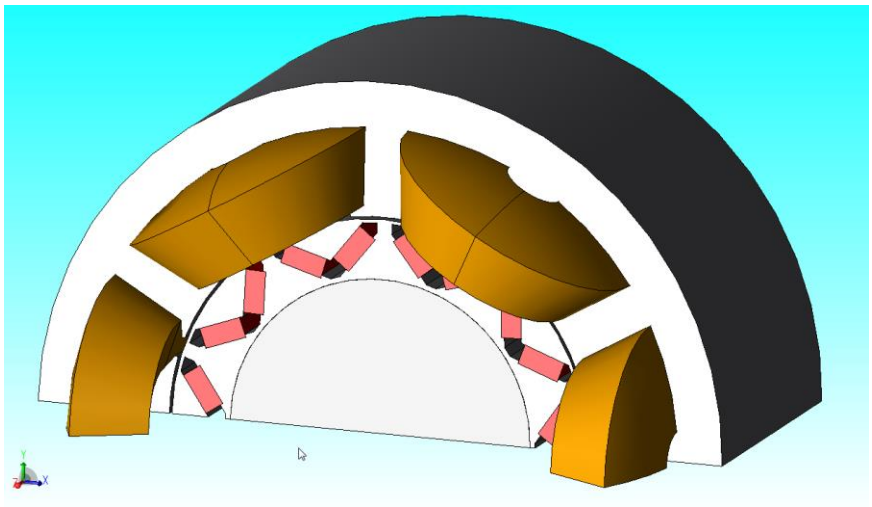

Fig. 6.25. 3D model for thermal simulation.

Table 6.2 Material mechanical properties

Part	Material	Density	Thermal Property
Stator core	M15 29G silicon steel	7650 kg/m^3	Thermal conductivity: 23 W/m/K Specific heat: 460 J/kg/K
Rotor core			
PM	N38SH	7500 kg/m^3	Thermal conductivity: 8.955 W/m/K Specific heat: 502 J/kg/K
Coil	Stranded wires	4000 kg/m^3	Thermal conductivity: 380 W/m/K Specific heat: 380 J/kg/K

Shaft	4140 steel	7850 kg/m^3	Thermal conductivity: 42 W/m/K Specific heat: 460 J/kg/K
Cover	Aluminum alloy	2700 kg/m^3	Thermal conductivity: 167 W/m/K Specific heat: 896 J/kg/K

The thermal property of the coils, however, needs to be averaged over the slots. When the space between wires is filled with impregnation resin, as shown in Fig. 6.26, the average thermal conductivity can be approximated by (6.7).

$$\lambda_{av} = \lambda_i \left(\frac{d}{\delta_i} + \frac{\delta_i}{d'} \right) \tag{6.7}$$

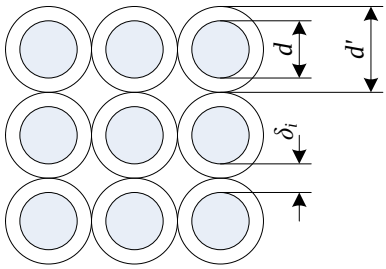

Fig. 6.26. Impregnated stranded round wire winding.

The thermal network of the machine is described in Fig. 6.27. The thermal resistance between the components can be modeled by contact thermal resistance, and the configurations of them are listed in Table 6.3 [106]. The cover, airgap and the air inside the cover are not physically modeled. The thermal transfer between the modeled components and the un-modeled components (air and air gap) are modeled by heat

transfer boundary, and the configurations of heat transfer boundary are also listed in Table 6.3.

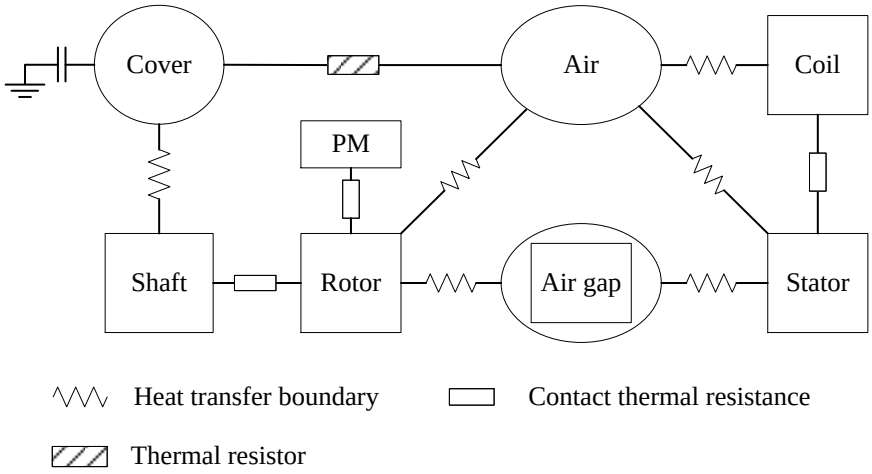

Fig. 6.27. Equivalent heat transfer network.

In the thermal network demonstrated in Fig. 6.27, the cover of the machine is not physically modeled in the FEA model. Instead, it is simplified as a heat transfer coefficient, which can be computed by (6.8).

$$q_h = h_c \cdot A_c \tag{6.8}$$

where, A_c is the heat transfer area, h_c is the convective heat transfer coefficient of air.

To simplify the analysis, it is assumed that the cooling air flowing through the surface of the machine is evenly distributed and there is no turbulence. The heat transfer coefficient can be approximated by $h_c = 3.89\sqrt{v_{\text{air}} / l_h}$, where, l_h is the length of the housing and v_{air} is the speed of cooling air. The heat capacitor of the cover can be computed by (6.9).

$$C = C_p \rho_c V_c \tag{6.9}$$

where, V_c is the volume of the cover, C_p and ρ_c are the specific heat and density of the cover material, which is listed in Table 6.2.

Table 6.3 Contact thermal resistance and heat transfer boundary configurations

Parameter		Derivation method	Associated variables
Contact thermal resistance	The contact faces between coil and stator core	Nomex 410: 0.12 W/m/K	Thickness: 0.3 mm
	The contact faces between magnets and core	JB weld glue: 0.59 W/m/K	Thickness: 0.05 mm
	The contact faces between rotor and shaft	Air: 0.027 W/m/K	Thickness: 0.04 mm
Heat transfer boundary between components and air	The contact faces between rotor and air	10 W/m^2/K	
	The contact faces between stator and air		
	The contact faces between coils and air		
Heat transfer boundary between components and air gap	The contact faces between stator and gap	$h = \frac{6.6}{10^5} \frac{v_r^{0.67}}{lg^{0.33}} \times 10^4$	lg = 0.05 cm $v_r = \frac{\pi \cdot ID_{rotor} \cdot \Omega}{60}$
	The contact faces between rotor and gap		
Heat transfer boundary between stator and housing	The contact faces between rotor and gap	$h = \frac{\lambda}{d}$	λ = 0.027 W/m/K d = 0.03×10^{-3} m
Heat transfer boundary between shaft and housing	The contact faces between rotor and shaft		Λ = 0.027 W/m/K d = 0.004 m

6.5.2. Steady State Thermal Performance

The temperature rise of the winding is measured by the thermal coupler buried in the winding at three operating points, 1200 rpm, 3000 rpm, and 4800 rpm. The operating point at 1200 rpm is in constant torque range; the operating point at 3000 rpm corresponds to the knee point and the operating point at 4500 rpm is in the field weakening range. At each operating point, the temperature is measured every 5 min until it approaches steady state. Here, steady state means that the temperature variation during one hour is less than 2 ℃. The measured winding temperatures are reported in Table 6.4.

Table 6.4 Measured and simulated winding temperature

	18 Nm, 1200 rpm	15 Nm, 3000 rpm	9 Nm, 4800 rpm
Experiment	79.5 ℃	89.6 ℃	95.8 ℃
Simulation	79.9 ℃	89.9 ℃	96.4 ℃

Due to the difficulties of estimating the average air speed, the heat transfer coefficient in the thermal model is calibrated by the experimental results. The steady state temperature distributions at three different speeds are simulated using the calibrated model, and they are depicted in Fig. 6.28. The average winding temperature is also reported in Table 6.4.

Because this machine is totally enclosed, and almost all the heat generated by the rotor is dissipated through the airgap and stator, the rotor appears to be much hotter than stator. The temperature difference between rotor and stator increases as the speed increases due to the increased rotor losses. The rotor components, including the rotor core, PM, and shaft, exhibit evenly distributed temperature.

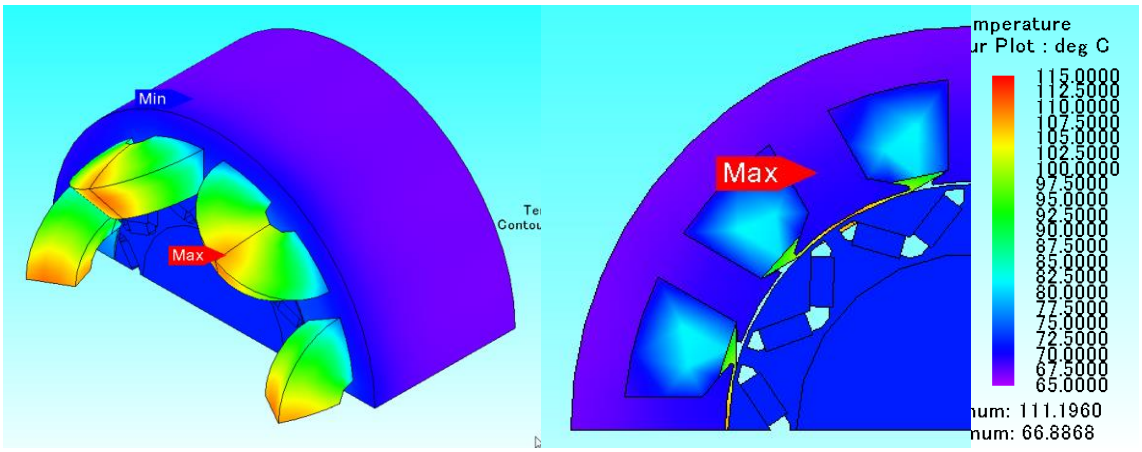

(a)

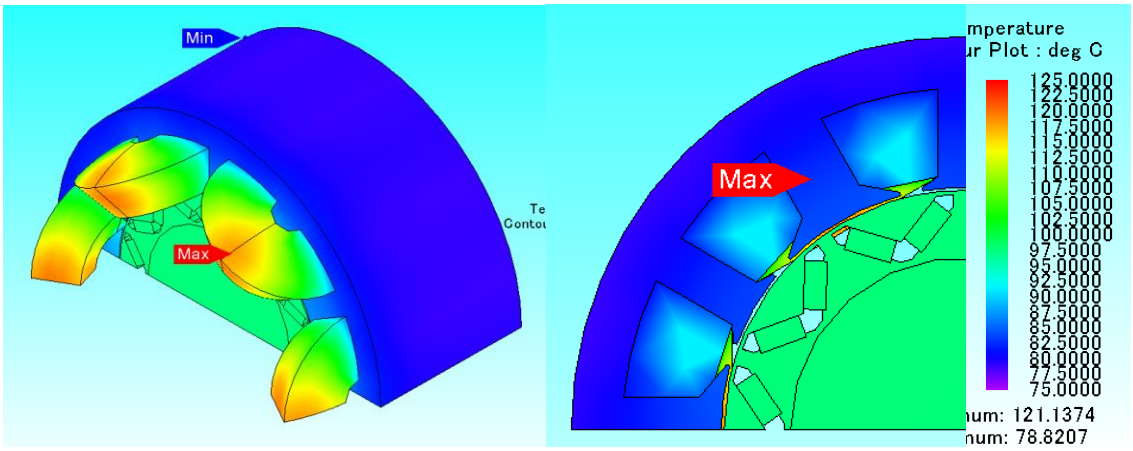

(b)

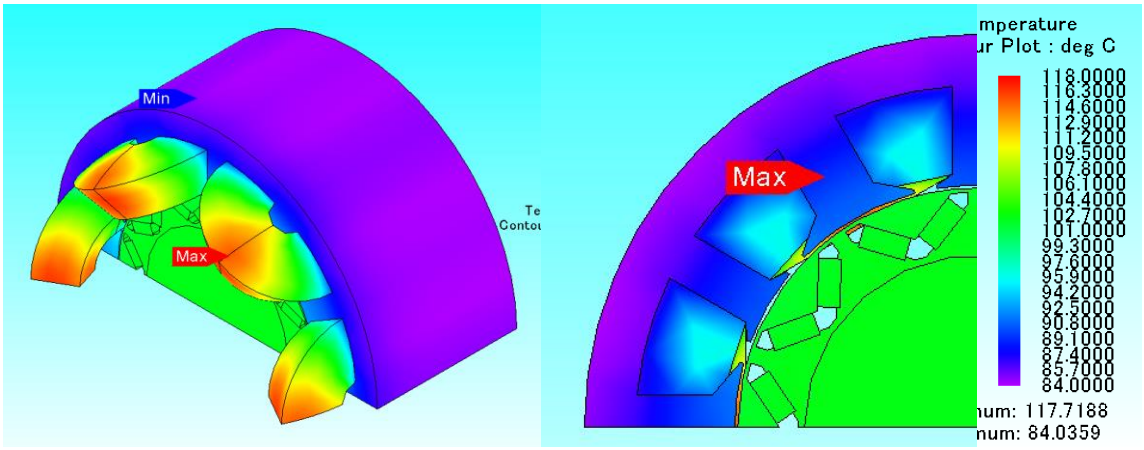

(c)

Fig. 6.28. Simulated steady state temperature distributions: (a) 18 Nm, 1200 rpm, (b) 15 Nm, 3000 rpm, and (c) 9 Nm, 4800 rpm.

The hot spot occurs on the end winding. When the machine is operated with continuous power rating, the maximum temperature of the winding is 125 ℃ and occurs at 3000 rpm.

6.5.3. Transient Thermal Performance

The transient thermal performance is simulated using the calibrated thermal model. The simulations are operated at 1200 rpm, 3000 rpm and 4800 rpm with full power load. In order to better simulate the real application, the initial temperatures are configured as the steady state temperatures of the machine under continuous power rating.

When the motor is fully loaded, the simulated winding temperature rises are illustrated in Fig. 6.29. At 1200 rpm, the winding temperature hits 100 ℃ in about 100 s. At 3000 rpm and 4800 rpm, due to the much higher initial temperature and higher losses, the winding temperature exceeds 100 ℃ in less than 30 s.

The winding temperature is measured experimentally under these 3 situations. When the motor is operated at 1200 rpm, the temperature is recorded every 10 s, and illustrated in Fig. 6.29 (a). The measured and simulated winding temperatures are very close and the error is within 2 ℃. At 3000 rpm and 4800 rpm, only the final temperature is measured and shown in Fig. 6.29 (b) and (c). The temperature difference is about 2 ℃ at 3000 rpm, and 5 ℃ at 4800 rpm. The simulated temperature rises match the measured results in 3 different cases.

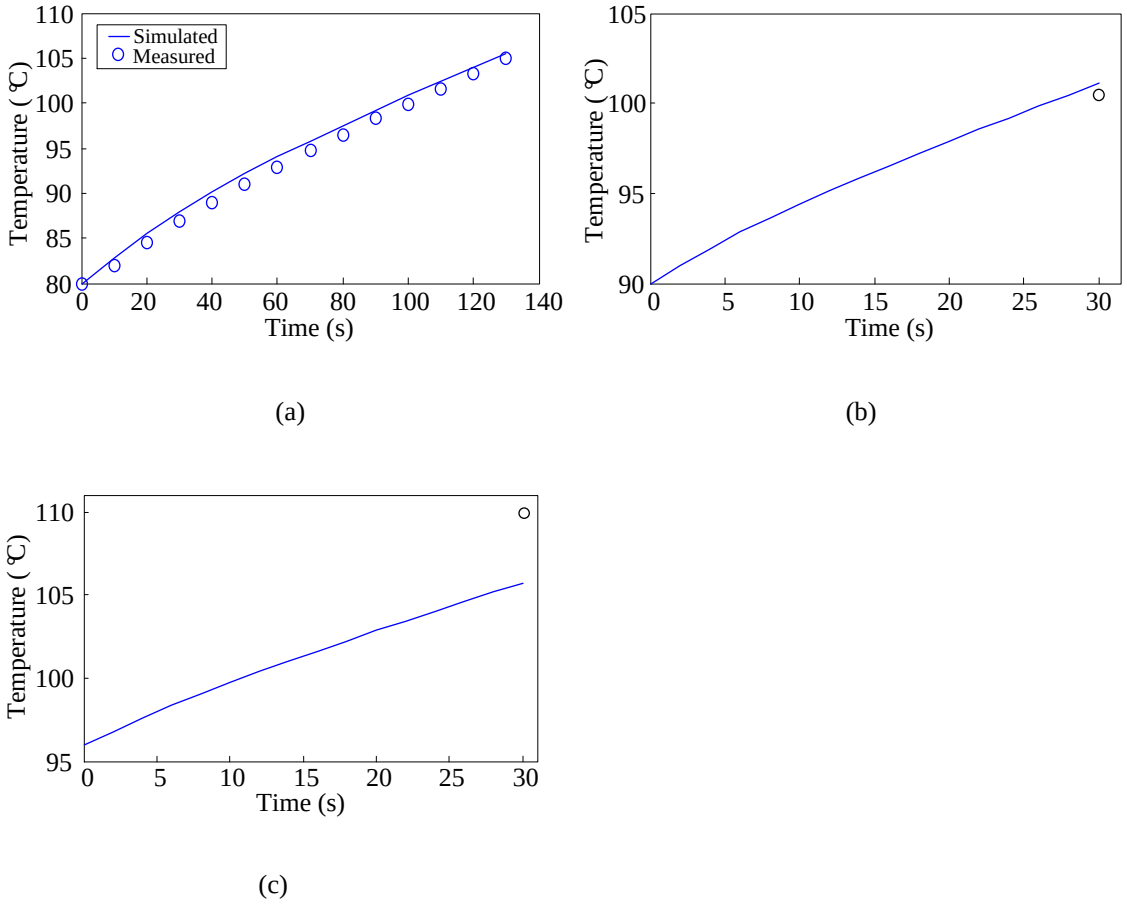

Fig. 6.29. Transient winding temperature rise: (a) 36 Nm, 1200 rpm, (b) 36 Nm, 3000 rpm, and (c) 24 Nm, 4800 rpm.

The agreement between simulation and experimental results suggests that the simulations can be used to estimate the temperature distribution in the prototype Fig. 6.30 shows the temperature distribution from last step of the simulations. Compared to the temperature distribution in Fig. 6.28, the rotor temperature does not change much. However, the winding temperature increases significantly.

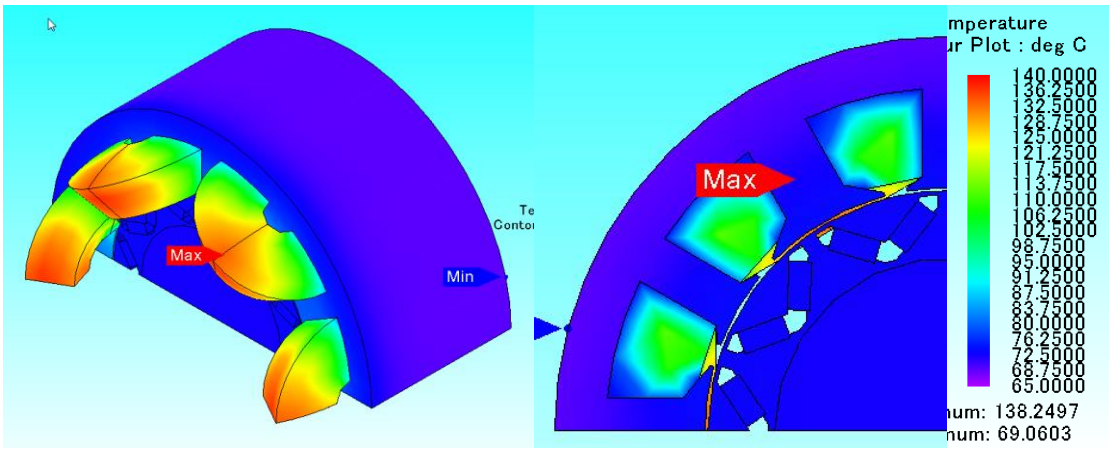

(a)

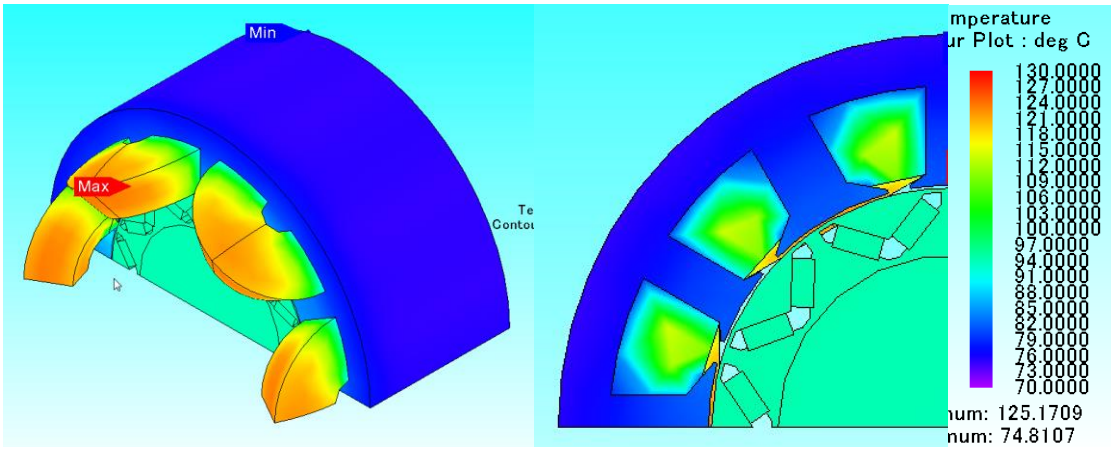

(b)

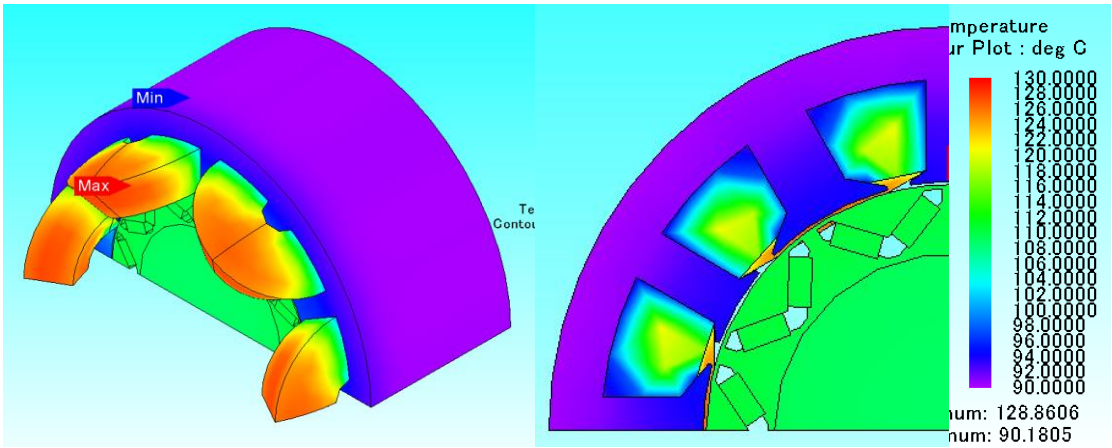

(c)

Fig. 6.30. Simulated final step temperature distributions of transient operation:

(a) 36 Nm, 1200 rpm, (b) 36 Nm, 3000 rpm, and (c) 24 Nm, 4800 rpm.

The rotor temperature is much higher than the stator, which suggests that the rotor of the FSCW machine may need special care of thermal management. In this case, the temperature of the magnets is below 120 ℃, which is within the temperature limit of the PM material (150 ℃).

6.6. CONCLUSIONS

The FSCW IPM machine prototyping and testing are discussed in this chapter. The method of the inverter and machine characterizations are introduced. The inverter nonlinearity is compensated and the machine parameters and flux linkage profiles are obtained experimentally.

The MTPA current profiles are derived using the characterized machine parameters, and they are applied on the torque feedforward control loop. Very high torque control accuracy and very smooth transient performance are achieved. The measured efficiency matches the predicted efficiency very well.

The thermal performance is validated by experiments and simulations. The FEA based thermal model is developed and the calibrated using the steady state experimental results. The transient temperature rises are simulated using the calibrated model, which demonstrate very good agreement with the experimental results.

Chapter 7
SUMMARY

7.1. CONCLUSIONS

This thesis presents the comprehensive inductance analysis for FSCW machines, and a SL FSCW IPM machine is designed, prototyped and tested.

In Chapter 2, state of art of the concentrated winding PM machines is reviewed. The FSCW PM synchronous machine is reviewed, and the advantages and disadvantages, topologies and related problems are discussed.

In Chapter 3, the comprehensive inductance analysis is conducted. The modified winding function based inductance calculation method is proposed. The turns function, which can be chosen flexibly, can be used directly for inductance analysis, and it greatly simplifies the inductance analysis. Based on the modified winding function method, the air gap inductance and mutual inductance of the FSCW are acquired. The inductance properties of the FSCW machine equipped with salient rotors are analyzed by introducing the equivalent air gap. The *d*- and *q*-axis inductance difference of the FSCW machines with salient rotors are derived and compared with traditional ISDW machines, and the closed form of the inductance difference ratio is obtained.

In Chapter 4, the design methodology of FSCW IPM machine is presented. The relationship between the machine parameters and torque-speed characteristic is derived, which can be used to guide machine topology selection. Thin rotor yoke bridge design is proposed to enhance the reluctance torque and reduce the core losses. The machine geometry is optimized to minimize the torque ripples using modified RSM method, which reduces the computational effort significantly. The designed SL FSCW IPM machine shows its advantages over traditional designs in terms of torque capability and/or losses.

In Chapter 5, the control strategy is discussed. The comprehensive mathematical model of the FSCW PM machines is derived based on the inductance analysis. Compared to the idealized PMSM machine model, there exist extra coupling terms. It is proven that the traditional FOC technology can be applied when windings are Y connected. The optimal current control strategies for PMSMs are developed based on the nonlinear optimization algorithm. The global loss minimization is developed and verified on the traditional ISDW IPM machine, and the current minimization is developed and applied on the FSCW IPM machine.

In Chapter 6, the FSCW machine is prototyped and tested. The voltage and current data in the control loop are utilized to characterize the machine, which greatly simplify the requirement for measuring equipment. The extended MTPA current profiles are obtained and applied on the torque feedforward control loop. The thermal model is developed and calibrated using the experimental steady state winding temperature. The transient thermal performance is also simulated and verified by experiments.

7.2. FURTHER WORK SUGGESTED

Research topics which can be further investigated in future research are as follows:

1. Multi-layer flux barriers have been applied on the ISDW SynRMs and PM-assisted SynRMs to achieve high saliency ratio. When FSCWs are employed, the discretized coils change the flux line distribution in the rotor. How to design the rotor with multi-layer flux barrier to improve the reluctance torque capability can be further studied.

2. The FSCW machine with SPP = 1/2 shows its advantage over other teeth/pole combinations in terms of saturation, but it features high torque ripple and cogging torque. The machine geometry needs to be modified to improve the torque ripple and cogging torque. This study can be combined with the multi-layer flux barrier rotor design.

3. In order to further improve the power density and torque density, better cooling technology can be applied. However, the FSCW machines exhibit high rotor losses, and the rotor may be over heated. More attention needs to be paid on active rotor cooling.

4. Machine parameters changes as temperature increases, and the machine performance will deteriorate. The parameters variation due to temperature change should be investigated and the optimal control strategy needs to be adjusted accordingly.

REFERENCES

[1] A. Emadi (Editor), *Advanced Electric Drive Vehicles*, Boca Raton, FL: CRC Press, ISBN: 978-1-4665-9769-3, Oct. 2014.

[2] Z.-Q. Zhu, "Fractional slot permanent magnet brushless machines and drives for electric and hybrid propulsion systems," *COMPEL - Int. J. Comput. Math. Electr. Electron. Eng.*, vol. 30, no. 1, pp. 9–31, Jan. 2011.

[3] Study of a Permanent Magnet Motor with MAXWELL 2D : Example of the 2004 Prius IPM Motor. Appl. Note.

[4] R. Fessler and I. BIZTEK Consulting, "Final Report on Assessment of Motor Technology for Traction Drives of Hybrid and Electric Vehicles," Oak Ridge National Laboratory, Washington, D.C., 2011.

[5] F. Magnussen and C. Sadarangani, "Winding factors and Joule losses of permanent magnet machines with concentrated windings," in *Proc. IEEE-IEMDC*, Madison, WI, Jun. 2003, vol. 1, pp. 333–339.

[6] J. Cros and P.Viarouge, "Synthesis of high performance PM motors with concentrated windings," *IEEE Trans. Energy Convers.*, vol. 17, no. 2, pp. 248–253, Jun. 2002.

[7] P. B. Reddy, A. M. El-Refaie, K.-K. Huh, J. K. Tangudu, and T. M. Jahns, "Comparison of interior and surface PM machines equipped with fractional-slot concentrated windings for hybrid traction applications," *IEEE Trans. Energy Convers.*, vol. 27, no. 3, pp. 593–602, Sep. 2012.

[8] R. Deodhar, S. Anderson, I. Boldea, and T. J. E. Miller, "The flux- reversal machine: a new brushless doubly-salient permanent magnet machine*," IEEE Trans. Ind. Appl.*, vol. 33, no. 4, pp. 925–934, 1997.

[9] T. H. Kim, "A study on the design of an inset-permanent-magnet-type flux-reversal machine," *IEEE Trans. Magn.*, vol. 45, no. 6, pp. 2859–2862, 2009.

[10][1] K. Nakamura, K. Murota, and O. Ichinokura, "Characteristics of a novel switched reluctance motor having permanent magnets between the stator pole-tips," in *2007 European Conference on Power Electronics and Applications*, 2007, pp. 1–5.

[11] Z. Q. Zhu, "Switched flux permanent magnet machines — Innovation continues," in *2011 International Conference on Electrical Machines and Systems*, 2011, pp. 1–10.

[12] A. Fasolo, L. Alberti, and N. Bianchi, "Performance comparison between switching-flux and IPM machine with rare earth and ferrite PMs," in *2012 XXth International Conference on Electrical Machines*, 2012, pp. 731–737.

[13] D. More, H. Kalluru, and B. G. Fernandes, "Comparative analysis of Flux Reversal machine and Fractional slot concentrated winding PMSM," in *2008 34th Annual Conference of IEEE Industrial Electronics*, 2008, pp. 1131–1136.

[14] Robert Bosch GmbH. (2008). *Gasoline Systems IMG – Integrated Motor Generator*. Available: http://products.bosch-mobility-solutions.com/specials/de/elektrifizierung/pdf/Bosch_E-Maschine_integrated_Motor.pdf

[15] Andrei Tutu (2013, Aug. 04). *Bosch Parallel Full Hybrid System Explained* [Online] Available: http://www.autoevolution.com/news/bosch-parallel-full-hybrid-system-explained-23159.html

[16] J. J. Germishuizen and M. J. Kamper, "IPM traction machine with single layer non-overlapping concentrated windings," *IEEE Trans. Ind. Appl.*, vol. 45, no. 4, pp. 1387–1394, 2009.

[17] L. Alberti, E. Fornasiero, and N. Bianchi, "Impact of the rotor yoke geometry on rotor losses in permanent-magnet machines," *IEEE Trans. Ind. Appl.*, vol. 48, no. 1, pp. 98–105, 2012.

[18] J. Wang, Z. P. Xia, and D. Howe, "Analysis of three-phase surface-mounted magnet modular permanent magnet machines," in *Proc. 2nd IEE Int. Conf. PEMD*, Mar./Apr. 2004, vol. 3, pp. 27–32.

[19] N. Bianchi and M. Dai Pre, "Use of the star of slots in designing fractional-slot single-layer synchronous motors," *Proc. Inst. Elect. Eng.-Electr. Power Appl.*, vol. 153, no. 3, pp. 997–1006, May 2006.

[20] N. Bianchi, S. Bolognani, and G. Grezzani, "Design considerations for fractional-slot winding configurations of synchronous machines," IEEE Trans. Ind. Appl., vol. 42, no. 4, pp. 997–1006, Jul./Aug. 2006.

[21] R. Krall, J. Krenn, and A. Schmid, "Comparison of leakage inductance between fractional slot winding and distributed winding," in *2014 16th International Power Electronics and Motion Control Conference and Exposition*, 2014, pp. 276–282.

[22] Z. Zhu and D. Howe, "Winding inductances of brushless machines with surface-mounted magnets," in *1997 IEEE International Electric Machines and Drives Conference Record*, 1997, pp. WB2/2.1–WB2/2.3.

[23] P. Ponomarev, P. Lindh, and J. Pyrhonen, "Effect of slot-and-pole combination on the leakage inductance and the performance of tooth-coil permanent-magnet synchronous machines," *IEEE Trans. Ind. Electron.*, vol. 60, no. 10, pp. 4310–4317, 2013.

[24] P. Ponomarev, Y. Alexandrova, I. Petrov, P. Lindh, E. Lomonova, and J. Pyrhonen, "Inductance calculation of tooth-coil permanent-magnet synchronous machines," *IEEE Trans. Ind. Electron.*, vol. 61, no. 11, pp. 5966–5973, Nov. 2014.

[25] A. M. El-Refaie, Z. Q. Zhu, T. M. Jahns, and D. Howe, "Winding inductances of fractional slot surface-mounted permanent magnet brushless machines," in *Conference Record - IAS Annual Meeting (IEEE Industry Applications Society)*, 2008, pp. 1–8.

[26] R. Dutta, M. F. Rahman, and L. Chong, "Winding inductances of an interior permanent magnet (IPM) machine with fractional slot concentrated winding," *IEEE Trans. Magn.*, vol. 48, no. 12, pp. 4842–4849, Dec. 2012.

[27] Q. Li, T. Fan, and X. Wen, "Armature-reaction magnetic field analysis for interior permanent magnet motor based on winding function theory," *IEEE Trans. Magn.*, vol. 49, no. 3, pp. 1193–1201, Mar. 2013.

[28] H. Chen, D. Li, R. Qu, Z. Zhu, and J. Li, "An improved analytical model for inductance calculation of interior permanent magnet machines," *IEEE Trans. Magn.*, vol. 9464, no. 6, pp. 1–8, June, 2014.

[29] Z. Q. Zhu, “Fractional slot permanent magnet brushless machines and drives for electric and hybrid propulsion systems,” *COMPEL - Int. J. Comput. Math. Electr. Electron. Eng.*, vol. 30, no. 1, pp. 9–31, Jan. 2011.

[30] Z. Q. Zhu and D. Howe, “Influence of design parameters on cogging torque in permanent magnet machines,” *IEEE Trans. Energy Convers.*, vol. 15, no. 4, pp. 407–412, 2000.

[31] W. Soong and T. J. E.Miller, “Field weakening performance of brushless synchronous AC motor drives,” *Proc. Inst. Elect. Eng.-Electr. Power Appl.*, vol. 141, no. 6, pp. 331–340, Nov. 1994.

[32] R. F. Schiferl and T.A. Lipo, “Power capability of salient pole permanent magnet synchronous motor in variable speed drive applications,” *IEEE Trans. Ind. Appl.*, vol. 26, no. 1, pp. 115–123, Jan./Feb. 1990.

[33] A. M. EL-Refaie and T. M. Jahns, “Optimal flux weakening in surface PM machines using concentrated windings,” *IEEE Trans. Ind. Appl.*, vol. 41, no. 3, pp. 790–800, May/Jun. 2005.

[34] A. M. EL-Refaie, T. M. Jahns, P. J. McCleer, and J. W. McKeever, “Experimental verification of optimal flux weakening in surface PM machines using concentrated windings,” *IEEE Trans. Ind. Appl.*, vol. 42, no. 2, pp. 443–453, Mar./Apr. 2006.

[35] Z. Zhu, D. Howe, and J. Mitchell, “Magnetic field analysis and inductances of brushless DC machines with surface-mounted magnets and non-overlapping stator windings,” *IEEE Trans. Magn.*, vol. 31, no. 3, pp. 2115–2118, May 1995.

[36] L. Chong and M. F. Rahman, “Saliency ratio optimization in an IPM machine with fractional-slot concentrated windings,” in *2008 International Conference on Electrical Machines and Systems*, 2008, pp. 2921–2926.

[37] L. Chong and M. F. Rahman, “Saliency ratio derivation and optimisation for an interior permanent magnet machine with concentrated windings using finite-element analysis,” *IET Electr. Power Appl.*, vol. 4, no. 4, pp. 249-258, 2010.

[38] M. Barcaro and N. Bianchi, “Torque components in integral- and fractional-slot IPM machines,” in *2011 IEEE International Electric Machines & Drives Conference (IEMDC)*, 2011, pp. 1340–1345.

[39] X. Chen, J. Wang, P. Lazari, and L. Chen, “Permanent magnet assisted synchronous reluctance machine with fractional-slot winding configurations,” *Proc. 2013 IEEE Int. Electr. Mach. Drives Conf. IEMDC 2013*, no. 266084, pp. 374–381, 2013.

[40] C. M. Spargo, B. C. Mecrow, J. D. Widmer, and C. Morton, “Application of fractional-slot concentrated windings to synchronous reluctance motors,” *IEEE Trans. Ind. Appl.*, vol. 51, no. 2, pp. 1446–1455, Mar. 2015.

[41] C. M. Spargo, B. C. Mecrow, J. D. Widmer, C. Morton, and N. J. Baker, “Design and validation of a synchronous reluctance motor with single tooth windings,” *IEEE Trans. Energy Convers.*, vol. 30, no. 2, pp. 795–805, Jun. 2015.

[42] N. Bianchi, S. Bolognani, and G. Grezzani, “Fractional-slot IPM servo- motors: Analysis and performance comparisons,” in *Proc. ICEM, 2004*, pp. 1–6.

[43] H. Murakami, H. Kataoka, Y. Honda, S. Morimoto, and Y. Takeda, “Highly efficient brushless motor design for an air-conditioner of the next generation 42 V vehicle,” in *Conf. Rec. IEEE IAS Annu. Meeting*, Oct. 2001, vol. 1, pp. 461–466.

[44] Z. Azar, L. J. Wu, D. Evans, and Z. Q. Zhu, “Influence of rotor configuration on iron and magnet losses of fractional-slot IPM machines,” in *5th IET International Conference on Power Electronics, Machines and Drives (PEMD 2010)*, 2010, pp. WE312–WE312.

[45] Z. P. Xia, Z. Q. Zhu, L. J. Wu, and G. W. Jewell, “Comparison of radial vibration forces in 10-pole/12-slot fractional slot surface-mounted and interior PM brushless AC machines,” in *The XIX International Conference on Electrical Machines - ICEM 2010*, 2010, pp. 1–6.

[46] Y. Asano, Y. Honda, H. Murakami, Y. Takeda, and S. Morimoto, “Novel noise improvement technique for a PMSM with concentrated winding,” in *Proc. PCC*, Osaka, Japan, Apr. 2002, vol. 2, pp. 460–465.

[47] P. B. Reddy, K. K. Huh, and A. M. El-Refaie, “Generalized approach of stator shifting in interior permanent-magnet machines equipped with fractional-slot concentrated windings,” *IEEE Trans. Ind. Electron.*, vol. 61, no. 9, pp. 5035–5046, 2014.

[48] J. Wang, V. I. Patel, and W. Wang, “Fractional-slot permanent magnet brushless machines with low space harmonic contents,” *IEEE Trans. Magn.*, vol. 50, no. 1, 2014.

[49] K. Wang, Z. Q. Zhu, and G. Ombach, “Synthesis of high performance fractional-slot permanent-magnet machines with coil-pitch of two slot-pitches,” *IEEE Trans. Energy Convers.*, vol. 29, no. 3, pp. 758–770, Sep. 2014.

[50] M. Gamba, G. Pellegrino, and A. Vagati, “A new PM-assisted synchronous reluctance machine with a nonconventional fractional slot per pole combination,” in *2014 International Conference on Optimization of Electrical and Electronic Equipment (OPTIM)*, 2014, pp. 268–275.

[51] L. Alberti and N. Bianchi, “Theory and design of fractional-slot multilayer windings,” *IEEE Trans. Ind. Appl.*, vol. 49, no. 2, pp. 841–849, Mar. 2013.

[52] P. B. Reddy, A. M. EL-Refaie, and K.-K. Huh, “Effect of number of layers on performance of fractional-slot concentrated-windings interior permanent magnet machines,” *IEEE Trans. Power Electron.*, vol. 30, no. 4, pp. 2205–2218, Apr. 2015.

[53] Y. Wang, R. Qu, and J. Li, “Multilayer windings effect on interior PM machines for EV applications,” *IEEE Trans. Ind. Appl.*, vol. 51, no. 3, pp. 2208–2215, May 2015.

[54]B. Prieto, M. Martinez-Iturralde, L. Fontan, and I. Elosegui, “Analytical calculation of the slot leakage inductance in fractional-slot concentrated-winding machines,” *IEEE Trans. Ind. Electron.*, vol. 62, no. 5, pp. 2742–2752, May 2015.

[55] Available: http://www.ycmpp.com/products_detail/&productId=cfb40914-1dca-4c1a-bc05-178cfcc11cea.html

[56] Available: http://www.thebackshed.com/Windmill/FPRewire.asp

[57] J. Hallberg, “Conceptual evaluation and design of a direct-driven mixer.” Master thesis, Department of Mechanical Engineering, Linkopings University, Linkoping, Sweden, 2005.

[58] Available: http://www.uratani-eng.com/english/service/renovation9.html

[59] T. A. Burress, S. L. Campbell, C. L. Coomer, C. W. Ayers, A. A. Wereszczak, J. P. Cunningham, L. D. Marlino, L. E. Seiber, and H. T. Lin, "Evaluation of the 2010 Toyota Prius hybrid synergy drive system," Oak Ridge National Laboratory, 2011.

[60] L. P. Zepp and J. James R. Hendershot, "Electrical machine construction using axially inserted teeth in a stator ring or armature," US 7042130 B2, 2006.

[61] H. Akita, Y. Nakahara, N. Miyake, and T. Oikawa, "New core structure and manufacturing method for high efficiency of permanent magnet motors," in *38th IAS Annual Meeting on Conference Record of the Industry Applications Conference*, 2003, vol. 1, pp. 367–372.

[62] R. H. Staunton, T. A. Burress, and L. D. Marlino, "Evaluation of 2005 Honda Accord hybrid electric drive system," Oak Ridge National Laboratory, 2006.

[63] T. Burress, "Benchmarking of competitive technologies," Oak Ridge National Laboratory, 2012.

[64] P. C. Krause, O. Wasynczuk, and S. D. Sudhoff, *Analysis of Electric Machinery and Drive Systems*. John Wiley & Sons, 2013.

[65] D. A. Staton, W. L. Soong, and T. J. E. Miller, "Unified theory of torque production in switched reluctance and synchronous reluctance motors," *IEEE Trans. Ind. Appl.*, vol. 31, no. 2, pp. 329–337, 1995.

[66] T. M. Jahns, G. B. Kliman, and T. W. Neumann, "Interior permanent-magnet synchronous motors for adjustable-speed drives," *IEEE Trans. Ind. Appl.*, vol. IA-22, no. 4, pp. 738–747, Jul. 1986.

[67] T. A. Lipo, *Analysis of Synchronous Machines,* 2nd ed. CRC Press, 2012.

[68] G. J. Li, J. Ojeda, E. Hoang, M. Lecrivain, and M. Gabsi, "Comparative studies between classical and mutually coupled switched reluctance motors using thermal-electromagnetic analysis for driving cycles," *IEEE Trans. Magn.*, vol. 47, no. 4, pp. 839–847, Apr. 2011.

[69] B. Gaussens, E. Hoang, O. De La Barrière, J. Saint-Michel, M. Lecrivain, and M. Gabsi, "Analytical approach for air-gap modeling of field-excited flux-switching machine: No-load operation," *IEEE Trans. Magn.*, vol. 48, no. 9, pp. 2505–2517, 2012.

[70] J. Pyrhönen, T. Jokinen, and V. Hrabovcová, *Design of Rotating Electrical Machines*. Hoboken, NJ, USA:Wiley, 2008.

[71] C. Tong, F. Wu, P. Zheng, B. Yu, Y. Sui, and L. Cheng, "Investigation of magnetically isolated multiphase modular permanent-magnet synchronous machinery series for wheel-driving electric vehicles," *IEEE Trans. Magn.*, vol. 50, no. 11, pp. 1–4, Nov 2014.

[72] J. K. Tangudu, T. M. Jahns, and A. EL-Refaie, "Unsaturated and saturated saliency trends in fractional-slot concentrated-winding interior permanent magnet machines," in *2010 IEEE Energy Conversion Congress and Exposition*, 2010, pp. 1082–1089.

[73] S. Morimoto, Y. Takeda, T. Hirasa, and K. Taniguchi, "Expansion of operating limits for permanent magnet motor by current vector control considering inverter capacity," *IEEE Trans. Ind. Appl.*, vol. 26, no. 5, pp. 866–871, 1990.

[74] W. L. Soong, “Field-weakening performance of brushless synchronous AC motor drives,” *IEE Proc. - Electr. Power Appl.*, vol. 141, no. 6, pp. 331–340, 1994.

[75] A. Adnanes and T. Undeland, “Optimum torque performance in PMSM drives above rated speed,” in *Conference Record of the 1991 IEEE Industry Applications Society Annual Meeting*, 1991, pp. 169–175.

[76] W. Soong, “Design and modelling of axially-laminated interior permanent magnet motor drives for field-weakening applications,” Ph.D. Dissertation, University of Glasgow, 1993.

[77] B. C. Mecrow, E. A. El-Kharashi, J. W. Finch, and A. G. Jack, “Segmental rotor switched reluctance motors with single-tooth windings,” *IEE Proc. - Electr. Power Appl.*, vol. 150, no. 5, pp. 591-599, Sep 2003.

[78] J. Park, S. Kim, J. P. Hong, and J. H. Lee, “Rotor design on torque ripple reduction for a synchronous reluctance motor with concentrated winding using response surface methodology,” *IEEE Trans. Magn.*, vol. 42, no. 10, pp. 3479–3481, Oct. 2006.

[79] D. C. Montgomery, *Design and analysis of experiments*, 8th ed. United States: Wiley, John & Sons, 2012.

[80] Seok-Hee Han, T. Jahns, and Z. Zhu, “Analysis of rotor core eddy-current losses in interior permanent-magnet synchronous machines,” *IEEE Trans. Ind. Appl.*, vol. 46, no. 1, pp. 196–205, 2010.

[81] S. H. Han, W. L. Soong, T. M. Jahns, M. K. Güven, and M. S. Illindala, “Reducing harmonic eddy-current losses in the stator teeth of interior permanent magnet

synchronous machines during flux weakening," *IEEE Trans. Energy Convers.*, vol. 25, no. 2, pp. 441–449, 2010.

[82] P. Pillay and R. Krishnan, "Modeling, simulation, and analysis of permanent-magnet motor drives. I. The permanent-magnet synchronous motor drive," *IEEE Trans. Ind. Appl.*, vol. 25, no. 2, pp. 265–273, 1989.

[83] N. Q. Dai, R. Dutta, and M. F. Rahman, "Comparative performance analysis of field-oriented control and direct torque control for a fractional-slot concentrated winding interior permanent magnet synchronous machine," *2012 XXth Int. Conf. Electr. Mach.*, pp. 879–885, Sep. 2012.

[84] M. N. Uddin, "New online loss-minimization-based control of an induction motor drive," *IEEE Trans. Power Electron.*, vol. 23, no. 2, pp. 926–933, 2008.

[85] S. Vaez, V. I. John, and M. A. Rahman, "An on-line loss minimization controller for interior permanent magnet motor drives," *IEEE Trans. Energy Convers.*, vol. 14, no. 4, pp. 1435–1440, 1999.

[86] J. Lee, K. Nam, S. Choi, and S. Kwon, "A lookup table based loss minimizing control for FCEV permanent magnet synchronous motors," in *2007 IEEE Vehicle Power and Propulsion Conference*, 2007, no. 1, pp. 175–179.

[87] Y. Nakamura, T. Kudo, F. Ishibashi, and S. Hibino, "High-efficiency drive due to power factor control of a permanent magnet synchronous motor," *IEEE Trans. Power Electron.*, vol. 10, no. 2, pp. 247–253, Mar. 1995.

[88] W. Xu, S. Member, and R. D. Lorenz, "Dynamic loss minimization using improved deadbeat-direct torque and flux control for interior permanent-magnet synchronous machines," *IEEE Trans. Ind. Appl.*, vol. 50, no. 2, pp. 1053–1065, 2014.

[89] W. Xie, X. Wang, F. Wang, W. Xu, R. Kennel, and D. Gerling, "Dynamic loss minimization of finite control set-model predictive torque control for electric drive system," *IEEE Trans. Power Electron.*, vol. 31, no. 1, pp. 849–860, 2016.

[90] H. Ge, B. Bilgin, and A. Emadi, "Global loss minimization control of PMSM considering cross-coupling and saturation," in *2015 IEEE Energy Conversion Congress and Exposition (ECCE)*, 2015, pp. 6139–6144.

[91] A. Emadi, *Energy-Efficient Electric Motors: Selection and Applications*, New York, NY: Marcel Dekker, ISBN: 0-8247-5735-1, Sept. 2004

[92] C. Cavallaro, A. O. DiTommaso, R. Miceli, A. Raciti, G. R. Galluzzo, and M. Trapanese, "Efficiency enhancement of permanent-magnet synchronous motor drives by online loss minimization approaches," *IEEE Trans. Ind. Electron.*, vol. 52, no. 4, pp. 1153–1160, Aug. 2005.

[93] C. Mademlis and N. Margaris, "Loss minimization in vector-controlled interior permanent-magnet synchronous motor drives," *IEEE Trans. Ind. Electron.*, vol. 49, no. 6, pp. 1344–1347, Dec. 2002.

[94] J. Lee, K. Nam, S. Choi, and S. Kwon, "Loss-minimizing control of PMSM with the use of polynomial approximations," *IEEE Trans. Power Electron.*, vol. 24, no. 4, pp. 1071–1082, Apr. 2009.

[95] Y. Jeong, S. Sul, S. Hiti, and K. M. Rahman, "Online minimum-copper-loss control of an interior permanent-magnet synchronous machine for automotive applications," *IEEE Trans. Ind. Appl.*, vol. 42, no. 5, pp. 1222–1229, Sep. 2006.

[96] Z. Li and H. Li, "MTPA control of PMSM system considering saturation and cross-coupling," in *2012 15th International Conference on Electrical Machines and Systems (ICEMS)*, 2012, pp. 1–5.

[97] M. Ionel, M. Popescu, M. I. McGilp, T. J. E. Miller, S. J. Dellinger, and R. J. Heideman, "Computation of core losses in electrical machines using improved models for laminated steel," *IEEE Trans. Ind. Appl.*, vol. 43, no. 6, pp. 1554–1564, 2007.

[98] Y. Ying, Z. Jianguo, and G. Youguang, "A permanent magnet synchronous motor model with core loss," *Japanese Soc. Appl. Electromagn. Mech.*, vol. 15, pp. 147–150, 2007.

[99] G. Slemon and R. Bonert, "Modeling of iron losses of permanent-magnet synchronous motors," *IEEE Trans. Ind. Appl.*, vol. 39, no. 3, pp. 734–742, May 2003.

[100] S. Boyd and L. Vandenberghe, *Convex Optimization*. Cambridge, Cambridge University Press, 2004.

[101] R. H. Staunton, C. W. Ayers, L. D. Marlino, J. N. Chiasson, and T. A. Burress, "Evaluation of 2004 Toyota Prius hybrid electric drive system," Oak Ridge National Laboratory , Oak Ridge, Tennessee, Tech. Report. 2006.

[102] I. R. Bojoi, E. Armando, G. Pellegrino, and S. G. Rosu, "Self-commissioning of inverter nonlinear effects in AC drives," in *2012 IEEE International Energy Conference and Exhibition (ENERGYCON)*, 2012, pp. 213–218.

[103] G. Cintron-Rivera, A. S. Babel, E. E. Montalvo-Ortiz, S. N. Foster, and E. G. Strangas, "A simplified characterization method including saturation effects for permanent magnet machines," *2012 XXth Int. Conf. Electr. Mach.*, pp. 837–843, Sep. 2012.

[104] Chen, J. Xiong, Z. Wan, J. Lei, and K. Zhang, "Time delay compensation method based on area equivalence for active damping of LCL-type converter," *IEEE Trans. Power Electron.*, vol. 8993, no. 99, pp. 1–1, 2016.

[105] R. Siebert, J. Schneider, and E. Beyer, "Laser cutting and mechanical cutting of electrical steels and its effect on the magnetic properties," *IEEE Trans. Magn.*, vol. 50, no. 4, pp. 1–4, Apr. 2014.

[106] Thermal analysis of an IPM motor, Jmag Application Note. JAC018an-07e. Appl. Note.